Dielectric studies on $Ba_5Nb_4O_{15}$–$BaWO_4$ bulk and thin films

A Thesis Submitted to
Indian Institute of Technology Guwahati
for the Degree of

Doctor of Philosophy

By

Anil Kumar C

Department of Physics
Indian Institute of Technology Guwahati
Guwahati - 781039
Assam, India
January 2017

INDIAN INSTITUTE OF TECHNOLOGY GUWAHATI
Department of Physics
Guwahati – 781039

STATEMENT

The present thesis entitled, **“Dielectric studies on $Ba_5Nb_4O_{15}$–$BaWO_4$ bulk and thin films”** has been carried out by me under the supervision of Dr. D. Pamu, Department of Physics, Indian Institute of Technology Guwahati. This work has not been submitted elsewhere for the award of any degree.

January, 2017

(**Anil Kumar C**)
Department of Physics,
Indian Institute of Technology Guwahati,
Guwahati – 781 039

INDIAN INSTITUTE OF TECHNOLOGY GUWAHATI
Department of Physics
Guwahati – 781039

CERTIFICATE

It is certified that the work described in this thesis, entitled “**Dielectric studies on $Ba_5Nb_4O_{15}$–$BaWO_4$ bulk and thin films**”, done by Mr. Anil Kumar C, a Ph.D. student of Department of Physics, Indian Institute of Technology Guwahati, for the award of degree of *Doctor of Philosophy* has been carried out under my supervision. This work has not been submitted elsewhere for the award of any degree.

January, 2017.

Dr. D. Pamu
Associate Professor,
Department of Physics,
Indian Institute of Technology Guwahati,
Guwahati – 781 039.

Dedicated to my family

ACKNOWLEDGEMENTS

Almost five years of hard work and the countless help and support from the people around me made it today possible to complete the thesis work.

It is honour for me to thank my research supervisor, Dr. D. Pamu, Department of Physics, for his constant support, guidance, encouragement, advices, and valuable discussions, which helped me to improve an understanding of the subject along with skills and successful culmination of my thesis work. I must acknowledge him for providing the unconditional freedom to work, think and express on whatever I have done in my research work by keeping the faith on my capabilities.

I am highly thankful to my doctoral committee members, Prof. Alika Khare (Chairman), Dr. Dilip Pal and Dr. S. Kanagaraj for their continuous academic guidance and checking my work progress and seminars during my Ph.D. Their valuable discussions and suggestions were truly encouraging for me.

I express my sincere thanks to Prof. S. Ravi for providing lab space and facilities and treated me as one of his students. I am also thankful to Prof. A. Perumal, Prof. A. Srinivasan, and Dr. Dilip Pal for extending lab facilities.

I would like to express my sincere gratitude to Prof. Poulose Poulose, head of the Department of the Physics, and former head of the departments, Prof. Saurabh Basu, for giving me the opportunity to work in the department and to use departmental facilities. I am also grateful to all the faculty members of the Physics department. I would also like to thank Dr. Sidananda Sarma for his technical assistance and friendly discussions. My special thanks to all scientific officers and staff members in our department and central instruments facility.

My special thanks to Mrs. S. Josephine for helping me in doing microwave dielectric measurements. I acknowledge Prof. P. K. Iyer for providing the electrical measurements of thin films.

The financial support for this thesis is provided by Indian Institute of Technology Guwahati and Ministry of Human Resource and Development. Also, I would like to express my heartfelt thanks to Department of Science and Technology (DST), New Delhi; Board of Research in Nuclear Sciences, Mumbai; Defense Research and Development Organization, New Delhi; and Board of Research in Fusion Science & Technology, Gandhinagar, Gujarat through research projects for various experimental facilities. The XRD facility provided by DST, New Delhi, through FIST program [SR/FST/PSII-020/2009] is also acknowledged.

I am also grateful to my seniors Dr. T. Santhosh Kumar, Dr. Ranjan Kumar Bhuyan, Dr. P. Mahesh and Dr. P. Rajender for sharing their knowledge and useful discussions. I would like to thank my research team members and colleagues Pallabi, Srinivas, Susmita, Bipul, Junmoni, Gyan, Bibhuti, Pratap, Sanjeev, Deep, Ram, Aakanksha and Jagan for their help, suggestions and enjoyable company. I am grateful to Dr. G. Murali and Dr. N. Subbarao for their help in electrical measurements.

I would like to thank my best friends at IIT Guwahati, especially, Ramakrishna, Venkanna, Ranganatha, Hari, Rajender, Ravi and Ajay for creating a friendly and homely atmosphere.

Finally, I would like to express my deepest gratitude to my family, especially, my parents (Jamuna Garu and Laxman Garu), brothers (Sunil and Susheel) and all other family members, who gave blessings, moral support and continuous encouragement.

Anil Kumar C

Abstract

In recent years, the microwave ceramics have attracted a great attention due to the remarkable progress in the wireless communication systems, such as cellular phones, direct broadcasting satellites, wireless local-area networks and global positioning systems. There is an enormous demand for microwave dielectric resonators (DRs) with high dielectric constant (ε_r), high - quality factor ($Q = 1/tan\delta$) and a near temperature coefficient of resonant frequency (τ_f) close to zero, due to these reasons the microwave dielectric ceramics have been studied extensively. DRs are ceramic specimens that can act as frequency determining component at microwave frequencies. DRs can create filter and select frequencies in oscillators, amplifiers and tuners. In addition, their low cost of product and excellent integrability to microwave integrated circuits (MICs) make them indispensable components in microwave oscillators, filters and in dielectric resonator antennas. These materials are also being used for making substrates for MICs, and low temperature co-fired ceramic (LTCC) based highly miniaturized microwave systems. Further, metal oxide surface coatings performing a wide range of applications in the antireflection coatings; complementary metal oxide semiconductor (CMOS) and optoelectronic devices, etc. During an analogous process, nanocrystalline thin film capacitors with low dielectric losses (low $tan\delta$), the appropriate permittivity (depending on the application) became important in microwave-based communication technologies. Besides this, thin films having lower crystallization temperature as compared to bulk samples. Further, manufacturing of high-energy storage thin film capacitors with high dielectric constant will make the miniaturization of microwave devices. Furthermore, it is also known that the physical and chemical properties of the films drastically deviate from the bulk properties due to the confined geometry and the properties of thin films significantly change with the processing parameters such as applied power, deposition time, substrate to target distance, Argon (Ar) to the oxygen (O_2) ratio, and working pressure, etc. Hence; it is important to study and understand the behavior of the films. Further, the use of metal oxide surface coatings are suitable in a wide range of applications such as antireflection coatings; microwave integrated circuits (MICs), complementary metal oxide semiconductor (CMOS) and optoelectronic devices.

Motivation of the Study

The $Ba_5Nb_4O_{15}$ (BNO) ceramics in bulk and thin film forms are promising for the above applications due to its excellent dielectric properties in both bulk and thin film forms; high dielectric constant (ε_r) ~ 39, Quality factor ($Q \times f_0$) ~ 23,700 GHz and temperature coefficient of resonance frequency (τ_f ~ +78 ppm/^{o}C). BNO ceramics reveals hexagonal perovskites structure with $P\overline{3}m1$ space group. Nevertheless, the disadvantage with this material is the formation of subordinate phases when the samples were prepared using the solid-state reaction method and higher sintering temperature, which limits the applications of this material in various applications. To address the above problems; we have chosen to prepare the BNO ceramics using the mechanical alloying method and small initial particle sizes. However, dielectric studies on bulk form of these BNO ceramics were reported by Jawahar *et al*. Conversely, a couple of reports were available on the BNO ceramics focused on reduction in sintering temperature with different additives. In general, to reduce the sintering temperature of the microwave ceramics, the following methods were adopted in the literature (i) smaller initial particle sizes, (ii) chemical processing methods and (iii) low melting glassy additives. Further, the addition of sintering aids significantly affected the dielectric response of the ceramics, especially the loss tangent. To minimize the problems associated with the above methods, the present study is aimed at the addition of the smaller concentrations of BNO nanoparticles to the micron sized BNO matrix as a sintering aid. It is well known that the smaller particles enhance the densification at lower sintering temperatures. In addition, due to the similar chemical nature, the addition of nanoparticles would not deteriorate the microwave dielectric properties. The addition of nanoparticles of same material as a sintering aid to the micronsized particle is not well understood, hence, this study. The effect of BNO nanosized particles addition on microstructure and microwave dielectric properties of a host BNO ceramics were carried out and discussed. However, Yu-Jen Hsiao et al. reported the synthesis of BNO ceramics by sol-gel process. Nevertheless, this study was only focussed on the microstructure, but there is no systematic study on BNO ceramics prepared by sol-gel process and their microwave dielectric resonator point of view. This motivated the authors to study the effect of BNO nanoparticles (prepared by sol-gel process) addition on micron sized BNO matrix to enhance the dielectric properties.

In addition, the low permittivities and high-quality factor values of the scheelite ceramics $BaWO_4$ (BWO) is regarded as promising material for microwave substrate applications. $BaWO_4$ ceramics are also promising for the above applications due to its excellent dielectric properties in bulk form: dielectric constant (ε_r) ~ 8.0, Quality factor ($Q\times f_0$) ~ 57 500 GHz and temperature coefficient of resonance frequency (τ_f ~ -78 ppm/°C). BWO ceramics reveal a tetragonal structure, and crystallize in the $I4_1/a$ space group. There are few reports available on the microwave dielectric properties of BWO ceramics in bulk form. $BaWO_4$ (BWO) ceramics have been prepared and characterized by using different experimental techniques. From the preparation of BWO ceramics with solid state reaction method, we observed that the sample experienced was brittle in nature (easily breaking) with an increase in the sintering temperature. Hence, we have prepared BWO ceramics with the mechanical alloying methods. Furthermore, among the high - ε_r and low loss dielectric materials, the $Ba_5Nb_4O_{15}$ - $BaWO_4$ composite ceramics have been studied broadly due to their promising microwave dielectric properties at lower sintering temperatures: ε_r = 16.9 - 21, $Q\times f_0$ = 49,500 – 56,700 GHz and τ_f = 8.9 to -4.3 ppm / °C. In the recent years, the Low temperature co-fired ceramics (LTCC) technology is widely used for miniaturization of microwave devices to reduce the size of wireless communication systems and this technology is well-known both for high volume, low cost application (wireless communication and car industry) and low volume high performance applications (military, space). Recently, the LTCC has become crucial in the development of various modules and substrates. In this technology, several thin layers of low-permittivity ceramic composites and conductors are combined, and the resulting multilayered LTCC modules that are generally used in the form of a 3D wiring circuit board today. The LTCC enables a versatile mix of passive microwave components like microstrips, striplines, antennas, filters, resonators, capacitors, inductors, phase shifters and dividers, making possible a whole matrix of design that are not practical on regular alumina or any soft substrates. Furthermore, these integrated components are interconnected with 3D stripline circuitry. Among the various components that could be realized in LTCC packages, the resonators and internal capacitors are important in terms of the latest technology. The internal capacitors are required to realize decoupling capacitors monolithically in LTCC packages, and the resonators are needed for filters of quarter wavelengths on the LTCC layer. However, the appropriate relative permittivity range for the resonators and the internal capacitors is 20-100 were reported by Delaney *et* *al*. The important characteristic requirements for the LTCC based material is that it should have lower sintering behaviour (< 1000 °C), chemical compatibility (material should not react with the conductive material used), control of shrinkage during sintering and low product cost. The recent development of LTCC technology is demanding for high frequency wireless communication systems, which is an advanced approach to fabricate the ceramic structures with high speed and high frequency processing devices in the electronic industry. In the present work, we developed $Ba_5Nb_4O_{15}$ - $BaWO_4$ composite ceramic matrix system with the addition of their own nanoparticles of $Ba_5Nb_4O_{15}$ and $BaWO_4$ and studied their effect on sintering temperature on their physical properties such as structural, microstructural, and microwave dielectric properties of the prepared composite ceramics. However, to the best of the author's knowledge, there is no study available on the preparation of nanoparticles of BNO and BWO ceramics and their addition as a sintering aid to BNO - BWO composite ceramics, hence this study.

In addition, it is well known that the optical, microstructural, electrical and dielectric properties are strongly dependent on thickness and the processing technique, and it is important to understand how the response of a material as a function of thickness. In contrast, to the best of the authors' knowledge, there is no report available on the BNO thin films; this motivated us to pursue this study. Therefore, this work focuses on deposition and characterization of nanocrystalline BNO thin films by Radio frequency (RF) magnetron sputtering. Study the effect of thickness on the structural, electrical and dielectric properties of BNO films. Furthermore, certain oxide films exhibit a chromic response and are extensively investigated due to their wide applications in smart windows, gasochromatic sensors, displays to block the infrared radiation, and in solar cell applications. Thermochromism arises due to the changes in optical properties with change in deposition temperature and is seen in a large number of compounds. The films change their optical response (non - reversible color changes upon heating) with the substrate temperature. Because the variation of temperature is one of the easiest approaches of aiming to change the nature of materials, it is appropriate to use the observation of thermochromism, particularly in the visible range. The thermal behaviour of the different materials may be divided into two divisions one exhibits non - reversible thermochromism over a wide temperature range, and the other displays a sharp interchange in optical properties at a particular temperature. The non reversible thermochromism can be used as protective layers and window color coatings. Nevertheless, there are very few studies available on BWO thin films and there is no report available on irreversible thermochromic nature of BWO films. Pontes et al. studied structural and optical properties of BWO films prepared by chemical route. Dinesh et al. demonstrated the growth of crystalline BWO films at room temperature and reported structural and microstructure of these films. Cho et al. obtained a highly crystallized BWO films at room temperature by using an electrochemical method. However, irreversible thermochromic behaviour was not observed in BWO films prepared by the above methods. Moreover, most of the studies were focussed on the room temperature crystallization of BWO films. Further, it is known that the properties of the films dependent upon the deposition technique. Furthermore, the systematic study on optical properties and growth of BWO films using RF plasma has not been studied earlier. In the current study, we report the growth of BWO films at different substrate temperatures using RF reactive magnetron sputtering technique. The significance of this study is to demonstrate irreversible thermochromic response and optical properties of BWO films for the first time. In addition, there are only few studies have been reported on optical properties of $BaWO_4$ thin films. To the best of our knowledge, there have been no reports on the optical, dielectric and electrical properties of $BaWO_4$and $Ba_5Nb_4O_{15}$ - $BaWO_4$ composite thin films deposited by RF magnetron sputtering. In general, to deposit the composite films, pulsed laser deposition is being used, which is a costly technique. Hence, in the present study, we have used RF magnetron sputtering to deposit nanocomposite BNO - BWO films. Sputtering has attracted a considerable attention due to its simplicity, large throughput, and deposition over a wide range of pressures and transfer of stoichiometry of the target to the films.

As a relentless effort in our research laboratory on microwave materials, we have chosen to investigate the $Ba_5Nb_4O_{15}$ and $BaWO_4$ in the bulk form prepared by the mechanical alloying method and semi alkoxide precursor (sol - gel) method. The $Ba_5Nb_4O_{15}$ - $BaWO_4$ composite has been prepared in the bulk form using the conventional solid - state reaction method. We have attempted different techniques to reduce the sintering temperature of the bulk $Ba_5Nb_4O_{15}$ and $Ba_5Nb_4O_{15}$ - $BaWO_4$ and have been successful to some extent. The $Ba_5Nb_4O_{15}$, $BaWO_4$ and $Ba_5Nb_4O_{15}$ - $BaWO_4$ thin films were prepared by the RF magnetron sputtering. The deposition parameters were optimized to fabricate uniform films with high adhesion to the substrate. We have deposited $Ba_5Nb_4O_{15}$, $BaWO_4$ and $Ba_5Nb_4O_{15}$ - $BaWO_4$ films from a ceramic target which is prepared using the optimized processing conditions of bulk $Ba_5Nb_4O_{15}$, $BaWO_4$ and $Ba_5Nb_4O_{15}$ - $BaWO_4$ ceramics.

The overall efforts in this study are to enhance the microwave dielectric properties of the bulk samples by improving the microstructure and relative density of this material prepared with the addition of their own nanoparticles prepared by sol - gel process. Furthermore, it is proposed to compare the microwave properties of $Ba_5Nb_4O_{15}$, $BaWO_4$ and $Ba_5Nb_4O_{15}$ - $BaWO_4$ in bulk and thin film forms. In addition, we have also investigated their optical and electrical properties, which could not only be useful in other applications but also helps in arriving at a comprehensive picture of the physics of these materials, and the results were compared with the existing literature.

The complete thesis contains six chapters. A brief description of the contents of each chapter is given below.

Chapter 1

First chapter provides the brief introduction to dielectric materials, dielectric resonators (DR) and related areas. A historical background and the development of dielectric resonators (DR) from the physics and device points of view are presented. The basic requirements of a material to be used as DR, a brief overview on DR materials, its mode characteristics and the applications are described. Furthermore, the importance of high dielectric constant and low loss films, the characteristics of SiO_2 in CMOS devices and the difficulties of its replacement are discussed. The basic applications of dielectric thin films were also been discussed. Subsequently, the importance of $Ba_5Nb_4O_{15}$ (BNO), $BaWO_4$ (BWO) and $Ba_5Nb_4O_{15}$ - $BaWO_4$ as a DR and a brief overview on its crystal structure and microwave dielectric properties are presented. The motivation behind choosing $Ba_5Nb_4O_{15}$ - $BaWO_4$ is presented towards the end of this chapter.

Chapter 2

In second chapter, various preparation and characterization techniques, being used for both the bulk and thin films of $Ba_5Nb_4O_{15}$, $BaWO_4$ and $Ba_5Nb_4O_{15}$ - $BaWO_4$ composite ceramics are presented. The $Ba_5Nb_4O_{15}$ and $BaWO_4$ ceramics have been prepared using mechanical alloying method and semi - alkoxide precursor (sol - gel) method. The $Ba_5Nb_4O_{15}$ - $BaWO_4$ composites have been prepared in the bulk form using the conventional solid - state reaction method. The effects of ball milling and sintering mechanism were discussed in detail. Structural properties were characterized using x-ray diffraction and microscopy techniques to obtain the microstructure. Apparent densities of the prepared $Ba_5Nb_4O_{15}$, $BaWO_4$ and $Ba_5Nb_4O_{15}$ - $BaWO_4$ composite ceramics measured by using Archimedes's method, dielectric constant (ε_r) and the quality factor values (Q) at microwave frequencies measured using the Hakki-Coleman dielectric resonator method as modified and improved by Courtney, and the measurements of electrical properties using impedance spectroscopy are discussed. In addition, an introduction to the RF magnetron sputtering technique for the thin film fabrication, the envelop technique to calculate the optical constants are given in detail. Furthermore, the details on the techniques used for electrical and the low-frequency dielectric properties of the films using a "Metal-Insulator-Metal (MIM) capacitor structure" and microwave dielectric properties of the films using the SPDR technique are also discussed in this chapter.

Chapter 3

This chapter describes the preparation of pure phase $Ba_5Nb_4O_{15}$ (BNO) ceramic in two different methods: while the former one is a mechanical alloying method, the later one is a conventional solid-state reaction method. BNO samples prepared by using the mechanical alloying method by optimizing the process conditions such as milling time, ball to powder ratio, milling speed, sintering temperature and sintering duration. The obtained best dielectric properties at microwave frequencies are $\varepsilon_r = 34$, $Q \times f_0 = 32.5$ THz (7 GHz) are attributed to increase in density and uniform grain size for the BNO samples milled for 40 h, sintered at 1250 ^{o}C. Furthermore, we have studied the effect of BNO nanoparticles (prepared by sol - gel process) on the microstructure, high frequency dielectric and microwave dielectric properties of bulk $Ba_5Nb_4O_{15}$ ceramics (prepared by conventional solid-state reaction method) are discussed. The BNO thin films prepared by RF magnetron sputtering are described by optimization of all processing conditions. The sputtering targets of BNO ceramics prepared by optimized processing conditions of the mechanical alloying method. The BNO thin films were deposited on to various substrates (amorphous SiO_2 and platinized silicon ($Pt/TiO_2/SiO_2/Si$)) under different oxygen mixing percentage (OMP) in the sputtering gas. The effects of OMP and post annealing temperature on the structural, microstructural, optical and dielectric properties were presented. To the best of the authors' knowledge, there is no report available on the BNO thin films; this motivated us to pursue these studies. Upon annealing, refractive indices of the films were found to be enhanced whereas the bandgap is decreased. The obtained refractive index values are in the range of 1.82-2.05, and 1.89-2.16 @ 550 nm for the as-deposited and annealed BNO films, respectively. The estimated optical bandgap values for the as deposited and annealed films are in the range of 4.13 - 4.36 *eV* and 4.07- 4.24

eV, correspondingly. The best dielectric properties were obtained for the BNO film with thickness of 450 nm are ε_r = 41 and $tan\delta$ = 0.0005 at 1 MHz. Split-post dielectric resonator method was used to measure dielectric properties at discrete microwave frequencies (5, 10 and 15 GHz) and are in the range of ε_r = 29.65 - 43.56 and $tan\delta$ = 0.0074 - 0.0020, for BNO annealed films. The detailed observations, discussion and possible explanations are presented in this chapter.

Chapter 4

In fourth chapter, we have prepared $BaWO_4$ (BWO) samples by using a mechanical alloying method. The crystal structure, microstructure, and microwave dielectric properties of BWO ceramics are discussed. The obtained best dielectric properties at microwave frequencies are ε_r = 16.3, $Q\times f_0$ = 38 THz (11.6 GHz) these are attributed to increase in density and uniform grain size for the BNO and BWO samples milled for 50 h, sintered at 800 ^{o}C, respectively. The BWO thin films were deposited by RF magnetron sputtering on amorphous SiO_2, and on platinized silicon ($Pt/TiO_2/SiO_2/Si$) substrates under the influence of different oxygen mixing percentage (OMP) in the sputtering gas by optimizing all processing conditions. The sputtering target of BWO was prepared by optimized processing conditions in the mechanical alloying method. The effects of OMP and post annealing temperature on the structural, microstructural, optical and dielectric properties were presented. To the best of the authors' knowledge, there is no report available on the BWO thin films; this motivated us to pursue these studies. BWO films have been deposited at different substrate temperatures (RT, 200, 400, 600 and 800 ^{o}C) using RF magnetron sputtering in pure argon plasma. BWO films deposited at 800 ^{o}C exhibit crystalline nature. First time we are reporting the irreversible thermochromic behaviour of $BaWO_4$ (BWO) films. The optical bandgap of BWO films increases significantly with an increase in Oxygen mixing percentage (OMP) during the deposition. The optical bandgap of the BWO films deposited at different temperatures in pure argon plasma, are in the range of 3.7 to 3.94 *eV* whereas the films deposited at 600 ^{o}C under different OMP plasma are in the range of 3.6 - 4.5 *eV*. Metal-Insulator-Metal (MIM) capacitors were fabricated under different OMPs for the films deposited on platinized silicon substrates. The measured dielectric properties show a progressive improvement with OMP and a maximum asset value of ε_r = 15 and $tan\delta$ = 0.019 at 1 MHz are obtained for the BWO film deposited at 50% OMP. Split-post dielectric resonator method was used to measure dielectric properties at discrete microwave frequencies (5, 10 and 15

GHz) and are in the range of ε_r = 11.94 - 18.16 and $tan\delta$ = 0.010 - 0.030, for BWO annealed films. The detailed observations, discussion and possible explanations are given in this chapter.

Chapter 5

In this chapter, we describe the prepared $Ba_5Nb_4O_{15}$ - $BaWO_4$ composite in the bulk form using the conventional solid - state reaction method. The best microwave dielectric properties of ε_r ~ 39, $Q \times f_0$ ~ 59.8 THz (9.44 GHz) were obtained for the BNO - BWO composite ceramics, sintered at 900 °C. Furthermore, studied the effect of BNO and BWO nanosized particles (prepared by sol - gel process) addition on the microstructure, high frequency dielectric and microwave dielectric properties of the $Ba_5Nb_4O_{15}$ - $BaWO_4$ composite ceramics are discussed. The BNO - BWO composite thin films were prepared by using RF magnetron sputtering. The dielectric constant of the BNO - BWO films enhanced with an increase in OMP, whereas the $tan\delta$ reduced significantly. The BNO - BWO films deposited in pure argon atmosphere exhibited low dielectric constant (18.7) and high loss tangent (0.0047) whereas the films deposited in pure oxygen plasma showed high dielectric constant (34) and low loss tangent (0.0011). Split-post dielectric resonator method was used to measure dielectric properties at discrete microwave frequencies (5, 10 and 15 GHz) and are in the range of ε_r = 22.47 - 49.81 and $tan\delta$ = 0.0038 - 0.0010, for BNO - BWO annealed films.

Chapter 6

The sixth chapter describes (i) the correlation between bulk and thin film properties of BNO, BWO and BNO - BWO (ii) summary of the thesis work, potential applications and (iii) possibilities for further research work.

ABBREVIATIONS

Units of measurement

mm	Millimeter
cm	Centimeter
μm	Micrometer
nm	Nanometer
Å	Angstrom
^{o}C	Centigrade (degree)
kHz	Kilo hertz
MHz	Mega hertz
GHz	Giga hertz
THz	Tera hertz
ppm	Parts per million
h	Hours
SCCM	Standard cubic centimeter per minute
kV	Kilovolt
eV	Electron-volt
gm	Gram
W	Watt
A	Ampere

Electrical measurements

ε_r	Dielectric constant
ε_m	Porosity corrected dielectric constant
$tan\delta$	Loss tangent
f_o	Resonant frequency
Q	Quality factor
Q_u	Unloaded quality factor
$Q \times f_o$	Product of Q and resonant frequency

τ_f (TCF)	Temperature co-efficient of resonant frequency
σ_{ac}	AC conductivity
J	Leakage current density
E	Electric field
C	Capacitance
d	Thickness
V	Unit cell volume
τ_0	Central relaxation time
$\Delta\varepsilon$	Dielectric relaxation strength
α and β	Symmetric and asymmetric distribution parameters
DC	Direct current
AC	Alternative current
E_A	Activation energy
ω	Angular frequency
k_B	Boltzmann constant

Optical measurements

α	Absorption coefficient
n	Refractive index
n_b	Bulk refractive index
P	Packing density
E_g	Optical bandgap
h	Planck’s constant
λ	Wavelength
c	Velocity of light
$h\nu$	Photon energy

Other parameters

θ	Angle
FWHM	Full width at half maximum
a, b, c	Lattice parameters

χ^2	Chi-square
R_{Bragg}	Bragg factor
R_f	Profile factor
F	Orientation factor
wt.	Weight
RT	Room temperature
RF	Radio frequency
OMP	Oxygen mixing percentage
SPDR	Split post dielectric resonator
MIM	Metal-insulator-metal
DSC	Differential scanning calorimetry
TGA	Thermal gravimetric analysis
XRD	X-Ray diffraction
SEM	Scanning electron microscopy
FESEM	Field emission scanning electron microscopy
EDS	Energy dispersive X-ray spectrometer
DR	Dielectric resonator
MA	Mechanical alloying
BNO	$Ba_5Nb_4O_{15}$
BWO	$BaWO_4$
LTCC	Low temperature co-fired ceramics

CONTENTS

LIST OF FIGURES

Chapter 3

Chapter 4

Chapter 5

LIST OF TABLES

Chapter 1

Chapter 3

Chapter 4

Chapter 5

Chapter 1

Introduction

1.1 Introduction

Over the past few decades, microwave dielectric materials are playing a significant role in communication technologies and in particular, wireless communication technologies, global positioning system (GPS), and direct broadcast satellite television (DBS TV) to environmental monitoring via satellites are one of the most important growth in the global electronic industry [1, 2]. The current development in microwave telecommunication, satellite broadcasting and intelligent transport systems (ITS) has led to ever-increasing demand for dielectric resonators (DRs), which are low loss ceramic specimens mainly used in wireless communication devices. The miniaturization of devices for the mobile phone and satellite communication systems using microwaves as the carrier is the biggest challenges for the research and development in contemporary materials science. In microwave wireless communication industry, the dielectric oxide ceramics have revolutionized by reducing the size and cost of filter, oscillator and antenna components in applications ranging from cellular phones to global positioning systems. In the recent years, the miniaturization of devices such as cell phones, provides a continuing driving force for the discovery and growth of increasingly sophisticated materials to carry out the same or improved function with decreased size and weight.

A DR is an electromagnetic component that shows resonance for a narrow range of frequencies with productive properties. The resonance is similar to that of a circular hollow metallic waveguide apart from the boundary being defined by a large change in permittivity rather than by a conductor. In general, dielectric resonators consist of ceramic specimen and the major key properties required for a DR are high dielectric constant (ε_r), high quality factor ($Q\times f_o$) (i.e., low loss), and temperature coefficient of resonant frequency close to zero (τ_f) [3 - 7]. The most favorable DR that satisfies these three properties at the same time is difficult to achieve in a particular material.

Initially, bulk metallic cavities were used as resonators, but were huge and they cannot be incorporated with microwave integrated circuits (MICs). On the other hand, stripline resonators have a poor quality factor and poor temperature stability resulting in the instability of the circuit. Therefore, the significance of DRs which are well, integrated with MICs with low loss and with thermally stable frequency, perticularly at millimeter (mm) wavelengths. The majority of the microwave-based device systems are placed in the frequency range 300 MHz - 300 GHz. The technological improvements in ceramic dielectric resonators have the advantage of being more miniaturized as compared to traditional microwave cavities, and have a considerably higher quality factors. The cavity resonators have been replaced with DRs in most microwave and millimeter-wave applications for reasons of cost, dimension, mass, stability, efficiency, tenability, ruggedness and ease of use. In addition, the DRs can create and filter frequencies in oscillators, amplifiers and tuners, in order to make important components in communication circuits to meet circuit designer's requirements. The low dielectric constant (ε_r) ceramics are used for millimeter-wave communication and also as substrates for microwave integrated circuits. The medium dielectric constant (ε_r) ceramics with dielectric constant in the range of 25 - 50 are used for satellite communications and in cell phone base stations. The high dielectric constant (ε_r) materials are used in mobile phones, where miniaturization of the device is very important. For millimeter wave and substrate application, a temperature stable, low dielectric constant and high ($Q \times f_o$) (low loss) materials are necessary for high speed signal transmission with minimum attenuation [8]. In the present chapter, a brief introduction and historical development of DRs with their technological importance are discussed. The fundamental physical prospects of dielectric resonators and the factors affecting the microwave dielectric properties are studied. Further, the optical and electronic applications of thin films with their importance in diverse areas of interest in the present technological world are also being described. Eventually, the crystal structure of $Ba_5Nb_4O_{15}$, $BaWO_4$ and $Ba_5Nb_4O_{15}$ -$BaWO_4$ ceramics and the motivation behind this present thesis work are presented.

1.2 Microwave dielectric resonators

1.2.1 Introduction to dielectric resonator

Dielectric Resonators (DRs) are ceramic specimens that can act as frequency determining component at microwave frequencies. DRs can create filters and select frequencies in oscillators, amplifiers and tuners used in modern communication systems. In addition, their low cost of production and excellent integrability to microwave integrated circuits (MICs) make them indispensable components in microwave oscillators, filters and in dielectric resonator antennas. Until recently, in the microwave communication devices, quartz, metallic and microstrip resonators were used.

Nevertheless, quartz resonators were used to generate, stabilize and filter frequencies in the communication devices and these resonators are not so attractive because of small signal-to-noise ratio obtainable with frequency multiplication to microwave frequencies and their bulky nature. Consequently, the metallic cavity resonators were developed and these resonators are difficult to integrate with the microwave integrated circuits (MICs). Afterward, microstrip resonators were developed. However, this one had high dielectric loss and poor temperature stability resulting in the instability of the circuit. Next attempt was the use of ceramic specimens in the form of dielectric resonators, which are resonating at the frequency of the carrier signal to allow that signal to be efficiently separated from other signals in the microwave band. This led to a profitable development of novel ceramic microwave DRs.

1.2.2 Historical development of dielectric resonator from literature review

Prior to discussing about certain materials, it is useful to review the historical development and the necessities of the materials simply from the application point of view of microwave dielectric properties.

Lord Rayleigh [9] depicted that an infinitely long cylinder of a dielectric specimen can serve as a guide for electromagnetic waves at certain frequencies, which means that the dielectric has the effect of causing the electromagnetic wave to be confined to the cylinder and its vicinity. In 1939, the term "**Dielectric Resonator**" was first introduced by Ritchtmeyer (from Stanford University) [10] and he theoretically predicted that a suitably shaped dielectric specimen could behave as microwave resonator. Nevertheless, the significant interest happened in this area in 1953, Schlicke [11] reported on super-high dielectric constant materials (~ 1000) and their applications as capacitors in low radio frequencies. Later in 1960 Okaya [12] found that a speciment of rutile TiO_2 acted as a resonator and soon in 1962 Okaya and Barash again discovered the DRs from Columbia University [13], while working on single crystal rutile (TiO_2) and their associated literature provided the first analysis of modes and resonator design. TiO_2 has high dielectric constant (≈ 100), low dielectric losses, and $\tau_f = +450$ ppm/^{o}C. Therefore, due to its poor temperature stability, TiO_2 was not placed into practical use. This causes large variation in resonant frequency. Afterwards, in 1968 Bolton [14] reported a temperature stable with maximum dielectric constants approximately 60 - 80 was attained for tungsten bronze structured $BaTiO_3$-Ln_2O_3-TiO_2. Later, Negas et al. [15] observed that the work of Bolton is rarely acknowledged in consequent literature, but provided the technical base for a host of investigations of tungsten bronze structure materials. A real breakthrough in ceramic technology took place in between late 1970s and early 1980s, when Masse et al.[16] built up the first temperature stable low loss barium-tetratitanate ($Ba_2Ti_4O_9$) together with (Mg, Ca)TiO_3 and $ZrTiO_4$ ceramics. However, temperature stable microwave DRs were developed by Konishi [17] and Ploudre [18] using the composite structure of positive and negative temperature coefficients. Later, substantial theoretical and experimental works were carried out and the use of DR was increased in extent rapidly. The microwave dielectric materials are used for different applications depending on the relative permittivity, particularly for high relative permittivity materials (ε_r = 70 - 120) for mobile telephone handset applications and very high Q- materials (40,000 $<Q\times f_o<$ 250,000) with medium relative permittivity (ε_r = 25 - 50) for base station applications [19]. Now-a-days almost more than 1500 microwave dielectric ceramics have been looked into for dielectric resonator applications [20]. Research is still continuing to find new materials with improved properties.

The most important reason for confinement of microwaves in and in the vicinity of a DR is its large value of dielectric constant (ε_r). The dielectric boundary will be a perfect reflector of microwave if the angle of incidence is larger than the critical angle $\theta_c = \sin^{-1}(1/\varepsilon_r)$. For large value of ε_r, θ_c is totally internally reflected. Depending on the geometry, the waves will undergo multiple internal reflections. The reflection co-efficient approaches unity as the dielectric constant increases. For this reason, Kajfez [21] considered the dielectric air boundary of a high dielectric material as an interface closer to a perfect magnetic conductor (PMC), in which the magnetic field tangential to its surface is zero. As the dielectric constant raises, the electric and magnetic fields are confined in and near the resonator resulting in small radiation losses.

1.2.3 Current state of materials developed for DR applications

At present, a large number of microwave dielectric materials have been developed with enhanced dielectric properties for useful purposes [22 - 28]. Initially, the production of microwave dielectric resonators were based on (Mg, Ca)TiO_3, $ZrTiO_4$ and $Ba_2TiO_9O_{20}$. Likewise, $CaTiO_3$ - $NdAlO_3$ (CTNA) and $ZrTiO_4$ - $ZnNb_2O_6$ (ZT - ZN) based ceramics prevails the base station resonator market. Recently, Ba(Co, Zn)$_{1/3}$Nb$_{2/3}$O$_3$ (BCZN) based ceramics are newly developed, which are cheaper and this material can be replaced instead of expensive material like Ba(Zn$_{1/3}$Ta$_{2/3}$)O$_3$ based materials [29]. M. T. Sebastian et al [30] surveyed and described more than 3500 microwave ceramics with their microwave dielectric properties.

1.2.3.1 Importance of perovskite structure and scheelite tungstate compounds used for DR applications

Compounds with perovskite structure with a general formula ABO_3 have been of continuous importance for many years [31]. The properties of perovskites depend critically on the nature of the metal atoms in the A and B sites. As a consequence, substitutions on the A and/or B sites allow varying their properties over wide ranges, which makes them adaptable to various technical requirements. Perovskites have been used in numerous applications such as dielectric resonators, filters and antennas in a vast field of domains like wireless communication devices, radar, direct broadcasting satellites and global positioning systems [32 - 34]. Tantalum-based ceramics such as $Ba_3ZnTa_2O_9$ (BZT) and $Ba_3MgTa_2O_9$ (BMT) are frequently used as materials for dielectric resonators, despite the elevated tantalum price. First attempt on the synthesis of complex perovskite was reported by Galasso and Pyle [35] and Galasso and Pinto [36] with the modification in the B-site. The structures that result when there exist perfect ordering in B-site with divalent and pentavalent ions in one set of compounds and trivalent and pentavalent ions in the other set of compounds (A = Pb and Ba: B′ = Mg, Zn, Y, Fe, Nd and Gd etc., and B″ = Nb and Ta). Some of the well known complex perovskite are $Ba(Zn_{1/3}Nb_{2/3})O_3$, $Sr(Zn_{1/3}Nb_{2/3})O_3$ [37, 38], $(Sr_xLa_{1-x})MnO_3$ [39], etc. The $A_5B_4O_{15}$ (A = Ba, Sr, Mg, Ca; B = Nb, Ta) dielectric ceramics have good microwave dielectric properties, including high relative permittivity (ε_r), high quality factor (Q), and low temperature coefficient of resonator frequency (τ_f). Both $CaWO_4$ and $PbWO_4$ are promising materials for the next generation of cryogenic phonon-scintillation detectors [40 - 42]. The scheelite tungstates are in fact technologically important materials within a wider scope, having been used during the last few years as solid-state scintillators [43 - 45] and in other optoelectronic devices [46 - 48]. A significant amount of research work on the structural behavior of AWO_4 compounds exists [49 - 52] and this corpus forms a solid background for understanding the main physical properties of these materials.

$Ba_5Nb_4O_{15}$ (BNO) ceramics are promising for the above applications due to its excellent dielectric properties in bulk form: high dielectric constant (ε_r) ~ 39, Quality factor ($Q\times f_o$) ~ 23.7 THz and temperature coefficient of resonance frequency (τ_f ~ +78 ppm/^{o}C). There are few reports available on synthesis of BNO ceramics by solid-state reaction method, and few authors have used different additives/sintering aids to reduce the sin-tering temperature and to tune the τ_f. Nonetheless, the addition of different supplements deteriorated the micro-wave dielectric properties, especially the loss tangent [53 - 55]. To reduce the sintering temperature of BNO ceramics, Hsiao and Chang [56] prepared the BNO ceramics through sol-gel process and the reported sintering temperatures were in between 700 and 900 °C; however, they did not study the microwave dielectric properties. The low permittivities and high-quality factor values of the scheelite ceramics $BaWO_4$ (BWO) regarded as a promising material for microwave substrate applications [57]. $BaWO_4$ ceramics are suitable for the above applications due to its excellent dielectric properties in bulk form: dielectric constant (ε_r) ~ 8.0, Quality factor ($Q\times f_0$) ~ 57.5 THz and temperature coefficient of resonance frequency (τ_f ~ -78 ppm/^{o}C). There are few reports available on the microwave dielectric properties of BWO ceramics in bulk form [57, 58]. In addition, there are only few studies that have been reported on optical properties of $BaWO_4$ thin films [59, 60]. To the best of our knowledge, there have been no reports on the dielectric and electrical properties of $BaWO_4$ thin films deposited by RF magnetron sputtering. Due to their excellent dielectric properties and cost effectiveness, all these materials are suitable for millimeter wave communication and as microwave substrates. Further, it is also found that these materials are highly resistant at elevated temperatures and highly reflective for wavelengths in UV region, which make them preferable materials for reflective optical coatings in aerospace applications. The $Ba_5Nb_4O_{15}$ - $BaWO_4$ composite ceramics have been studied broadly due to their promising microwave dielectric properties at lower sintering temperatures: ε_r = 16.9 - 21, $Q\times f_0$ = 49.5 - 56.7 THz and τ_f = 8.9 to -4.3 ppm / ^{o}C [61]. These composite ceramics are promising materials for microwave and millimeter wave applications. Further, the addition of B_2O_3 to BNO - BWO composite considerably elevated the densification process and lowered the sintering temperature (~ 900 ^{o}C) and this composite material is compatible with Ag electrodes [62]. Hence, the BNO - BWO composite is suitable for LTCC applications.

1.2.4 Future requirements of the DR materials

Technological advances of the future require innovations aimed at envisioning, predicting, designing, developing and manufacturing of microwave dielectric materials with prescribed form, and properties customized for desired performance requirements and applications. Hence, basic understanding of microwave ceramics is needed to improve existing materials and find out new materials for advanced applications. In order for microwave dielectric ceramics to be used in base stations, they must certainly offer a marketable advantage over competing technologies. Particularly, metal cavities offer an alternative to ceramic resonators. The $Q\times f_o$ factors of metal cavities are noticeably lower (~ 6 THz) but they are two orders of magnitude cheaper. The high price of ceramics comes from the expensive raw materials such as Nb_2O_5 and Ta_2O_5, and the complex fabrication processes needed to ensure best possible properties. Hence, ceramics are only used where high Q is paramount and miniaturization is essential. At the same time, the efforts are focused on to improve Q, particularly by minimizing the extrinsic losses of the microwave ceramics.

Over the competing technologies, ceramics offer a distinct advantage in the use of irregular geometries to induce multimode resonance, by reducing space and cost. During ceramic processing, unusual shapes and designs also lay down new challenges to ceramists to control ε_r, Q and τ_f [63]. The microwave ceramic resonator market for base station technology has matured and industry is concentrating primarily on improvement on Q and saving its cost [63]. New applications for low loss microwave ceramics are constantly emerging such as global positioning systems (GPS), low temperature co-fired ceramics (LTCC) for embedded microwave circuitry, tunable filters and higher frequency applications for advanced radar technology [63]. Moreover, in the 21st century, the environmental circumstances are a big issue. As a result, microwave ceramics need to be environmental friendly.

1.3 Physics of DR materials

1.3.1 Polarization mechanisms in dielectrics

Polarization is an ordering in space of an electrically charged unit under the influence of an external electric field. This causes the formation of an electric moment in the entire volume of the dielectric and in each separate polarizing unit (atom, ion or molecule). Linear dielectrics show a direct proportionality between the induced electric dipole moment p acquired by the polarizable unit during the process of polarization and the intensity E of the electric field acting on it as given by $p = \alpha E$, where, α is known as polarizability reflecting the properties of individual polarizable unit, which is the most important microscopic electrical parameter of a dielectric. Under the influence of an electric field on dielectric material four types polarization mechanisms can occur, i.e. interfacial, dipolar, ionic and electronic. Piling up of mobile charge carriers at physical barrier such as grain boundary causes for interfacial polarization or space charge polarization. At low frequencies, this mechanism gives rise to high dielectric constant and in some cases may extend up to 10^3 Hz. In the zero field, the permanent dipoles will be randomly oriented and the system has no net polarization, but an electric field will tend to align these dipoles and the materials will acquire a net moment. This is called orientational polarization. In other words, the perturbation of thermal motion of the ionic or molecular dipoles, producing a net dipolar orientation in the direction of the applied field. Two mechanisms can be operative in this case [64]. (a) In linear dielectrics dipolar polarization results from the motion of the charged ions between the interstitial positions in ionic structures parallel to the applied field direction. The mechanism is active in the 10^3 - 10^6 Hz range. (b) Molecules having permanent dipole moment may be rotated about an equilibrium position against an elastic restoring position. Its frequency of relaxation is very high of the order of ~ 10^{11} Hz. The dipolar polarization contributes to the dielectric constant in the sub-infrared range of frequencies. The displacement of positive and negative ions with respect to each other gives rise to ionic polarization. The mechanism contributes to the dielectric constant at infrared frequency range (~10^{12} - 10^{13} Hz). When an electric field is applied, the valence electron cloud shifts with respect to the nucleus the atom acquires a dipole moment. This occurs at high frequencies of about 10^{15} Hz. The mechanisms of these four polarizations are illustrated schematically in Fig. 1.1. Each of these involves a short - range motion of charge and contributes to the total polarization of the material, and at microwave frequencies, ionic and electronic polarizations contribute to the dielectric properties [65].

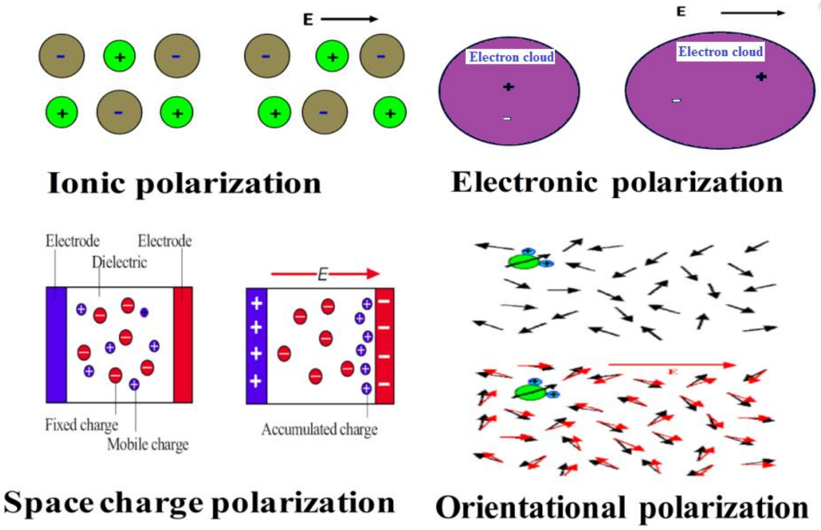

Fig. 1.1: *Different types of polarization mechanisms appear in a dielectric [66].*

1.3.2 Theory of dielectric losses

Dielectric loss is one of the most relentless problem in materials science and the far infrared spectroscopy have been used to help in the characterization of the dielectric properties of some low loss materials in the microwave region [67 - 69]. Many microwave dielectric loss mechanisms are classified in to two categories: (i) intrinsic and (ii) extrinsic [70, 71]. Inherent losses in crystals arise because of anharmonic lattice forces that mediate the interaction between the crystal and phonons. This leads to damping of the optical phonons and, therefore, of the microwave field. These losses are called as intrinsic losses and this mechanism is dependent on the composition, crystal structure and independent of the processing conditions and microstructure. On the other hand, losses in ceramics caused by extended dislocations, grain boundaries, porosity, impurities and secondary phases are termed as extrinsic dielectric losses and which can be minimized by the careful material processing. In the far infrared region the intrinsic factors play a vital role since the intrinsic dielectric losses are much stronger than the extrinsic ones [72, 73]. In principle, it should therefore be possible to extract the value of intrinsic losses in the microwave region from the infrared data if the extrapolation law is known. In the following section a complete theory of intrinsic dielectric losses are discussed.

Approximately 30 years ago, Wakino et al. [68, 69] proposed propound infrared (IR) reflectivity spectroscopy as a tool for investigating the intrinsic microwave (MW) dielectric properties of dielectric resonators. It is well known that the main infrared dispersion of the permittivity is given by the sum of polar phonon contributions,

$$\varepsilon^{*}(\omega)=\varepsilon^{'}(\omega)-i\varepsilon^{''}(\omega)=\varepsilon_{\infty}+\sum_{j=1}^{n}\frac{\Delta\varepsilon_{j}\omega_{j}^{2}}{\omega_{j}^{2}-\omega^{2}+i\omega\gamma_{j}} \tag{1.1}$$

Where, ε_{∞} is the permittivity at optical frequencies, ω_j and γ_j are the frequencies and damping constant of the j^{th} polar phonon, respectively; $\Delta\varepsilon_j$ denotes the mode contribution to the static permittivity $\varepsilon'(0)$ of the j^{th} polar lattice mode. Wakino et al. [68, 69] mentioned that extrapolating this model from IR down to MW range, i.e., at $\omega << \omega_j$ gives constant real part of the permittivity,

$$\varepsilon^{'}(\omega)=\varepsilon_{\infty}+\sum_{j=1}^{n}\Delta\varepsilon_{j} \tag{1.2}$$

While the dielectric losses ε'' are proportional to frequency,

$$\varepsilon'' = \tan\delta = \omega \sum_{j=1}^{n} \frac{\Delta\varepsilon_j \gamma_j}{\omega_j^4} \tag{1.3}$$

At high temperatures (around and above room temperature), the phonon damping should be linearly temperature dependent, i.e,

$$\varepsilon''(\omega, T) \propto \omega \times T \tag{1.4}$$

This implies that the dielectric loss could be linearly extrapolated from the IR range down to MW region. The method described above was used in the study of many MW ceramics and it was shown that it gives rather good estimation of intrinsic MW losses. Although Eq. (1.1) is valid only in the range near phonon frequencies and the use of this formula is not theoretically justified for frequencies much lower than ω_j , i.e., in MW range.

Afterward, Gurevich and Tagantsev [72, 73] formulated a comprehensive microscopic phonon transport theory and have shown that depending on crystalline symmetry, temperature interval, frequency range and some parameters of the phonon spectrum, the frequency and temperature dependence of intrinsic dielectric loss can be described by a power law [73].

$$\varepsilon''(\omega, T) \approx \omega^n \times T^m \tag{1.5}$$

Where n = 1 - 5 and m = 1 - 9. In the MW range far below the frequencies of the mean phonon damping, two-phonon difference decay process dominated at room and medium-high temperatures and the theory predicts,

$$\varepsilon''(\omega, T) \approx \omega \times T^2 \tag{1.6}$$

We note that at low temperatures Eq. (1.6) is not valid, but Eq. (1.5) with steeper temperature dependences is theoretically expected. Eq. (1.3) shows that in case of prevailing intrinsic losses, the product of quality factor (Q) and frequency f ($\omega = 2\pi f$) is estimated to be constant, a rule which holds, at least for many ceramics. Further, it is extensively accepted that the intrinsic dielectric losses can be estimated by spectroscopic methods such as Fourier Transform Infrared Spectroscopy (FTIR) [74] and therefore this method is now often is used for the characterization of classical microwave ceramics and related compounds [75].

1.4 Major requirements of material for DR applications

1.4.1 High dielectric constant (ε_r)

Dielectric resonator material with high dielectric constant (ε_r) in the range 20 - 100 or more are needed for applications. High dielectric constant facilitates miniaturization of the devices and the miniaturization is proportional to $1/(\varepsilon)^{1/2}$. A cylindrically shaped DR sustains an electromagnetic standing wave within its volume because of the total multiple internal reflections at the dielectric air interface. The wavelength of the standing wave is about equal to the diameter of the cylinder and is given by [76],

$$\lambda_d \approx D_r \approx \frac{c}{f_o \varepsilon_r^{1/2}} \tag{1.7}$$

Where, λ_d is the wavelength of the standing wave along the diameter (D_r) of the resonator, c is the velocity of the electromagnetic waves in vacuum; f_o is the resonant frequency in GHz and ε_r is the relative permittivity of the resonator. Hence, if the relative permittivity is increased, the size of the resonator may be decreased while still maintaining a specific resonant frequency, i. e., larger dielectric constants enable miniaturization.

1.4.2 High quality factor (Low dielectric loss)

Any type of defects such as grain boundaries, stacking faults, chemical or structural disorder, point defects, planar defects, line defects, inclusions, secondary phases, twinning, porosity etc contribute losses. For an ideal crystal quality factor (Q) is approximately equal to the reciprocal of the dielectric loss ($\tan\,\delta$). In the microwave region, the loss is mainly due to the interaction of the applied field with phonons [77]. Most preferably, larger the value of Q, better is the device performance. Further, it can be defined as the measure of energy loss or dissipation per cycle with respect to the energy stored in the fields inside the resonator and is given by [78],

$$Q = 2\pi \frac{\text{maximum energy stored per cycle}}{\text{average energy dissipated per cycle}}$$

$$Q = \frac{2\pi W_o}{PT} = \frac{\omega_o W_o}{P} \tag{1.8}$$

Where, W_o is stored energy, P is power dissipation and ω_o is the resonant angular frequency and $T = 2\pi/\omega_o$ is the time period.

Ideal dielectrics have no losses since, its electrical conductivity is zero, but the real dielectric materials are partially conducting. Hence, electromagnetic signal looses power as it goes through a dielectric material. For DR applications Q-factor is important and losses should be minimum. When a resonant circuit or cavity is utilized as a load in a microwave circuit, the quality factor is called loaded Q-factor, which can be determined by the ratio of resonant frequency (f_o) to the half power bandwidth (Δf_o), measured at 3 dB below the maximum height at resonance [79], by using following relation,

$$Q_l = \frac{f_o}{\Delta f_o} \tag{1.9}$$

It is therefore, a direct measure of the ability of the resonating body to select a given frequency. Higher the Q value, better is the signal to noise ratio, so that the risk of cross talk within a given frequency range reduces.

The loaded-Q factor (Q_l) arises, when a dielectric resonator is connected to some external circuit. This is the overall Q-factor of the material including both internal losses [called as unloaded Q-factor (Q_u)] and external losses. For cavity resonators, the power loss due to conductors, dielectric fills and radiation can be contributed to Q_u as given by,

$$\frac{1}{Q_u} = \frac{1}{Q_d} + \frac{1}{Q_c} + \frac{1}{Q_r} \tag{1.10}$$

Where, $1/\,Q_d$ is the dielectric loss, $1/\,Q_c$ is the loss due to conductivity of the metallic plates and $1/\,Q_r$ is the loss due to radiation. The majority of the resonant cavities are completely shielded, so that there is no radiation effect, and hence this term can be neglected. Therefore, the total loss of the system is given by,

$$\frac{1}{Q_l} = \frac{1}{Q_o} + \frac{1}{Q_{ext}} \tag{1.11}$$

Where, $1/\,Q_l$ is the total loss of the system, $1/\,Q_o$ is the total internal loss and $1/\,Q_{ext}$ is the loss due to external coupling. Nevertheless, the quality factor of a DR can only be measured as the loaded value (Q_l) by keeping in an external circuit. Therefore, it is essential to have a relation between the two forms of quality factor (Q_l and Q_u) and is given by,

$$Q_u = \frac{Q_l}{(1-\beta_c)} \tag{1.12}$$

Where, β_c is the coupling coefficient. To get accurate value of Q_u, weakly coupled case ($\beta_c < 1$) is preferred [19]. The value of coupling constant can be calculated,

$$\beta_c = 10^{\frac{-S_{21}}{20}} \tag{1.13}$$

Where, S_{21} is the insertion loss of the resonating system.

There are three important mechanisms for microwave absorption: 1) losses in ideal crystals because of anharmonic lattice forces which mediate interaction between crystal lattice and phonons 2) losses in real but homogeneous crystals caused by the periodicity defects (isotopes, dopant atoms, vacancies, etc.) and 3) losses in real inhomogeneous ceramics by extended dislocations, grain boundaries, pores and secondary phases. The first category of loss can be influenced by modifying the composition itself by changing the crystal structure. The other categories of loss depend on many irrelevant factors and hence could be influenced by additives and processing conditions.

1.4.3 The coefficient of temperature variation of the resonant frequency (τ_f)

The ceramic dielectric resonators having another essential advantage are the temperature stability. The resonant frequency of the circuit will tend to shift over temperature as a result of environment factors such as the size and linear thermal expansion coefficient of the metal DR enclosure, the position of the resonator within the cavity, type of resonator support, temperature dependence of other circuit elements, etc. This shifting in resonant frequency can be significantly affected by the DR's intrinsic temperature coefficient of resonant frequency (τ_f). Therefore, the temperature coefficient of resonant frequency (τ_f) can be defined as the drift in the resonant frequency with respect to temperature. This eventually determines how well a resonator will function when there is fluctuation in temperature. The electronic device with microwave resonators requires τ_f values as close to zero as possible. The origin of τ_f is related to linear expansion coefficient (α_L) which affects the resonator dimensions and the temperature coefficient of relative permittivity (τ_ε) [76, 79]. Mathematically the relationship is

$$\tau_f = -\alpha_L - \frac{1}{2}\tau_\varepsilon \tag{1.14}$$

Using the Clausius-Mosotti equation, Bosman and Havinga [80] derived an expression for τ_ε at a constant pressure, as follows:

$$\tau_\varepsilon = \frac{1}{\varepsilon_r}\left(\frac{\partial \varepsilon_r}{\partial T}\right)_P = \frac{(\varepsilon_r - 1)(\varepsilon_r + 2)}{\varepsilon_r}(A + B + C) = \left(\varepsilon_r - \frac{2}{\varepsilon_r} + 1\right)(A + B + C) \qquad (1.15)$$

Where, $A = \frac{1}{3V}\left(\frac{\partial V}{\partial T}\right)_P$, $B = \frac{1}{3\alpha_m}\left(\frac{\partial \alpha_m}{\partial V}\right)_T\left(\frac{\partial V}{\partial T}\right)_P$ and $C = \frac{1}{3\alpha_m}\left(\frac{\partial \alpha_m}{\partial T}\right)_V$ and

α_m = total polarizability, V = volume, T = temperature, P = pressure, and ε_r = relative permittivity.

Each of the terms in this equation describes a change in dielectric behaviour as a function of temperature. As a result of the thermal expansion of the lattice, there is a reduction in the concentration of bonds that can become dipoles and this is described by term *A* in the equation. Although there is a reduction in the concentration of particles available for polarization as the lattice expands, the increase in volume enables an increase in the polarizability of a given bond (term *B*). The final term *C*, represents the change in polarizability as a function of temperature.

Further, the τ_f is related to the temperature coefficient of capacitance (τ_c) by the following relation [81],

$$\tau_f = \frac{1}{2}(\tau_C - \alpha_L) \qquad (1.16)$$

Experimentally, τ_f is measured by following the drift in the resonance peak frequency (f_o) as the temperature is gradually varied. One can also calculate the coefficient of temperature variation of the resonant frequency (τ_f) which determines the frequency stability and τ_f is defined by using following equation:

$$\tau_f = \frac{1}{f_o} \times \frac{\Delta f}{\Delta T}\ ppm/^oC \qquad (1.17)$$

Where, Δf is the change in resonant frequency over a temperature difference of ΔT and f_o is the resonant frequency at room temperature (25 °C).

It is clearly revealed that a material with a significantly large τ_f is not useful in a microwave circuit as it cannot maintain its resonant frequency with changes in the operating temperature [79]. Hence, it is important to have a τ_f value that is as close to 0 ppm / °C, so that the signal does not change during device operation. On the other hand, in reality a small non zero value of τ_f (± 2 ppm/°C) is mandatory to compensate for thermal expansion of the microwave cavity and other components in the circuit. A material with a small positive value of τ_f variation can frequently be combined with another material with a small negative τ_f variation to build the resonator temperature stable.

1.5 Applications of microwave dielectric ceramics

Dielectric oxide ceramics have revolutionized the microwave wireless communication industry by reducing the size and cost of filter, oscillator and antenna components in applications ranging from cellular phones to global positioning systems. Ceramic resonators can be made into different geometries (examples: cylindrical, tubular, toroids, spheres, parallelepiped and cubes etc.) to suit the purpose of the component and are shown in Fig. 1.2 (a). In order to function the DR, conventionally puts within a silver-coated square cavity, as illustrated in Fig. 1.2 (b). Typically, many hundreds of these cavities will reside in the base stations of cellular network. A typical microwave oscillator consists of an active device (a diode or transistor) and a passive frequency determining resonate element (see Fig. 1.2 (c)). Its major applications include mobile-phone communication and satellite television receivers (TVRO and DBS). While DR filter (see Fig. 1.2 (d)) consists of ceramic resonator discs mounted in a particular way inside a metal cavity and are frequently used in radar and communication systems.

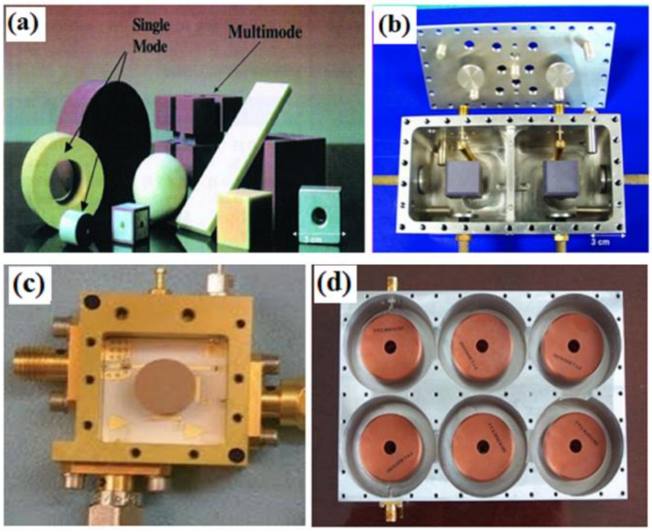

Fig.1.2: *(a)Various geometries of microwave dielectric resonators and filters and (b) DRs in a silver – coated air filled cavity [82] (c) Tuneable dielectric resonator oscillator and (d) Dielectric resonator filter (BL Microwave Ltd.).*

Under normal conditions, miniature dielectric filled coaxial resonators are used in wireless handsets such as cellular phones and personal communication systems (PCS)

[83]. Other distinctive practical applications include: wireless FAX, video recording devices, internet browsing capability, short messaging service (SMS), motion sensors, video games, high memory capacity for storage of personal media such as downloaded music and movies and personal organizer. It has been possible only to add all of these applications due to the materials development that has led to the miniaturization of device components. At a recent time, DRs are also broadly used in the range of 1 to 60 GHz [84]. Due to this extension of carrier frequency the research of ultrahigh speed communication system has been ongoing. For example, 60 GHz carrier frequency will be used soon for next generation Audio/Video (AV) centre at home. This will focus on the significance of materials with high quality factor rather than high dielectric constant.

Further, DRs are being used in making an important device in microwave integrated circuits due to its small size, light weight, low cost along with enhanced features like low loss, temperature compensated performance with good coupling and frequency tunability characteristics. At present, new applications such as, direct broadcasting satellite (DBS), 3G filters, intelligent transport system (ITS), ultra high speed wireless local-area networks, low temperature co-fired ceramics (LTCC) for embedded microwave circuitry and higher frequency applications for advanced radar technology as well as for high frequency temperature compensating capacitors [19] for DRs are persistently emerging.

In the recent years, the low temperature co-fired ceramics (LTCC) technology is widely used for miniaturization of microwave devices to reduce the size of wireless communication systems and this technology is well-known both for high volume, low cost application (wireless communication, car industry) and low volume high performance applications (military, space). Recently, the LTCC has become essential in the development of various modules and substrates [85 - 87]. In this technology, several thin layers of low-permittivity ceramic composites and conductors are combined, and the resulting multilayered LTCC modules that are generally used in the form of a 3D wiring circuit board today. The LTCC enables a versatile mix of passive microwave components like microstrips, striplines, antennas, filters, resonators, capacitors, inductors, phase shifters and dividers, making possible a whole matrix of design that are not practical on regular alumina or any soft substrates. Furthermore, these integrated components are interconnected with 3D stripline circuitry [85, 88, 89]. Among the various components that could be realized in LTCC packages, the resonators and internal capacitors are important in terms of the latest technology. The internal capacitors are required to realize decoupling capacitors monolithically in LTCC packages, and the resonators are needed for filters of quarter wavelengths on the LTCC layer. The appropriate relative permittivity range for the resonators and the internal capacitors is 20-100 [90, 91].

Hitoshi Ohsato [92] has plotted the quality factor ($Q \times f_o$) as a function of dielectric constant values for many of the published properties of tungsten-bronze and perovskite microwave dielectric ceramics and is illustrated in Fig.1.3 for the application point of view. Dielectric resonator materials used for millimetre-wave applications are required to have ultra high quality factor ($Q \times f_o$), low dielectric constant (ε_r < 15) and small temperature coefficient of resonant frequency (τ_f). In this point of view, many aluminate, forsterite and willemite based dielectric ceramics have attracted much attention due to their ultrahigh-Q and low ε_r. Common examples: Al_2O_3 [93], Mg_2SiO_4 [94] and Zn_2SiO_4 [95] with typical microwave dielectric properties of dielectric constants between 5 - 10 and high $Q \times f_o$ of 150 - 400 THz.

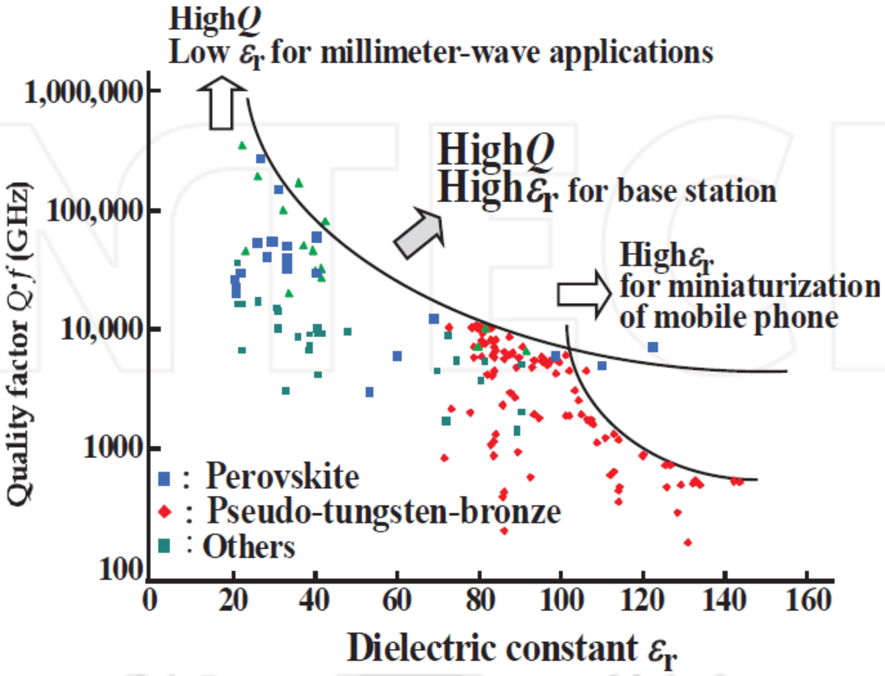

Fig. 1.3: *Variation of $Q \times f_o$ as a function of ε_r for different microwave dielectric ceramics [92].*

1.6 Thin film applications

Thin film science and technology play an important role in the present - day electronic industries. Thin film technology has been developed primarily for the need of the integrated circuit industry. The demand for development of smaller and smaller devices with higher speed, especially in new generation of integrated circuits requires advanced materials and modern processing techniques suitable for future giga scale integration (GSI) technology. In this regard, physics and technology of thin films can play an important role to achieve this goal. Thin films as a two - dimensional system are important to many real - world problems. Their material costs are very small as compared to the corresponding bulk material and they perform the same function when it comes to surface processes. Thus, knowledge and determination of the nature, functions and properties of thin films can be used for the development of new technologies for future applications. Thin film technology is based on three foundations: fabrication, characterization and applications. Some of the important applications of thin films are in microelectronics, communication, optical electronics, catalysis, surface coating of all kinds and in energy generation and conservation strategies.

Optically active thin film coatings, especially those with controllable light absorptance, transmittance, or reflectance, are of great interest because of their many potential applications. Single layers or layer systems can be used for different types of devices, which can reversibly alter their optical properties as a function of changes in external conditions, as temperature, intensity of irradiation, or applied external potential. In the near future, optically active thin films may be utilized to regulate the throughput of radiation energy for windows in buildings and cars, to maintain comfortable lighting and temperature, in sunglasses, as an optically active filter, or in systems with variable reflectance, as automotive rear view mirrors, in displays, as road signs, and so forth.

Thin films with changeable optical characteristics can be obtained by different physical and chemical processes in a large number of materials. These substances, recently named "chromogenics" embrace both inorganic and organic materials. A wide variety of optically active coatings have been discovered which appear suitable for use in technical systems. The mechanisms responsible for the variation of the optical properties of films may basically be divided into three different types: thermochromism, photochromism, and electrochromism.

i.) **Thermochromic** films change their optical properties as a function of the substance's temperature. The films alter their optical data reversibly when heated, and return to their original properties when cooled to the starting temperature.

ii.) **Photochromism** may be defined as a reversible absorption change undergone by a film when exposed to a certain type of irradiation, which regains the original properties when placed in the dark. This type of material has been investigated amply in glasses so far, but not in thin films.

iii.) Electrochromism is a unique property of thin films or thin film systems to change color, due to an applied potential, and change back to the original state by a potential reversal. From a technological point of view, thin electrochromic films are the best investigated and they are the most promising candidates for various applications in the proximate future.

Recent past, oxide films exhibit thermochromic response are extensively investigated due to their wide applications in smart windows, gasochromatic sensors, displays to block the infrared radiation, and in solar cell applications [96 - 98]. Thermochromism arises due to the changes in optical properties with change in deposition temperature and is seen in a large number of compounds [99]. The films alter their optical data (non - reversible color changes on heating) with the substrate temperature. Since the variation of temperature is one of the simplest methods of attempting to change the stage of materials, it is convenient to use the observation of thermochromism, especially in the visible range. The thermal behaviour of the different materials may be divided into two categories. One exhibits non - reversible thermochromism over a wide temperature range, the other exhibits a sharp change in optical properties at a definite temperature.

Furthermore, thin films have also great importance and significance for a large variety of industrial applications. The use of metal oxide surface coatings is performing a wide range of applications in the antireflection coatings; microwave integrated circuits (MICs), complementary metal oxide semiconductor (CMOS) and optoelectronic devices [100, 101]. Due to the comparatively eminent inertness of ceramic materials will make this type of thin films coatings used for wear and corrosion-resistant coatings [102]. Besides the thin films having been lowering crystallization temperature as compared to bulk samples and the manufacturing of high-energy storage thin film capacitors with high dielectric constant will make applications in the miniaturization of microwave constituents.

Researchers have succeeded in developing the techniques for extremely well controlled (atomic layer by layer) growth of thin films, and are currently active in computer modelling for predicting physical and chemical properties of new thin films materials. Thus, it is clear that the thin films are useful for optics (laser mirrors and transmission increasing coatings), electronics (layer of insulators, semiconductors, and conductors on ICs), packaging (aluminum foils), and so on.

1.7 $Ba_5Nb_4O_{15}$ - $BaWO_4$: Interesting system in both bulk and thin film forms

1.7.1 Bulk $Ba_5Nb_4O_{15}$ - $BaWO_4$ composite for microwave applications

Recently, dielectric materials based on the perovskite systems, has brought much more attention in the field of microwave engineering. Among these systems, $Ba_5Nb_4O_{15}$ - $BaWO_4$ are recognized as good candidates for high frequency applications. This is due to their extremely low dielectric loss, medium to high dielectric constant and low temperature coefficient of resonant frequency (τ_f). The $Ba_5Nb_4O_{15}$ - $BaWO_4$ composite ceramics have been studied extensively due to their excellent microwave dielectric properties of $\varepsilon_r = 16.9 - 21$, $Q\times f_0 = 49.5 - 56.7$ THz and $\tau_f = 8.9$ to -4.3 ppm / ^oC [27]. Hence, they offer a great stability to specific applications such as duplexers, filters, low phase-noise dielectric resonator oscillators and other applications. This composite is compatible with Ag electrodes and therefore, is more suitable for LTCC microwave devices. The more detail about its bulk form is discussed in the motivation section.

1.7.2 Crystal structure of $Ba_5Nb_4O_{15}$ and $BaWO_4$

Galasso et al. [103] showed that these $Ba_5Nb_4O_{15}$ ceramics reveals hexagonal perovskite structure and crystallized them in the $P\bar{3}m1$ space group. This type of material is called cation-deficient perovskites if written in the perovskite form (ABO_3), and $A_5B_4O_{15}$ is reduced to $AB_{0.8}O_3$. There is a vacancy of 0.2B cation per 1A cation, i.e., overall 1B cation vacancy per 5A cations. The BNO ceramics also have the closest packing of oxygen and barium ions into five layers. The niobium ions are located in the octahedral holes between layers. One layer of the octahedral hole does not have niobium ions to obtain the charge neutrality. Therefore, there is an empty octahedra, which results in the loss of face sharing on the NbO_6 sublattice, and this structure implies strong anharmonicity. Jawahar et al [104] showed that a considerable distortion can be noted in the empty octahedral which has the great electrostatic valence imbalance. The $Ba_5Nb_4O_{15}$ shows a hexagonal structure (Fig. 1.4 (a)) with $\varepsilon_r = 39$, $Q\times f_o = 23{,}700$ and $\tau_f = 78$ ppm/ ◦C. The $Ba_5Ta_4O_{15}$ has a lower $\varepsilon_r = 28$ than that of $Ba_5Nb_4O_{15}$, even though its tantalum has larger ionic polarizability. This is because the lattice of $Ba_5Ta_4O_{15}$ is stable whereas that of $Ba_5Nb_4O_{15}$ could collapse to a lower symmetry. Lattice anharmonicity causes a relatively higher permittivity for $Ba_5Nb_4O_{15}$ compound. $BaWO_4$ ceramics revealed the tetragonal system with $I_{41/a}$ space group, construction of 1×1×1 unit cell of $BaWO_4$ as shown in Fig. 1.4 (b). In $BaWO_4$ unit cell, the tungsten atoms are coordinated to four oxygen atoms in a tetrahedral configuration. The oxygen coordination polyhedra are slightly distorted, presenting different bonding angles (108.56 ° and 111.30 °) between O-W-O [105]. The barium atoms are coordinated to eight oxygen atoms localized in the corners of the tetragonal unit cell. The crystal structure is highly ionic for the Ba^{2+} cations and tetrahedral $[WO_4]^{2-}$ anions. The bonds between Ba-O and W-O were highlighted outside of the unit cell as shown in Fig. 1.4 (b).

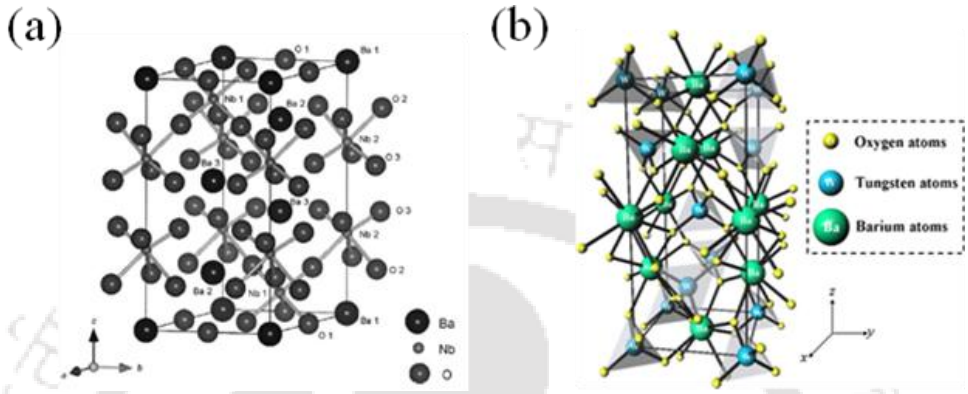

Fig.1.4: *(a) Crystal structure of $Ba_5Nb_4O_{15}$ compound (b) 1×1×1 unit cell of $BaWO_4$ tetragonal structure.*

The typical lattice parameters of $Ba_5Nb_4O_{15}$ ceramics are $a = b = 5.79240$ Å, $c = 11.7775$ Å and $BaWO_4$ ceramics are $a = b = 5.62340$ Å, $c = 12.68840$ Å. The Wyckoff position, atomic coordinates of the $Ba_5Nb_4O_{15}$ and $BaWO_4$ systems are given in the **Table 1.1 and 1.2**.

Table 1.1: *Occupied Wyckoff position, atomic coordinates of $Ba_5Nb_4O_{15}$ (BNO) system [103].*

Atoms	**Wyckoff positions**	***x***	***y***	***z***
Ba1	*a*	0.00000	0.00000	0.00000
Ba2	*d*	0.33333	0.66667	0.79400
Ba3	*d*	0.33333	0.66667	0.43490
Nb1	*d*	0.00000	0.00000	0.68200
Nb2	*c*	0.33333	0.66667	0.10900
O1	*e*	0.50000	0.00000	0.00000
O2	*i*	0.16800	0.16190	0.61300
O3	*i*	0.16200	0.16800	0.19200

Table 1.2: *Occupied Wyckoff position, atomic coordinates of $BaWO_4$ (BWO) system [106].*

Atoms	**Wyckoff positions**	***x***	***y***	***z***
Ba	*4b*	0.00000	0.24800	0.62000
W	*4a*	0.00000	0.25100	0.12000
O	*16f*	0.12240	0.01660	0.20304

1.8 Motivation of the present thesis work

The current thesis work is focused on $Ba_5Nb_4O_{15}$ - $BaWO_4$ composite ceramics bulk and thin film forms. However, before preparing and studying the properties of this composite, it is essential to understand the $Ba_5Nb_4O_{15}$ and $BaWO_4$ ceramics individually and hence we have studied their properties also in bulk and thin film form. The $Ba_5Nb_4O_{15}$ (BNO) and $BaWO_4$ (BWO) ceramics are interesting due to their excellent dielectric properties in bulk form: good dielectric constant (ε_r) ~ 39.0 and 8.0, Quality factor ($Q\times f_o$) ~ 23.7 THz and 57.5 THz and temperature coefficient of resonance frequency (τ_f ~ +78 ppm/^{o}C and -78 ppm/^{o}C), respectively [107 - 109]. The BNO and BWO ceramics reveals hexagonal perovskites structure and tetragonal structure with $P\bar{3}m1$ and $I4_1/a$ space group. Nevertheless, the disadvantage with BNO material is the formation of subordinate phases and BWO ceramics are brittle in nature (easily breaking) when the samples were prepared using solid-state reaction method and higher sintering temperature, which limits the applications of these materials in various applications. To address the above problems; we have chosen to prepare the BNO and BWO ceramics using the mechanical alloying method and with small initial particle sizes. The present study is also aimed at the addition of the smaller concentrations of BNO nanoparticles to the micron sized BNO matrix as a sintering aid. It is well known that the smaller particles enhance the densification at lower sintering temperatures. In addition, due to the similar chemical nature, the addition of nanoparticles would not deteriorate the microwave dielectric properties. The addition of nanoparticles of same material as a sintering aid to the micronsized particle is not well understood, hence, this study. The effect of BNO nanosized particles (prepared by sol-gel process) addition on microstructure and microwave dielectric properties of a host BNO ceramics were carried out and discussed. Furthermore, among the high - ε_r and low loss dielectric materials, the $Ba_5Nb_4O_{15}$ - $BaWO_4$ composite ceramics have been studied broadly due to their promising microwave dielectric properties at lower sintering temperatures: ε_r = 16.9 - 21, $Q\times f_0$ = 49.5 - 56.7 THz and τ_f = 8.9 to -4.3 ppm / °C [27, 28]. The recent development of LTCC technology is demanding for high frequency wireless communication systems, which is an advanced approach to fabricate the ceramic structures with high speed and high frequency processing devices in the electronic industry [110 - 114]. The important characteristic requirements for the LTCC based materials is that it should have lower sintering behaviour (< 1000 °C), chemical compatibility (material should not react with the conductive material used), control of shrinkage on sintering and low product cost. In the present work, we have developed $Ba_5Nb_4O_{15}$ - $BaWO_4$ composite ceramic matrix system with the addition of their own nanoparticles of $Ba_5Nb_4O_{15}$ and $BaWO_4$ and studied their effect on sintering temperature on their physical properties such as structural, microstructural, and microwave dielectric properties of the prepared composite ceramics. However, to the best of the author's knowledge there is no study available on the preparation of nanoparticles of BNO and BWO ceramics and their addition as a sintering aid to BNO - BWO composite ceramics, hence this study.

Also, there have been no reports on the optical, dielectric and electrical properties of $Ba_5Nb_4O_{15}$, $BaWO_4$ and $Ba_5Nb_4O_{15}$ - $BaWO_4$ composite thin films deposited by RF magnetron sputtering. In general, to deposit the composite films, pulsed laser deposition is being used, which is a costly technique. Hence, in the present study, we have used Radiofrequency (RF) magnetron sputtering to deposit nanocomposite BNO - BWO films. Sputtering has attracted a considerable attention due to its simplicity, large throughput, deposition over a wide range of pressures and transfer of stoichiometry of the target to the films. In addition, oxide films exhibit chromic response are extensively investigated due to their wide applications in smart windows, gasochromatic sensors, displays to block the infrared radiation, and in solar cell applications. Nevertheless, there are very few studies available on BWO thin films and there is no report available on irreversible thermochromic nature of BWO films. Pontes et al. [115] studied structural and optical properties of BWO films prepared by chemical route. Dinesh et al. [116, 117] demonstrated the growth of crystalline BWO films at room temperature and reported structural and microstructure of these films. Cho et al. [118] obtained highly crystallized BWO films at room temperature by using electrochemical method. However, irreversible thermochromic behaviour was not observed in BWO films prepared by the above methods. Moreover, most of the studies were focussed on the room temperature crystallization of BWO films. Further, it is known that the properties of the films dependent on the deposition technique. Also, the systematic study on optical properties and growth of BWO films using RF plasma has not been studied earlier. In the current study, we report the growth of BWO films at different substrate temperatures using RF reactive magnetron sputtering technique. The significance of this study is to demonstrate irreversible thermochromic response and optical properties of BWO films for the first time. In addition, there are only few studies have been reported on optical properties of $BaWO_4$ thin films.

As a relentless effort in our research laboratory on microwave materials, we have chosen to investigate the $Ba_5Nb_4O_{15}$ and $BaWO_4$ in the bulk form prepared by the mechanical alloying method and semi alkoxide precursor (sol - gel) method. The $Ba_5Nb_4O_{15}$ - $BaWO_4$ composite have been prepared in the bulk form using the conventional solid - state reaction method. We have attempted different techniques to reduce the sintering temperature of the bulk $Ba_5Nb_4O_{15}$ and $Ba_5Nb_4O_{15}$ - $BaWO_4$ and have been successful to some extent. The $Ba_5Nb_4O_{15}$, $BaWO_4$ and $Ba_5Nb_4O_{15}$ - $BaWO_4$ thin films were prepared by the RF magnetron sputtering. The deposition parameters can be optimized to fabricate uniform films with high adhesion to the substrate. We have deposited $Ba_5Nb_4O_{15}$, $BaWO_4$ and $Ba_5Nb_4O_{15}$ - $BaWO_4$ films from a ceramic target which is prepared using the optimized processing conditions of bulk $Ba_5Nb_4O_{15}$, $BaWO_4$ and $Ba_5Nb_4O_{15}$ - $BaWO_4$ ceramics.

The overall efforts in this study are to enhance the microwave dielectric properties of the bulk samples by improving the microstructure and relative density of this material prepared with the addition of their own nanoparticles prepared by sol - gel process. Furthermore, it is proposed to compare the microwave properties of $Ba_5Nb_4O_{15}$, $BaWO_4$ and $Ba_5Nb_4O_{15}$ - $BaWO_4$ in bulk and thin film forms. In addition, we have also investigated their optical and electrical properties, which could not only be useful in other applications but also helps in arriving at a comprehensive picture of the physics of these materials, and the results were compared with the existing literature.

1.9 References:

[1] C. L. Huang, C. F. Tseng, T. J. Yang, *J. Am. Ceram. Soc.* **91** (2008) 2201.

[2] C. L. Huang, J. J. Wange, Y. P. Chang, *J. Am. Ceram. Soc.* **90** (2007) 858.

[3] C. L. Huang, J. F. Tseng, *Mater. Letts.* **58** (2004) 3732.

[4] R. J. Cava, *J. Mater. Chem.* **11** (2001) 54.

[5] D. Pamu, G. L. Narayana Rao, K. C. J. Raju, *J. Alloy. Compd.* **475** (2009) 745.

[6] K. Sudheendran, K. C. J. Raju, R. S. Katiyar, *Solid State Commun.* **150** (2010) 1928.

[7] D. Pamu, P. D. Raju, A. K. Bhatnagar, *Solid State Commun.* **149** (2009) 1932.

[8] M. M. Krzmanc, M. Logar, *J. Am. Ceram. Soc.* **94** (2011) 2464.

[9] Rayleigh, *Phil. Mag.* **43** (1892) 123.

[10] R. D. Ritchtmeyer, *J. Appl. Phys.* **10** (1939) 391.

[11] H. M. Schlicke, *J. Appl. Phys.* **24** (1953) 187.

[12] A. Okaya, *Proc. IRE.* **48** (1960) 1921.

[13] A. Okaya, L. F. Barash. *Proc. IRE.* **50** (1962) 2081.

[14] R. L. Bolton, Ph.D Thesis, *University of Illinois, Urbana-Champaign, IL*, (1968).

[15] T. Negas, G. Yeager, S. Bell, R. Amren, *Proc. Int. Conf. Chem. Electron. Ceram. Mater.*, NIST Special Publication, **804** (1990).

[16] D. J. Masse, R. Readey, C. Hatwig, *Proc. IEEE.* **59** (1971) 1628.

[17] Y. Konishi, *Techn. Rep.NHK*, Tokyo, Japan, **111** (1971).

[18] J. K. Plourde, *IEEE MTT-S Digest*, **202**(1973).

[19] M. Reaney, D. Iddles, *J. Am. Ceram. Soc.* **89** (2006) 2063.

[20] M. T. Sebastian, "*Dielectric Materials for Wireless Communications*", Elsevier Science Publishers, Oxford (2008).

[21] D. Kajfez, "Dielectric resonators", D. Kajfez, and P. Guillon (Eds.), *Artech House*, Norwood (1986).

[22] W. B. Li, H. H. Xi, and D. Zhou, *J. Electron. Mater.* **44**, 4250 (2015).

[23] D. W. Kim, J. R. Kim, C. K. Kim, *J. Am. Ceram. Soc.* **85** (2002) 2759.

[24] Y. H. Jo, D. J. Shin, R. K. Gupta, Y. S. Cho, *J. Ceram. Soc. Jpn.* **115** (2007) 978.

[25] J. L. Solano, S. Radescu, G. Aquilanti, *Phys. Stat. Sol. B* **244** (2007) 325.

[26] M. M. Krzmanc, M. Logar, *J. Am. Ceram. Soc.* **94** (2011) 2464.

[27] H. Zhuang, Z. Yue, F. Zhao, L. Li, *J. Am. Ceram. Soc.* **91** (2008) 3275.

[28] H. Zhuang, Z. Yue, F. Zhao, J. Pei, L. Li, *J. Alloys Compd.* **472** (2009) 411.

[29] M. Reaney, D. Iddles, *J. Am. Ceram. Soc.* **89** (2006) 2063.

[30] M. T. Sebastian, H. Jantunen, *International Materials Reviews* **60** (2015) 392.

[31] F. Luck, *Catal. Today* **53** (1999) 81.

[32] Y. C. Chen, *IEEE Trans. Ultrason. Ferroelectr. Freq. Control* **58** (2011) 2531.

[33] M. T. Sebastian, Dielectric Materials for Wireless Communication; Elsevier: Amsterdam, the Netherland, 2008.

[34] W. Wersing, *Solid State Mater. Sci.* **1** (1996) 715.

[35] F. Galasso, J. Pyle, *Inorganic Chemistry* **2** (1963) 482.

[36] F. Galasso, J. Pinto, Nature, **207** (1965) 70.

[37] E. L. Colla, I. M. Reaney, N. Setter, *Journal of Applied Physics* **74** **(**1993) 3414.

[38] M. Onada, J. Kuwata, K. Toyama, S. Nomura, *Japanese Journal of Applied Physics* **21** (1982) 1707.

[39] H. Kozuka, H. Yamada, K. Koumoto, *J. Mater. Chem. A* **1** (2013) 3249.

[40] G. Angloher, C. Bucci, L. Stodolsky, H. Wulandari, *Nucl. Instrum. Methods Phys. Res. A* **520** (2004) 108.

[41] G. Angloher, M. Bruckmayer, M. Stark, S.Uchaikin, L. Zerle, *Astroparticle Physics* **18** (2002) 43.

[42] S. Cebrian, N. Coron, J. A. Villar, *Astroparticle Physics* **21** (2004) 23.

[43] A. A. Annenkov, M. V. Korzhik, P. Lecoq, *Nucl. Instrum. Methods Phys. Res. A* **490** (2002) 30.

[44] Compact Muon Solenoid (CMS), Technical Proposal, CERN/LHC 93-98, p.1 (1994).

[45] M. Kobayashi, H. Yahagi, *Nucl. Instrum. Methods Phys. Res. A* **333,** 429 (1993).

[46] M. Nikl, P. Bohacek, A. Stolovich, S. Zazubovich, M. Bacci, *J. of Luminescence* **1136** (2000) 87.

[47] M. Nikl, P. Bohacek, N. Mihokova, M. Ishii, *J. Appl. Phys.* **91** (2002) 5041.

[48] A. Brenier, G. Jia, Ch. Tu, *J. Phys.: Condens. Matter* **16** (2004) 9103.

[49] D. Errandonea, D. Häusermann, *phys. stat. sol. (b)* **235** (2003) 162.

[50] P. Rodríguez-Hernández, R. S. Kumar, G. Aquilanti, *J. Phys. Chem. Solids* **67** (2006) 2164.

[51] D. Errandonea, phys. stat. sol. (b) **242** (2005) R125.

[52] A. Grzechnik, W. A. Crichton, *phys. stat. sol. (b)* **242** (2005) 2795.

[53] R. Muhammad, C. R. Rambo, H. Khan, *Int. J. Mater. Res. (*formerly Z. Metallkd.), **431** (2014) 105.

[54] C. T. Lee, C. T. Chen, C. Y. Huang, *Jpn. J. Appl. Phys.*, **47** (2008) 4634.

[55] Y. H. Jo, D. J. Shin, R. K. Gupta, Y. S. Cho, *J. Ceram. Soc. Jpn.* **115** (2007) 978.

[56] Y. J. Hsiao, Y. H. Chang, *J. Am. Ceram. Soc.* **90** (2007) 2287.

[57] M. M. Krzmanc, M. Logar, *J. Am. Ceram. Soc.* **94** (2011) 2464.

[58] J. L. Solano, S. Radescu, R. S. Kumar, *Phys. Stat. Sol. B* **244** (2007) 325.

[59] F.M. Pontes, E.R. Leite, *J. Eur. Ceram. Soc.* **23** (2003) 3001.

[60] R. Dinesh, T. Fujiwara, T. Watanabe, *J. Mater. Sci.* **41** (2005)1541.

[61] H. Zhuang, Z. Yue, F. Zhao, J. Pei, L. Li, *J. Alloys Compd.* **472** (2009) 411.

[62] H. Zhuang, Z. Yue, F. Zhao, L. Li, *J. Am. Ceram. Soc.* **91** (2008) 3275.

[63] M. Reaney, D. Iddles, *J. Am. Ceram. Soc.* **89** (2006) 2063.

[64] H. Sreemoolanadhan, J. Isaac, S. Solomon, M. T. Sebastian, K. A. Jose, P. Mohanan, phys. Stat. Sol. (a) **143** (1994) K45.

[65] B. Tareev, "*Physics of dielectric materials*" Mir Publishers, Moscow (1975).

[66] http://images.slideplayer.com/15/4661485/slides/slide_2.jpg

[67] V. M. Ferreira, F. Azhough, J. L. Baptista, R. Freer, *Ferroelectrics*, **133** (1992) 127.

[68] K. Wakino, M. Murata, H. Tamura, *J. Am. Ceram. Soc.* **69** (1986) 34.

[69] H. Tamura, D. A. Sagala, K. Wakino, *Jpn. J. Appl. Phys.* **25** (1986) 787.

[70] L. Liu, M. Flores, N. Newman, *PRL*, **109** (2012) 257601.

[71] D. Pamu, K. Sudheendran, K. C. James Raju, Anil K. Bhatnagar, *Vacuum*, **81** (2007) 686.

[72] V. L. Gurevich, Transport in Phonon Systems, North Holland, Amsterdam, (1986).

[73] V. L. Gurevich, A. K. Tagantsev, *Adv. Phys*. **40** (1991) 719.

[74] J. Petzelt, S. Pecesova, S. Kamba, V. Zeleny, *Ferroelectrics*, **93** (1989) 77.

[75] R. Kudesia, A. E. Mc Hale, R. A. Condrate, R. L. Synder, *J. Mater. Sci*. **28** (1993) 5569.

[76] D. Kajfez, "*Dielectric resonators*", Chapter 4, Artech House, Norwood (1986).

[77] W. Wersing, Electronic Ceramics, Ed B. C. H. Steele (1991) Elsevier Pub Co.Inc.

[78] J. Bahl, P. Bhartia, "*Microwave Solid State Circuit Design"*, Wiley, New York, (1988).

[79] A. J. Moulson, J. M. Herbert, "*Electroceramics*", Champman and Hall, London, (1990).

[80] A. J. Bosman, E. E. Havinga, *Phys. Rev*. **129** (1963) 1593.

[81] R. C. Buchanan, "*Ceramic Materials for Electronics*", Marcel Dekker, New York, (1986).

[82] M. Reaney, and D. Iddles, *J. Am. Ceram. Soc.* **89** (2006) 2063.

[83] S. R. Fiedziuszko, I. C. Hunter, S. N. Stilzer, K. Wakino, *IEEE Trans. Microw. Theory Technol*. **50** (2002) 706.

[84] A. P. S. Khanna, *Dielectric Resonators*, Chapter 10, D. Kajfez and P.Guillon (Eds.) Artech House, Norwood (1986).

[85] R. R. Tummala Rao, *J. Am. Ceram. Soc.* **74** (1991) 895.

[86] A. L. Eustice, S. J. Horowitz, J. J. Stewart, A. R. Travis, H. T. Sawhill, Low temperature cofireable ceramics. A new approach for Electronic packaging. Proc. 36th Electronic Component Conference, IEEE, Seattle (1986) New York, 37.

[87] J. Muller, H. Thust, K. H. Drue, *Int. J. Microcircuits Electron. Packaging.* **18** (1995) 200.

[88] M. A. Rodriguez, P. Yang, D. Dimos, *J. Electroceram.* **5** (2000) 217.

[89] H. T. Sawhil, *Ceram. Trans.* **26** (1987) 307.

[90] K. W. Long, K. M. Luk, *IEEE Antenna Propagation* **43** (1995) 517.

[91] K. Delaney, J. Barret, J. Barton, R. Doyle. *IEEE Trans. Adv. Pack.* **22** (1999) 68.

[92] H. Ohsato, *J. Ceram. Soc. Jpn.* **113** (2005) 703.

[93] C. L. Huang, J. J. Wange, C. Y. Huang, *J. Am. Ceram. Soc.* **90** (2007)1487.

[94] H. Ohsato, T. Tsunooka, H. Ogawa, *J. Electroceram.*, **17** (2006) 445.

[95] Y. Guo, H. Ohsato, K. I. Kakimoto *J. Eur. Ceram. Soc.* **26** (2006)1827.

[96] J. Zhou, Y. Gao, C. Cao, L. Dai, X. Liu, *Scientific Reports* **3** (2013) 3029.

[97] R. Baetens, A. Gustavsen, *Sol. Energy. Mater. Sol. Cells* **94** (2010) 87.

[98] C. M. Lampert, *Solar Energy Materials* **11** (1984) 1.

[99] C. G. Granqvist, "Handbook of inorganic electrochromic materials, Amsterdam, Elsevier," 1995.

[100] G. Balakrishnan, R. Thimurugesan, E. Mohandas, V. Ganesan, D. Sastikumar, *Appl. Surf. Sci.* **257** (2011) 8506.

[101] C. Y. Ma, F. Lapostolle, P. Briois, Q. Y. Zhang, *Appl. Surf. Sci.* **253** (2007) 8718.

[102] G. L. Liu, Z. R. Huang, J. H. Wu, X. J. Liu, *Surf. Coat. Technol.* **207** (2012) 204.

[103] F. Galasso, L. Katz, *Acta Cryst.* **14** (1961) 647.

[104] I. N. Jawahar, P. Mohanan, M. T. Sebastian, *Mater. Lett.* **57** (2003) 4043.

[105] http://www.jcrystal.com/steffenweber/JAVA/JSV/jsv.html

[106] D. Errandonea, J. Pellicer-Porres, *Phys. Rev. B* 73 (2006) 224103.

[107] C. Vineis, P. K. Davies, T. Negas, *S. Bell, Mater. Res. Bull.* **31** (1996) 431.

[108] S. H. Yoon, D. W. Kim, S. Y. Cho, K. S. Hong, *J. Eur.Ceram. Soc.* **26** (2006) 2051.

[109] Y. Zhang, N.A.W. Holzwarth, R.T. Williams, *Phys. Rev. B* **57** (1998) 12738.

[110] L. Golonka, P. Bembnowicz, R. Tadaszak, *Optica Applicata* **41** (2011) 383.

[111] T. Joseph, M. T. Sebastian, M. V. Jacob, H. Sreemoolanadhan, *Int. J. Appl. Ceram. Technol.* **8** (2011) 854.

[112] C. H. Shen, C. L. Huang, *Int. J. Appl. Ceram. Technol.* **7** (2010) 207.

[113] L. J. Golonka, *Bulletin of the Polish Academy of Sciences Technical Sciences* **54** (2006) 221.

[114] J. Mazierska, M. V. Jacob, A. Harring, J. K. Peter Barnwell, "*Journal of the European Ceramic Society* **23** (2003) 2611.

[115] F. M. Pontes, M. A. Maurera, A. G. Souza, E. Longo, E. R. Leite, R. Magnani, J. *Eur. Ceram. Soc.* **23** (2003) 3001.

[116] R. Dinesh, T. Fujiwara, T. Watanabe, *J. Mater. Sci.* **41** (2005) 1541.

[117] R. Dinesh, T. Fujiwara, M. Yoshimura, *Solid State Sciences* **8** (2006) 1074.

[118] W. S. Cho, M. Yoshimura, *J. Am. Ceram. Soc.* **80** (1997) 2199.

Chapter 2

Preparation methods and characterization techniques

Throughout the course of investigation an attempt was made on preparation of BNO, BWO and BNO - BWO composites by using different preparation methods and experimental techniques used for evaluating, structural, optical, microstructural, impedance and microwave dielectric properties. In the present chapter, a brief description of preparation methods and analysis techniques used for both bulk and thin films of BNO, BWO and BNO - BWO composite ceramics were given.

2.1 Preparation of bulk BNO, BWO and BNO – BWO ceramics

The polycrystalline ceramic materials are having well crystalline grains and imperfections like pores, grain boundaries, etc. Since, preparation of these materials is a challenge because of brittle refractories and densifying with proper shaping of these materials without crack is a difficult task. This section upholds the preparation methods being used for the bulk and thin films of BNO, BWO and BNO - BWO composite ceramics. There were few available methods for the synthesis of these materials were mechanical alloying, conventional solid state reaction and chemical methods [1-3], which were used to prepare these materials with maximum feasible densification and characterized these materials in the microwave region (i.e., interaction of microwave with ceramic materials). In the current thesis work, all the above methods were used to prepare BNO, BWO and BNO - BWO composite in bulk form.

2.1.1 Mechanical alloying method

In the last four decades, mechanical alloying and milling upholds to be an interesting field of investigation. The mechanical alloying method can be used to make synthesis of a variety of equilibrium and non-equilibrium alloy phases such as solid solutions, intermetallics, quasicrystals, amorphous alloys, and bulk metallic glasses. In mechanical alloying process, powder particles experience a repeated process of cold welding, fracturing, and rewelding in a high-energy ball mill [4].

Nevertheless, the existing method of mechanical alloying begins with mixing the powder particles in the right fraction and filling the powder mix into the mill and in addition with the grinding medium, generally which consist steel balls. The powder particles were mixed and milled for the desired length of time to achieve the composition of every powder particle is the identical as the magnitude of the elements in the starting powder mix. Later, the obtained powders were pressed into cylindrical shapes and sintered at different temperatures to attain the required microstructure and properties. To get the required material phase and/or microstructure, the optimization of a number of variables are necessary with the mechanical alloying method. The required optimization parameters to obtain the final constitution of the powder are type of mill, milling container, milling speed, milling time, type, size, and size distribution of the grinding medium, ball-to-powder weight ratio, extent of filling the vial, milling atmosphere, process control agent, and temperature of milling [4, 5]. All these process variables are not completely independent. For example, the optimum milling time depends on the type of mill, size of the grinding medium, temperature of milling, ball-to-powder ratio, etc. In general, the mechanical alloying experiments carrying on with planetary ball mill which is used to mill and make fine powder particles (e.g., few hundred grams of powder). Fig. 2.1 shows the photographic outlook of a planetary ball mill which is being used to prepare the powders.

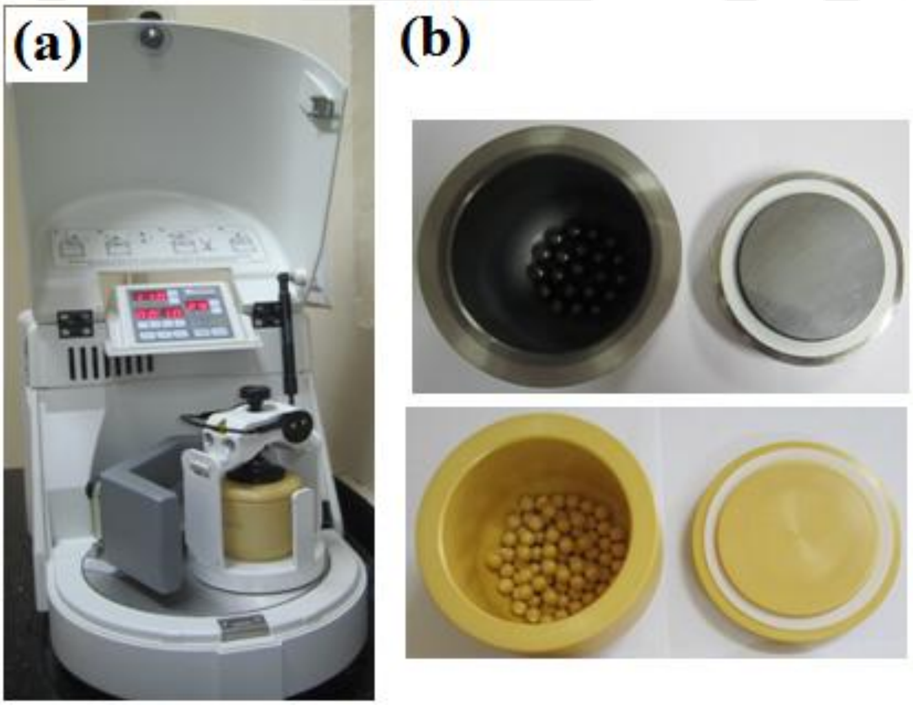

Fig.2.1: *(a) Photographic view of planetary ball mill (b) Tungsten carbide and zirconia jars with balls.*

In the current study, planetary ball mill (M/s Fritsch Pulverisette 6, Germany) was employed for mechanical alloying process. The tungsten carbide and zirconium vials and different diameters of spherical 5 and 10 mm tungsten carbide/zirconium balls are used. The ball-to-powder weight ratio of 10:1 and milling speed of 400 rpm maintained during the milling process. In order to avoid excess heating, it is programmed to stop for 5 minutes after every 10 minutes of continuous milling.

2.1.2 Conventional solid state reaction method

In the condensed matter physics experimental research, synthesis of high quality materials with desired properties is plays a significant role. Depending upon the requirements (application point of view), the solid samples can be synthesized in variety of shapes and sizes, such as, single crystals, amorphous solids, thin films, thick films, polycrystalline powder, etc. The solid state reaction method is the mainly used for the preparation of polycrystalline materials from a mixture of inorganic solid starting materials and this method is the simplest and cost - effectiveness for producing bulk ceramics. Nevertheless, one of the foremost inabilities is the need of high processing temperatures to attain best properties. Both the thermodynamics and kinetic factors are important in solid - state reactions since, solids react together only at higher temperatures [6]. There are few significant steps are involved in conventional solid state reaction method are: (1) select appropriate starting materials (a) fine grain powders to maximize surface area, (b) reactive starting reagents are better than inert and (c) well defined compositions, (2) high temperature calcination (3) green body preparation and (4) sintering. As each of these steps affects the final ceramic properties, they must all be understood clearly [6].

2.1.2.1 Preparation of ceramic powders

(a) Stoichiometric weighing of raw materials

In the ceramic method, the familiar route is the mixed oxide route. In this method, mineral oxides of the constituent cations are weighed accurately and rigorous mixing in stoichiometric proportions.

$$5BaCO_3 + 2Nb_2O_5 \rightarrow Ba_5Nb_4O_{15} + 5CO_2 \tag{2.1}$$

$$2BaCO_3 + 2WO_3 \rightarrow 2BaWO_4 + 2CO_2 \tag{2.2}$$

According to above chemical equations, the desired ratios of the reagents are weighed. The starting materials with the high-purity powders of (99.99%) $BaCO_3$, WO_3 from (M/s Sigma Aldrich, St. Louis, MO), Nb_2O_5 (M/s Nuclear Fuel complex, Hyderabad, India) are weighed properly to achieve required stoichiometry, to attain phase pure compounds, and to maintain reproducible microwave dielectric properties. To weigh the reagents, electronic balance (M/s Mettler Toledo, Model AG135) with precision up to four decimal places is used.

(b) Homogeneous mixing of reagents

The different and distinct reagents are to be mixed uniformly in order to increase the point of contacts between the reagents, which will act as product layer formation centers. The mixing and milling of reagents would get rid of from agglomeration and reduces particle sizes. The agglomeration of powder particles will densify more rapidly which results in pores. During the mixing process, the micron sized powder particles, agglomerates are broken and defects are introduced into the grains that improve the diffusion mechanism. Hence, the initial stoichiometric reagents mixture must be mixed in a uniform manner with an appropriate mixing medium. In the current study, the mixture of constituent powders were mixed at speed of 200 rotations per minute for 5-20 *h* in distilled water medium using a planetary ball mill (M/s Fritsch, Pulverisette 6, Germany) using tungsten/zirconium jar with 5 and 10 mm diameter of tungsten/zirconium balls.

2.1.2.2 Calcination

Calcination is a thermal treatment process below the melting point (i.e., lower temperatures prior to sintering) and applied to ores and other solid materials to bring (1) thermal decomposition, (2) phase transition and (3) to remove volatile fractions such as CO_2, H_2O. Calcination is done in the solid state reaction method and there are few modifications achieved by the calcination stage such as coarsening, decomposition, reaction and dehydration [7]. Coarsening involves crystallite growth or fusing or bonding small particles together to produce larger particles. Decomposition involves converting compositions such as carbonates, nitrates, sulphates and acetate to a solid oxide and a gas. The major key factors such as temperature, duration of heating and atmosphere are significant at calcination stage and which influence the shrinkage during sintering. In the present case, the reagents being oxides do not undergo any decomposition. With the help of the X - ray diffraction pattern (XRD) of the calcinated products, the completion of reaction, desired phase formation and existence of impurity or secondary phases are identified.

2.1.2.3 High density green body preparation

(a) Particle size reduction

Size reduction is a process of reducing large solid unit masses, coarse particles or fine particles. Size reduction may be achieved in two methods. (1) Precipitation method, in which substance is dissolve in appropriate solvent. This method is suitable for the production of raw materials. Inorganic chemicals, such as calcium carbonate, magnesium carbonate, and yellow mercuric oxide, were prepared by precipitation method. (2) Mechanical process, in which mechanical force is introduced by using different equipments like ball mill, colloid mill, etc. The particle size reduction of the complex oxides after the calcination stage is important to homogenize the formed phase. It is well known that small size particles can be compacted well, which in turn yields higher density at lower sintering temperatures. In general, the planetary ball mills are used for milling the powders to attain particle size reduction. In our case, a planetary ball mill was employed to achieve the initial stoichiometric mixing before the calcination and to reduce the particle size of the calcined ceramic powders. Tungsten carbide/zirconia vials and different diameters of spherical 5 and 10 mm diameter tungsten carbide/zirconia balls are used. All the processing parameters were optimized to achieve smaller size particles. In the milling process, the particle experiences mechanical stresses at their contact points due to compression, shear with the milling medium or with other particles. The mechanical stress leads to elastic and inelastic deformation. If the stress is greater than the ultimate strength of the particle, it will fracture the particles.

(b) Polymer as a binding agent

Binders are substances that increase the mechanical strength of green ceramic bodies so they can pass through production steps, before firing, without breakage. Binders have great impact on the properties of granules, such as bulk density, flow rate and compaction behaviour by which porosity of green body decreases [8]. A good binder for ceramic applications should provide high green strength and appropriate elastic properties for handling and shaping during the post forming stage [9]. The main two popular binders for dry pressed ceramics are polyvinyl alcohol (PVA) and polyethylene glycol (PEG). The research trends suggest that 3 - 4 wt. % of PVA or PEG which are water thinnable polymeric dispersions are ideal binders for the fabrication of microwave dielectric ceramics. In general, PVA binders provide high green strength while PEG binders provide high green density. PVA at low level of usage of the binder will not affect the dielectric properties as it evaporates around 400 °C. In the current work, we have used PVA as a binder to prepare the microwave dielectric ceramics and densification behaviour has been characterized.

(c) Uniaxial die pressing

The shape forming method for powders is inexpensive and suitable for high-volume production of simple shapes (limited geometrical possibilities) such as refractories, tiles, electronic ceramics, etc. Uniaxial pressing involves the compaction of powder into a rigid die by applying pressure in a single axial direction through a rigid punch or piston. The press is usually mechanical or hydraulic. The compaction of the powder should be done slowly to facilitate the escape of the entrapped air. After reducing the particle size of the calcined powder, the fine powder is compacted into cylindrical specimens (green pellets). To make the green pellets of the ceramic powder, rust free rigid dies are used. To make the inner walls of the die smooth, stearic acid is used as an internal lubricant. The pressure gradient on the die as a function of the distance from the upper punch is given by the equation,

$$P_X = P_a e^{\frac{-4\mu KL}{D}} \tag{2.3}$$

where, μ is the coefficient of friction, P_a is the applied pressure, L is the length and D is the diameter of the powder compact and K is a constant [10]. It is evident that the pressure distribution of a powder compact is more uniform when length to diameter ratio is smaller. For the microwave dielectric measurements, we prepare samples with the D/L ratio ≈ 2.0 and hence the pressure distribution is quite uniform in the powder compact. Pressure of 50 - 150 MPa is more ideal for ceramic processing.

2.1.2.4 Solid state sintering process

Sintering is the consolidation, under the effect of temperature, of powdery agglomerate, a non-cohesive granular material (often called compact, even though its porosity is typically 40% and therefore its compactness is only 60%), with the particle of the starting powder "welding" with one another to create a mechanically cohesive solid, generally a polycrystal. Sintering is the basic technique for the processing of ceramics, but other materials can also use it: metals, carbides bound by a metallic phase and other cermets, as well as natural materials, primarily snow and ice. In fact, the term sintering includes four phenomena, which take place simultaneously and often compete with each other.

a) Consolidation: development of necks that "weld" the particles to one another;
b) Densification: reduction of the porosity, therefore overall contraction of the part (sintering shrinkage)
c) Grain coarsening: coarsening of the particles and the grains
d) Physicochemical reactions: in the powder, then in the material under consolidation.

Sintering is possible only if the atoms can diffuse to form the necks that weld the particles with one another. The transport of matter can occur in vapor phase, in a liquid, by diffusion in a crystal, or through the viscous flow of a glass. Most mechanisms are activated thermally because the action of temperature is necessary to overcome the potential barrier between the initial state of higher energy (compacted powder) and the final state of lower energy (consolidated material). Atomic diffusion in ceramics is sufficiently rapid only at temperatures higher than 0.6 - 0.8 T_F, where T_F is the melting point (in K). For alumina, for example, which melts at around 2,320 K the sintering temperature chosen is generally around 1,900 K.

In ceramics, porosity is an important parameter, which governs many of its properties. For maximizing properties such as the dielectric constant, quality factor, mechanical strength, translucency and thermal conductivity, it is desirable to minimize porosity as low as possible. Therefore, the principal goal of sintering is the reduction of compact porosity. The development of microstructure and densification during sintering is a direct consequence of mass transport through several possible paths and one of these paths is usually predominant at any given stage of sintering [11]. They are (i) evaporation /condensation (ii) solution/precipitation (iii) lattice diffusion and (iv) surface diffusion or grain boundary diffusion.

Sintering can occur in the presence or absence of a liquid phase. In solid state sintering, densification is achieved through changes in particle shape without particle rearrangement or the presence of the liquid. In liquid phase sintering, the compositions and firing temperatures are chosen such that some liquid is formed during processing which aids compaction. There are three major stages in the sintering process and are shown in Fig. 2.2.

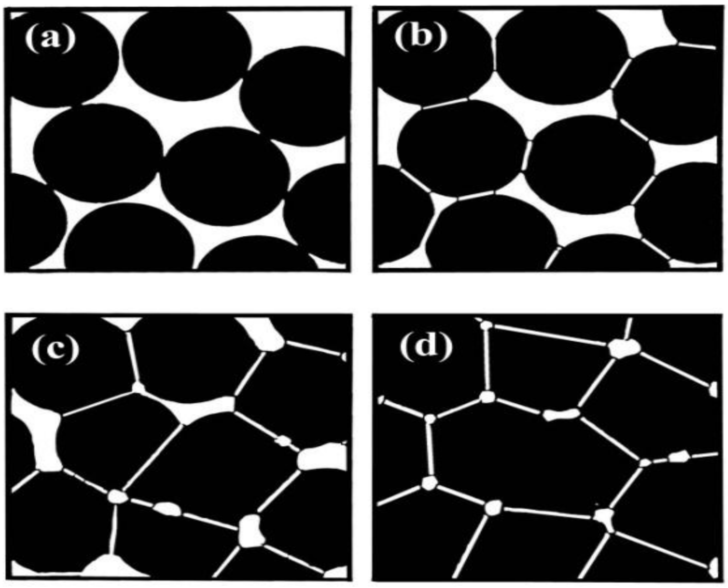

Fig. 2.2: *(a - b) Initial stage, (c) Intermediate stage and (d) Final stage of sintering* [12].

Stages of sintering: The microstructure of a powder compact, consisting initially of discrete particles, evolves continuously during sintering. However, it is sometimes convenient to divide the process into three idealized stages defined in terms of the microstructure, to force correspondence between simple, established sintering models. The initial stage would begin as soon as some degree of atomic mobility is achieved and, during this stage, sharply concave necks form between the individual particles. The amount of densification is small, typically the first 5% of linear shrinkage, and it can be considerably lower if coarsening mechanisms are very active. In the intermediate stage, the high curvatures of the initial stage have been moderated and the microstructure consists of a three-dimensional interpenetrating network of solid particles and continuous, channel-like pores. This stage is considered valid to ~ 5 - 10% porosity and therefore covers most of the densification. Grain growth (coarsening) starts to become significant. As sintering proceeds, the channel-like pores break down into isolated, closed voids, which mark the start of the final stage. Grain growth can be more extensive in the final stage and difficulties are commonly encountered in the removal of the last few percent of porosity [13].

Solid state sintering involves movement of atoms that in turn is dependent on temperature and concentration of structural imperfections such as vacancies and interstitials. The process variables in sintering are (a) sintering temperature (b) sintering time (c) sintering atmosphere. The factors affecting solid state sintering are (a) particle size and particle size distribution (b) particle shape (c) uniformity of green microstructure (d) particle composition and (e) green density [13]. Solid state sintering of mixed cation oxides that are used in DRs is an ambipolar diffusion process in which anions and cations must be transported from the source to sink without kinetic de - mixing. The rate limiting mechanism will be slowest moving species along the fast path. Therefore, the rate of sintering depends on the diffusivities and additives that influence diffusion. Additives often help to decrease the rate of coarsening in the earlier stages of sintering, increase the rate of densification and decrease the rate of grain growth.

2.1.2.5 Recrystallization and grain growth

Recrystallization is a type of reorganization process in which large crystallites are formed from smaller crystallites. The process is heating - rate dependent: the lower the heating rate, the more time there is for reorganization. In general, two types of recrystallization processes occur (i.e., primary and secondary recrystallization). Primary recrystallization is the process by which nucleation and growth of a new generation of strain - free grains occur in a matrix which has been plastically deformed [14]. Secondary recrystallization, sometimes called abnormal or discontinuous grain growth, is the process by which a few large grains are nucleated and enlarge at the expanse of fine grained, but essentially strain free matrix. Grain growth is the process by which the average grain size of the nearly strain free material increases continuously during heat treatment without change in the grain size distribution.

Primary recrystallization process has its driving force in the increased energy of a matrix which has been plastically deformed. If the isothermal change in grain size of strain free crystals in a deformed matrix is measured after an initial induction period, there is a constant rate of grain growth for the new strain free grains. If the grain size is d [14], then

$$d = U(t - t_0) \tag{2.4}$$

Where, U is the growth rate (cm/sec), t is the time and t_o is the induction period. The induction period corresponds to the time required for unstable embryos present to grow to the size of a stable nucleus. For a nucleus to be steady, its size must be larger than some critical diameter at which the lowered free energy of the new grain is equal to the increased surface free energy. If an unlimited number of sites are available, the rate of nucleation increases to some constant rate after an initial induction period and exponential increase of rate of nucleation with increase in temperature. Whether or not primary recrystallization occurs, an aggregate of fine-grained crystals increases in average grain size when heated at elevated temperatures. With the increase in grain size, it is apparent that some grains must shrink and disappear. An equivalent way of looking at grain growth is the rate of disappearance of small grains. Afterwards, the driving force for the process is the difference in energy between the fine - grained material and the larger grain size product resulting from the decrease in grain boundary area and the total boundary energy [14].

2.1.2.6 Liquid phase sintering

Liquid phase sintering is a consolidation technique of powder compacts containing more than one component at a temperature above the solidus of the components and hence in the presence of a liquid. Unlike solid state sintering, the microstructure change during liquid phase sintering is fast because of fast material transport through the liquid. When liquid coats at each grain, the material shows higher density at lower temperatures with a less tendency for exaggerated grain growth. If the liquid is distributed uniformly and the grain size is about 1 μm, one needs less than one volume percentage liquid phase to coat the grains. The wetting liquid concentrates at the particle contacts and forms a meniscus, which exerts an effective compressive pressure on the compact. There is a rapid rearrangement of particles into higher density configuration [14, 15]. After the initial rearrangements, further densification takes place as particle contacts flatten under the compressive stress applied to the point contacts by capillary pressure. The contact flattening occurs through dissolution at the particle contacts and transport of the materials towards stress free interfaces. This leads to appreciable grain growth compared to solid state sintering.

2.1.3 High temperature sintering furnace

To obtain the highly densified materials and to optimize desired dielectric properties of samples, high temperature furnaces were used. In the current study, commercial high temperature sintering furnace (M/s Lenton, UAF 16/5, UK) with the maximum operating temperature of 1650 ^{o}C was used to sinter the samples. All the BNO, BWO and BNO - BWO composite ceramics were sintered within the given temperature for 3 - 5 *h* with heating and cooling rates of 8 - 15 ^{o}C/min and 1 - 2 ^{o}C/min, respectively.

Fig. 2.3: *Photographic view of high temperature sintering furnace.*

The furnace is connected to programmable controller by which set temperature (the heating rate and time duration of heating at a specific temperature) is controlled. The insulated door opens upwards and outwards keeping the hot face insulation away from the operator. The photograph of high temperature sintering furnace being used to prepare the samples is shown in Fig. 2.3.

2.2 Characterization Techniques

In order to understand the mechanism and operational details of equipment to extract best experimental data, experimental tools are required for an experimentalist. A number of experimental tools are used to study the characteristic properties of the different samples. The phase purity of prepared samples was examined by high power X-ray diffraction (XRD) technique with Cu-Kα (λ = 1.5406 Å) radiation (M/s Rigaku, TTRAX-III 18 kW). The Archimedes's method was used to calculate the relative densities of the sintered samples. The particle size of the sol - gel processed calcined powders were measured using Delsa Nano C (Beckman coulter, Model no: A53878). The particle size, shape and crystallinity of the prepared nanopowders and microstructure of sintered composites were observed by using a transmission electron microscope (TEM) (M/s JEOL, JEM 2100) and scanning electron microscope (SEM) (M/s LEO, 1430vp), field-emission scanning electron microscopy (FESEM) (M/s Zeiss, Sigma), respectively. The thermal analysis of dried powder was performed by using the differential scanning calorimetric (DSC) / thermogravimetric (TGA) analysis (M/s Netzsch, STA449F3A00). For optical characterizations of the films, UV-VIS-NIR spectrophotometer (M/s SHIMADZU, UV 3101PC) are used. The dielectric properties of the samples were analyzed using vector network analyzer (M/s Rohde & Schwarz, ZVA24) and Impedance analyzer (M/s Agilent Technologies Pvt. Ltd., E4991A) attached with an automated temperature controller (BDS 2200 and 2300, M/s Novocontrol, GmBH). The dielectric constants and dielectric loss of the films were calculated from the capacitance-frequency response as a function of temperature in the low frequency (20 Hz -1 MHz) using a LCR meter (M/s Wayne Kerr Electronics Pvt. Ltd., 1J43100) connected to computer via RS232 connection. The Raman spectra of the prepared samples were recorded using a Raman spectrometer (LABRAM HR800 developed by JOBIN YVON).

2.2.1 X-ray diffraction

Powder X - ray diffraction (XRD) is a non-destructive and rapid analytical technique primarily used for phase identification of a crystalline material and can furnish information on unit cell dimensions. XRD is now a common technique for the study of crystal structures and atomic spacing. XRD is based on constructive interference of monochromatic X - rays and a crystalline sample. These X - rays are generated by a cathode ray tube, filtered to produce monochromatic radiation, collimated to concentrate, and directed toward the sample. Powder XRD is most widely used for the identification of unknown crystalline materials (e.g. minerals, inorganic compounds). The applications include the characterization of crystalline materials, determination of unit cell dimensions, determination of crystal structure using Rietveld refinement, and make textural measurements, such as the orientation of grains, in a polycrystalline sample.

The interaction of the incident rays with the sample produces constructive interference when conditions satisfy Bragg's equation (Bragg's law):

$$2d\sin\theta = n\lambda \tag{2.5}$$

Where, λ is the wavelength, d is the spacing between the planes and θ is the Bragg angle [16]. The constructive interference only occurs for certain θ's correlating to a *(hkl)* plane, specifically when the path difference is equal to 'n' wavelengths. The instrument is based on the Bragg-Brentano geometry as shown in Fig. 2.4. In this geometry, the source to sample distance and the sample to detector distance are kept equal. A Perspex sheet with rectangular groove was used for sample mount, where the powder sample was filled uniformly in the groove.

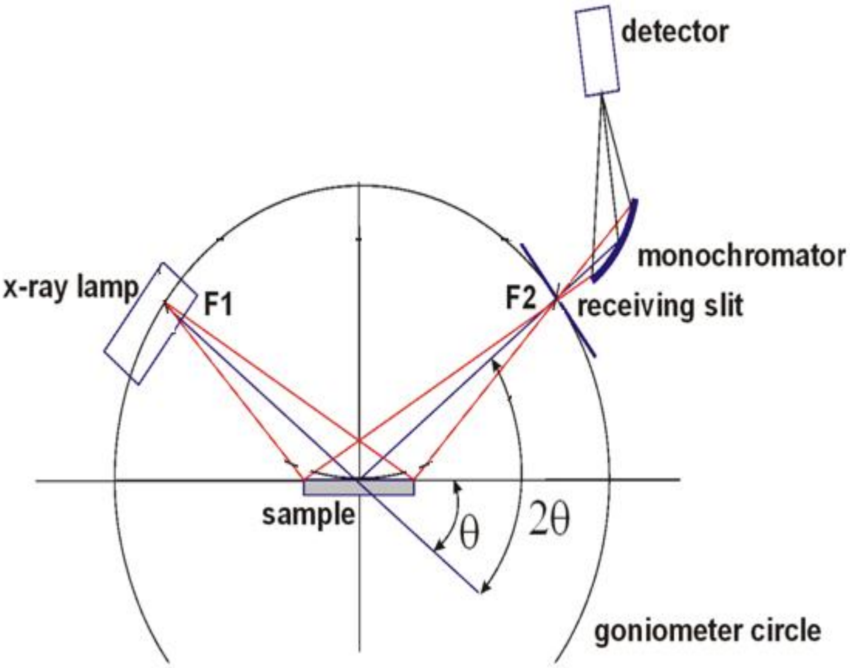

Fig. 2.4: *Schematic ray diagram of X-ray diffractometer [16].*

Fig.2.5: *Photograph of the X-ray diffractometer (Rigaku RINT 2500, TTRAX III).*

In the present work, two types of X-ray diffractometers were used to characterize the samples. One is Seifert X-ray diffractometer with Cu-Kα (λ = 1.5406 $\AA$) radiation operating at 40 kV and 30 mA (1.2 kW). The other one is Rigaku (TTRAX - III, 18 kW) XRD with Cu-Kα (λ = 1.5406 $\AA$) radiation. A photographic view of the XRD instrument (Rigaku) used in the present study is shown in Fig. 2.5. The scanning step size was 0.01°. Calibration using a Si standard was done to account for the instrumental line broadening and the value was approximately 0.005°.

The XRD patterns were also analyzed with the help of Reitveld refinement method using Fullprof program [17]. The background was refined using a polynomial function.

2.2.2 Scanning electron microscopy

In the current thesis work all the surface morphology (microstructural images) and compositional investigation of the BNO, BWO and BNO - BWO composite based samples have been accomplished by using scanning electron microscopy (SEM) equipped with Oxford energy dispersive spectrometer (EDS). Basic principles of SEM and EDS analysis are given briefly.

To defeat the limitations of optical microscopy, electron microscopes were developed in the 1930s and offer increased magnification and resolution. Cambridge Instruments built a first commercialized SEM. Further, to investigate and interpreting microstructures of materials, SEM is extensively used in the field of material science and it is fully based on the interaction of an incident electron beam and the solid sample [18]. Electron bombardment can produce an extensive diversity of emissions from the sample, including backscattered electrons, secondary electrons, Auger electrons, X-rays, visible photons and so on.

i) Secondary Electrons: If an incident electron beam interacts with a sample surface, it will strike the electron out of its orbital shell and the atom will become ionised. For the reason that the incident electron loses little energy during each collision, multiple collisions are possible, continuing until the incident electron no longer has the energy to dislodge secondary electrons. Each freed secondary electron has a very small kinetic energy (< 50 eV), which is independent of the incident electron energy. If generated close enough to the sample surface (< 10 nm), these secondary electrons can escape to be collected by the detector. As a direct result, secondary electron imaging is closely related to sample topography.

ii) Backscattered Electrons: If an incident electron beam knocks the nucleus of surface atom, the electron will scatter 'backward' out of the sample as a backscattered electron (BSE). These electrons have high energies, typically between 50 *eV* and that of the original incident electron. The production of backscattered electrons varies directly with atomic number, and thus backscattered electron images can be used to discern differences in sample atomic number.

iii) Auger Electrons: As a result of secondary electron generation, a vacancy is left in an ionised atom's electron shell. To fill this vacancy, an electron from a higher energy outer shell (from the same atom) can drop down to fill the vacancy. This creates an energy surplus in the atom that can be corrected by emitting an outer electron, an Auger electron. Auger electrons have a characteristic energy unique to the element from which they are emitted and can be used to give compositional information about the target sample. Auger electrons have a relatively low kinetic energy and are only emitted from shallow sample depths (< 3 nm).

iv) Characteristic X-rays: This X-rays could be produced by interactions of the incident electron beam with a sample surface. Similar to the Auger electron generating process, the excess energy produced by reshuffling electrons to fill shell vacancies can also be emitted in the form of an X-ray rather than an Auger electron. X-rays have a characteristic energy unique to the element from which they originate and so provide compositional information about a sample.

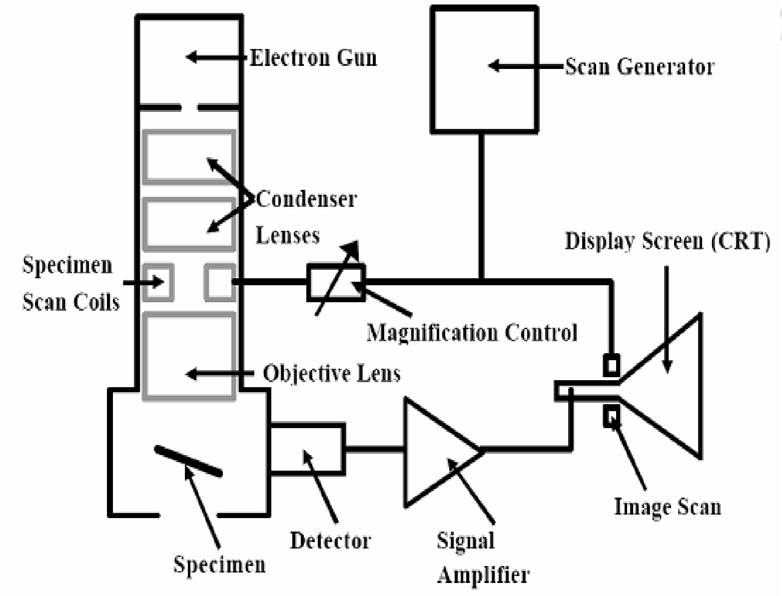

Fig. 2.6: *Schematic diagram of a scanning electron microscope.*

An SEM consists of three distinct parts: an electron column; a detection system; and a viewing system. Fig. 2.6 shows a schematic diagram of a simple SEM. Scan generator could be used to control the two electron beams: (1) incident electron beam, and (2) cathode ray tube (CRT) screen. The incident beam is scanned across the sample, line by line, and the signal from the resulting secondary electrons is collected, detected, amplified and used to control the intensity of the second electron beam.

The spatial resolution of the SEM is fully dependent on diameter (spot size) of the electron probe beam at the specimen surface. In a SEM system, the diameter of the incident electron beam is demagnified using two or more electron lenses before it reaches the sample surface. Simultaneously to determine the resolution of the SEM, key factor is the effective diameter of the electron source. Basically, thermionic and field emission electron guns are in present use. The diameters of the electron beam originating from these gun types are about 20 - 50 μm and 10 nm, correspondingly. Thus, field emission SEM (FESEM) is the electron source of choice for high-resolution SEM images.

For elemental analysis of samples, energy dispersive X-ray spectroscopy (EDS or EDAX is an analytical technique) is used. Its characterization potentialities initiate from the fact that each element has a unique atomic structure, which emits its unique characteristic X-ray. To stimulate the emission of characteristic X-rays from a specimen, a beam of X-rays is put into focus for the sample being studied. At rest, an atom within the sample contains ground state electrons in separate energy levels or electron shells bound to the nucleus. The incident beam possibly will excite and emit an electron from an inner shell and the specified outcome in an electron vacancy in the shell. An outer higher energy shell electron fills the vacancy and the energy variation between the upper energy shell and the lower energy shell is released in the form of an X-ray. The atoms of every element release X-rays with unique amounts of energy during the above process. Thus, we get the EDS spectrum describing how often an X-ray is received for each energy level. In general an EDS spectrum, displays peaks corresponding to the energy levels for which the X-rays had been received. Each of these peaks is unique to an atom, and consequently represents to a single element. The intensity of the peaks depends on the concentration of the elements present.

2.2.3 Field-emission scanning electron microscopy

The field emission scanning electron microscope (FE-SEM) works with high-energy beam of electrons instead of light and it images a sample surface via raster scanning over it. The electrons interact with the atoms comprising the sample to produce signals that contain information about surface topography, composition and other properties, such as electrical conductivity. The function of the electron gun is to provide a large and stable current in a small beam. There are two classes of emission source: thermionic emitter and field emitter. Emitter type is the main difference between the scanning electron microscope (SEM) and the field emission scanning electron microscope (FE-SEM). Thermionic Emitters use electrical current to heat up a filament; the two most common materials used for filaments are tungsten (W) and lanthanum hexaboride (LaB_6). When the heat is enough to overcome the work function of the filament material, the electrons can escape from the material.

Thermionic sources have relative low brightness, evaporation of cathode material and thermal drift during operation. Field emission is one way of generating electrons that avoids these problems. A field emission source (FES); also called a cold cathode field emitter, does not heat the filament. The emission is achieved by placing the filament in a huge electrical potential gradient. The FES is usually a wire of tungsten (W) fashioned into a sharp point. The significance of the small tip radius (~ 100 nm) is that an electric field can be concentrated to an extreme level, becoming so big that the work function of the material is lowered and electrons can leave the cathode. The FE source reasonably combines with scanning electron microscopes (SEMs) whose development has been supported by advances in secondary electron detector technology. The acceleration voltage between cathode and anode is commonly in the order of magnitude of 0.5 to 30 *kV*, and the apparatus requires an extreme vacuum ($\sim 10^{-6}$ *Pa*) in the column of the microscope. Because the electron beam produced by the FE source is about 1000 times smaller than that in a standard microscope with a thermal electron gun, the image quality will be markedly improved; for example, resolution is on the order of ~2 nm at 1 *keV* and ~1 nm at 15 *keV*. To resolve a feature on the specimen surface, the beam diameter must be smaller than the feature (still containing high current density). Therefore it is necessary to condense the electron beam.

Fig. 2.7: *Photographic view of the field emission scanning electron microscopy.*

In the current thesis work ZEISS made FE-SEM (ΣIGMA) was used to study the surface morphology of nanocrystalline samples. A photographic view of the FE-SEM (M/s Sigma Zeiss, Germany) used in the present study is shown in Fig. 2.7. The advantages of FE - SEM over SEM are as follows, (1) FE - SEM produces clearer, less electrostatically distorted images with spatial resolution down to 1 nm. This is nearly 3 to 6 times better than conventional SEM; (2) Smaller area contamination spots can be examined at electron accelerating voltages compatible with EDS; (3) Closer to the immediate material surface can be probed due to the reduced penetration of low kinetic energy electrons; (4) High quality, low voltage images are obtained with negligible electrical charging of samples. (Accelerating voltages range from 0.5 to 30 *kV*).

In order to observe FE-SEM for objects, the sample needs to be coated with conducting electrode if it is electrically non-conducting. This can be done by coating the sample with an extremely thin layer (1.5 - 3.0 nm) of gold or carbon by using respective coater. In the present thesis work, the samples were electrically non-conducting and a thin layer of gold was coated over the samples before mounting for the FE-SEM observation.

2.2.4 Transmission electron microscopy (TEM)

TEM is one of the most powerful techniques in materials science, which has been widely used in the characterization of nanocrystalline microstructures. It has the ability to examine the constitutional characteristics of these nanocrystalline microstructure such as grain shape and size, crystallinity and chemical variations at a resolution down to the nanometer scale. With advanced design, modern TEM enables to detect the lattice defects, atoms and even their movements can be seen.

The first practical TEM was built by Albert Prebus and James Hillier at the University of Toronto in 1938 using concepts developed earlier by Max Knoll and Ernest Ruska. Since then, the TEM has had considerable development and is now become a versatile tool of characterization in material science and biology. Fig. 2.8 shows the schematic diagram of TEM and it usually consists of six basic components, as follows:

a) Source providing illumination: An electron source, commonly used in all TEM, comprises a filament, which emits electrons either by thermal heating (a so-called thermionic filament) or through application of high electric field to a metal filament tip generating field emission electrons (so-called field-emission filament). The field-emission filament is a lot more expensive and requires much higher vacuum than the thermionic filament, but offers a very stable source with a greater resolution and longer life-time.

b) Electrodes: These include a cathode, which accelerates the electrons generated from the filament to a high energy, ranging from a few hundreds to over million volts. Although a higher voltage can produce a higher resolution, in fact, most TEM instruments are operated at energies between 100 *kV* and 400 *kV*. This is to reduce sample damage and the cost of the instrument while still achieving an electron wavelength as short as possible.

c) An optical system: This consists of a series of electromagnetic lenses, such as condenser lens, objective lens, projective lens as well as intermediate lens. These lenses help to focus the electrons to produce a small probe beam and form images of samples. The objective lens is the heart of the microscope. The spherical and chromatic aberrations inherent in the objective lens are the major limitations to the resolution of the TEM instrument.

d) A sample chamber: This is where the sample is positioned, and is directly above the objective lens. It is important that the chamber is spacious enough to allow the samples to be viewed with a wide range of tilting necessary for the crystal orientation examination as well as for the chemical analysis.

e) Camera(s): Images of the samples can be acquired using a video/scanned camera which is located beneath a phosphor screen where the images are seen. The photographs are taken by lifting up the screen and exposing the film in the camera. However, this recording method has been gradually replaced by using a charge-coupled device (CCD) camera, which collects a digital image which can be stored in a computer.

f) Vacuum system: The TEM runs at a very high vacuum, which is maintained by a vacuum system. In most cases, such a system comprises a combination of two types of pumps, i.e. mechanical and turbomolecular pumps.

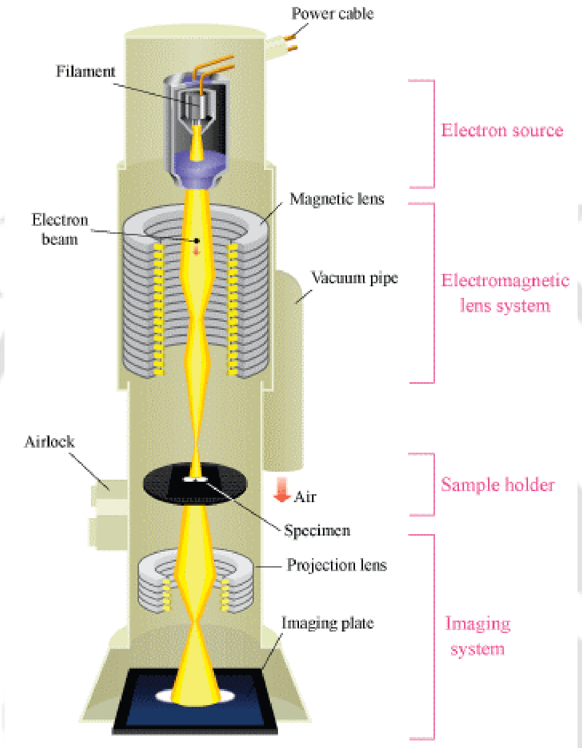

Fig. 2.8: *Schematic diagram of transmission electron microscopy [19].*

Thermionically emitted electrons from the gun are accelerated to 100 *keV* or higher and are first projected onto the specimen by means of the condenser lens system. The scattering process experienced by these primary electrons during their passage through the specimen determines the kind of information obtained. Elastic scattering, involving no energy loss, when electrons interact with the potential field of the ion core, gives rise to diffraction patterns. Inelastic interactions between beam and matrix electrons at heterogeneities such as grain boundaries, dislocations, secondary phases, defects, density variations, etc., cause complex absorption and scattering effects, leading to a spatial variation in the intensity of the transmitted beam. Images can be formed in a number of ways. The bright field image is obtained by intentionally excluding all diffracted beams and only allowing the central beam passing through the specimen. This is done by placing suitably sized apertures in the back focal plane of the objective lens. Intermediate and projection lenses then magnify this central beam. Dark field images are also formed by magnifying a single beam; here one of the diffracted beams is chosen by means of an aperture that blocks the central beam and the other diffracted beams.

By selected area (electron) diffraction, abbreviated as SAD (SAED), ring like structure is imaged, which corresponds to the particular plane of that element or compound. If only diffused rings appear then the system would be in an amorphous phase. In the present investigation, SAD pattern has been employed to identify the crystalline nature of the mechanically alloyed BNO and sol-gel prepared BNO and BWO samples.

2.2.5 Thermal analysis

Thermal analysis is a group of techniques that study the properties of materials as a function of temperature. In differential scanning calorimetry (DSC), the heat flow to and from a sample and a reference material is measured as a function of temperature as the sample is heated, cooled or held at constant temperature. The measurement signal is the energy absorbed by or released by the sample in milliwatts. DSC permits to detect endothermic and exothermic effects, measure peak areas (transition and reaction enthalpies), determine temperatures that characterize a peak or other effects, and measure specific heat capacity. DSC can be used to measure a number of characteristic properties of a sample like fusion, crystallization events and glass transition temperatures (T_g), oxidation and other chemical reactions [20]. Thermogravimetric analysis (TGA) measures the weight and therefore the mass of a sample as a function of temperature. TGA permits to detect changes in the mass of a sample (gain or loss), evaluate stepwise changes in mass (usually as a percentage of the initial sample mass), and determine temperatures that characterize a step in the mass loss or mass gain curve. The TGA curve gives the information about the thermal stability of the material, decomposition temperature (lowest temperature at which the cumulative mass change reaches a magnitude), and the temperature at which the reaction is complete and the reaction interval [20]. In the current investigation, DSC/TGA is used to determine the melting and crystallization temperature of the sol-gel processed dried BNO and BWO ceramic powders.

2.2.6 Particle size analyzer

The particle size distribution of calcined powder was measured using electrophoretic light scattering method [21]. It is the method used to determine the velocity of the particles suspended in a liquid medium under an applied electric field. In order to determine the speed of the particles movement, the particles are irradiated with a laser light, and the scattered light emitted from the particles is detected. Since the frequency of the scattered light is shifted from the incident light in proportion to the speed of the particles movement, the electrophoretic mobility of the particles could be measured from the frequency shift of the scattered light. In the current work, Delsa Nano C (Beckman coulter, Model no: A53878) was used to measure the particle sizes of the calcined powders prepared using sol - gel process.

2.2.7 Density measurement

Precise density measurements are a significant part of characterizing the physical properties of ceramics. The densities of the sintered (fired) pellets were determined using Archimedes technique. According to Archimedes principle, when a body is immersed partially or completely in a fluid, it experiences an upward force (buoyant force) which is equal to the weight of the liquid displaced by it. The relative densities of the sintered pellets calculated using the following expression:

$$\rho_a = \left(\frac{w_1}{w_2 - w_3} \right) \times \rho_w \ \text{gm/cm}^3 \tag{2.6}$$

where, w_1 is the weight of the sintered pellet in air,w_2 is the weight of the sintered pellet immersed in liquid medium (distilled water), w_3 is the weight of the sintered pellet after removed from liquid medium (distilled water) and ρ_w density of liquid medium (water = 1 gm/cm^3). The relative densities of sintered pellets were calculated using the formula:

$$\text{Relative density} = \frac{\rho_a}{\text{theoretical density}} \tag{2.7}$$

2.2.8 Microwave characterization

The increasing demand for the development of high-speed, high frequency devices require a complete understanding of the properties of materials functioning at microwave frequencies [22]. In general, the microwave methods for materials characterization fall into two categories: non-resonant methods and resonant methods. Non-resonant methods are often used to obtain a general knowledge of electromagnetic properties over a wide frequency range, while resonant methods are used for low loss dielectric materials to get accurate knowledge of dielectric properties at a single microwave frequency or at several discrete microwave frequencies [23]. The presence of air gaps is one of the most important factors limiting the measurement accuracy of high permittivity solid materials, unless the electric field of the mode of interest does not have a component perpendicular to the surfaces of the sample. This is the situation for TE_{0np} modes of cylindrical cavities and dielectric resonators. Therefore, methods employing these modes are considered to be among the most accurate [24]. The quasi-$TE_{01\delta}$ mode of operation (often called the TE_{011}-mode) is the mode most commonly used by manufacturers of dielectric materials for making dielectric loss tangent measurements.

The important characteristics of a dielectric resonator (DR) are dielectric constant, loss tangent and temperature dependence of resonant frequency. The permeability of most of these materials is equal to that of free space, as they are nonmagnetic materials. A parallel plate dielectric resonator structure known as Courtney set up is used to measure the dielectric constant of the bulk dielectric material. The principle involved in the measurement is rather simple. The resonant frequency of a $TE_{01\delta}$ mode is measured for a dielectric resonator radius 'a' and height 'L'. Afterwards, the dielectric constant is computed using the Courtney procedure [24]. Hakki and Coleman first introduced the procedure. The error analysis and investigation of temperature effects were later made by Courtney [25]. Another cylindrical cavity made up of invar is used to measure the temperature coefficient of resonant frequency of the cylindrical DR. The negligible coefficient of thermal expansion of invar material helps to increase the accuracy of this measurement.

2.2.8.1 Vector network analyzer

In microwave engineering, network analyser is a most important instrument used to examine a wide variety of materials, components, circuits and systems. A measurement of the reflection from and/or transmission through a material along with knowledge of its physical dimensions provides the information to characterize the permittivity and permeability of the material. Network analyser is a swept frequency measurement equipment to completely characterize the complex network parameters in comparatively less time without any degradation in accuracy and precision. Two types of network analysers are available: scalar and vector network analysers. Scalar network analyser measures only the magnitude of reflection and transmission coefficients while the vector network analyser measures both the magnitude and phase. Note that magnitude and phase of a component can be critical to the performance of a communication system. A vector network analyser (VNA) can provide information on a wide range of these devices, i.e., from active devices such as amplifiers and transistors to passive devices such as capacitors and filters.

A basic network analyser is designed to show graphically a plot of the voltage gain or loss of a network versus frequency. The network analyser measures the magnitude, phase and group delay of two-port networks to characterize their linear behaviour. A vector network analyser consists of a signal source, a receiver and a display. The source launches a signal at a single frequency to the material under test. The receiver is tuned to that frequency to detect the reflected and transmitted signals from the material. The measured response produces the magnitude and phase data at that frequency. The source is then stepped to the next frequency and the measurement is repeated to display the reflection and transmission measurement response as a function of frequency. The ratio of the output to the input level is displayed as *dB* which is the voltage gain or loss of the network.

Consider a circular cylindrical rod of relative dielectric constant ε_r, permeability μ_0, length *L*, and radius *a* placed between two large perfectly conducting plates. If the dielectric material is isotropic, then the characteristic equation for this resonant structure operating in the TE_{0nl} mode is

$$\alpha \frac{J_0(\alpha)}{J_1(\alpha)} = -\beta \frac{K_0(\beta)}{K_1(\beta)} \tag{2.8}$$

Where, $J_0(\alpha)$ and $J_1(\alpha)$ are the Bessel functions of the first kind of orders zero and one, respectively, $K_0(\beta)$ and $K_1(\beta)$ are the modified Bessel functions of the second kind of orders zero and one, respectively. The parameters α and β depend on the geometry, the resonant wavelength and dielectric properties. Thus,

$$\alpha = \frac{2\pi a}{\lambda_0}\left[\varepsilon_r - \left[\frac{c}{v_p}\right]^2\right]^{1/2} \tag{2.9}$$

$$\beta = \frac{2\pi a}{\lambda_0}\left[\left(\frac{c}{v_p}\right)^2 - 1\right]^{1/2} \tag{2.10}$$

C is the velocity of light and v_p the phase velocity in the structure so that

$$\frac{c}{v_p} = \left(\frac{l\lambda_0}{2L}\right) \tag{2.11}$$

Where, l is the number of longitudinal variations of the field along the axis, L is length of the DR, D is diameter of the DR, λ_0 is free space resonant wavelength. It is seen that the characteristic equation is a transcendental equation and hence, a graphical solution is necessary. The resulting mode charts are given by Hakki et al. [24] where each value of β_l corresponds α_n. The characteristics equation and the resulting charts are universal as per as permittivity concerned.

In the present investigation, a vector network analyzer (M/s Rohde & Schwarz, ZVA24) was used for the measurement of microwave dielectric properties of BNO, BWO and BNO - BWO composite ceramics.

2.2.8.2 Measurement of dielectric constant (ε_r)

This can be done by using transmission method introduced by Hakki and Coleman and modified by Courtney [25]. This setup is having two parallel plates with an adjustment for varying distance between the two plates. Two bent monopoles (rigid coaxial cables) are provided for coupling electromagnetic waves to the DR and are suitably mounted to move in any of the x, y and z directions. One can identify the modes of the DR by moving the bent monopoles in all three directions. The number of standing waves in z-directions indicates the third subscript of resonant mode. By rotating the rigid coaxial cables around its own axis, it is possible to find the maximum field in horizontal direction or vertical direction. Subsequently, the first subscript can be found by placing the coaxial cable at different angles in the plane of parallel plates. Once the resonant frequency of $TE_{01\delta}$ mode is measured, the relative dielectric constant for the dielectric resonator with known dimensions can be calculated using the below equations

$$\beta_l = \frac{2\pi a}{\lambda_0}\left[\left(\frac{l\lambda_0}{2L}\right)^2 - 1\right]^{\frac{1}{2}} \tag{2.12}$$

$$\varepsilon = \left(\frac{\alpha_n \lambda_0}{2\pi a}\right)^2 + \left(\frac{l\lambda_0}{2L}\right)^2 \tag{2.13}$$

Where, β_l corresponds to α_n, which can be obtained from the mode chart given in [25] one of the characteristic equation.

2.2.8.3 Measurement of unloaded quality factor (Q_u)

To measure the Q factor of microwave resonators, various methods are applied [26 - 30]. However, all the methods do not consider practical effects produced by a real measurement system such as noise, crosstalk, coupling losses, transmission line delay and impedance mismatch. Inadequate accounting of these effects may lead to significant uncertainty in the measured Q factor of the DR.

The Q factor measured for the DR under end shorted condition using parallel plate resonant method is very low, since the losses occur due to conducting plates, radiation etc. Therefore, to reduce these effects, in our present study, we have used a transmission mode cavity proposed by Krupka et al. [23] to measure unloaded quality factor of the DR. This measurement is done using reflection method by placing the sample over a low loss quartz spacer with height 4 mm inside a cylindrical copper cavity having 10 mm height and 24 mm diameter (inner dimensions). The inner side of the cavity was finely polished and silver plated to reduce radiation loss. The use of low loss single quartz spacer reduces the effect of losses due to the surface resistivity of the cavity. Samples with diameter / length (D/L) ratio of 1.8 - 2.2 are preferable to get maximum mode separation and to avoid interferences from other modes. Microwaves are fed into the sample using the loop coaxial antennas, which provides a magnetic coupling to excite the transmission mode resonance spectrum of dielectric cylinder. The rigid coaxial cable is provided at the center of the cavity (as shown in Fig. 2.9 (a)) for electromagnetic field coupling and it can be moved in and out for adjusting between weak and strong coupling.

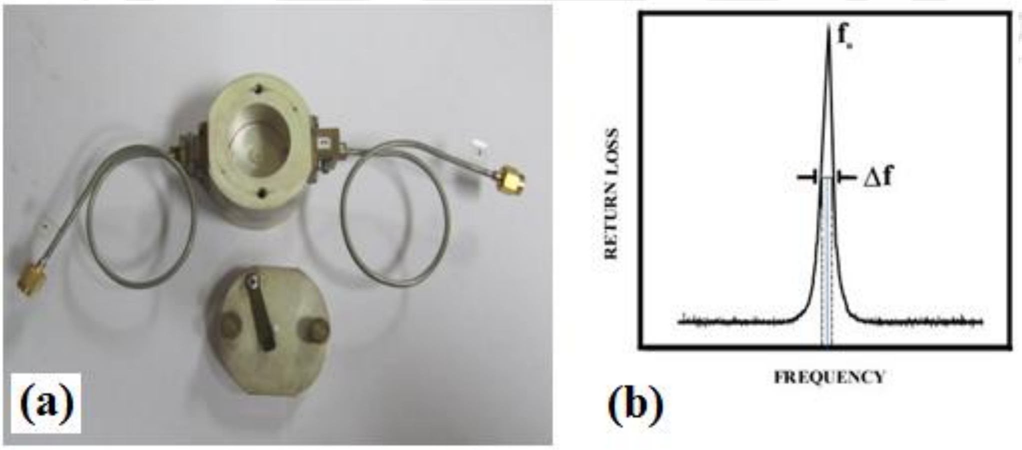

Fig. 2.9: *(a) QWED Krupka resonator cavity used to measure the Q- factor and dielectric constant (b) the method of calculating Q- factor from resonant mode using Eq.2.14.*

The cavity is connected to the VNA through a rigid coaxial cable with connectors on both the ends (THRU). The network analyzer is set in S_{21} mode and performed the calibration. The coaxial cable is adjusted in such a way that weak coupling exists between the rigid coaxial cable and DR. By identifying the $TE_{01\delta}$ mode, the resonant frequency can be obtained. The 3 *dB* bandwidth of the spectrum to calculate loaded *Q* factor (Q_l), from the resonance spectrum (Fig. 2.9 (b)) is given by,

$$Q_l = \frac{f_0}{\Delta f} \tag{2.14}$$

One can assume that the unloaded *Q* factor is equal to loaded *Q* factor if coupling is weak (S_{21} at resonance < 45 *dB*, and couplings are symmetric). The unloaded Q_u value is calculated using the coupling coefficient β_c, and loaded Q_l value using the relation [23],

$$Q_u = \frac{Q_l}{(1-\beta_c)} \tag{2.15}$$

Where, β_c is the coupling coefficient is equal to $10^{\frac{-S_{21}}{20}}$. Further rigorous electromagnetic analysis must be performed to evaluate the dielectric constant of the sample under test. Rayleigh-Ritz's method has been used in the computer program for calculating the dielectric constant.

2.2.9 RF impedance/Material analyzer

In the current thesis work, the broadband dielectric properties of the BNO, BWO and BNO - BWO composite ceramic samples were measured in the frequency range of 1 MHz - 1 GHz using RF impedance / Material Analyzer (M/s Agilent Technologies, E4991A) attached with dielectric cell and automated temperature controller (BDS 2200 and 2300, M/s Novocontrol, GmBH). The temperature of the system can be varied from -140 °C to 400 °C with maximum heating / cooling rate of 20 °C/ min. Fig. 2.10 shows the photograph of the RF impedance / Material analyzer and which is used to study the broadband dielectric properties.

Fig. 2.10: *Photographs of the RF impedance/material analyzer equipped with temperature control systems used to measure the dielectric properties.*

2.2.10 Raman Spectroscopy

Raman spectroscopy is a form of vibrational spectroscopy, much like infrared spectroscopy. Nevertheless, whereas infrared bands arise from a change in the dipole moment of a molecule due to an interaction of light with the molecule, Raman bands arise from a change in the polarizability of the molecule due to the same interaction. This means that these observed bands (corresponding to specific energy transitions) take place from specific molecular vibrations. When the energies of these transitions are plotted as a spectrum, they can be used to identify the molecule as they provide a “molecular fingerprint” of the molecule being observed. Certain vibrations that are allowed in Raman spectroscopy are forbidden in IR spectroscopy, whereas other vibrations may be observed by both techniques although at considerably different intensities thus these techniques can be thought of as complementary. In Raman spectroscopy, by varying the frequency of the radiation, a spectrum can be produced, showing the intensity of the exiting radiation for each frequency. This spectrum will show which frequency of radiation have been absorbed by the molecule to raise it to higher vibrational energy states.

When light is scattered from a molecule or crystal, the majority photons are elastically scattered. The scattered photons have the same energy (frequency) and, consequently, wavelength, as the incident photons. On the other hand, a small fraction of light (approximately 1 in 10^7 photons) is scattered at optical frequencies different from, and typically lower than, the frequency of the incident photons. The process leading to this inelastic scatter is termed the Raman effect. Raman scattering can occur with a change in vibrational, rotational or electronic energy of a molecule. If the scattering is elastic, the process is called Rayleigh scattering. If it’s not elastic, the process is called Raman scattering.

Since, discovery of the Raman effect in 1928 by Sir. C.V. Raman, for which he got the Nobel Prize in 1930 for his work, Raman spectroscopy has become an established as well as a practical method of chemical analysis and this method is applicable to many different chemical species [31]. If the substance being studied is illuminated by monochromatic light, for example from a laser, the spectrum of the scattered light consists of a strong line (the exciting line) of the same frequency as the incident illumination together with weaker lines on either side shifted from the strong line by frequencies ranging from a few to about 3500 cm^{-1}. The lines of frequency less than the exciting lines are called Stokes lines, the others anti-Stokes lines. Raman spectroscopy is very significant practical tool for quickly identifying molecules and minerals. A Raman spectrometer was deployed on the Viking landers in 1972 and in other missions. Raman spectroscopy also has important scientific applications in studying molecular structure. To characterize the samples with Raman spectroscopy, samples may be in the form of solids (particles, pellets, powders, film, and fibers), liquids (gels, pastes), and gases.

2.3 Thin film fabrication and characterization techniques

The $Ba_5Nb_4O_{15}$, $BaWO_4$ and $Ba_5Nb_4O_{15}$ - $BaWO_4$ composite materials have been frequently used in bulk form and therefore most of the studies were paying attention to study of bulk properties. $Ba_5Nb_4O_{15}$, $BaWO_4$ are excellent microwave dielectric materials with wide bandgap and high refractive index suitable for optical and electronic applications. Therefore, their practical applications in optical response are very promising. To the best of our knowledge, the growth of thin films using $Ba_5Nb_4O_{15}$, $BaWO_4$ and $Ba_5Nb_4O_{15}$ - $BaWO_4$ microwave dielectric ceramics as target materials has not been reported so far. Therefore, brief histories of various thin film fabrication techniques are discussed below.

A thin film is a solid or liquid such that one of its linear dimensions is very small in comparison with the other two dimensions. Thin films (layers of material) have a thickness ranging from fractions of a nanometer to several micrometers in thickness. Thin films have very attractive properties that are quite different from those of the bulk materials which they are made of. Further the fact that their properties depend on a number of interrelated parameters, and also on the technique in use for their fabrication. The preparation techniques of thin films are generally classified into two categories: (a) Chemical vapor deposition (CVD) and (b) Physical vapor deposition (PVD).

2.3.1 Chemical vapor deposition

Chemical vapor deposition (CVD) is a process where one or more volatile precursors are transported via the vapor phase to the reaction chamber, where they decompose on a heated substrate. CVD is a widely used materials-processing technology. The majority of its applications involve applying solid thin-film coatings to surfaces and it has been used to deposit a very wide range of materials.

2.3.2 Physical vapor deposition

In physical vapor deposition (PVD), the depositing material will be transferred from solid, liquid or gas phase into a vapor phase by different vaporization methods and condensed on a suitable substrate kept at different substrate temperatures after the transport as a molecular beam in vacuum or by diffusion through a diluted background gas (working gas atmosphere). PVD is divided into two major categories: (i) Thermal evaporation and (ii) sputtering.

2.3.2.1 Thermal evaporation

This process involves that when heating a solid material inside a high vacuum chamber, taking it to a temperature at which it produces some vapor pressure. Inside the vacuum, even a relatively low vapor pressure is sufficient to raise a vapor cloud inside the chamber. This evaporated material now constitutes a vapor stream, which traverses the chamber and hits the substrate, sticking to it as a coating or film.

2.3.2.2 Sputtering

Sputtering is a process whereby atoms are ejected from a solid target material due to bombardment of the target by energetic particles. It only happens when the kinetic energy of the incoming particles is much higher than conventional thermal energies (>> 1 *eV*). In 1852, Sir W. R. Grove first invented the sputtering phenomenon. Sputtering is commonly used for thin film deposition, especially to obtain stoichiometric thin films (i.e., without changing the composition of the original material) from target material. Physical sputtering is driven by momentum exchange between the ions and atoms in the material, due to collisions [32]. The average number of atoms driven out from the target per incident ion is called the sputter yield and depends on the ion incident angle, the energy of the ion, the masses of the ion, target atoms, and the surface binding energy of atoms in the target. The incident ions set off collision cascades in the target, when such cascades recoil and reach the target surface with energy above the surface binding energy, an atom can be ejected. Sputtered atoms ejected into the gas phase are not in their thermodynamic equilibrium state, and tend to deposit on all surfaces in the vacuum chamber. A substrate (such as a wafer) placed in the chamber will be coated with a thin film. Sputtering usually uses argon plasma.

A simple source of ions for sputtering is provided by the glow discharge due to an applied electric field between two electrodes at low pressures [33]. The glow discharge in sputtering is significantly dependent on the work function of the target material and pressure of the environmental gas [32, 34]. When a certain value of voltage is reached between the electrodes the gas breaks down to conduct the electricity. The glow discharge maintains itself at a stable voltage and referred to as a normal glow and the region whereas the voltage and current increase together are called abnormal glow. A luminous layer, which covers the cathode partially in the normal glow and completely in the abnormal glow, is known as a cathode glow. A fairly well-defined region of relatively low luminosity known as Crookes or cathode dark space is found next to it. A bright negative glow region, Faraday dark space and then a positive column region follows this in sequence. The cathode dark space is the most significant region. Most of the applied voltage is dropped (cathode fall) across it. Ions and electrons created at the breakdown are accelerated across this region. The different regions in the discharge are illustrated in Fig. 2.11. The energetic electrons generate more ions by collision with the gas atoms in the negative glow and the energetic ions strike the cathode to produce sputtered flux and secondary electrons, which are necessary to sustain the glow. The effective sputtering is possible only when both the number of ions and their energy are large and controllable. There are different types of sputtering techniques proposed for thin film deposition such as direct current (DC), radio frequency (RF), magnetron and reactive sputtering [35].

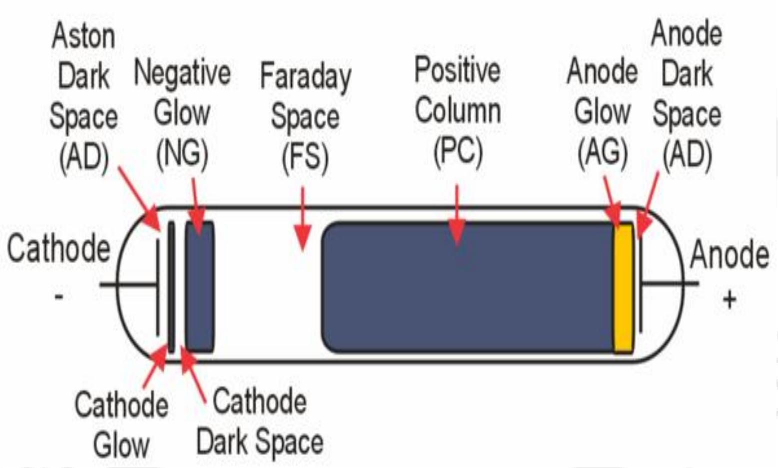

Fig. 2.11: *Different regions in a typical glow discharge [35].*

(i) DC sputtering

This technique is the simplest among the sputtering techniques. In this method, the target (cathode) and substrate (anode) are given a DC bias (~ 1 *Kv*). The Ar^+ ions in plasma (ionized by the energetic electrons confined by the magnetic field around the target) will be accelerated toward cathode, hit the target and transfer the energy sputtering the target to substrate surface. DC sputtering suffers from two major drawbacks as compared to conventional evaporation: (i) low deposition rates and (ii) high thermal load of the substrate due to bombardment of secondary electrons. DC sputtering works with all conductive target materials. However, it’s not possible to sputter insulating materials with this technique because the +*Ve* charged ions can’t flow through the insulator and hence the electric circuit is interrupted. So the potential at the cathode drops and the +*Ve* ions are no longer accelerated towards the target. Schematic view of direct current (DC) sputtering is shown in Fig. 2.12.

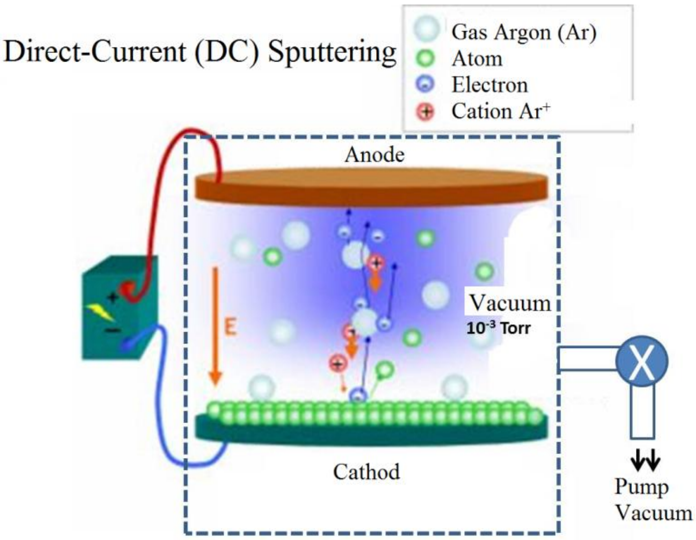

Fig. 2.12: *Schematic representation of direct current (DC) sputtering [36].*

(ii) RF Sputtering technique

RF sputtering process was widely used for the deposition of insulating thin films. Quartz target was used to deposit SiO_2 film. The resistivity (ρ) of the quartz is 10^{16} Ω-cm. To draw a current density (*J*) of 0.1 mA/cm^2, cathode needs a voltage of $V = 0.1J\rho \rightarrow V=10^{12}$ Volts, which is not feasible to generate physically and apply for practical works. This confirms that a target with resistivity exceeding 10^6 Ω-cm cannot be sputtered using DC sources.

The radio-frequency (RF) sputtering is used to sputter insulators as well as conducting materials, as showed in Fig.2.13. Frequently, a large capacitor (500-2000 *pF*) is placed in series between the RF power supply and the powered electrode. The large series capacitor permits a considerable negative bias to develop on the cathode, on average half of the value of the applied peak-to-peak RF voltage (see Fig. 2.14). This bias is then the acceleration voltage for ions from the plasma, which move much slowly to respond to the applied RF potentials.

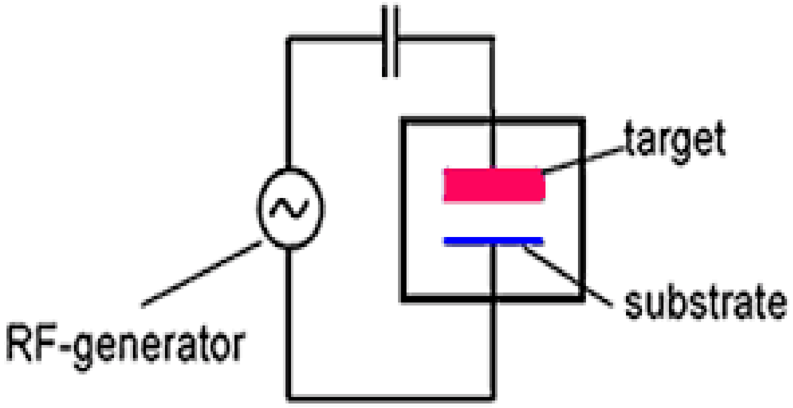

Fig. 2.13: *Schematic of RF sputtering chamber [37].*

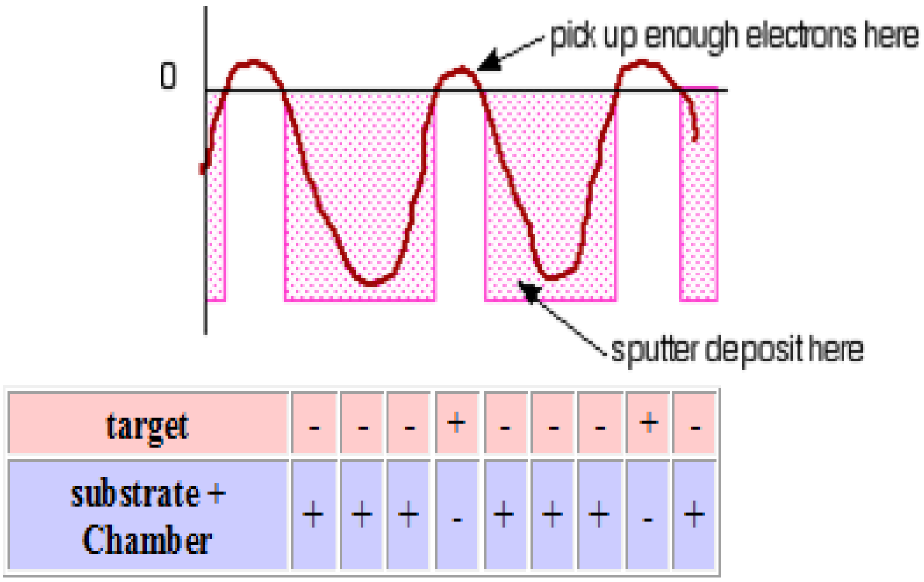

target	-	-	-	+	-	-	-	+	-
substrate + Chamber	+	+	+	-	+	+	+	-	+

Fig. 2.14: *Variation of RF bias with time and the responses of target and substrate with RF bias [37].*

The RF generator is effectively used to maintain the discharge and to avoid charge build-up throughout the sputtering of insulating materials. Because the positive charges don't need to flow through the target the sputtering of non-conducting materials is also possible. The electrons and ions show different types of responses with the RF frequency: (i) For frequencies less than about 50 kHz: (a) Electrons and ions in plasma are mobile (both follow the switching of the anode and cathode), (b) Basically DC sputtering of both surfaces, (ii) For frequencies above 50 kHz: (a) Ions (heavy) can no longer follow the switching, (b) Electrons can neutralize positive charge build up and the electrons oscillating in the glow region acquire more energy to cause ionization collisions, reducing the need for secondary electrons to sustain the discharge, (c) The electron movement delivers a short current pulse when the cathode is positive and smaller current when the cathode is negative, resulting zero average current. RF voltage can be coupled through any impendence, so that the electrodes need not be a conductor. The typical RF frequency used is 13.56 MHz. The major drawbacks of RF sputtering when compared to conventional evaporation is that the low deposition rates and high thermal load of the substrate due to bombardment of secondary electrons.

(iii) Magnetron sputtering technique

In a magnetron sputtering configuration, both an electric field (*E*) and a magnetic field (*B*) are used to confine the electrons near the cathode surface. The main difference between magnetron sputtering and a basic DC sputtering system is that the addition of a strong magnetic field nears the target area. This field causes traveling electrons to spiral along magnetic flux lines near the target instead of being attracted toward the substrate. The magnetron sputtering phenomena can be explained on the basis of (1) electron motion in parallel electric and magnetic fields and (2) perpendicular electric and magnetic fields.

(1) Electron motion in parallel electric and magnetic fields: When the magnetic field of strength ***B*** is superimposed on the electric field ***E*** between the target and substrate, electrons within the dual field environment experiences the well-known Lorenz force in addition to the electric force, i.e.,

$$F = m\frac{dv}{dt} = -q(E + (v \times B)) \tag{2.16}$$

Where, q is charge, m – mass, and v – velocity of electron.

Case I* : *E and ***B*** is parallel. When electrons are emitted exactly normal to the target surface and parallel to both fields, then it results $v\times\mathbf{B}\rightarrow 0$ (see Fig. 2.15 (a)). Electrons are only influenced by the electric field, which accelerates them towards anode.

Case II* : *E = 0 and only ***B*** field. If an electron is launched from the cathode with velocity v at an angle θ with respect to ***B***, then the electron experiences a force $qv\mathbf{B}\sin\theta$ in direction perpendicular to ***B***. The electron orbit in a circular motion with a radius *r* is determined by a balance of the centrifugal force and Lorentz force involved (see Fig. 2.15 (b)).

$$qvB\sin\theta = \frac{m(v\sin\theta)^2}{r} \Rightarrow r = \frac{mv\sin\theta}{qB} \qquad (2.17)$$

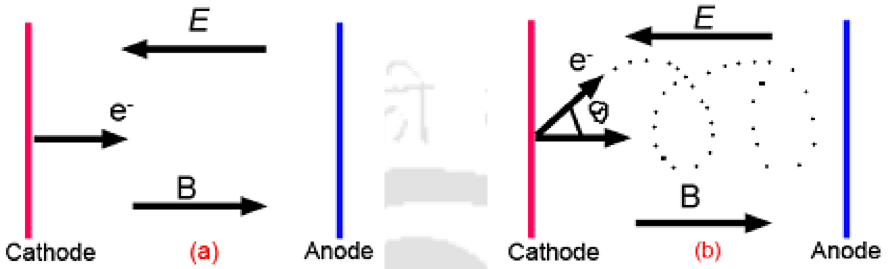

Fig. 2.15: *Motion of the electron under the magnetic field with (a) electron velocity and magnetic field directions are parallel, (b) electron velocity and magnetic field directions are angled at θ [37].*

(2) Perpendicular electric and magnetic fields: In magnetron, electrons preferably don't even reach the anode but are trapped near the target, increasing the ionization efficiency there. This is achieved by employing a magnetic field oriented parallel to the target and perpendicular to the electric field. Practically this is accomplished by placing bar magnets behind the target. Hence, the magnetic field lines emanates first normal to the target, then bend with a component parallel to the target surface and eventually return, completing the magnetic circuit. Electrons emitted from cathode are initially accelerated toward the anode, executing a helical motion in the process, but when they encounter the region of the parallel magnetic field, they are bent in an orbit back to the target. The chief reason of its success is high deposition rate of up to 1 *μm/min* for aluminium.

In magnetron sputtering, the plasma is concentrated directly in-front of the cathode by means of a magnetic field. The substrate is exposed only to the flow of sputter material with few secondary electron bombardments. Fig. 2.16 shows the effect of magnetic field on the glow discharge. When compared to conventional sputtering the advantages of magnetron sputtering are increased sputtering rates (~ 5 - 10 times) due to high plasma density around target, low discharge voltages of 300 to 1000 *V* due to the reduced plasma impendence resulting from high plasma density, and low thermal load of the substrate due to deflection of secondary electrons in the magnetic field.

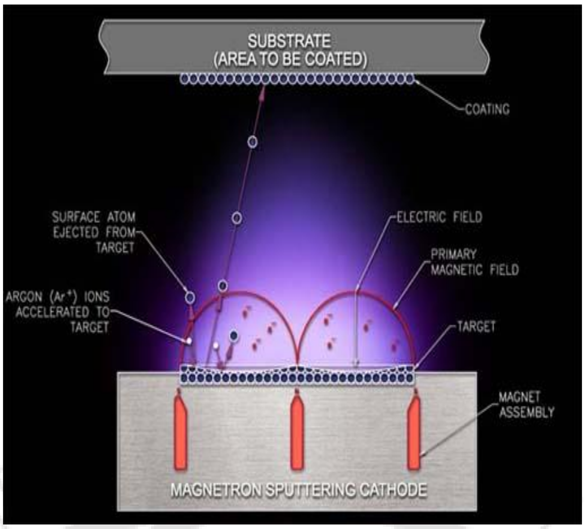

Fig. 2.16: *Schematic presentation of magnetron sputtering gun assembly* [38].

(iv) Reactive magnetron sputtering

In most cases, argon is being used as inert sputtering gas to keep away from the chemical reactions between the target and sputtered gas. Nevertheless, some cases such as the deposition of nitrides and oxides, reactive gases are deliberately added with argon to react with sputtered material. This type of sputtering process is called as a reactive magnetron sputtering [39]. The addition of reactive gases to the sputtering chamber can importantly affects the deposition rate and stoichiometry of the compound.

(v) RF reactive magnetron sputtering

In general, the argon (Ar) is being used as sputtering gas to avoid the chemical reactions between the insulating/dielectric target and sputtered gas. Nevertheless, when a reactive gas species such as oxygen or nitrogen is introduced in to chamber, thin films of compounds such as oxides and nitrides are deposited by the sputtering of the appropriate metal targets. This process is known as reactive magnetron sputtering. This process is used in practice for high rate of deposition of insulating metal oxide films and stoichiometry of the compound.

In the current study, RF reactive magnetron sputtering system (M/s Advanced Process Technologies, Pvt. Ltd., India) has been chosen for the deposition of pure $Ba_5Nb_4O_{15}$, $BaWO_4$ and $Ba_5Nb_4O_{15}$ - $BaWO_4$ composite thin films. Fig. 2.17 shows the photographic image of the RF reactive magnetron system. The RF sputtering system consists of a vacuum chamber carrying with pumping systems, sputtering source, heating assembly, and rotating substrate holder. The advantages of RF reactive magnetron sputtering is that the low-temperature crystallization, thickness uniformity, high deposition rates and high adhesion, good stoichiometric thin films, large throughput, and less expensive.

Fig. 2.17: *Photographic view of the RF reactive magnetron sputtering system.*

2.3.3 Optical properties

Optical properties of the films have been studied broadly mainly because of their applications in various optical and electro-optical devices and it has been found that there is often a considerable deviation of optical parameters from that of a bulk material [40]. The optical properties of the thin films were calculated using envelope technique [41]. The spectral transmission characteristics of the films deposited onto transparent substrates measured in the wavelength range of 200 - 1200 nm were measured using a UV - VIS - NIR spectrophotometer (M/s SHIMADZU, UV 3101PC). The fundamental optical constants such as refractive index (n), absorption coefficient (α), and optical bandgap (E_g) of the thin films were determined from transmission spectra.

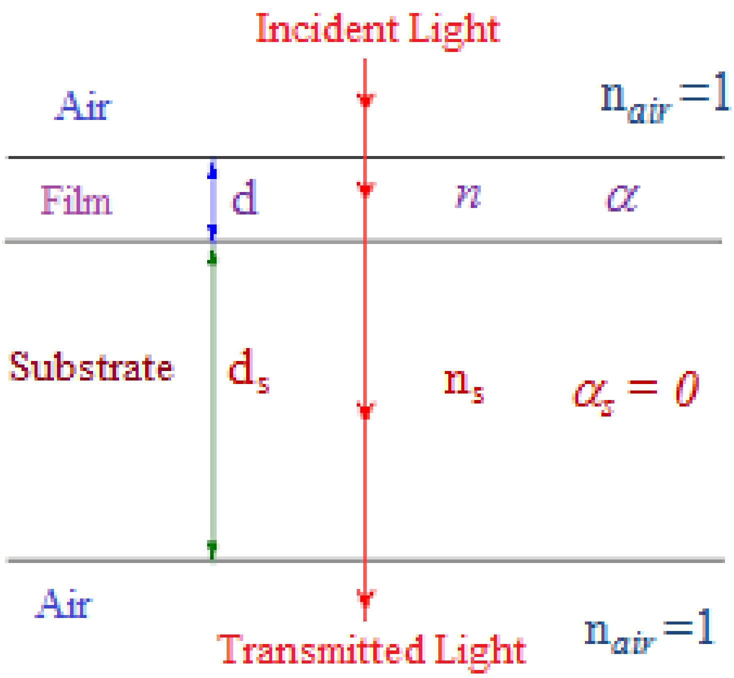

Fig. 2.18: *Thin film on a transparent substrate.*

As shown in the Fig. 2.18, a film of refractive index n with the thickness d, deposited onto a transparent substrate having the refractive index n_s and thickness d_s. When the light is incident on a film of refractive index n, coated on to a substrate of refractive index s, then at the air-film, film-substrate and substrate-air interfaces, part of the incident light is reflected and part of it is transmitted. Since the reflected and transmitted beams originate from a single coherent source, the beams exhibit interference effects.

The condition for the constructive interference is,

$$2nd = m\lambda \tag{2.18}$$

Where, m is the order of interference, it is an integer for maxima and half integer for minima.

The typical transmittance spectrum of the film deposited onto a transparent substrate is shown in Fig. 2.19. It is assumed that the transmission is a continuously varying function of wavelength; therefore, an envelope can be drawn across the spectrum by connecting the all maxima and all minima.

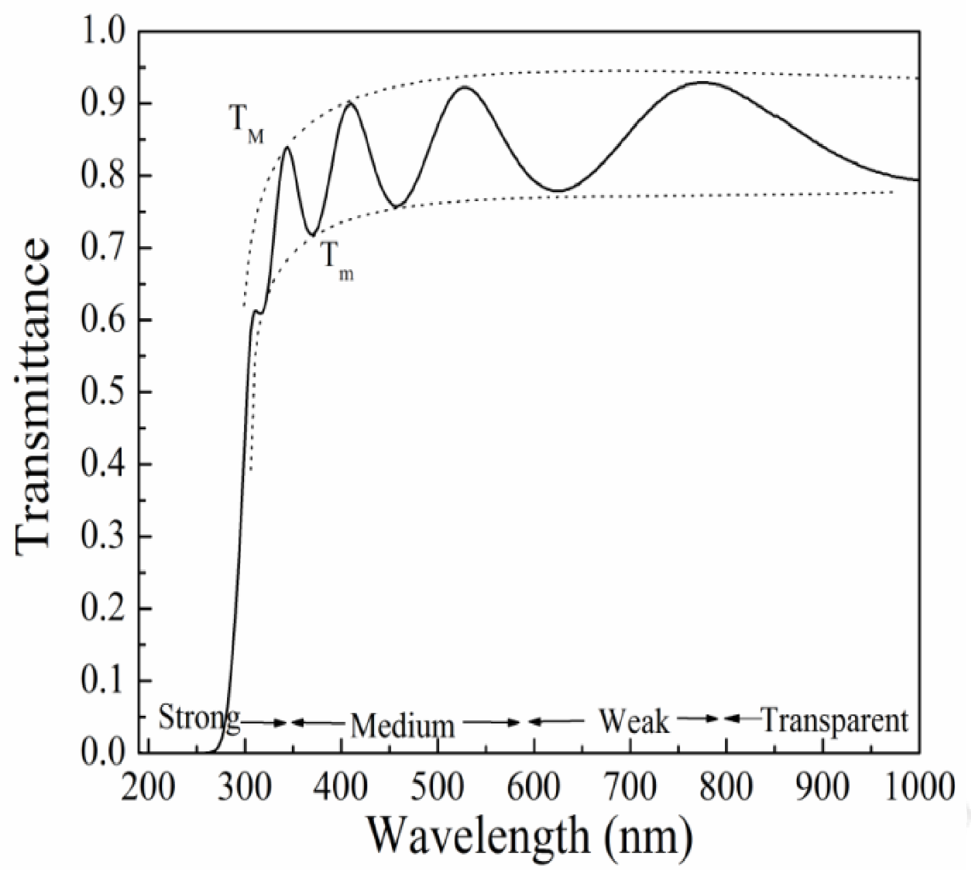

Fig. 2.19: *Typical transmittance spectrum of a thin film [41].*

The expression for the transmittance (T) for normal incidence is given as [41],

$$T(\lambda, n_s, n, d, \alpha) = \frac{Ax}{B - Cx\cos\phi + Dx^2} \tag{2.19}$$

Where, $A = 16n^2 n_s$,

$B = (n + 1)^3 (n + n_s)^2$

$C = 2(n^2-1)(n^2-n_s^2)$

$D = (n - 1)^3 (n - n_s^2)$

$\phi = 4\pi nd/\lambda$

$x = \exp(-\alpha d)$.

The extreme values of transmission at the constructive and destructive interference fringes are obtained by using the interference condition $\cos\phi = +1$ for maxima (T_M) and $\cos\phi = -1$ for minima (T_m) in equation 2.19.

The refractive index of the films calculated using the following expression,

$$n = \sqrt{N + \sqrt{N^2 - n_s^2}} \tag{2.20}$$

Where,
$$N = 2n_s \frac{T_M - T_m}{T_M T_m} + \frac{n_s^2 + 1}{2} \qquad (2.21)$$

$$n_s = \frac{1}{T_s} + \sqrt{\frac{1}{T_s^2} - 1} \qquad (2.22)$$

If n_1 and n_2 are the refractive indices at two successive maxima (or minima) at wavelengths λ_1 and λ_2, then according to the constructive interference equation,

$$2n_1 d = m_1 \lambda_1 \qquad (2.23)$$

and
$$2n_2 d = m_2 \lambda_2 \qquad (2.24)$$

by solving the both equations using the rule $|m_1 - m_2| = 1$, then we get thickness of the film using the following expression.

$$d = \frac{\lambda_1 \lambda_2}{2(n_1 \lambda_2 - n_2 \lambda_1)} \qquad (2.25)$$

From the Beer-Lambert's law [42],

$$I = I_0 \exp(-\alpha d) \qquad (2.26)$$

Where, I_0 is the incident light intensity, I is the intensity of the light at wavelength λ, d is the thickness of the film, and α is the absorption coefficient, which can be related to the transmittance as,

$$\alpha = \frac{-\ln T_\alpha}{d} \qquad (2.27)$$

Where, $T_\alpha = (T_M T_m)^{0.5}$.

Further, knowing the values of α, the optical bandgap (E_g) of the films can be calculated using the Tauc relation [43],

$$(\alpha h\nu)^m = B(h\nu - E_g) \qquad (2.28)$$

The E_g of the films would be obtained from the extrapolated linear portion of $(\alpha h\upsilon)^m$ versus $(h\upsilon)$ curve, where $h\upsilon$ is the incident photon energy, B is a measure of crystalline order, and m determines the type of electronic transition between the valence band and conduction band. In the current thesis, the E_g has been calculated by assuming an allowed direct electronic transition (m = 2). The error associated with the measurement of n and d is ± 0.02 and ± 10 nm, respectively.

2.3.4 Surface profilometer

The thickness and rate of deposition of the thin films deposited on amorphous SiO_2 (transparent substrates) and platinized silicon substrates were measured using stylus profiler (M/s Veeco Dektak, 150). The stylus profilometer measures the thickness of thin films electromechanically by moving the thin films below a diamond-tipped stylus. A high precision X-Y stage moves the thin films beneath the stylus according to the given program (scan length, speed and force), where the stylus is mechanically coupled with the linear variable differential transformer (LVDT). As the films moves under the stylus, surface variations of films cause the vertical displacements in the stylus. These vertical displacements are converted into electrical signals by LVDT and further the signals are converted to digital format through an analog-to-digital converter, where it can be displayed on the computer screen. Scan length and scan speed can be fine-tuned to increase or decrease analysis time and resolution.

2.3.5 Low frequency dielectric measurement and *I-V* characteristics

For the low frequency dielectric measurements and leakage current characteristics (*I-V*) of deposited oxide thin films (deposited on Pt coated Si substrates), metal-insulator-metal (MIM) type test structures were fabricated. Silver top electrodes (diameter 0.4 mm and 150 nm thick) were deposited on top of the oxide layer and deposited by dc sputtering / thermal evaporation using a shadow mask.

An LCR meter is a renowned electronic test equipment used to measure the inductance (*L*), resistance (*R*), capacitance (*C*) and dissipation factor of capacitors in the radio frequency region (low frequency) by parallel plate capacitor method of an electronic component. These parameters will give an approximate calculation of quantities such as ε_r and loss tangent ($tan\ \delta$) which in turn aids to calculate the fairly accurate resonant frequency and size of the DR to evaluate the *Q* factor. In order to form a capacitor, the parallel plate capacitor method is used and it requires sandwiching a thin sheet of the material between two electrodes. The dielectric properties are to be measured by using the capacitance of a parallel plate capacitor in vacuum is compared with one in the presence of the material. Then relative permittivity is calculated using the following relation [44],

$$C = \frac{\varepsilon_r \varepsilon_o A}{d} \qquad (2.29)$$

Where C is the capacitance of the material and ε_r and ε_o are the relative permittivities of the material and free space, respectively.

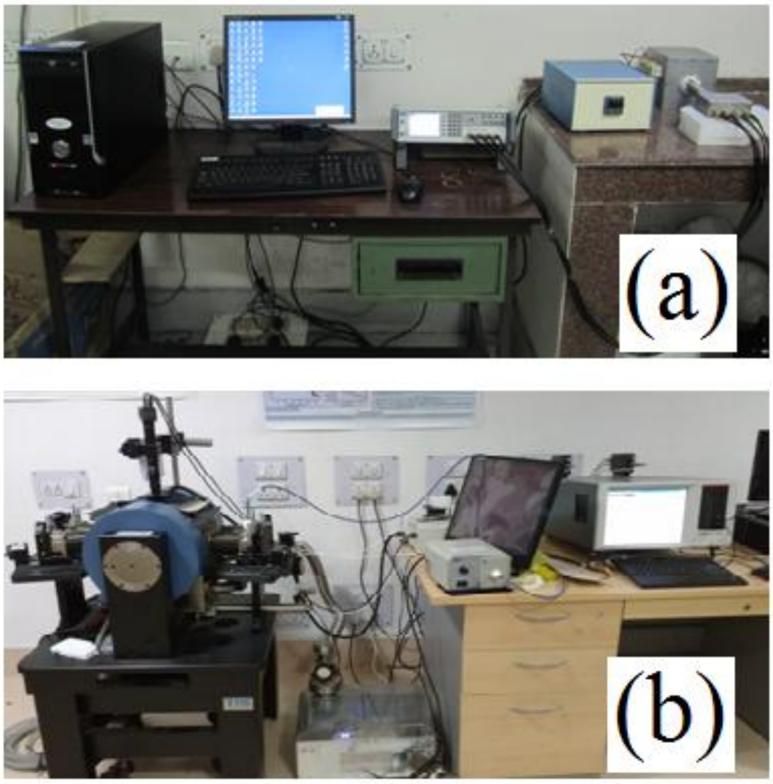

Fig. 2.20: *Photographs of the (a) LCR meter used to measure the dielectric properties and (b) Keithley 4200 semiconductor systems along with probe station.*

The majority of the dielectric thin films are based on the application of an external voltage, which can lead to the occurrence of leakage current. The understanding of origin of the conduction is very significant to decrease the leakage current in the films. Consequently when thin films are subjected to external voltage, it is essential to study the charge transport in thin films to identify the conduction mechanisms and which is responsible for the leakage current. In the present thesis, the dielectric constants and dielectric loss of the films were calculated from the capacitance–frequency response as a function of temperature in frequency range of 20 Hz to 1 MHz were measured using an LCR meter (M/s Wayne Kerr Electronics Pvt. Ltd., 1J43100) connected to a computer via RS232 connection and leakage current characteristics (*I*-*V*) of the thin films were measured using a parameter analyzer (M/s Keithely, 4200 SCS) connected with a probe station (J Microtechnology LMS 2709 DC), which is shown in Fig. 2.20.

2.3.6 Microwave dielectric properties of thin films using split post dielectric resonator method

The microwave dielectric properties of thin films were determined by using a vector network analyzer (M/s Rohde & Schwarz, ZVA24) by employing the split-post dielectric resonator (SPDR) method at 5, 10, and 15 GHz's [45]. This method is attractive for accurate non - destructive measurements of low - loss substrates. Low loss materials are nearly non dispersive so that the dielectric constant and loss tangent will stay constant over a range of frequencies.

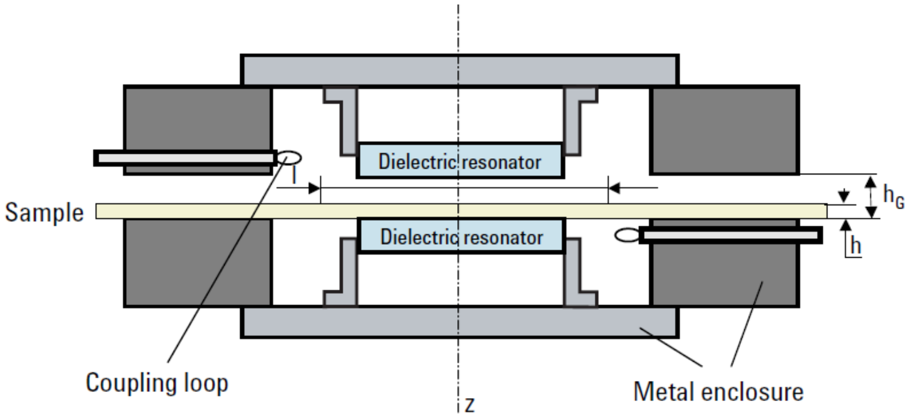

Fig. 2.21: *Typical cross sectional view of SPDR fixture [45].*

In order to use the oxide films in the microwave integrated circuits and in the electronic applications, it is important to know the dielectric response of these films at microwave frequencies. To obtain the dielectric properties of the oxide films at microwave frequencies, resonant techniques are being used because of their sensitivity and precision. However, these resonant techniques would give the response of the oxide film only at one spot frequency. The split-post dielectric resonator (SPDR) technique is a non destructive technique employed to measure the complex dielectric properties of thin films at microwave frequencies. This method enables us to find the correlation between the resonant frequency, complex permittivity and quality factor (*Q*) of substrates and dielectric thin film at a specific frequency. The dielectric response of the oxide films would be obtained in two stages. Initially, the resonant frequency and *Q* factor of the bare substrate would be obtained; afterwards, the resonant frequency and *Q* factor of the SPDR having the dielectric film deposited on the same substrate would be measured [46, 47].

SPDR oscillates in the $TE_{01\delta}$ mode, which has only an azimuthal electric field component so the electric field stand by continuous across the dielectric interfaces, that causes the system insensitive to the presence of air gaps between the tested film and the cavity. The real part of permittivity (ε_r) of the dielectric films is calculated by using the measured resonant frequencies and thickness of the film as an iterative solution to the following expression.

$$\varepsilon_r^{'} = 1 + \frac{f_0 - f_s}{h f_0 K_\varepsilon(\varepsilon_r^{'}, h)} \tag{2.30}$$

Where h = thickness of the film under test, f_o = resonant frequency of empty resonant fixture, f_s = resonant frequency of the resonant fixture with dielectric film, K_ε = slowly varying function of ε_r and h, the iterations using the formula (2.30) converge rapidly. The cross section of a SPDR is shown in Fig. 2.21.

The dielectric loss tangent is determined using the following expression

$$\tan\delta = (Q^{-1} - Q_{DR}^{-1} - Q_c^{-1}) / p_{es} \tag{2.31}$$

Where, Q is the unloaded Q-factor of the SPDR containing the dielectric film and P_{es} is the electrical energy-filling factor of the sample. Q_c is the Q-factor depending on the metal losses for the SPDR comprising the dielectric thin film and Q_{DR} is the Q-factor depending on the loss tangent in the dielectric resonators. The uncertainty in ε_r and $\tan\delta$ is estimated as,

$$\frac{\Delta\varepsilon_r}{\varepsilon_r} \leq 0.15\% + T\frac{\Delta h}{h} \tag{2.32}$$

Where, $1 < T < 2$, and $\Delta\tan\delta = \pm 2.0\times10^{-5}$.

The significant advantage of the split – post dielectric resonator is the irrational shape of the sample under the test. However, the sample should have a uniform thickness with smaller dimensions than for a metal-cavity resonator, also the feasibility to measure thin films [48].

2.4 References

[1] R. E. Carter, *J. Chem. Phys*. **34** (1961) 2010.

[2] M. N. Rahaman, *Ceramic processing and sintering*, Marcel Dekker, Inc, New York (2003).

[3] D. Seagal, *Chemical synthesis of advanced ceramic materials*, Cambridge University Press, Cambridge (1991).

[4] C. Suryanarayana, "*Mechanical Alloying and Milling*", Marcel Dekker, New york, (2004).

[5] C. Suryanarayana, *Prog. Mater. Sci*. **46** (2001) 1.

[6] S. Penn and N. Alford, *Handbook of low and high dielectric constant materials and their applications phenomena, Properties and Applications,* (Editor Hari Singh Nalwa), Academic Press, (1999).

[7] D. W. Richerson, Modern Ceramic Engineering, Properties, Processing, and use in design. 3rd Ed., Taylor and Francis, London, (2006).

[8] X. K. Wu, D. W. Whitman, W. L. Kaufell, W. C. Finch and D. I. Cumbers, *Ceram. Eng. Sci. Proc.* **18** (1997) 422.

[9] P. Winiewski, M. Szafran, G. Rokicki, *Key Eng. Mater. Euro Ceram.-VIII,* **264** (2000) 428.

[10] S. J. Kang, *Sintering, densification, grain growth and microstructure*, *Elsevier*, Amesterdam, (2002).

[11] R. L. Coble, *J. Appl. Phys.* **32** (1961) 787.

[12] A. M. Guzmán, P. Rodríguez, *The AZo journal of materials online,* DOI: 10.2240/azojomo0201.

[13] W. D. Kingery, M. Berg, *J. Appl. Phys.* **26** (1955) 1205.

[14] W. D. Kingery, H. K. Bowen, D. R. Uhlmann, *Introduction to ceramics*, John Wiley and Sons, New York (1975).

[15] M. W. Barsoum, *Fundamentals of Ceramics*, CRC Press, New York, (2003).

[16] D. Cullity, *X-ray Diffraction*, Addison-Wesley, Reading, MA (1956).

[17] R. A. Young, *The Rietveld Method*, Oxford university press, New York, (1996).

[18] P. J. Grundy, G. A. Jones Electron microscopy in the study of materials, Edward Arnold Publishers Limited (1976).

[19] http://www.hk-phy.org/atomic_world/tem/tem02_e.html

[20] A. John Dean, *The Analytical Chemistry Handbook*, McGraw Hill Inc., New York, (1995).

[21] R. Xu, Particle size characterization: Light Scattering Methods, *Kluwer Acadamic Publications*, USA.

[22] D. Kajfez, P. Guillon (eds.), Dielectric Resonators Norwood, MA, *Artech House* (1986).

[23] J. J. Krupka, K. Derzakowskiz, B. Riddlex, J. B. Jarvisx, *Meas. Sci. Technol*. **9** (1998) 1751.

[24] B. W. Hakki, P. D. Coleman, *IEEE Trans. Microwave Theory Technol*. **8** (1960) 402.

[25] W. E. Courtney, *IEEE Trans. Microwave Theory Technol*. **18** (1970) 476.

[26] Y. Kobayashi, M. Katoh, *IEEE Trans. Microwave Theory Technol*. **33 (**1985) 586.

[27] E. L. Ginzton, *Microwave Measurements*, McGraw Hill Book Co., Boston, (1957).

[28] E. J. Vanzura, J. E. Roger, *Proc. IEEE Conference on instrumentation and Measurement Technology*, May 15-16, Atlanta, (1991).

[29] T. Miura, M. Kobayashi, *IEICE Transactions on Electronics* **E7** (1994) 900.

[30] M. T. Sebastien, *Dielectric Materials for Wireless Communications*, Elsevier Science Ltd, Netherlands (2008).

[31] C. V. Raman, K. S. Krishnan, *Nat.* **121** (1928) 501.

[32] M. M. Abdelrahman, *Brazilian Journal of Physics* **40** (2010) 26.

[33] K. Wasa, M. Kitabatake, H. Adachi, *Thin film materials technology*: Sputtering of compound materials" *Springer, Verlag*, Berlin (2004).

[34] K. Hine, The Second International Symposium on Atomic Technology IOP Publishing, Journal of Physics: Conference Series **106** (2008) 012019.

[35] K. Wasa, M. Kitabatake, H. Adachi, *Thin film materials technology*: Sputtering of compound materials” *Springer*, *Verlag*, Berlin (2004).

[36] https://energisurya.files.wordpress.com/2013/10/dc-sputtering.jpg.

[37] http://nptel.ac.in/courses/115103039/module16/lec39/2.html.

[38] http://www.angstromsciences.com./sputtering-technology.

[39] W. D. Sproul, D. J. Christie, D. C. Carter, *Thin Solid Films* **491** (2005) 1.

[40] A. Goswami, *Thin Film Fundamentals*, New Age International Pvt Ltd Publishers (2008).

[41] R. Swanpoel, *J. Phys. E: Sci. Instrum*. **16** (1983) 1214.

[42] D. F. Swinehart, *J. Chem. Educ*. **39** (1962) 333.

[43] J. C. Tauc, Optical Properties of Solids, F. Abeles ed. *North-Holland Publishing*, Amsterdam (1972).

[44] W. D. Kingery, M. Berg, *J. Appl. Phys.* **26** (1955) 1205.

[45] J. Krupka, A. P. Gregonry, O. C. Kochard, R. N. Clarke, B. Riddle, *J. Eur. Ceram. Soc*. **21** (2001) 2673.

[46] J. Krupka, R. G. Geyer, J. B. Jarvis, J. Ceremuga, pp.21-24,DMMA'96 Conference, Bath, U.K. 23-26 Sept. (1996).

[47] J. Krupka, K. Derzakowski, M. V. Jacob, B. L. Givot, Proc. MIKON’2008, May 19-23, (2008).

[48] J. Krupka, *Meas. Sci. Technol.* **17** (2006) R55.

Chapter 3

Dielectric studies on $Ba_5Nb_4O_{15}$ bulk and thin films

3.1 Introduction

Recent past, due to the rapid development in the wireless communication, there is an enormous demand for microwave dielectric resonators (DRs) with high dielectric constant (ε_r), high - quality factor ($Q = 1/tan\delta$) and a near temperature coefficient of resonant frequency (τ_f) close to zero [1 - 4]. DRs have been widely used in a variety of applications ranging from communication devices to satellite services. Further, a material with $\varepsilon_r < 20$, high Q - factor and temperature stability is used for type - I ceramic capacitor applications. It was observed that some hexagonal perovskite oxides have been found to be the candidate materials for dielectric resonators in the base station of telecommunication systems and type - I capacitors [5, 6]. Among the hexagonal perovskites; $Ba_5Nb_4O_{15}$ (BNO) ceramics are promising due to its excellent dielectric properties in bulk form: high dielectric constant (ε_r) ~ 39, Quality factor ($Q\times f_0$) ~ 26.3 THz and temperature coefficient of resonance frequency (τ_f ~ +79 ppm/^{o}C) and were first investigated by Galasso and Katz [7, 8]. In order to use BNO ceramics in type - I ceramic multilayer capacitor applications, it is important to understand the dielectric response over a broad range of measurement frequency. Nonetheless, the drawback of BNO is the formation of secondary phases whenever the samples were prepared using solid - state reaction method and require higher sintering temperature (> 1400 ^{o}C), which limits the applications of this material in various communication devices [7, 8].

There are few reports available on synthesis of BNO ceramics by solid - state reaction method, and few authors have used different additives / sintering aids to reduce the sintering temperature and to tune the τ_f. Nonetheless, the addition of different supplements detoriated the microwave dielectric properties, especially the loss tangent [6, 9, 10]. To reduce the sintering temperature of BNO ceramics, Hsiao et al. [11] prepared the BNO ceramics through sol - gel process and the reported sintering temperatures were in between 700 - 900 ^{o}C; however, they did not study the microwave dielectric properties. Zhou et al. [12] prepared the BNO ceramics by molten salt method, and the reported dielectric properties were: $\varepsilon_r \sim 39.2$, $Q\times f_0 = 27.2$ THz and $\tau_f \sim 72$ ppm/°C. Generally, three methods were adopted to reduce the sintering temperature of microwave ceramics: (i) addition of low softening glassy or liquid phase sintering aids [6], (ii) chemical methods [11] and (iii) small particle sizes prepared by mechanical alloying [13]. Reduction of particle size by mechanical alloying reveals that the mechanical activation can accelerate solid - state reaction, which occurs at elevated sintering temperatures or high pressures. However, to the best of the author's knowledge, there is no study available on mechanically alloyed BNO ceramics. Further, most of the studies on these ceramics were centered on reduction of sintering temperature, elimination of secondary phases and tuning of τ_f [8]. Conversely, there is no report on the impedance spectroscopy and broadband dielectric properties of these ceramics measured both at low and high temperatures, which would help us to understand the dielectric behaviour of these ceramics, particularly the loss tangent. In this study, to minimize the processing temperature, mechanical alloying has been employed to prepare the BNO ceramics.

Mechanical alloying method is a convenient method for the synthesis of wide range of nanosized metallic and ceramic powders in an efficient and economical manner [14, 15]. It has many advantages; such as simplicity, relatively inexpensive to produce nanoparticles and applicable to variety of materials [16]. The most valuable advantage of mechanical synthesis is the activated energy via mechanical deformation instead of a large thermal energy (high temperature). Furthermore, this process avoids the calcination stage, which helps to minimize the fraction of secondary phases and non uniform grain growth. Furthermore, the greatest possible extent reactivity of the mechanically alloyed powders possesses a higher sinterability as compared to the powders synthesized by a conventional solid - state reaction and most of the wet - chemical processes [17]. Mechanical alloying not only makes the material finer but also incorporates structural changes, phase transformations and even solid - state reactions among the solid reagents. These physical and chemical modifications occur due to the effective transformation of mechanical energy of the grinding media to the powders and the intensive mechanical force during the milling process [18]. Taking all this into account, we have adopted mechanical synthesis method to prepare the BNO ceramics and to see the influence of mechanical alloying on phase formation, crystal structure, microstructure, as well as on microwave dielectric properties of BNO ceramics. In addition, broadband dielectric properties are measured both at low and high temperatures, and the impedance spectroscopy of the BNO ceramics has been reported for the first time.

In addition to the above study, to reduce the sintering temperature of BNO ceramics, we have also added the smaller concentrations of BNO nanoparticles to the micron sized BNO ceramic matrix as a sintering aid. It is well known that the smaller particles enhance the densification at lower sintering temperatures [19 - 22]. Due to the similar chemical nature, the addition of nanoparticles would not deteriorate the microwave dielectric properties. The addition of nanoparticles of same material as a sintering aid to the micronsized particle is not well understood, hence, this study. The effect of BNO nanosized particle addition on microstructure and microwave dielectric properties of a host BNO ceramics were carried out and discussed. Hsiao et al. [11] reported the synthesis of BNO ceramics by sol-gel process. However, this study was only focussed on microstructure, but there is no systematic study on BNO ceramics prepared by sol-gel process in the microwave dielectric resonator point of view. This motivated the authors to study the effect of BNO nanoparticles (prepared by sol-gel process) addition on micron sized BNO matrix to enhance the microwave dielectric properties.

Cryogenic electronics is a fast growing branch of electronics where the operation of electronic devices and circuits, and systems were performed at cryogenic temperatures. The main reason for operating electronic devices at cryogenic temperatures is to improve the performance of the electronic devices such as lower noise, increased efficiency, higher speed, etc. There are some low-temperature electronic applications such as deep-space probes and planetary missions (Mars, Jupiter, Moon, etc.), satellite communication systems with space-based radar and medical electronics and the study of the material properties at low temperatures is essential [23]. However, there are no reports available regarding the dielectric properties of BNO ceramics added with its own nanosized particles with different (1, 2 and 3 wt%) weight percentages characterized at low temperatures. In the present study, the broadband (1 MHz - 0.1 GHz) dielectric response of BNO ceramics added with nanosized BNO particles were studied over the temperature range of -140 ^{o}C to 200 ^{o}C.

Further, the use of metal oxide surface coatings is performing a wide range of applications in the antireflection coatings; microwave integrated circuits (MICs), complementary metal oxide semiconductor (CMOS) and optoelectronic devices [24, 25]. Due to the comparatively eminent inertness of ceramic materials will make this type of thin films coatings used for wear and corrosion-resistant coatings [26]. Besides, the thin films having been lowering crystallization temperature as compared to bulk samples and the manufacturing of high-energy storage thin film capacitors with high dielectric constant is suitable in the miniaturization of microwave constituents. Further, it is also known that the physical and chemical properties of the films drastically deviate from the bulk properties due to the confined geometry and the properties of thin films significantly changes with the processing parameters such as RF power, deposition time, substrate to target distance, oxygen mixing percentage (OMP), and working pressure. Hence consequently, it is important to study and understand the behavior of the films. Hence, it is important to understand the thickness dependence of these properties.

$Ba_5Nb_4O_{15}$ (BNO) ceramics are promising for the above applications due to its excellent dielectric properties in bulk form. In addition, it is well known that optical, electrical and dielectric properties are strongly dependent on thickness and the processing technique, and it is important to understand how the response of a material varies with thickness. In contrast, to the best of the authors' knowledge, there is no report available on the BNO thin films; this motivated us to pursue this study. Therefore, this work focuses on deposition and characterization of nanocrystalline BNO thin films by RF reactive magnetron sputtering. Study the effect of thickness on the structural, electrical and dielectric properties of BNO films systematically.

3.2 Experimental Details

3.2.1 Synthesis of BNO ceramics by mechanical alloying method

$Ba_5Nb_4O_{15}$ (BNO) ceramics were synthesized by the mechanical alloying (MA) process from individual high - pure oxide powders (99.99%) $BaCO_3$ from (M/s Sigma Aldrich, St. Louis, MO) and Nb_2O_5 (M/s Nuclear Fuel complex, Hyderabad, India). The starting materials were mixed according to desired stoichiometry ratio, and the powders were ball milled for 40 hours (*h*) using planetary ball mill (M/s Fritsch Pulverisette 6, Germany) with the following parameters : (i) ball - to - powder ratio of 10:1; ball diameters of 5 and 10 mm; ball and vial material: tungstun carbide; milling speed of 400 rpm. The ball milling process was stopped periodically for every 5 *h* and collected some powder for further analysis. After drying and sieving, the samples were uniaxially pressed into pellets with dimensions of 10 mm in diameter and 4 - 5 mm in thickness under a pressure of 200 *MPa*. The pellets were sintered in the range of 1200 - 1350 ^{o}C for 5 *h* in air. The heating and cooling rates were 15 ^{o}C / min and 1 ^{o}C / min, respectively.

3.2.2 Synthesis of BNO nano sized particles prepared by sol-gel process

The BNO nanopowders were prepared using the high - pure chemicals; barium nitrate (99.95%) $Ba(NO_3)_2$, niobium penta chloride (99.90%) $NbCl_5$, ethylene glycol (99%) $C_2H_6O_2$, and ethanol (90%) C_2H_5OH from (M/s Alfa Aesar, Hyderabad, India), and citric acid anhydrous (99.5%) $C_6H_8O_7$ (M/s Fisher Scientific, Mumbai, India). Initially, the starting chemicals $Ba(NO_3)_2$ and $Nb(OC_2H_5)_5$ were dissolved in the distilled water with the desired stoichiometry ratio. Niobium ethoxide $Nb(OC_2H_5)_5$ was prepared from niobium penta chloride $NbCl_5$, and ethanol C_2H_5OH, according to the general reaction [11].

$$NbCl_5 + 5C_2H_5OH \rightarrow Nb(OC_2H_5)_5 + 5HCl \qquad (1)$$

The aqueous solutions of $Ba(NO_3)_2$ and $Nb(OC_2H_5)_5$ added to citric acid (chelating agent) in molar ratio of 1:2, ethylene glycol was used as a stabilizing or capping agent. Further, solution was dried in an oven at 120 ^{o}C and calcined at 700 ^{o}C for 2 *h* to obtain BNO powders.

3.2.3 Synthesis of BNO micron sized particles by solid-state reaction method

The micron sized BNO polycrystalline powders were prepared using the conventional solid-state reaction method. The starting materials with stoichiometric mixtures of the high-purity powders of (99.99%) $BaCO_3$ from (M/s Sigma Aldrich, St. Louis, MO), (99.95%) Nb_2O_5 (M/s Nuclear Fuel complex, Hyderabad, India) were ball milled for 5 *h* with distilled water as a medium using tungsten carbide jar and balls in a planetary ball mill (M/s Fritsch GmbH, Germany). The wet mixtures of the powders were dried and calcined at 1000 ^{o}C for 5 *h*. The calcined BNO powder again mixed with BNO nano sized particles (prepared by sol-gel process) with different (1, 2 and 3 wt%) weight percentages for duration of 5 *h* in a planetary ball mill. Afterwards, these powders were pressed into pellets with dimensions of 10 mm in diameter with 4 - 5 mm in thickness, and the pellets were sintered in the temperature range of 900 - 1200 ^{o}C for 3 *h* in air. The maintained heating and cooling rates were 10 ^{o}C / min and 2 ^{o}C / min, respectively.

3.2.4 Synthesis of BNO sputtering target and deposition of BNO thin films by RF magnetron sputtering

The BNO polycrystalline sputtering target was prepared using the mechanical alloying method to avoid the subordinate phases. The high-purity powders of $BaCO_3$

(99.99%), Nb_2O_5 (99.95%) were used as starting materials and were weighed in accordance with their stoichiometry. The weighed powders were ball milled for 40 *h* using tungsten vial and balls in a planetary ball mill. It was found that the pure BNO phase is obtained for the samples milled for 50 *h*. Afterwards BNO powders were pressed into a cylindrical target of 62 mm in diameter with 4 mm in thickness. The BNO target was sintered at 1250 °C for 5 *h*. The BNO thin films were deposited by RF magnetron sputtering on <100> oriented Pt/Ti/SiO_2/Si and amorphous SiO_2 substrates at ambient temperatures. The deposition chamber was pumped down to a base pressure of 5.0×10^{-6} *Torr*. The substrate to target distance was maintained at 6 cm. A mixture of high pure argon (99.999%) and oxygen (99.999%) were introduced into deposition chamber using mass - flow controllers. The sputtering pressure of 5×10^{-3} *mTorr* is maintained constantly throughout the deposition process by varying the argon / oxygen ratio in a standard cubic centimeter per minute (SCCM) in the sputtering gas, at a fixed RF power of 40 *W* for a constant duration of 3 *h*. The BNO target was pre-sputtered in argon ambience for 10 minutes to remove the impurities on the target surface. The rate of deposition under different oxygen mixing percentage (OMP) has been optimized to achieve the constant thickness of the film. The thickness of the films deposited on amorphous SiO_2 substrates and Pt coated film was estimated using the surface profilometer (M/s Veeco Dektak, 150). The as deposited BNO films were X-ray amorphous and to obtain the crystallinity; BNO films were annealed at 700 °C for 3 *h* in air.

3.2.5 Characterization techniques

The relative densities of the sintered samples were calculated by Archimedes's method. Crystal structures of the as prepared, sintered and thin film samples were analyzed by using a high power X-ray diffraction (XRD) technique with Cu-Kα radiation (λ = 1.5406 *Å*) (M/s Rigaku, TTRAX-III 18 *kW*). Further, XRD patterns of bulk samples were refined by using Rietveld refinement technique and FullProf program [27]. The particle size, shape and crystallinity of the prepared nanopowders were identified by using a transmission electron microscope (TEM) (M/s JEOL, JEM 2100). Microstructural and chemical compositions of the bulk and thin films were examined through scanning electron microscope (SEM) (M/s LEO, 1430vp) and field emission scanning electron microscope (FESEM) (M/s Zeiss, Sigma). The dielectric constant (ε_r), and quality factor (*Q*) values at microwave frequencies were measured using the Hakki - Coleman dielectric resonator method [23, 28]. Broadband dielectric spectroscopy evaluates the complex dielectric function $\varepsilon = \varepsilon' - i\varepsilon''$ of materials in dependence on frequency. ε reflects the molecular relaxation and transport processes of the material, which depend on any other physical quantity like e.g. temperature, time, superimposed electromagnetic fields, pressure, etc. Therefore, applications in science and technology seem to be almost unlimited, such as studies of the charge transport in semiconductors, organic crystals, ceramics, etc [28]. The change in various physical parameters and their characteristic properties that affect the performance of these materials can be known and explained using complex impedance spectroscopy. The temperature-dependent broadband dielectric properties (-140 to 400 ^{o}C) and the impedance spectroscopy of BNO ceramics are studied using the impedance analyzer (M/s Agilent Technologies Pvt. Ltd., E4991A) attached with an automated temperature controller (BDS 2200 and 2300, M/s Novocontrol, GmBH). The Raman spectra of the BNO ceramics were recorded using a Raman spectrometer (LABRAM HR800 developed by JOBIN YVON).

To study the electrical and dielectric properties Ag - BNO - Pt (MIM) capacitor structures were fabricated under different film thickness. Silver top electrodes of diameter 0.4 mm and 150 nm thick were deposited by dc sputtering using a shadow mask. The dielectric constants and dielectric loss of the films were calculated from the capacitance-frequency response as a function of temperature in frequency range of 20 Hz to 1 MHz using the LCR meter (M/s Wayne Kerr Electronics Pvt. Ltd., 1J43100). The leakage current mechanism of BNO film capacitors at room temperature was measured using a parameter analyzer (M/s Keithely, 4200 SCS). Spectral transmission characteristics in the wavelength range 200 - 800 nm were measured using a UV - VIS - NIR spectrophotometer (M/s SHIMADZU, UV 3101PC).

3.3 Results and Discussions

3.3.1 Mechanically Alloyed $Ba_5Nb_4O_{15}$ (BNO) Ceramics

3.3.1.1 XRD and TEM analysis

To see the effect of milling on phase formation of BNO ceramics, milled powders are collected for every 5 *h*. XRD patterns of the BNO powders milled for different milling hour are shown in Fig. 3.1. Interestingly, after milling for 10 *h*, the peaks related to parent oxides ($BaCO_3$ and Nb_2O_5) disappeared completely. Furthermore, the XRD patterns reveal the formation of both BNO and $BaNb_2O_6$. Further, peaks corresponding to $BaNb_2O_6$ are dominated the BNO phase. With increasing milling time, the intensities of the peaks related to BNO are found to be improved. Even after milling for 40 *h*; $BaNb_2O_6$

phase could not be eliminated completely. It is known that $BaNb_2O_6$ forms at the low temperatures, in order to obtain the pure BNO phase, the samples have to be heated at high temperatures (> 1200 °C) [29].

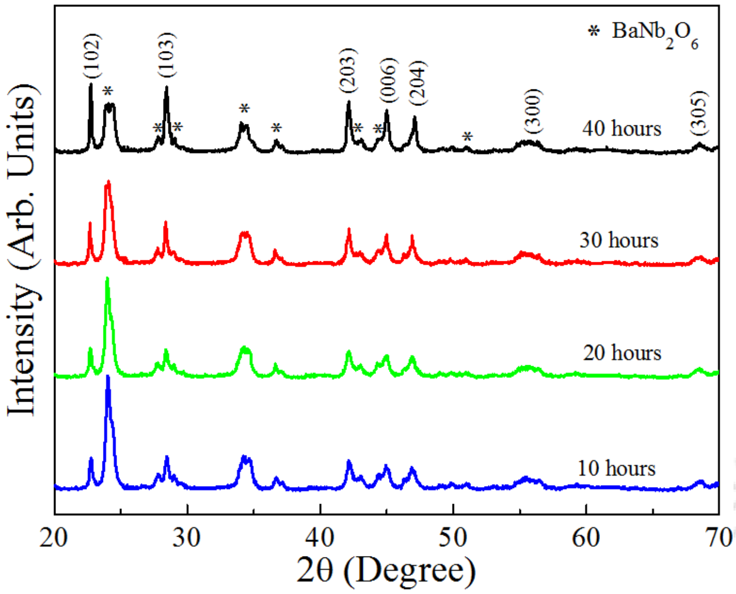

Fig. 3.1: *XRD patterns of $BaCO_3$ and Nb_2O_5 powders milled for 10, 20, 30, and 40 h.*

The weight ratios of BNO (hexagonal) and $BaNb_2O_6$ (orthorhombic) phases are calculated using the following expression [30].

$$W_{BaNb_2O_6} = \left\{1/[1+1.265(I_{BNO}/I_{BaNb_2O_6})]\right\} \times 100 \qquad (2)$$

Where, $W_{BaNb_2O_6}$ denotes the weight fraction of the orthorhombic phase, I_{BNO} *(103)* and $I_{BaNb_2O_6}$ *(301)* are the intensities of hexagonal and orthorhombic phases, correspondingly. The weight fraction of the orthorhombic phase found to be 72.5%, 74.1, 59.6 and 39.8% for the samples milled for 10, 20, 30 and 40 *h*, respectively. In addition, with an increase in the milling time from 10 *h* to 40 *h*, $BaNb_2O_6$ could not be suppressed completely. The formation of $BaNb_2O_6$ can be attributed to the difference in the extent of mechanical energy. The formation of $BaNb_2O_6$ and BNO phases by the mechanical alloying process can be explained as follows: during the mechanical alloying process, the mechanical energy of the milling medium would be transferred to the parent oxides. Whenever balls collide with a container, some amount of powder is trapped in between them and the mechanical energy of the medium would break the bonds and deform the powders with an increase in milling time, which results in the formation of alloy phases starting from prealloyed powders. So, the milled powders pressed into cylindrical samples are sintered at 1250 °C. The XRD patterns of these samples indicate that the samples milled for 40 *h* exhibited a pure BNO phase whereas the other samples exhibited $BaNb_2O_6$, which may be due to the presence of large fraction of $BaNb_2O_6$ weight percentage in the as milled powders. Hence, for further studies, samples milled for 40 *h* are considered. The present study clearly demonstrates the formation of BNO phase at an ambient temperature, which is attributed to the intense transfer of mechanical energy during the alloying process.

To optimize the sintering temperature, the samples milled for 40 *h* were sintered at different temperatures for a constant duration and the XRD patterns of these samples along with Rietveld refinement are depicted in Fig. 3.2. Samples sintered at 1200 °C exhibit a small peak related to $BaNb_2O_6$ phase, which may be attributed to the insufficient sintering temperature, whereas the samples sintered above 1200 °C did not show the signature of this phase.

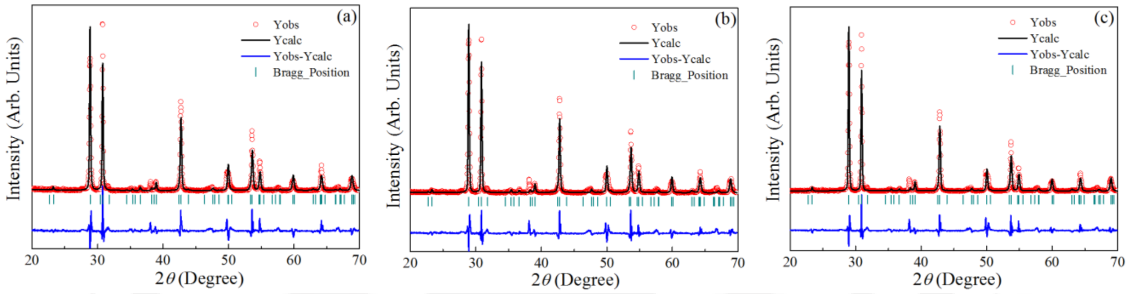

Fig. 3.2: *XRD patterns along with Rietveld refinement of $Ba_5Nb_4O_{15}$ ceramics sintered at (a) 1200 °C, (b) 1250 °C and (c) 1300 °C for 5 h. The circles and solid line represent the experimental and the Rietveld refined data, respectively. The dotted line at the bottom shows the difference between the obtained data and the refined data. The vertical bars correspond to the allowed Bragg's peaks.*

The X-ray diffraction pattern of $Ba_5Nb_4O_{15}$ ceramics along with the Rietveld refinement data of the BNO samples, sintered at 1200 °C, 1250 °C and 1300 °C for 5 *h* is shown in Fig. 3.2 (a - c), respectively. The refinement was carried out by considering $P\bar{3}m1$ space group. The lattice parameters, atomic positions of the Ba, Nb, and O atoms, and occupancy are refined. The corresponding lattice constant values are $a = b = 5.79 \pm 0.002$ *Å*, $c = 11.77 \pm 0.002$ *Å*, which are in agreement with earlier reports [JCPDF file # 17-0794]. The fitting parameters (i) $\chi^2 \approx 10.541$, 9.342 and 10.134 (ii) R_{Brag} factor ≈ 8.482, 7.612 and 9.321 and (iii) R_f factor ≈ 8.921, 9.123 and 8.421 for BNO ceramics sintered at 1200 °C, 1250 °C and 1300 °C, respectively.

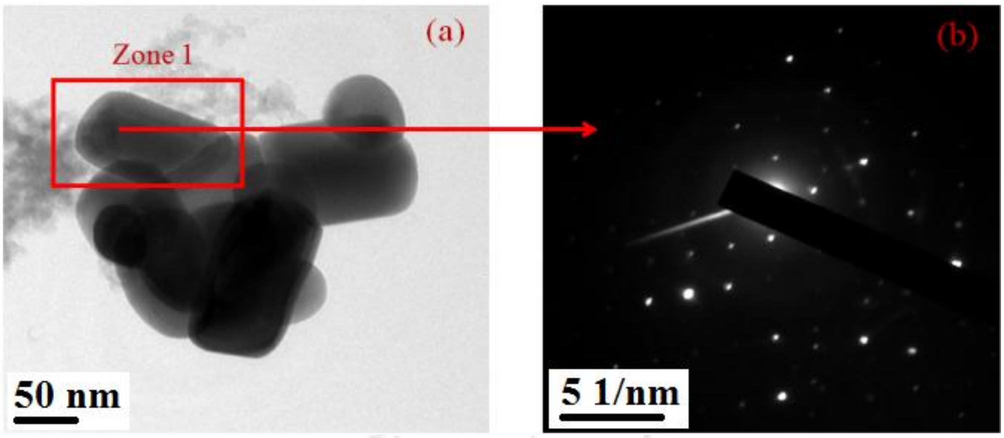

Fig. 3.3: *TEM image of the BNO powders (a) milled for 40 h (b) selected area diffraction (SAD) pattern of the zone 1(Fig. 3.3 (a)).*

The TEM micrograph of the BNO ceramics milled for 40 *h* shown in Fig. 3.3 (a) and it revealed the rod - shaped nanocrystals, whose diameters are found to be around 80 nm. The main reason for rod - shaped nanocrystals might be due to the high speed grinding of the initial particles of $BaCO_3$ and Nb_2O_5 breaks into discrete particle shapes with increasing ball milling time at ambient temperatures. Fig. 3.3 (b) shows the selected area diffraction (SAD) pattern of the 40 *h* milled powder and this revealed the individual diffraction spots, and all these correspond to the inter planar spacing (d - spacing) of the hexagonal BNO ceramics, which suggested the polycrystalline nature of the sample. Therefore, the mechanical alloying process between $BaCO_3$ and Nb_2O_5 at the ambient temperatures took place to form BNO ceramics because of the high - energy transfer to the powders during the milling process.

3.3.1.2 Microstructures

The obtained microstructures of the BNO ceramics, sintered at different temperatures are depicted in Fig. 3.4 (a - c). It is observed that the BNO ceramics sintered at 1200 ^{o}C show a slightly porous microstructure, that can be attributed to the insufficient sintering temperature and the presence of the secondary phase, whereas the sample sintered at 1250 ^{o}C reveal a uniform microstructure with good densification and is ascribed to the deformed small initial particle sizes that enhanced the nucleation and densification of the BNO ceramics. However, the samples sintered at 1300 ^{o}C and above exhibited abnormal grain growth this can be due to the higher thermal energy, which accelerates the grain growth over nucleation.

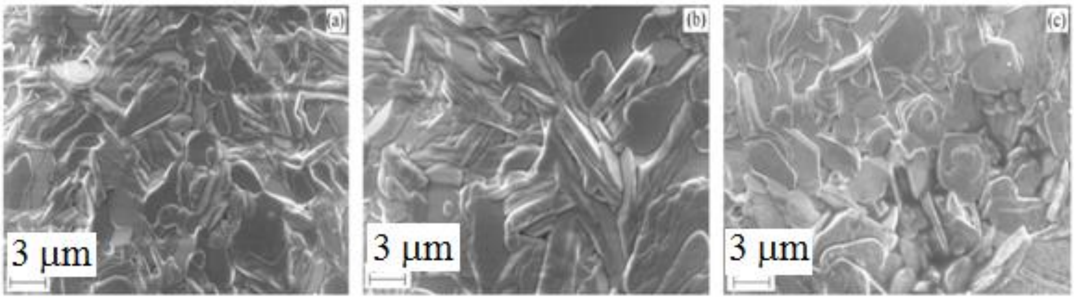

Fig. 3.4: *SEM images of BNO ceramic sintered at (a) 1200 °C, (b) 1250 °C and (c) 1300 °C for 5 h.*

The obtained uniform microstructure and maximum relative densities can be described as follows: BNO powders milled for 40 *h* would be in a deformed state with higher surface reactivity. Small particle sizes exhibit a large surface area, which is a driving force for densification. The effect of particle size on sintering is well explained by Herring's scaling law, and it demonstrates the effect of powders with similar shapes but different particle size on microstructural change in compacts being sintered under the same sintering mechanism [31, 32]. The rate of sintering velocity is inversely proportional to the initial particle size and it plays a vital role in the densification of the prepared ceramics. During the sintering process, the particle rearrangement occurs as a result the pores are eliminated by obtaining the uniform microstructure. In the present study, the BNO ceramics reveal higher densities at lower sintering temperatures as compared to the earlier reports [33, 34].

3.3.1.3 Broadband dielectric properties as a function of temperature

The frequency (1 MHz – 0.5 GHz) dependent dielectric properties of BNO ceramics, sintered at 1250 °C, measured in the temperature range of (-140 to 400 °C) are depicted in Fig. 3.5. It is observed that in the temperature range of -140 to 320 °C, both the dielectric constant, and loss tangent of BNO ceramics showed a stable behaviour up to 0.2 GHz, above that they increase with a rise in applied frequency up to 0.5 GHz. Further, the dielectric constant of the BNO ceramics enhanced progressively with an increase in measurement temperature up to 320 °C above that the dielectric constant decreases. On the other hand, the loss tangent of the ceramics increases slightly with a rise in temperature up to 320 °C above that it drastically increases, and this may be due to the relaxation behaviour (in the temperature range of 350 to 400 °C), which is induced by the temperature. Further, it is interesting to note that the variations in the loss tangent are significant at low temperatures and its stable even at high temperatures up to 320 °C. The variations in dielectric constant with temperature can be described as follows: at low temperatures (-140 to 20 °C), the arrangement of dipoles along the direction of the field would be difficult due to the lower thermal energy, but slight increase in dielectric constant at low temperatures can be associated to variations in the polarization volume, which is explained using Clausius - Mossotti relation [35]. As the temperature increases, the orientation of dipoles is assisted by thermal energy and increase in the anharmonicity in the lattice contributes to the improvement in dielectric constant [36, 37]. The observed low loss tangents below room temperature can be attributed to the reduction in the anharmonic lattice forces, which mediate between the phonons and crystal lattice.

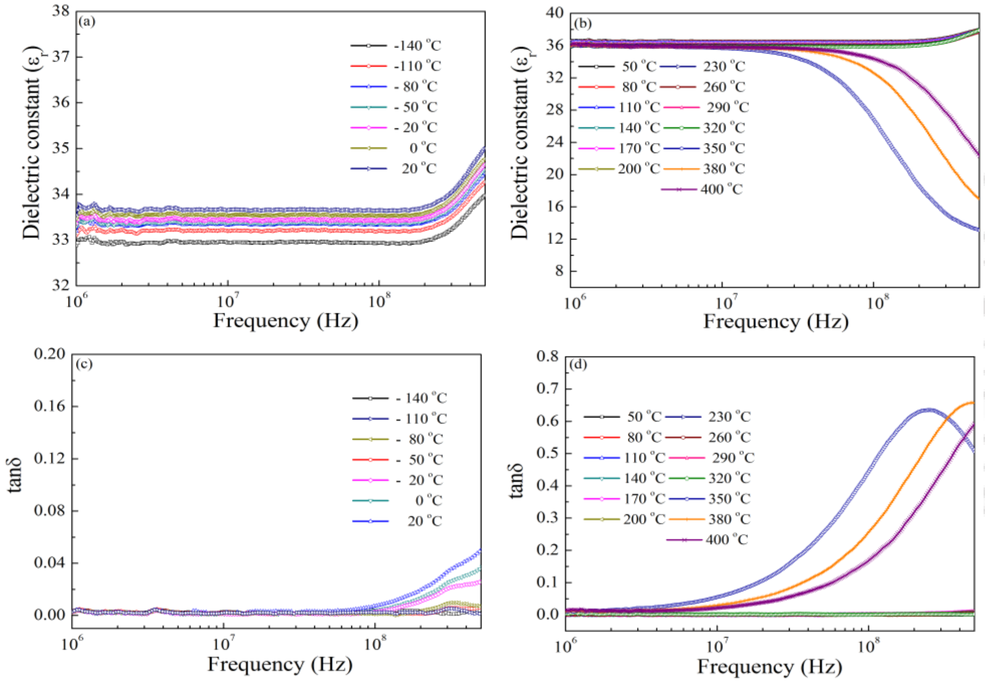

Fig. 3.5: *Variations in dielectric constant as a function of frequency measured in the temperature range of (a) (-140 °C to 20 °C) (b) (50 °C to 400 °C). Variations in loss tangent as a function of frequency measured in the temperature range of (c) (-140 °C to 20 °C) (d) (50 °C to 400 °C).*

The obtained dielectric response has been used to understand the relaxation process. Fig. 3.5 (b) and (d) shows, the relaxation behaviour of ε_r and *tanδ* observed at high temperatures, which is shifted towards the higher-frequency side with an increase of temperature above 350 °C. It may be possible that the origin of relaxation is found in this BNO material correspond to the change in orientation of dipole moments caused by grain

- grain interface, and that is rarely seen in the impedance spectroscopy. In the BNO ceramics, the atoms/molecules cannot orient themselves in the low temperature region. As the temperature increases, the orientation of the dipoles promotes the relaxation behaviour. The relaxation peaks in higher frequency are related with orientation of dipole moments, which do not involve long - range displacement of mobile charge carriers. **Table 3.1** shows the measured dielectric constant (ε_r) and loss tangent ($tan\delta$) values of BNO ceramics, measured at different temperatures and at distinct frequencies. The extracted ε_r values increases from -140 °C to 50 °C and reduces at 400 °C for all discrete frequencies. The reduction in dielectric constant and increase in loss tangent values at 400 °C is due to the relaxation behaviour of BNO ceramics. It is observed that the samples sintered at 1250 °C, showed a good dielectric response as compared to the samples sintered at 1200 °C and 1300 °C and is attributed to the uniform grain growth and maximum relative density.

***Table 3.1**: Measured dielectric constant (ε_r) and loss tangent ($tan\delta$) values of BNO ceramics at different temperatures and at discrete frequencies.*

Sintering temperature	**Measured frequency**	**-140 °C**		**50 °C**		**400 °C**	
		ε_r	$tan\delta$	ε_r	$tan\delta$	ε_r	$tan\delta$
1200 °C	1 MHz	32.00	0.001	35.60	0.004	35.04	0.049
	100 MHz	30.23	0.030	32.80	0.010	31.56	0.062
	0.2 GHz	30.51	0.030	34.23	0.100	29.86	0.210
1250 °C	1 MHz	33.05	0.001	36.51	0.003	36.06	0.049
	100 MHz	33.65	0.002	36.50	0.004	33.36	0.002
	0.2 GHz	33.71	0.004	36.52	0.005	31.08	0.320
1300 °C	1 MHz	33.00	0.009	34.23	0.007	33.27	0.178
	100 MHz	30.50	0.020	34.50	0.060	31.54	0.236
	0.2 GHz	28.61	0.040	30.56	0.050	25.70	0.450

3.3.1.4 Impedance spectroscopy

The Cole - Cole plots for the BNO ceramics, sintered at 1250 °C are shown in Fig. 3.6. To examine the obtained dielectric response of BNO system, we have plotted ε'' versus ε' measured at different temperatures 350 °C, 380 °C and 400 °C. Hexagonal perovskite BNO ceramics reveal a distribution of relaxation times, because there are always some nonuniformities in local domains, which will alter a response of individual dipoles or charges in dielectric materials. Havriliak - Negami (HN) equation is the most frequently used function for the description of the properties of dielectric materials in the frequency domain.

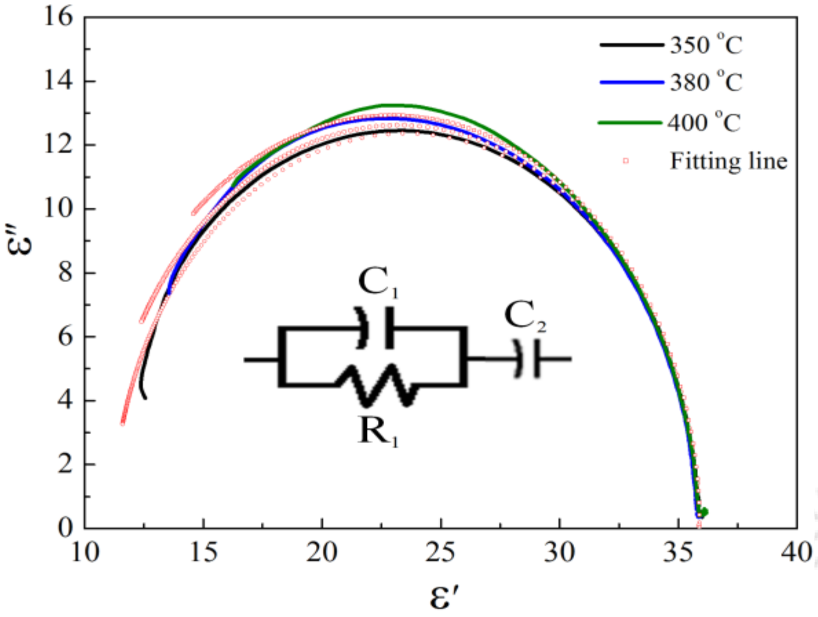

Fig. 3.6: *Cole-Cole plots, measured at different temperatures 350 °C, 380 °C and 400 °C, for BNO ceramics sintered at 1250 °C, (inset) shows an equivalent circuit, which describes the electrical response of polycrystalline BNO ceramics.*

In the frequency domain, the explanations of dielectric relaxation are often described by the HN empirical equation for complex permittivity ε^* can be expressed

$$\varepsilon^*_{HN} = \varepsilon_\infty + \frac{\varepsilon_\circ - \varepsilon_\infty}{[1+(j\omega\tau_\circ)^\alpha]^\beta} \tag{3}$$

Where, ε_o is limited low - frequency permittivity, ε_∞ is the high - frequency dielectric constant, τ_o is the central relaxation time, α and β are shape parameters ranging between 0 and 1, which describe the symmetric or asymmetric broadening of the relaxation time distribution function, respectively. The measured data is analyzed using equation (3) and found a single relaxation peak that yields a full semicircle arc in the complex plane. Further, the obtained quantitative HN function parameters are shown in **Table 3.2**, which is subjected to the elaborated analysis of the relaxation at a given temperature. The measured parameters $\Delta\varepsilon = \varepsilon_o - \varepsilon_\infty$ represents the change in relative permittivity, where ε_o is the intersection with ε'- axis at low frequency, ε_∞ is the intersection with ε'- axis at high frequency and τ is the characteristic relaxation time.

***Table 3.2**: Obtained HN parameters (From WinFIT$_{3.4}$ software) from the fitting data to the equation for BNO bulk ceramics.*

BNO Sintering temperature (°C)	**Measured temperature (°C)**	$\Delta\varepsilon$	τ_o [s] $\times (10^{-10})$	α	β
1200	350	17.39±3.40	2.30±0.42	0.98±0.007	1.00±0.33
	380	21.24±3.50	1.55±0.25	1.00±0.008	0.96±0.28
	400	28.75±1.10	2.05±0.13	1.00±0.005	1.00±0.08
1250	350	24.06±0.06	12.45±0.14	1.00±0.002	1.00±0.01
	380	25.87±0.07	12.86±0.05	1.00±0.001	0.89±0.23
	400	24.46±0.06	3.68±0.01	0.96±0.001	0.98±0.31
1300	350	10.22±0.05	84.42±1.80	0.99±0.004	1.00±0.02
	380	10.85±0.11	724.50±8.2	0.99±0.009	1.00±0.01
	400	11.41±0.53	1314±22.0	0.98±0.024	1.00±0.03

Inset of Fig. 3.6 shows the equivalent circuit of parallel R_1C_1 combination in series with capacitance C_2 greatly aids the process of fitting observed dielectric data. The interesting feature of dielectric spectroscopy is being applied to the studies aimed at the evolution of direct correlation between the response of a real system, and an idealized model circuit composed of discrete electrical components. In such modelling studies one seeks to match experimental impedance with the impedance of an equivalent circuit composed of ideal resistors and capacitors. To fit the impedance data to an equivalent circuit, which is representative of the physical processes taking place in the system under investigation and the properties of linear systems are unchanged in passing from ionic materials to electronic. Any electrode material system in a measuring cell has a geometrical capacitance $C_g = C_\infty = C_1$ and a bulk resistance $R_b = R_\infty = R_1$ in parallel with it. These elements lead to the time constant $\tau = R_\infty C_\infty$, which is the dielectric relaxation time of the basic material [38]. In the simplest equivalent circuit, the resistance describes the net loss because of the dissipative contributions due to electrode polarization and dipole relaxations occur at lower and higher frequencies, respectively. On the other hand, the capacitance strengthens the quality of dielectric material to store the electric field by using the polarization mechanism. It is also possible that a parallel R_1C_1 combination can arise from specific adsorption at an electrode, possibly associated with a delayed reaction process [38]. In the equivalent circuit, the parallel R_1C_1 combination may express the idea that oxide ions are sequentially blocked at grain interiors and additional series capacitance

C_2 arises due to grain boundary regions where good intergranular contact is established. The obtained equivalent circuit parameters extracted from Cole - Cole plots are tabulated in **Table 3.3.**

***Table 3.3**: Obtained equivalent circuit parameters (From WinFIT$_{3.4}$ software) from Cole-Cole plots.*

BNO Sintering temperature (°C)	**Measured temperature (°C)**	R_1	$C_1 \times (10^{-12})$	$C_2 \times (10^{-12})$
1200	350	9.92±0.080	8.17±0.300	10.92±0.010
	380	8.16±0.065	4.75±0.320	10.91±0.013
	400	6.60±0.026	3.09±0.360	10.90±0.015
1250	350	64.10±0.180	5.78±0.029	12.80±0.008
	380	31.94±0.110	5.38±0.045	12.79±0.009
	400	19.51±0.089	4.95±0.077	12.80±0.012
1300	350	210.50±0.73	29.32±0.074	11.35±0.004
	380	2000±9.400	26.19±0.052	11.46±0.009
	400	3609±25.00	25.09±0.071	11.57±0.016

3.3.1.5 Relative density and microwave dielectric properties

The variation in relative density of the samples milled for 40 *h* as a function of sintering temperature is shown in Fig. 3.7 (a). It is observed that as the sintering temperature increases form 1200 °C to 1250 °C, the relative density improved significantly and decreases thereafter. The obtained lower density at 1200 °C may be due to the insufficient sintering temperature and presence of $BaNb_2O_6$ phase and decrease in density above 1250 °C can be attributed to the abnormal grain growth, which is seen from SEM image (Fig. 3.4 (c)). The samples sintered at 1250 °C exhibited a maximum relative density of 97.3%. The enhancement in the relative density for the samples, sintered at 1250 °C is mainly ascribed to the following factors: (i) suppression of $BaNb_2O_6$ phase at this temperature (ii) small initial particle size and (iii) uniform grain growth. The disappearance of $BaNb_2O_6$ phase would promote the uniform grain growth and elimination of pores, which accelerates the increase in relative density. The significance of this study is that mechanically alloyed BNO ceramics showed a maximum density at lower sintering temperatures as compared to the earlier reports [33, 34].

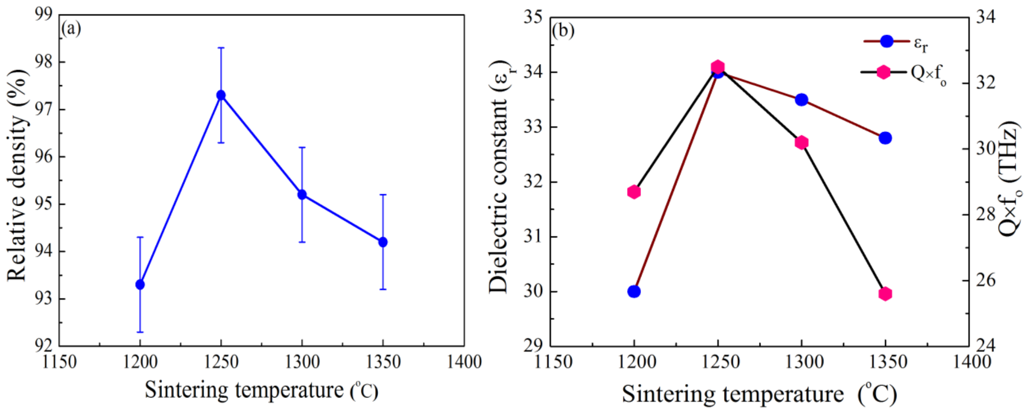

Fig. 3.7: *Variations in (a) relative density as a function of sintering temperature for BNO ceramics, (b) dielectric constant and* $Q\times f_0$ *values of BNO ceramics sintered at different temperatures.*

It is known that all the electrical energy of the resonant mode is stored inside the dielectric resonator and if no losses occur due to external fields, and the product of quality factor (Q) and resonance frequency (f_o) is a tool for estimating the performance of a dielectric resonator material. Fig. 3.7 (b) shows the dielectric constant and $Q\times f_0$ values of BNO ceramics sintered at different sintering temperatures. It is observed that both the dielectric constant and $Q\times f_0$ followed a similar trend with relative density as a function of sintering temperature, which suggests that the microwave dielectric properties of the BNO ceramics are influenced by the relative density. The obtained $Q\times f_0$ values are in the range of (25.6 - 32.5 THz) at 7 GHz for BNO ceramics, sintered at different temperatures. The maximum $Q\times f_0$ values of (32.5 THz) at 7 GHz is obtained for the sintering temperature 1250 ^{o}C is attributed to the highest relative density with bigger grains and pore - free microstructure. Generally, the specimen with larger grain size is expected to have a high $Q\times f_0$ because the grain growth decreases the grain boundary area. Many microwave dielectric loss mechanisms are suggested including intrinsic and extrinsic factors [39, 40]. Inherent losses in crystals arise because of anharmonic lattice forces that mediate the interaction between the crystal and phonons. This leads to damping of the optical phonons and therefore, of the microwave field. These losses are called as intrinsic losses. Losses in ceramics caused by extended dislocations, grain boundaries, inclusions and secondary phases are termed as extrinsic. These losses are caused by either dipole relaxations of impurities concentrated at interfaces at relaxations of space charge polarizations present at interfaces. The variation of $Q\times f_0$ value with sintering temperature is attributed to the changes in the amount of scatterings caused by grain size, grain boundary, relative density and pores. The decrease in $Q\times f_0$ values at higher temperatures (> 1250 °C) can be attributed to the lower densities. Since, the grain boundary is a plane defect, it decreases the $Q\times f_0$ value because the grain growth decreases the grain boundary area. Its known that the single crystal is expected to have highest $Q\times f_0$ value. The observed dielectric constant values are in the range of 30 - 34. The BNO samples sintered at 1250 °C exhibiting the maximum dielectric constant of 34. The obtained $Q\times f_0$ and ε_r values are higher as compared to the earlier reports [8, 33, 34]. The improvement in the dielectric response may be due to the elimination of secondary phase, maximum relative density and uniform microstructure. From this study, it can be shown that the mechanical alloying method played an important role on the relative density, uniform microstructure and crystal structure, which governs the microwave dielectric properties of BNO ceramics.

The measured dielectric constant (ε_r) values were used to correct the porosity corrected dielectric constant values using the following equation [41].

$$\varepsilon_r = \varepsilon_m\left(1-\frac{3P(\varepsilon_m-1)}{2\varepsilon_m+1}\right) \qquad (4)$$

Where, ε_r is the experimental dielectric constant, ε_m is the dielectric constant corrected for porosity and P is the fractional porosity. The porosity corrected values are bit higher than the experimental values and porosity corrected values are tabulated in **Table 3.4**.

Table 3.4: *Relative density, measured microwave dielectric constant (ε_r) and dielectric constant corrected for porosity (ε_m) values of BNO ceramics, sintered at different temperatures.*

BNO Sintering temperature (°C)	Relative density (%)	ε_r (Measured) @ 7 GHz	ε_m (porosity corrected)
1200	93.30 ± 1	30.0	33.35
1250	97.30 ± 1	34.0	35.42
1300	95.20 ± 1	33.5	36.09
1350	94.20 ± 1	32.8	35.92

3.3.2 $Ba_5Nb_4O_{15}$ Ceramics Supplemented with their own nanoparticles

3.3.2.1 Structural and morphological studies

Fig. 3.8 (a) shows the XRD patterns of the $Ba_5Nb_4O_{15}$ (BNO) ceramics, without the addition of nanoparticles, sintered at 1250 °C for 5 *h*, and Fig. 3.8 (b) display the XRD pattern of the BNO nanosized powder, which is calcined at 800 ^{o}C for 2 *h* and BNO ceramics added with different *x* wt% of nanosized particles (*x* = 1 - 3), sintered at 1100 ^{o}C for 3 *h* in air.

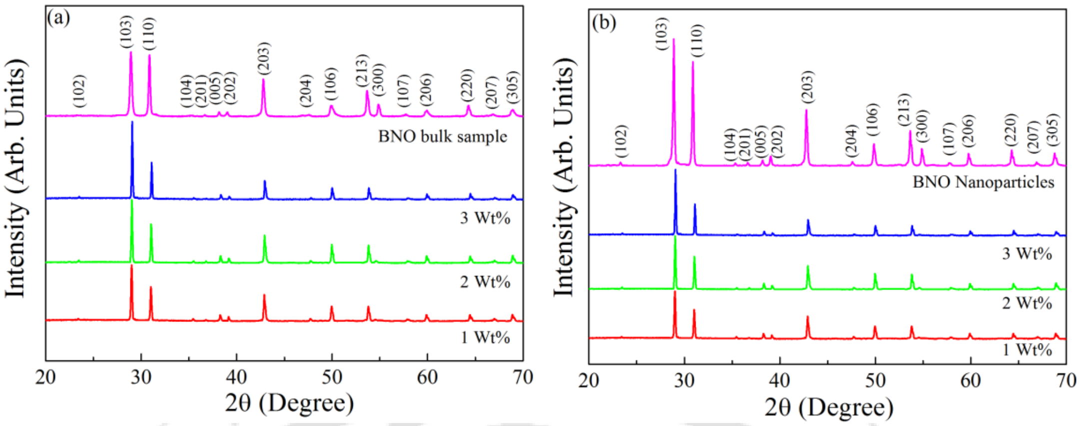

Fig. 3.8: *(a) shows the XRD pattern of the BNO ceramics sintered at 1250 ^{o}C for 5 h, (b) display the XRD pattern of the BNO nanosized particles powder, which is calcined at 800 ^{o}C for 2 h and BNO ceramics added with x wt% of nanosized particles (x = 1 - 3), sintered at 1100 ^{o}C for 3 h.*

All the samples displayed the polycrystalline nature and the samples added with various *x* wt% showed a prominent peak in the vicinity of 29^{o}, and 31^{o} representing the (103), and (110) reflections, respectively. The variations in intensities of these reflections enhanced with an increase in the wt% of the BNO nanosized particles and the average crystallite size of the samples with *x* = 1, 2 and 3 wt% are found to be 56.3, 57.9, and 62.2 nm, respectively.

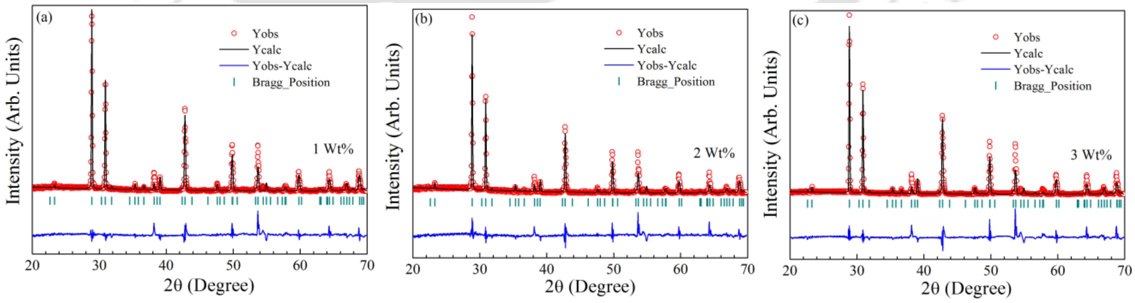

Fig. 3.9: *(a - c) shows the XRD patterns along with Rietveld refinement for various compositions of BNO ceramics with x wt% of nanosized particles, sintered at 1100 ^{o}C for 3 h.*

Fig. 3.9 (a - c) shows the Rietveld refinement of BNO ceramics with *x* wt% of nanosized particles (*x* = 1 - 3), sintered at 1100 ^{o}C for 3 *h*. The lattice parameters, atomic positions of the Ba, Nb, and O atoms, and occupancy have been refined by using fullprof software. The refinement was carried out by considering $P\bar{3}m1$ space group. The corresponding lattice constant values are tabulated in **Table 3.5**. The obtained values are in agreement with the earlier reports [JCPDF file # 17-0794].

***Table 3.5**: Unit cell parameters of the BNO ceramics with x wt% of nanosized particles, evaluated from the XRD patterns and the average grain sizes of different compositions, sintered at 1100 °C for 3 h.*

***x* (wt%)**	***a* (Å)**	***b* (Å)**	***c* (Å)**	***V* (Å)**	$\alpha = \beta \neq \gamma$ **(°)**	**Grain size (*µm*)**
1	5.782865	5.782865	11.772858	393.7023	90 = 90 ≠ 120	1.62
2	5.784128	5.784128	11.776699	394.0028	90 = 90 ≠ 120	2.13
3	5.788051	5.788051	11.785320	394.8263	90 = 90 ≠ 120	2.41

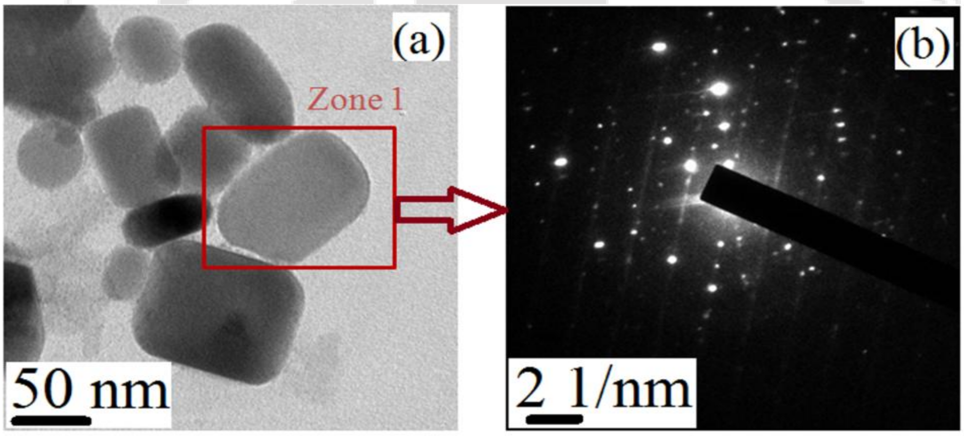

***Fig. 3.10:** TEM image of the BNO calcined powders (a) prepared by sol – gel process (b) selected area diffraction (SAD) pattern of the zone 1(Fig. 3.10 (a)).*

Fig. 3.10 (a) shows the TEM image of BNO nanosized particles prepared by sol - gel process. TEM micrograph reveals the BNO nanoparticles with spherical and cylindrical shapes with average particle diameters of 45 and 60 nm, respectively. The deviation from spherical shape to cylindrical shape may occur due to the larger particles, which often have elongated. The function of ethylene glycol during preparation of BNO nanoparticles not only works as a binder, but also prevents the process of agglomeration of BNO nanoparticles and limits the diameter of the particles. The individual diffraction spot of the BNO nanopowder was exposed by selected area diffraction (SAD) pattern, which is shown in Fig. 3.10 (b). These entire patterns correspond to inter planar spacing (d - spacing) of sample and confirmed the polycrystalline nature of the hexagonal BNO ceramics.

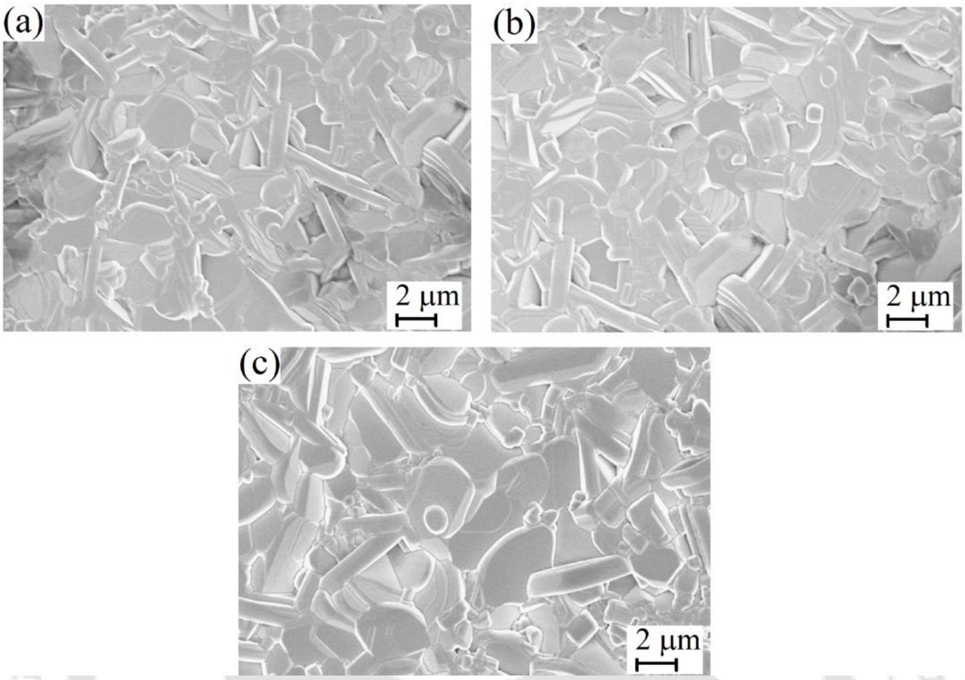

***Fig. 3.11:** (a - c) shows the SEM images of various compositions of BNO ceramics added with different x wt% of nanosized particles, sintered at 1100 °C for 3 h.*

Fig. 3.11 (a - c) shows the SEM micrographs of BNO ceramics with *x* wt% of nanosized particles ($x = 1 - 3$), sintered at 1100 °C for 3 *h*. The microstructures of the samples prepared with $x > 3$ wt% are non-uniform and displayed the abnormal growth. On the other hand, the samples with $x = 1 - 3$ wt% samples reveal the dense microstructures are thermodynamically feasible, which accelerates the grain growth over nucleation with an average grain size of 1.62 - 2.41 µm. With increasing the *x* wt% of BNO nanoparticles beyond 3 wt%, there is an enhancement in grain growth. The supplement of BNO nanoparticles to the micronsized BNO matrix as a sintering additive is the alteration of the competition between nucleation and grain growth.

Further, Energy dispersive spectroscopy (EDS) has been used for identifying the elemental composition of the specimen. The elemental analysis of the BNO ceramics with *x* wt% of nanosized particles confirmed the presence of all elemental BNO signals, and no signatures of other impurities were detected and the elemental percentage of the sample is shown in **Table 3.6**.

Table 3.6: *Elemental analysis for the BNO ceramics with x wt% of nanosized particles, sintered at 1100 °C for 3 h.*

Element	Weight (%)	Atomic (%)	Required	Obtained
Ba (L)	52.80	20.77	5	4.9848
Nb (L)	28.68	16.68	4	4.0032
O (K)	18.52	62.55	15	15.0120

The variation in relative density of BNO ceramics added with different *x* wt% of nanosized particles (*x* = 1 - 3) as a function of sintering temperature is shown in Fig. 3.12. It is found that the relative density of all the samples improved with an increase in temperature up to 1100 °C and falls off thereafter. Furthermore, the relative density of the samples improved with an increment in the wt% of BNO nanoparticles up to *x* = 3 wt%, and the BNO ceramics added with *x* = 3 wt% of BNO nanoparticles displayed a maximum relative density of 97.8 % of the theoretical density. The achieved lower densities below and above 1100 °C can be attributed to the insufficient sintering temperature and abnormal grain growth, respectively.

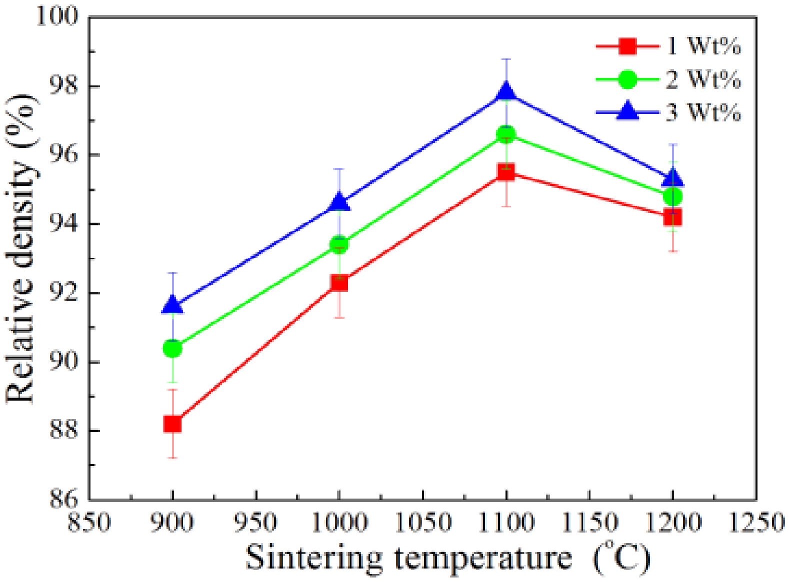

Fig. 3.12: *Variations in relative density as a function of sintering temperature for various compositions of BNO ceramics with x wt% of their nanosized particles (x =1 - 3 wt%).*

It is interesting to note that the addition of BNO nanoparticles to the BNO matrix significantly reduced the sintering temperature from 1380 °C to 1100 °C [33]. The attained maximum relative densities and larger uniform grain size are described as follows: it is known that the sintering velocity is inversely proportional to the particle size. When a different particle sizes, and shapes of BNO nanoparticles added to the micron sized BNO matrix, surface energy of the particles plays a significant role on the densification. When the particle size of the powder is small, the powder has a large surface-to-volume ratio due to its small radius of curvature in comparison with a similar volume of bulk solid. When a micron sized BNO powder compact is sintered in the presence of BNO nanoparticles, the density of the compact increases because of the lower melting temperature of the nanoparticles as a result BNO nanoparticles would act as a liquid phase sintering aid. When particles of different sizes are dispersed in a ceramic matrix, material transport occurs from small to large grains because of the difference in solubility between the grains. Therefore, small grains dissolve and large grains grow further, and the average grain size increases and this phenomenon are called as 'Ostwald ripening'. From this study, it's clear that the BNO ceramics without the addition of nanoparticles exhibited the maximum density of 94% at 1250 ^{o}C where as with addition of BNO nanoparticles the samples displayed a highest relative density of 97.8% at 1100 ^{o}C itself.

3.3.2.2 Broadband dielectric properties at cryogenic temperatures

Figs. (3.13 - 3.15) represents the broadband dielectric properties of BNO ceramics with x wt% of nanosized particles, measured over the temperature range of -140 ^{o}C to 200 ^{o}C. It is observed that both in the low and high temperature ranges (-140 ^{o}C to 20 ^{o}C), and (40 ^{o}C to 200 ^{o}C), the observed values of dielectric constant (ε_r) and loss tangent ($tan\delta$) of samples showed nearly a stable response with frequency up to 30 MHz except for the sample with x = 3 wt% shifted to 20 MHz in the high temperature range. Further, as the frequency increases, the dielectric constant of the samples decreases whereas the loss tangent is enhanced, which is a characteristic of a linear dielectric. In addition, with a rise in measurement temperature, the dielectric response of the BNO ceramics was amplified. At low temperatures, the dipoles would be frozen as a result they cannot contribute much to the dielectric constant; on the other hand, thermal energy facilitates the dipole orientation, which causes an increase in the dielectric constant. The loss tangent is minimum at cryogenic temperatures, and is attributed to the smaller damping constants, as a result; the intrinsic loss in the samples was minimized whereas the disorderness in the samples increases with temperature. Interestingly, in both the low and high temperature ranges, a step like behaviour is observed in ε_r and $tan\delta$ with an increase in applied frequency up to 0.1 GHz.

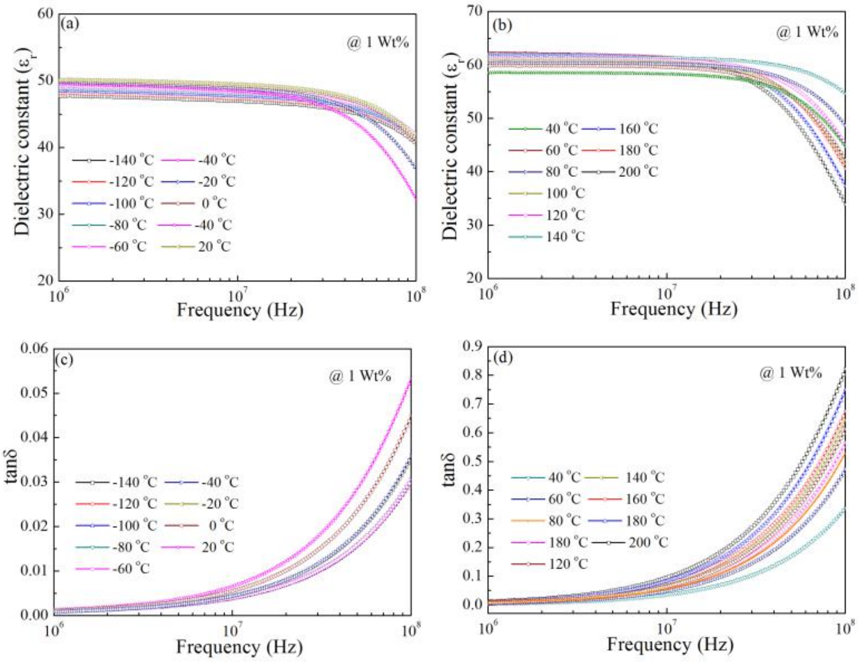

Fig. 3.13: *Variations in dielectric constant as a function of frequency measured in the temperature range of (a) (-140 °C to 20 °C) (b) (40 °C to 200 °C). Variations in loss tangent as a function of frequency measured in the temperature range of (c) (-140 °C to 20 °C) (d) (40 °C to 200 °C) for compositions of BNO ceramics with x wt% of nanosized particles (x = 1 wt %).*

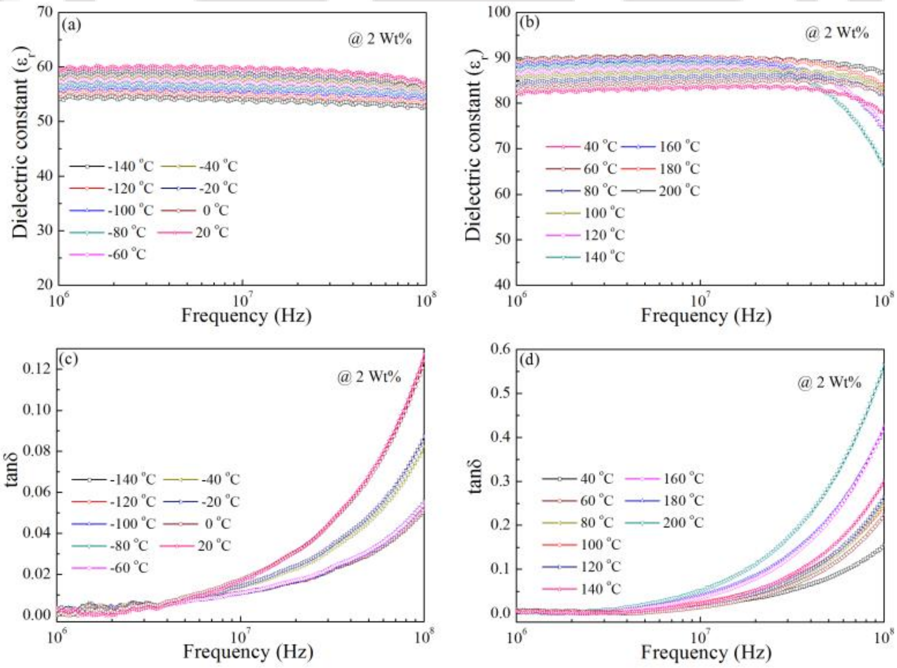

Fig. 3.14: *Variations in dielectric constant as a function of frequency measured in the temperature range of (a) (-140 °C to 20 °C) (b) (40 °C to 200 °C). Variations in loss tangent as a function of frequency measured in the temperature range of (c) (-140 °C to 20 °C) (d) (40 °C to 200 °C) for compositions of BNO ceramics with x wt% of nanosized particles (x = 2 wt %).*

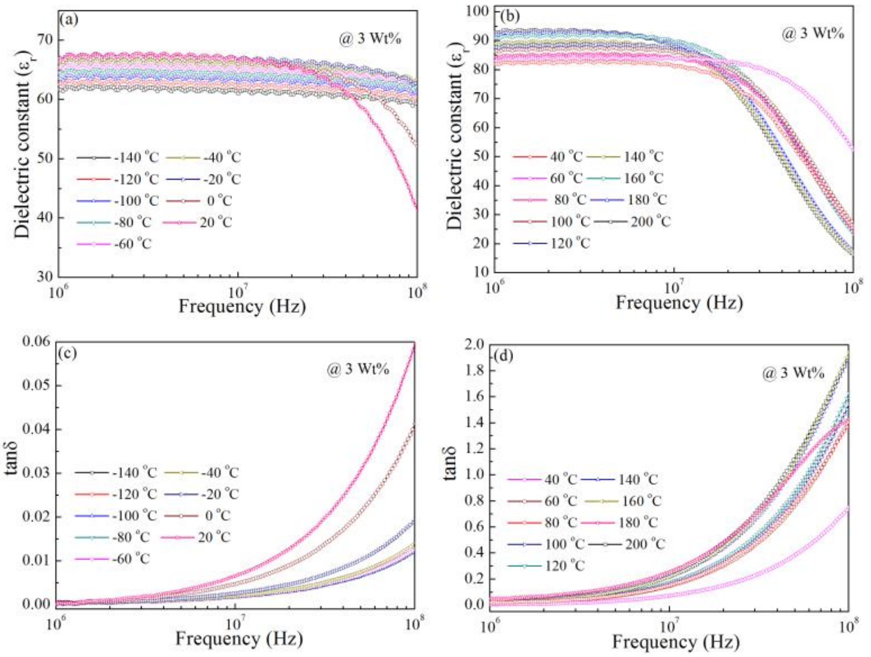

Fig. 3.15: *Variations in dielectric constant as a function of frequency measured in the temperature range of (a) (-140 °C to 20 °C) (b) (40 °C to 200 °C). Variations in loss tangent as a function of frequency measured in the temperature range of (c) (-140 °C to 20 °C) (d) (40 °C to 200 °C) for compositions of BNO ceramics with x wt% of nanosized particles (x = 3 wt %).*

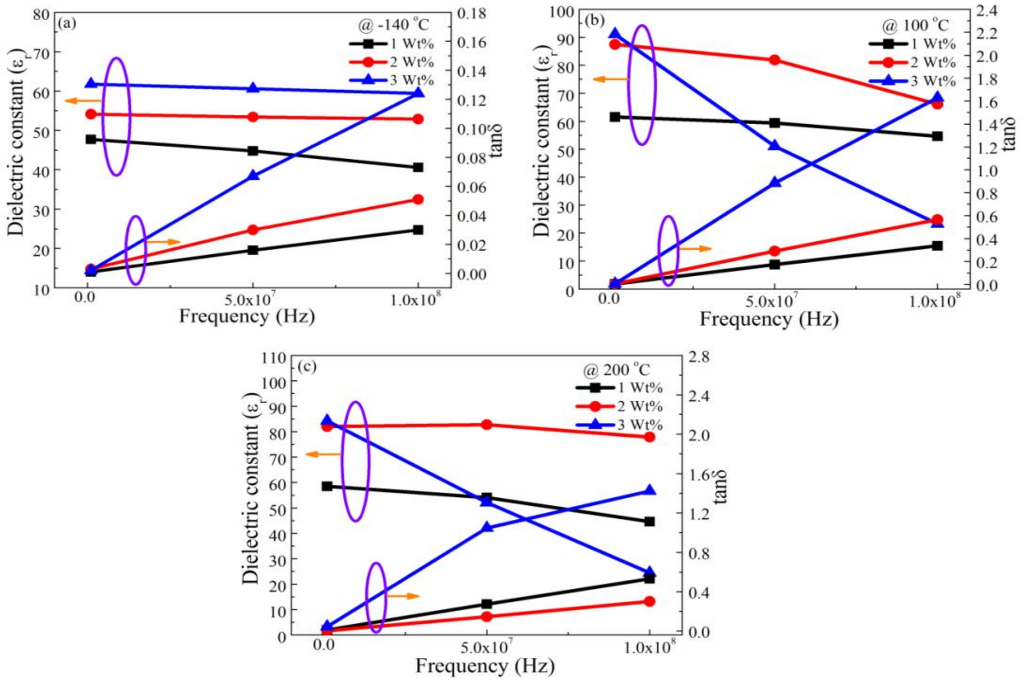

Fig. 3.16: *Variations in dielectric constant (ε_r) and loss tangent (tanδ) as a function of frequency for the BNO ceramics with x wt% of nanosized particles and measured at (a) -140 °C (b) 100 °C (c) 200 °C.*

The polarization mechanisms that are studied in the dielectric spectroscopy enable us to understand the dielectric performance of the samples. The observed stable behaviour of ε_r in the measured BNO ceramics might be due to the polarization that arises from the orientation of permanent dipoles and ionic polarization. The change in dielectric constant, relaxation behaviour with an increase in temperature is attributed to these two major polarization mechanisms. Further, it is observed that the *tanδ* increases in the high frequency region with a rise in temperature from -140 ^oC to 200 ^oC. This might be due to the fast movement of molecules in the transient cage formed by its neighbours. Fig. 3.16 (a - c) shows the variation in dielectric constant (ε_r) and loss tangent (*tanδ*) as a function of frequency for the BNO ceramics with *x* wt% of nanosized particles and measured at different temperatures. It is noticed that with an increase in the measurement frequency, the dielectric constant (ε_r) decreases where as the loss tangent (*tanδ*) increases.

3.3.2.3 Electrical conductivity

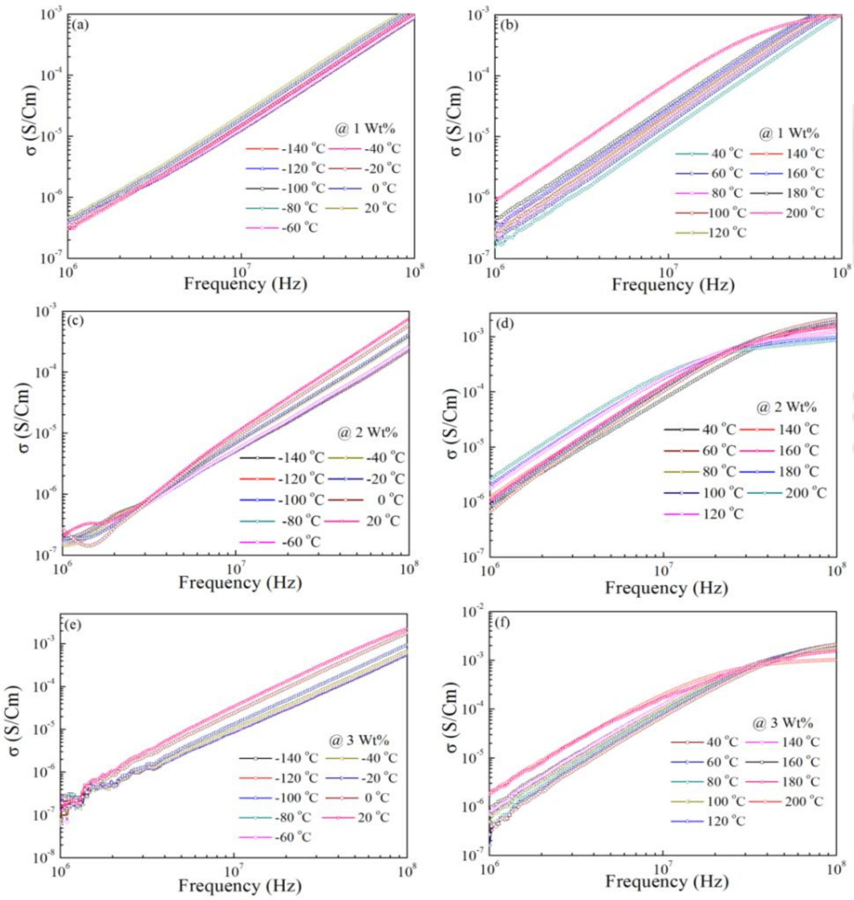

Fig. 3.17: *The ac conductivity (σ_{ac}) versus frequency (f) at different temperatures for various compositions of BNO ceramics, added with x wt% of nanosized particles (a, b) x = 1 wt%, (c, d) x = 2 wt%, and (e, f) x = 3 wt%.*

Fig. 3.17 shows the variation of the ac conductivity as a function of frequency (1MHz - 0.1 GHz) measured at distinctive temperatures for the BNO ceramics added with different *x* wt% of nanosized particles. It is observed that, the conductivity increases linearly with increasing frequency. This reveals that the conduction mechanism in the high frequency region corresponds to the reorientational hopping motion of charge carriers that takes place through the trapped sites isolated by energy barriers of various heights. The rise in conductivity at high frequencies might also be due to the number of charge carriers with low barrier height, and they respond easily to the high frequency.

Further, the frequency dependent ac conductivity at different temperatures indicated that the conduction process is thermally activated process. The phenomena of frequency dependent conductivity can be described by the Jonschers law given by [42]

$$\sigma_{ac}(\omega) = A\omega^s \qquad (5)$$

Where, $\sigma_{ac}(\omega)$ is the total conductivity, *A* is the temperature dependent constant, and *s* is the power law exponential term, which has been used to characterize the electrical conduction in disorder ionic glasses, amorphous semiconductors, ionic conductors and some other crystals [43]. The exponent *s* always lies within 0 to 1. Besides $1 < s < 2$, corresponds to a localized (or) reorientational hopping motion (1 MHz - 0.1 GHz) and also a significant aspect of the low temperature / high frequency process. According to jump relaxation model, the values of *s* depend on mobile ions, which may find various energetically favourable positions in a given neighbourhood, performing a localized hopping motion without leaving it [44].

Fig. 3.18 shows the temperature dependent frequency exponent *s* with pre - exponential factor *Log A*. The obtained value of *s* and *Log A* decreases and simultaneously increases with *x* wt% of nanosized particles. The decrease in *s* values with increasing frequency, and temperature is might be due to the large polaron hopping mechanism. In the present study, we observed that the value of $s > 1$, which has been reported for chalcogenide materials [45].

Fig. 3.19 shows the variation of AC conductivity (σ_{ac}) versus *1000/T* of BNO ceramics with *x* wt% of nanosized particles, measured at 0.1 GHz. The activation energy (E_a) of the mobile charge carriers had been calculated using the Arrhenius relation from the slope of each curve, and the expression is given below

$$\sigma_{ac} = \sigma_0 exp^{(-E_a/k_BT)} \tag{6}$$

Where, σ_o is pre-exponential factor, E_a is the activation energy; K_B is the Boltzmann constant and T is the absolute temperature. The extracted activation energies are found to be E_a = 0.0037, 0.0019 and 0.0010 *eV* for the BNO ceramics added with nanosized particles with x = 1, 2, and 3 wt%, respectively.

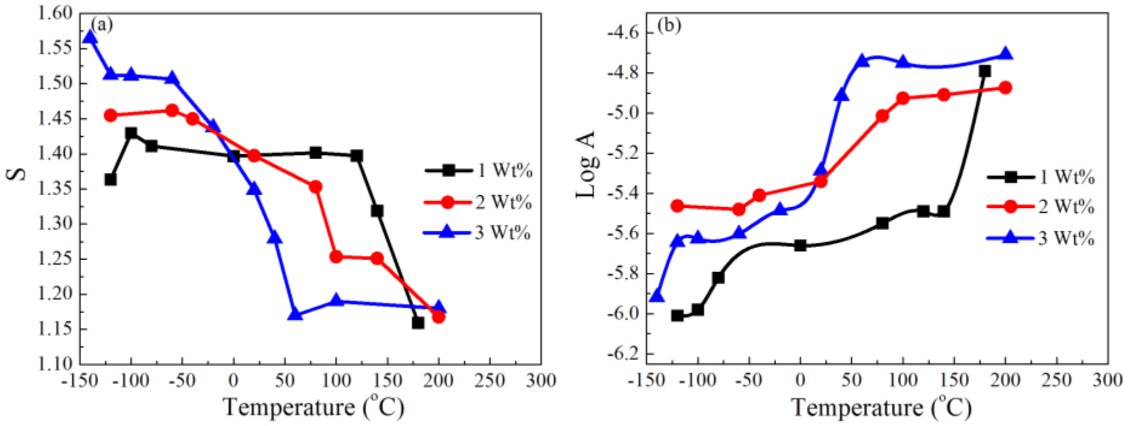

Fig. 3.18: *Variation in ac conductivity parameters (a) s (b) Log A at different temperatures for various compositions of BNO ceramics added with x wt% of nanosized particles.*

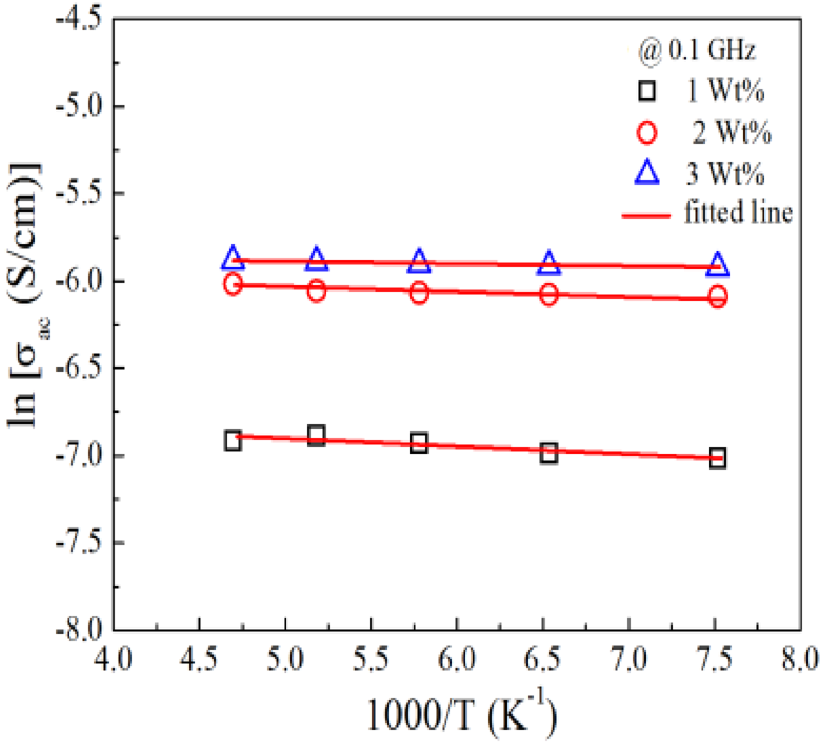

Fig.3.19: *variation of ln σ_{ac} versus 1000/T for BNO ceramics with x wt% of nanosized particles and measured at 0.1 GHz.*

3.3.2.4 Impedance spectroscopy

Fig. 3.20 displays the Cole - Cole plots of BNO ceramics with x wt% of nanosized particles (x = 1 - 3), sintered at 1100 °C. In order to study the broadband dielectric relaxation in polycrystalline samples, we have plotted ε'' versus ε' in the complex plane measured over the temperature range of 80 °C to 200 °C. Havriliak - Negami (HN) equation is a combination of the Cole-Cole and the Cole-Davidson functions. The HN equation for complex permittivity ε^* is the most frequently used function for the description of the properties of dielectric materials and their relaxation behaviour within the frequency domain and which is described as

$$\varepsilon^*_{HN} = \varepsilon_\infty + \frac{\varepsilon_\circ - \varepsilon_\infty}{[1+(j\omega\tau_\circ)^\alpha]^\beta} \qquad (7)$$

Where, ε_o is the low - frequency permittivity, ε_∞ is the high - frequency dielectric constant, τ_o is the central relaxation time, for the fractional shape parameters α and β, which describe the symmetric and asymmetric broadening of the complex dielectric function $0 < \alpha,\ \alpha\beta \leq 1$ holds. The experimental data is examined in detail using the equation (7) and found a single relaxation peak that generates a semicircle arc in the complex plane. Further, the obtained quantitative HN function parameters are shown in **Table 3.7** and **Table 3.8,** which are subjected to the elaborated analysis of the relaxation at a given temperature. The measured parameters $\Delta\varepsilon = \varepsilon_o - \varepsilon_\infty$ represents the change in relative permittivity (or) dielectric relaxation strength, where ε_o is the intersection with ε'- axis at low frequency, ε_∞ is the intersection with ε'- axis at high frequency and τ is the characteristic relaxation time.

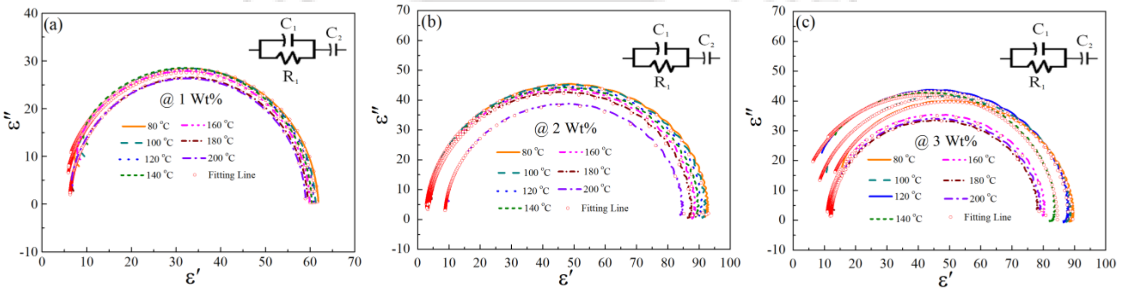

Fig. 3.20: *Cole-Cole plots, measured at different temperatures (80 °C - 200 °C), for various compositions of BNO ceramics with x wt% of nanosized particles, (inset) shows an equivalent circuit, which describes the electrical response of polycrystalline BNO ceramics added with x wt% of nanosized particles.*

Table 3.7: *Obtained HN parameters (From WinFIT$_{3.4}$ software) from the fitting data to the equation for BNO ceramics with x wt% of nanosized particles, measured at different temperatures (80 ^{o}C - 140 ^{o}C), and sintered at 1100 ^{o}C for 3 h.*

BNO Nano addition in weight (%)	**Fit parameters of test sample**	**80 ^{o}C**	**100 ^{o}C**	**120 ^{o}C**	**140 ^{o}C**
1 Wt%	$\Delta\varepsilon$	55.84 ± 0.15	53.62 ± 0.92	55.12 ± 0.24	54.98 ± 0.18
	$\tau_o\ [s]\times(10^{-11})$	140.3 ± 1.80	606.4 ± 2.50	102.1 ± 1.70	117.2 ± 1.60
	α	0.99 ± 0.002	1.00 ± 0.005	1.00 ± 0.002	1.00 ± 0.002
	β	1.00 ± 0.013	1.00 ± 0.05	1.00 ± 0.017	1.00 ± 0.014
2 Wt%	$\Delta\varepsilon$	90.29 ± 0.87	89.65 ± 0.12	88.02 ± 0.09	87.33 ± 0.12
	$\tau_o\ [s]\times(10^{-11})$	360.2 ± 2.70	287.7 ± 2.80	421.5 ± 3.50	367.1 ± 3.90
	α	1.00 ± 0.001	1.00 ± 0.002	1.00 ± 0.002	1.00 ± 0.002
	β	1.00 ± 0.006	1.00 ± 0.009	1.00 ± 0.007	1.00 ± 0.009
3 Wt%	$\Delta\varepsilon$	77.78 ± 0.08	81.11 ± 0.09	84.08 ± 0.14	87.17 ± 0.07
	$\tau_o\ [s]\times(10^{-11})$	77.94 ± 0.16	98.53 ± 0.23	69.12 ± 0.22	38.83 ± 0.93
	α	1.00 ± 00	1.00 ± 00	1.00 ± 00	1.00 ± 0.004
	β	1.00 ± 00	1.00 ± 00	1.00 ± 00	1.00 ± 0.019

Table 3.8: *Obtained HN parameters (From WinFIT$_{3.4}$ software) from the fitting data to the equation for BNO ceramics with x wt% of nanosized particles, measured at different temperatures (160 ^{o}C - 200 ^{o}C), and sintered at 1100 ^{o}C for 3 h.*

BNO Nano addition in weight (%)	**Fit parameters of test sample**	**160 ^{o}C**	**180 ^{o}C**	**200 ^{o}C**
1 Wt%	$\Delta\varepsilon$	54.31 ± 0.38	54.10 ± 0.20	53.05 ± 0.25
	$\tau_o\ [s]\times(10^{-11})$	839.3 ± 1.90	111.0 ± 1.60	432.2 ± 1.60
	α	1.00 ± 0.003	1.00 ± 0.002	0.99 ± 0.001
	β	1.00 ± 0.025	1.00 ± 0.015	1.00 ± 0.003
2 Wt%	$\Delta\varepsilon$	85.98 ± 0.16	84.23 ± 0.18	77.41 ± 0.42
	$\tau_o\ [s]\times(10^{-11})$	273.2 ± 3.60	254.5 ± 3.60	507.9 ± 7.10
	α	1.00 ± 0.003	1.00 ± 0.003	1.00 ± 00
	β	1.00 ± 0.012	1.00 ± 0.013	1.00 ± 00
3 Wt%	$\Delta\varepsilon$	86.05 ± 4.60	84.98 ± 0.08	79.89 ± 2.50
	$\tau_o\ [s]\times(10^{-11})$	40.95 ± 3.5	34.69 ± 1.1	48.48 ± 2.9
	α	1.00 ± 0.008	1.00 ± 0.006	1.00 ± 0.006
	β	1.00 ± 0.120	1.00 ± 0.027	1.00 ± 0.079

Inset of Fig. 3.20 displays the equivalent circuit of parallel R_1C_1 combination in series with capacitance C_2 considerably aids the process of fitting observed from the dielectric data. In order to fit the impedance data to an equivalent circuit, which is an instance of the physical processes taking place in the system under systematic study and the properties of linear systems are unaltered in passing from ionic to electronic materials. The measuring cell consists of any electrode material system has a geometrical capacitance $C_g = C_\infty = C_1$ and a bulk resistance $R_b = R_\infty = R_1$ in parallel with it. These elements contribute to the time constant $\tau = R_\infty C_\infty$, which is the dielectric relaxation time of a material under study. The one more probability is that the parallel R_1C_1 combination might arise from specific adsorption at an electrode, perhaps associated with a delayed reaction process. In the R-C parallel circuit, R_1C_1 combination possibly will convey the idea that oxide ions are sequentially blocked at grain interiors and additional series capacitance C_2 arises due to grain boundary regions where good intergranular contact is established [38]. The acquired equivalent circuit parameters are shown in **Table 3.9** and **Table 3.10**, which are deduced from Cole - Cole plots.

Table 3.9*: Obtained equivalent circuit parameters (From WinFIT$_{3.4}$ software) from Cole-Cole plots measured for BNO ceramics with x wt% of nanosized particles (x = 1 - 3 wt%), measured at different temperatures (80 °C - 140 °C), and sintered at 1100 °C for 3 h.*

BNO Nano addition in weight (%)	**Fit parameters of test sample**	**80 °C**	**100 °C**	**120 °C**	**140 °C**
1 Wt%	R_1	24.80 ± 0.07	10.25 ± 0.05	18.12 ± 0.05	21.05 ± 0.05
	$C_1\times(10^{-12})$	4.52 ± 0.08	3.23 ± 0.21	4.30 ± 0.09	4.32 ± 0.08
	$C_2\times(10^{-12})$	50.31± 0.04	50.14 ± 0.07	49.89 ± 0.04	49.58± 0.04
2 Wt%	R_1	57.10± 0.08	46.00 ± 0.08	67.78 ± 0.12	59.94 ± 0.12
	$C_1\times(10^{-12})$	1.84± 0.04	1.72 ± 0.05	2.12 ± 0.04	1.90 ± 0.05
	$C_2\times(10^{-12})$	60.95 ± 0.03	60.49 ± 0.04	59.79 ± 0.04	59.09 ± 0.04
3 Wt%	R_1	11.84± 0.03	15.84 ± 0.04	11.74 ± 0.03	7.01 ± 0.04
	$C_1\times(10^{-12})$	7.10 ± 0.11	4.28 ± 0.11	1.02± 0.13	0.01± 0.34
	$C_2\times(10^{-12})$	56.64 ± 0.04	56.24 ± 0.05	55.73 ± 0.05	55.54 ± 0.1

Table 3.10: *Obtained equivalent circuit parameters (From WinFIT$_{3.4}$ software) from Cole-Cole plots measured for BNO ceramics with x wt% of nanosized particles (x = 1 - 3 wt%), measured at different temperatures (160 °C - 200 °C), and sintered at 1100 °C for 3 h.*

BNO Nano addition in weight (%)	**Fit parameters of test sample**	**160 °C**	**180 °C**	**200 °C**
1 Wt%	R_1	15.03 ± 0.05	20.18 ± 0.05	79.00± 0.15
	$C_1\times(10^{-12})$	3.76± 0.12	4.26 ± 0.08	5.69 ± 0.04
	$C_2\times(10^{-12})$	49.26± 0.05	48.88 ± 0.04	48.4 ± 0.03
2 Wt%	R_1	45.03 ± 0.09	42.24 ± 0.09	88.69 ± 1.3
	$C_1\times(10^{-12})$	1.99± 0.06	2.32 ± 0.06	2.63± 0.35
	$C_2\times(10^{-12})$	58.33 ± 0.04	57.53 ± 0.04	55.44 ± 0.3
3 Wt%	R_1	7.50 ± 0.05	6.45 ± 0.05	7.80 ± 00
	$C_1\times(10^{-12})$	0.01 ± 0.33	0.01 ± 0.43	0.35± 0.39
	$C_2\times(10^{-12})$	54.84 ± 0.1	53.82 ± 0.1	53.52 ± 0.3

3.3.2.5 Microwave dielectric properties

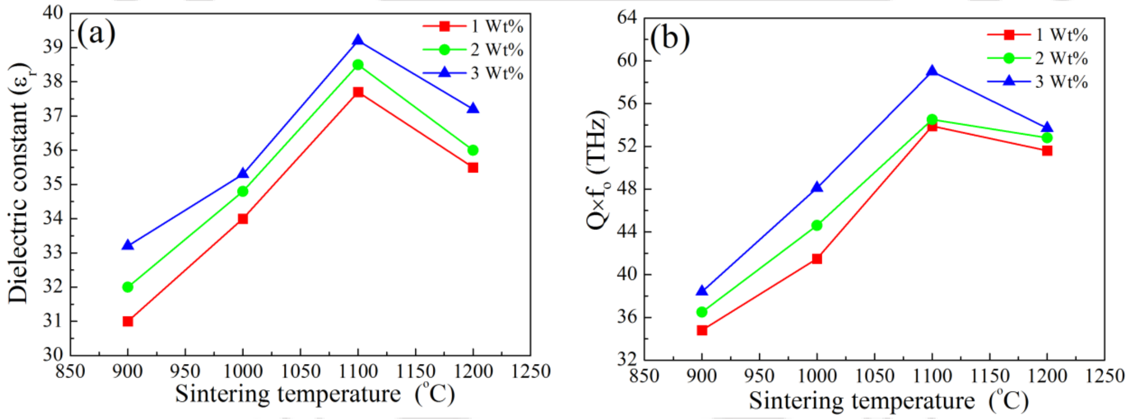

Fig. 3.21: *Variations in (a) dielectric constant, (b) Q×f_0 values for various compositions of BNO ceramics added with x wt% of nanosized particles.*

The Hakki - Coleman resonant technique is the best method, which is used to measure the dielectric properties of materials with a similar geometry to the way they are used in microwave device applications. Since, the microwave energy is mainly contained within the material and prevents from the influence of external losses. Fig. 3.21 (a, b) demonstrate the dielectric constant (ε_r) and $Q\times f_0$ of BNO ceramics with x wt% of nanosized particles (x = 1 - 3), as a function of temperature. With a rise in temperature, both the ε_r and $Q\times f_0$ values increased to a maximum asset value and decreased thereafter.

Indeed, the significant changes of these properties are attributed to the relative density, which follows a similar trend shown in Fig. 3.12, and the densification plays a critical role in controlling the dielectric loss.

The observed ε_r and $Q\times f_0$ values are in the range of 31.0 - 39.2 and 34.8 - 59 THz for BNO ceramics with x wt% of nanosized particles, sintered at different temperatures. It is noticed that the sample with x = 3 wt%, sintered at 1100 ^{o}C showed a maximum ε_r of 39.2 and $Q\times f_0$ of 59 THz at 6.52 GHz, and these values are higher as compared to the earlier reports [33]. From this study, it is interesting to note that the BNO ceramics added with their own nanoparticles reduced the sintering temperature but also significantly improved the microwave dielectric properties, especially the quality factor.

3.3.2.6 Raman spectroscopy of BNO ceramics

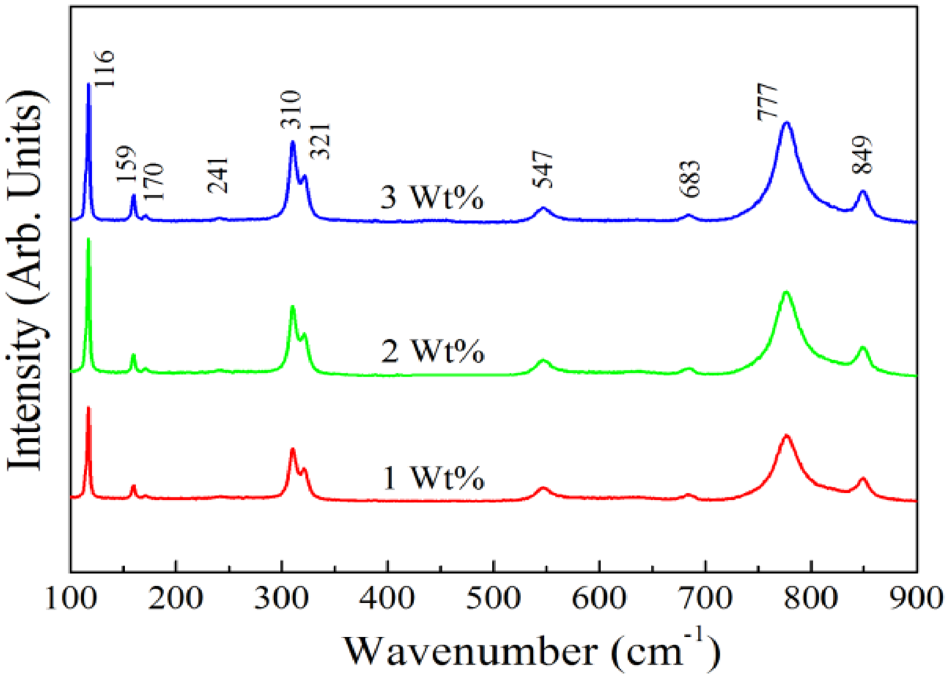

Fig. 3.22: *(a) Raman spectra of BNO ceramics with x wt% of nanosized particles, sintered at 1100 ^{o}C for 3 h.*

Fig. 3.22 shows the Raman spectra of BNO ceramics with x wt% of nanosized particles obtained in the range of 100 to 900 cm^{-1}, excited by the 488 nm line of an Ar - ion laser processed at room temperature. The prepared samples exhibited all the vibration modes at 116, 159, 170, 241, 310, 321, 547, 683, 777, 849 cm^{-1} and are in agreement with the earlier reports [46]. Further, the vibration modes appeared at 310, 321cm^{-1} and 777, 849 cm^{-1} can accommodate very strong bands, and the observed intensities of these peaks and their broadening decreases with increasing *x* wt%. However, the broadening is normally assigned to the anharmonic decay of optical phonons [47] and these results complement the obtained XRD patterns.

3.3.3 Nanocrystalline $Ba_5Nb_4O_{15}$ (BNO) thin films deposited by RF magnetron sputtering

3.3.3.1 Structural and morphological studies

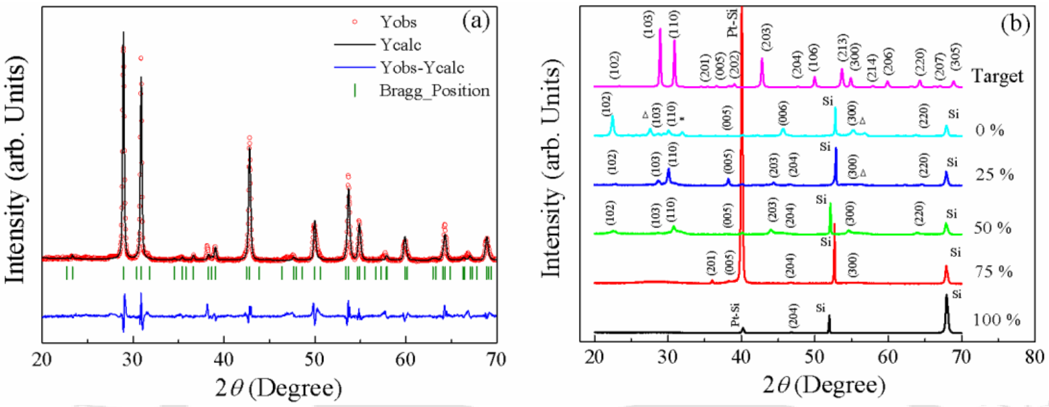

Fig. 3.23: (a) XRD pattern along with Rietveld refinement of $Ba_5Nb_4O_{15}$ ceramic target material. (b) XRD patterns of BNO sputtering target and thin films deposited on Pt-Si substrates at different oxygen mixing percentage (OMP) and annealed at 700 °C for 3 h. (Δ = α-$Ba_4Nb_2O_9$, ∗ = $BaNb_2O_6$,).

To prevent the formation of secondary phases and to reduce the sintering temperature, BNO ceramics were prepared using mechanochemical synthesis method. The phase formation of the BNO ceramics was occurred after milling for 40 *h*. The x-ray diffraction pattern of BNO ceramics along with the Rietveld refinement data of the sputtering target, sintered at 1250 °C for 5 *h* is shown in Fig. 3.23 (a). The refinement was carried out by considering $P\overline{3}m1$ space group. The lattice parameters, atomic positions of the Ba, Nb, and O atoms, and occupancy are refined. The corresponding lattice constant values are $a = b = 5.79 \pm 0.002$ *Å*, $c = 11.77 \pm 0.002$ *Å* which are in agreement with earlier reports [JCPDF file # 17-0794]. The fitting parameters (i) $\chi^2 \approx 8.583$, (ii) R_{Brag} factor ≈ 7.718 and (iii) R_f factor ≈ 9.125 for BNO target system. BNO thin films deposited on platinized silicon substrates at ambient temperatures under various oxygen mixing percentages (OMPs) (0, 25, 50, 75 and 100 %) depicts amorphous nature. It is known that oxide films naturally grow in an amorphous state unless the energy is supplied in the form of ion bombardment or in the form of temperature during the deposition and also due to the lattice mismatch between the substrate and the film [48]. However, post annealing at 700 °C for 3 *h* in air, all the thin films are partially crystalline in the hexagonal perovskites crystal structure and the XRD patterns of the BNO sputtering target and films deposited on platinized silicon substrates are shown in Fig. 3.23 (b).

It is interesting to note that the films deposited in pure argon exhibit α-$Ba_4Nb_2O_9$ [JCPDF file # 35-1154] and $BaNb_2O_6$ [JCPDF file # 13-0451] as subordinate phases along with the BNO phase. With an increase in oxygen mixing percentage (OMP) from 25% to 100% in the deposition chamber, the secondary phases disappear. Further the crystallinity of the films enhanced with an increase in OMP up to 50% above that the crystallinity of the films diminishes. Films deposited at 50% OMP exhibit better crystallinity as compared to the films deposited at 25% OMP. It is interesting to note that BNO films were obtained even in the pure oxygen atmosphere that shows that the target poisoning is partial. However, even after annealing at 700 °C, the films were partially crystalline with strong glassy background. The obtained better crystallinity under pure argon ambience may be due to the large momentum transfer of ions (heavier argon atoms). With an increase in OMP, the rate of deposition decreases due to the oxidation of the target and also due to lighter oxygen ions, which result in poor crystallinity.

Table 3.11: *The deposition rates of as- deposited BNO films on platinized silicon substrates under different OMPs, for a constant duration of 3 h.*

BNO Films as-deposited at different OMP (%)	RF Power (W)	Thickness (nm)	Deposition rate (nm/minute)
0	40	568 ± 5	3.1
25	40	534 ± 5	2.9
50	40	497 ± 5	2.7
75	40	461 ± 5	2.5
100	40	429 ± 5	2.4

Further, it is also observed that with an increment in OMP, the relative intensities of the emission lines changes and may be due to the variations in the energies of ions in the plasma. These variations may cause slight changes during the growth and orientations of the films in a particular plane. In addition, it is as well observed that with an increment in OMP, the full width at half maximum declines, which shows the decrease in crystallite size. The average crystallite sizes obtained using the Scherer's expression and are in the range of 21 - 43 nm. Furthermore, films deposited in pure argon atmosphere exhibit secondary phases whereas the films deposited beyond 50% OMP exhibit poor crystallinity. Hence, it is decided to study the electric and dielectric properties of the BNO films as a function of thickness, deposited at 50% OMP. The thickness and deposition rates of as-deposited BNO films on platinized silicon substrate at different OMPs shown in **Table 3.11**.

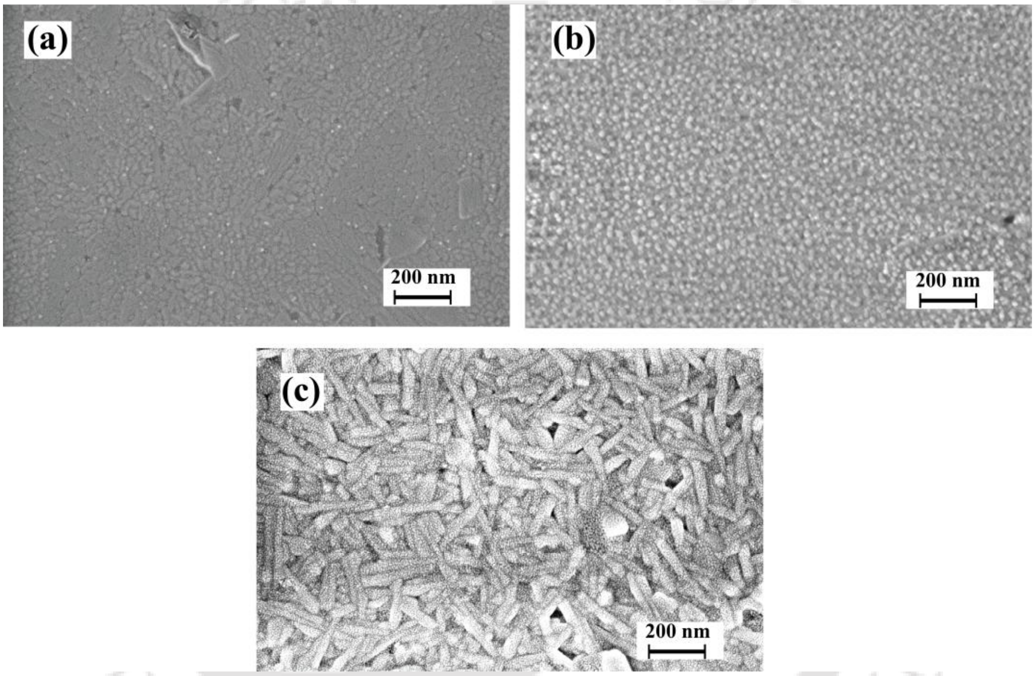

Fig. 3.24: *FESEM micrographs of the BNO films deposited on Pt-Si substrates at 50% OMP, and annealed at 700 °C for a constant duration of 3 h with different thicknesses (a) 150 nm, (b) 250 nm, and (c) 450 nm.*

FESEM images of the BNO films deposited on platinized silicon substrates and annealed at 700 °C for a constant time duration of 3 h under 50% OMP with different thicknesses are shown in Fig. 3.24 (a - c), where a, b, and c corresponds to the films' thickness of 150, 250 and 450 nm, respectively. The FESEM images of as-deposited films and the films deposited below 100 nm did not show any significant features in the surface morphology. As the thickness increases, the grain size improved gradually. Interestingly, all the annealed films reveal the nanogranulars, nanorods and are distributed uniformly on the film surface. The average diameters of nanogranulars and nanorods are found to be in the range of 20 to 45 nm. Further; the grains of BNO films have well defined boundaries, denser in structure with an increase in the thickness of the film. Furthermore, as the thickness of the films enhances, the nucleation of the small crystals takes place, this tends to increase the grain size. In addition, with an increase in thickness, the formation of nanogranulars and nanorods is prominent. The elemental analysis of the annealed BNO film deposited at 50% OMP with different thicknesses of 150, 250 and 450 nm, are summarized in **Table 3.12.** It is found that the composition of the target is nearly achieved in the BNO films. The present study confirms that the multicomponent material can be easily grown in a stoichiometric state by using RF magnetron sputtering technique.

Table 3.12: *Elemental analysis of the sputtering target and the films with different thicknesses.*

Bulk BNO target /BNO films thickness (nm) at 50 (O_2/(O_2+Ar)) %	**Element**	**Weight (%)**	**Atomic (%)**	**Required**	**Obtained**
Bulk BNO Target	O (K)	18.53	62.55	15	15.01
	Nb (L)	28.70	16.69	4	4.00
	Ba (L)	52.77	20.76	5	4.99
150 nm BNO Film	O (K)	18.45	62.44	15	14.99
	Nb (L)	28.73	16.74	4	4.02
	Ba (L)	52.82	20.82	5	4.99
250 nm BNO Film	O (K)	18.50	62.50	15	15.00
	Nb (L)	28.89	16.80	4	4.03
	Ba (L)	52.61	20.70	5	4.97
450 nm BNO Film	O (K)	18.46	62.46	15	14.99
	Nb (L)	28.66	16.70	4	4.01
	Ba (L)	52.88	20.84	5	5.00

3.3.3.2 Optical properties

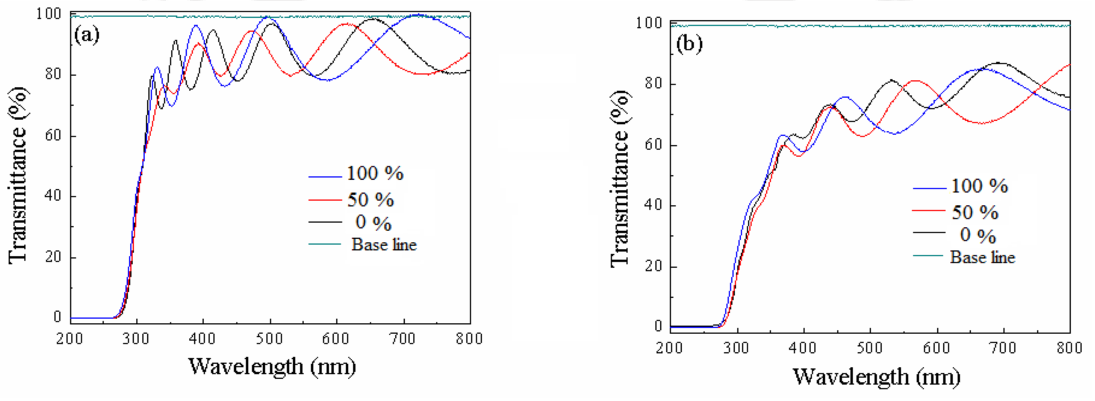

Fig. 3.25: *Transmittance spectra of (a) as deposited and (b) annealed films deposited under different OMPs.*

The optical behaviour of the nanocrystalline BNO films were studied for the films deposited on amorphous SiO_2 substrates. Further, the optical response of the films with respect to thickness is minimal and hence the optical constants of the BNO films are studied as a function of OMP. The spectral transmittance of amorphous and nanocrystalline BNO films are depicted in Fig. 3.25 (a) and 3.25 (b), respectively. The transmittance spectra of nanostructured BNO thin films show a transparency about 90 % and 80 % for as-deposited and annealed films in the visible region, correspondingly. Further, a transparent oscillating and a strong absorption were observed in the transmittance spectra of both the films. Both the films exhibit peaks and valleys that are associated with the reflections from the incident light from the air-film, and film-substrate due to interference. The strong absorption was observed at wavelengths below 350 nm, 400 nm as deposited and annealed films, respectively and the annealed films exhibit the red shift. In addition, the annealed films exhibit lower transmittance as compared to the as deposited films and this may be attributed to the increase in average grain size and grain boundary, which scatters the light. The property of high transmittance in the visible region makes BNO films as a good candidate for transparent window layer applications.

The variation in a refractive index of both the as deposited and annealed films as a function of OMP is shown in Fig. 3.26 (a). It is observed that the refractive index of the annealed films is higher compared with as deposited films. On annealing, the increase in the refractive index is attributed to the improvement in the crystallinity of the films. This is obvious because the as deposited films were deposited at ambient temperature and at this temperature films will be highly disorder due to the low adatom mobility. This causes the poor nucleation, which results in lower refractive indices. Further, the refractive index of both the films increases linearly up to 50% OMP above that it started decreasing, and this is attributed to the crystallinity of the films and these results complement the XRD studies. The obtained refractive index values are in the range of 1.82-2.05, and 1.89-2.16 @ 550 nm for the as-deposited and annealed films, respectively. The variation in optical bandgap as a function of OMP for the as-deposited and annealed films was shown in Fig. 3.26 (b). The Tauc equation [49] was used to estimate the optical bandgap of films, which was given by

$$(\alpha h\upsilon) = c(h\upsilon - E_g)^{\gamma} \qquad (8)$$

Where, α is the optical absorption coefficient, $h\upsilon$ is the incident photon energy, c is energy independent constant, E_g is the optical bandgap and γ is a constant which characterizes the nature of band transition. γ = 0.5, 1.5 correspond to direct allowed and direct forbidden transition and γ = 2, 3 correspond to indirect allowed and indirect forbidden transitions respectively.

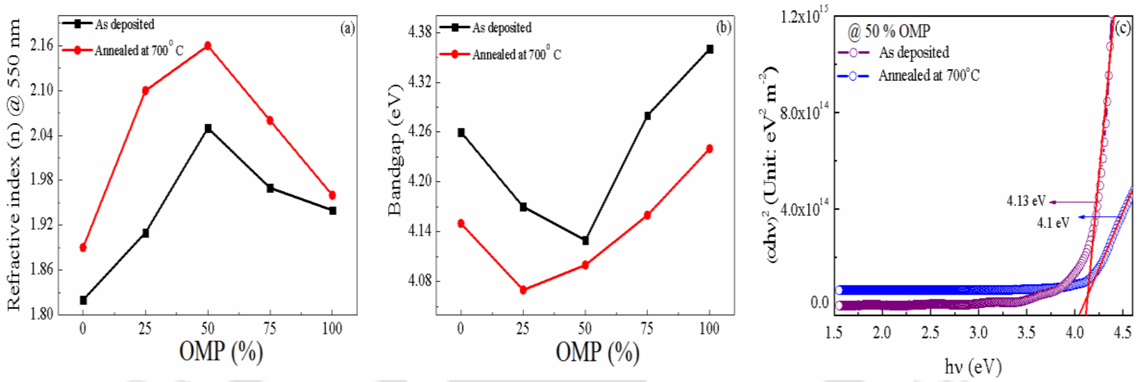

Fig. 3.26: *Variation in (a) refractive index, (b) bandgap of BNO films as a function of OMP and (c) Absorption edges of as deposited and annealed BNO film deposited at 50%OMP.*

The optical absorption coefficient (α) was calculated from the transmittance (T) using the fallowing equation

$$\alpha = -\ln(T)/d \qquad (9)$$

Where, d = BNO film thickness in nm and T is defined by T = I_T/I_O where, I_T and I_O are the intensities of radiation coming out of the film and incident radiation, correspondingly. The values of optical bandgap E_g can be obtained from the extrapolation of the straight-line portion of the $(\alpha h\upsilon)^2$ Vs $h\upsilon$ plot to $h\upsilon = 0$. It is observed that the optical bandgap of both as-deposited and annealed films improved with an increase in OMP and as-deposited films showed higher values as compared to the annealed films. The observed variation in bandgap may be attributed to the improvement in the crystallinity, increase in particle size of the films that is associated to decrease of energy levels within the optical bandgap and was confirmed from optical transmittance spectra as shown in Fig. 3.25. Another possibility is lowering of bandgap can be due to electro negativity of transition metal Nb^{5+} ions and increased width of a conduction band [50]. The estimated optical bandgap values for the as deposited and annealed films are in the range of 4.13 - 4.36 *eV* and 4.07- 4.24 *eV*, respectively. The obtained bandgap values are higher when compared to the bulk bandgap of the BNO ceramics (E_g = 3.63 *eV* and 3.9 *eV*) [11, 51]. In the present study, the achieved higher bandgap of the BNO films are attributed to the partial crystallinity of the films. It is known that when the crystalline phase of the film is embedded in the predominantly amorphous matrix, there are large deviations in the optical bandgap of the films from the bulk values [52]. The obtained optical bandgap values indicate that the deposited films were in the stoichiometric state because the optical bandgap is an indirect estimate of the stoichiometry of the films. The absorption edge of the as deposited and annealed film deposited at 50% OMP are depicted in Fig. 3.26 (c) which displays the variations in the optical bandgap of the as deposited and annealed films and complements the variations in the absorption edges in the transmittance spectra.

3.3.3.3 Dielectric properties

To study the dielectric response of the BNO films, Ag/BNO/Pt/Ti/SiO_2/Si thin film capacitors were fabricated with three different (150, 250, 450 nm) thicknesses and the films were deposited at 50% OMP at an ambient temperatures for the time duration of 65, 105 and 180 minutes, respectively. The frequency dependence of dielectric constant (ε_r) and loss tangents (*tanδ*) for the Ag/BNO/Pt/Ti/SiO_2/Si capacitors are shown in Fig. 3.27 (a) and 3.27 (b), correspondingly. It is observed that at low frequencies, all the samples exhibit larger dielectric constants and higher *tanδ* and beyond 200 kHz, there is a little dispersion in ε_r. This can be attributed to the interfacial polarization in this frequency range. Beyond 200 kHz, the reduction in both the dielectric constant and higher *tanδ* could be due to the dipole polarization which is active in this frequency range (200 kHz to 1 MHz), and is a typical behaviour of the linear dielectrics and can be explained on the basis of Maxwell's polarization theory and Koop’s two-layer model [53]. Further, with an increase in thickness, the dielectric constant of the films increases whereas the loss decreases. The variation in dielectric constant and *tanδ* as a function of thickness and measured at 1 MHz is shown in Fig. 3.27 (c). It is evident that with a rise in thickness, the dielectric constant of the films increases exponentially whereas the dielectric loss is found to decrease linearly. The simultaneous improvement in dielectric constant and reduction in tanδ with an increase in thickness can be attributed to the enhancement in the degree of crystallinity of the films, improvement in the microstructure, and reduction in rms roughness.

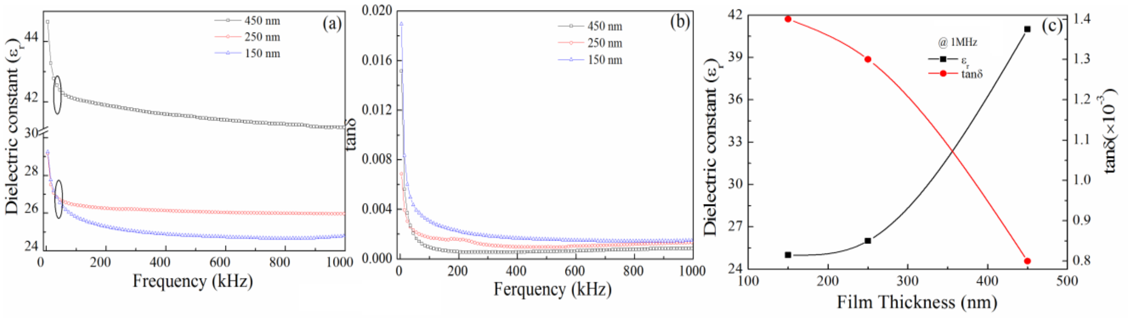

Fig. 3.27: *Variation in (a) dielectric constant, (b) loss tangent of BNO thin films deposited at different thicknesses as a function of frequency and (c) Plot of dielectric constant and loss tangent versus film thickness, measured at 1 MHz.*

Further, $Ag/BNO/Pt/Ti/SiO_2/Si$ structures can be considered as the two parallel plate capacitors coupled in series. This assembly can be interrelated to the electrode – BNO films interfacial layer (dead layer) and bulk. Hence, the total capacitance (c) of $Ag/BNO/Pt/Ti/SiO_2/Si$ structure can be written as $\frac{1}{c} = \frac{1}{c_i} + \frac{1}{c_b}$ where c_i and c_b designate the capacitance of the interfacial layer and bulk sample, respectively. In addition, the dielectric constant of BNO thin film capacitor with distinct thicknesses can be expressed as

$$\frac{t}{\varepsilon} = \frac{t_i}{\varepsilon_i} + \frac{t - t_i}{\varepsilon_b} \approx \frac{t_i}{\varepsilon_i} + \frac{t}{\varepsilon_b} \qquad (10)$$

Where, t and t_i are the total thickness of the film and the interfacial layer and ε, ε_i and ε_b are the dielectric constants of the film, interfacial layer and bulk BNO, respectively [54, 55]. The approximation in equation (10) is reasonable, because the total thickness of the films is much higher as compared to interfacial (dead) layer. Further, the contributions from the dead layer and bulk BNO to the dielectric constant can be estimated by plotting t/ε vs t, gives a linear curve which is depicted in Fig. 3.28. The values of ε_b and t_i/ε_i can be extracted from the reciprocal of the slope and y-intercept through the linear fitting. The obtained values for dead layer and bulk BNO dielectric constant is found to be 15.21 nm and 37.03, respectively. The dead layer occurs between the BNO film and of the electrodes, which arise due to the oxygen diffusion and changes in the surface chemistry of electrode interfaces or may be due to the formation of reactive layer at the electrode interface. Further with an increase in thickness, the surface diffusion reduces at the film – electrode interface and the influence of dead layer diminish, which result in low losses.

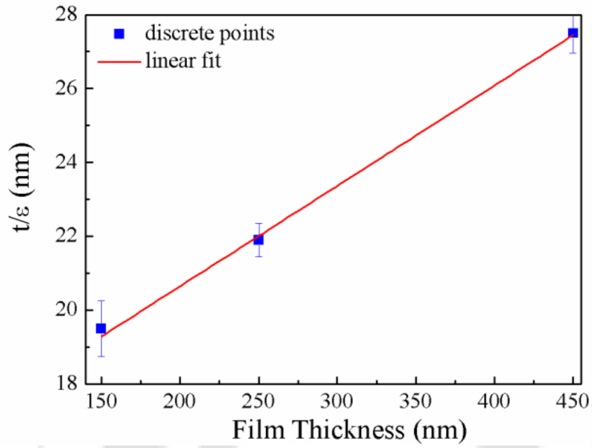

Fig. 3.28: *Plot of t/ε versus thickness of film (discrete points) and solid line represents linear fit.*

The temperature dependence of dielectric constants and *tanδ* of BNO films fabricated with different thickness are shown in Fig. 3.29 (a) and 3.29 (b), respectively. It is observed that as the temperature raises, both the dielectric constant and *tanδ* of BNO films increases progressively. Further, the loss tangent is higher for the films with lower thickness. The improvement in dielectric constant with temperature can be explained as follows: thermal energy facilitates the alignment of the dipoles in the field direction which enhances the dielectric constant of the films. On the other hand, with an increase in thermal energy, mobility, conductivity and the vibration of atoms causes the enhancement in dielectric loss.

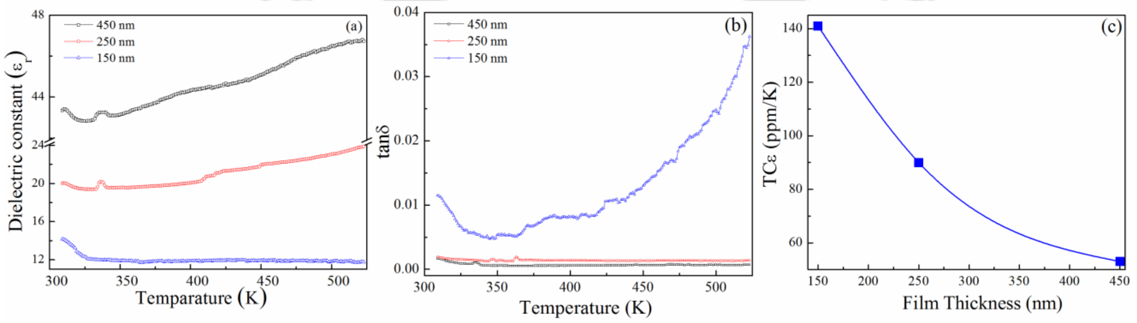

Fig. 3.29: *Variation in (a) dielectric constant (b) loss tangent of BNO thin films deposited at different film thicknesses as a function of temperature and (c) plot of TCε versus film thicknesses.*

The microwave dielectric properties of as - deposited and annealed BNO thin films were measured at 5, 10 and 15 GHz using a split post dielectric resonator (SPDR) method are tabulated in **Table 3.13** and **Table 3.14**, respectively.

Table 3.13: *Microwave dielectric properties of as-deposited BNO thin films on quartz substrates measured by using split post dielectric resonator method.*

As-Deposited films						
	At 5 GHz		At 10 GHz		At 15 GHz	
OMP (%)	ε_r	$tan\delta$	ε_r	$tan\delta$	ε_r	$tan\delta$
0	33.41	0.054	30.74	0.062	28.68	0.074
50	35.55	0.032	31.43	0.045	29.94	0.050
100	36.73	0.025	32.57	0.030	30.27	0.041

Table 3.14: *Microwave dielectric properties of annealed BNO thin films on quartz substrates measured by using split post dielectric resonator method.*

After Annealing						
	At 5 GHz		At 10 GHz		At 15 GHz	
OMP (%)	ε_r	$tan\delta$	ε_r	$tan\delta$	ε_r	$tan\delta$
0	40.23	0.0064	35.45	0.0070	29.65	0.0074
50	41.17	0.0044	36.64	0.0058	30.80	0.0063
100	43.56	0.0020	38.48	0.0042	31.65	0.0052

In both the cases, it is found that the dielectric properties show a profound frequency dispersion that is expected in the case of a linear dielectric. Furthermore, as the OMP increases, the dielectric properties of the films enhanced and films deposited in pure oxygen plasma exhibited the best microwave dielectric properties. The annealed films show better dielectric response as compared to the as deposited films and are attributed to the improvement in crystallinity and enhanced uniform grain sizes.

The temperature stability of the dielectric constant of the BNO films is evaluated by calculating the temperature coefficient of dielectric constant ($TC\varepsilon$). $TC\varepsilon$ is obtained by using the following expression

$$TC\varepsilon = \frac{\Delta\varepsilon_r}{\varepsilon_0 \Delta T}(ppm/^{o}C) \tag{11}$$

Where, $\Delta\varepsilon_r$ is the change in ε_r with respect to the value ε_0 (T = 300 K) and ΔT is the change in temperature relative to 300 K. The variation in $TC\varepsilon$ as a function of thickness is shown in Fig. 3.29 (c). It observed that all BNO films revealed positive $TC\varepsilon$ values across. It is evident that as the film thickness increases, the $TC\varepsilon$ of BNO films decreases linearly and the film with 450 nm thickness exhibits a better stability (53 ppm/K).

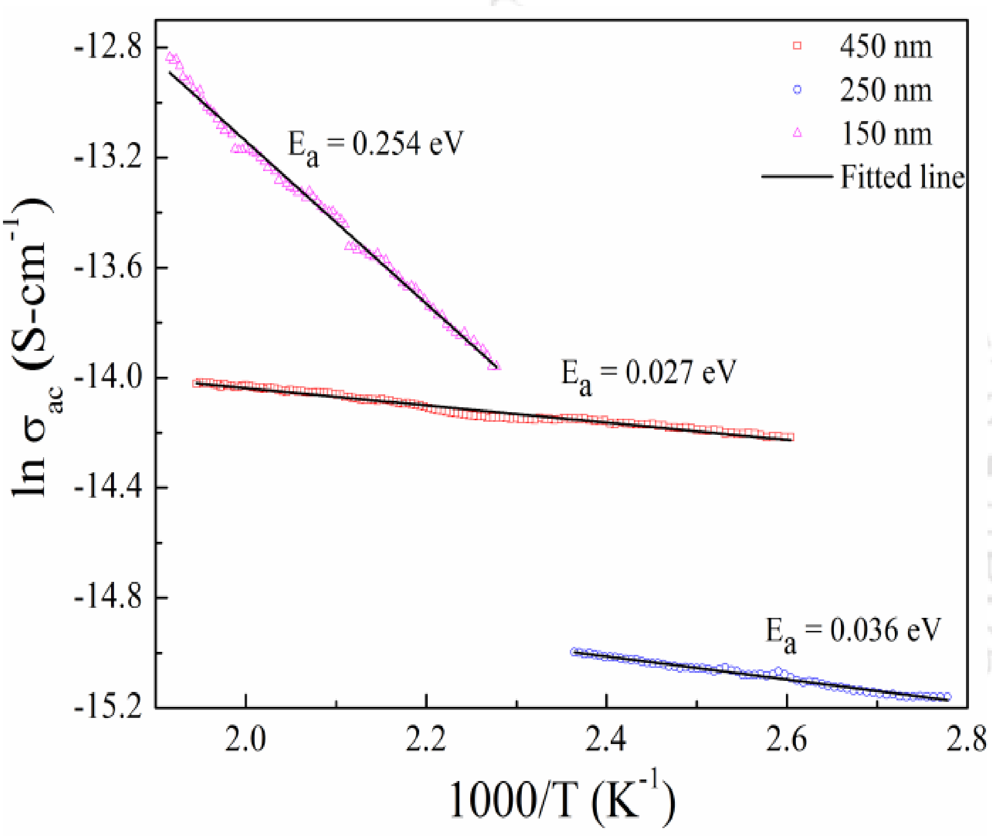

Fig. 3.30: *Variation of σ (ac) versus 1000/T.*

Fig. 3.30 shows the variation of AC conductivity (σ_{ac}) of BNO films with different thicknesses versus *1000/T*, measured at 1 MHz. The slope of each curve gives the activation energy of the mobile charge carriers and calculated using the Arrhenius relation [given in equation (6)]. The extracted energies are found to be E_a = 0.254, 0.036 and 0.027 *eV* for the films with 150, 250 and 450 nm, respectively. The E_a depends on the average film thickness. The activation energy for film of 150 nm is one order more than 250, 450 nm films. So these reflections may be due to size effects that are appeared because of quantum confinement of charge carriers within the particles.

3.3.3.4 Electrical properties of BNO film capacitors

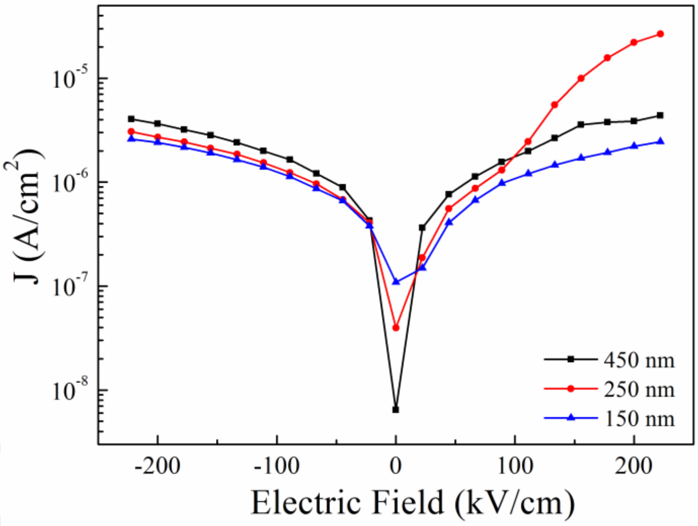

Fig. 3.31: *Leakage current densities of BNO films measured at different applied electric field ranges.*

Fig. 3.31 shows the room-temperature leakage current density characteristics for the Ag/BNO/Pt/Ti/SiO_2/Si (MIM) capacitors as a function of thickness. The leakage currents were measured with a voltage step of 1 Volt and step duration of 10 sec. The average leakage current density is about less than 10^{-6} A/cm^2 at an applied electric field of 50 kV/cm. As the thickness of the film increases, the leakage current density of the BNO films decreases. The leakage current density magnified with electric field, which may be due to the structured grain boundaries and crystal defects. The J-E characteristics of the BNO films showed a combined response of grain, grain boundaries and film-electrode interfaces. The asymmetric J-E curves may be associated with the different interfacial layer indentation between the bottom electrodes-film and film-top electrode interfaces.

Fig. 3.32 shows the logarithmic dependence of current density as a function of logarithmic electric field for BNO thin films. Here, the conduction behaviour of BNO films with different thickness is described on the basis of ohmic and space charge-limited current (SCLC) model [56, 57]. In the negative electric field region; the BNO films follow an Ohmic conduction ($J \sim E^{\alpha} : \alpha \sim 1$) behaviour. The obtained α values are found to be 0.84, 0.88 and 0.96 for film thickness of 150, 250 and 450 nm, respectively. On the other hand, in the positive electric field region, BNO films exhibit both the Ohmic and SCLC ($J \sim E^{\alpha} : \alpha \rangle\rangle 1$) nature. The extracted α values are 1.19, 1.39 and 1.14 for film thickness of 150, 250 and 450 nm, correspondingly in the positive electric field region and $\alpha = 3.45$ observed for film thickness of 450 nm which shows the SCLC conduction.

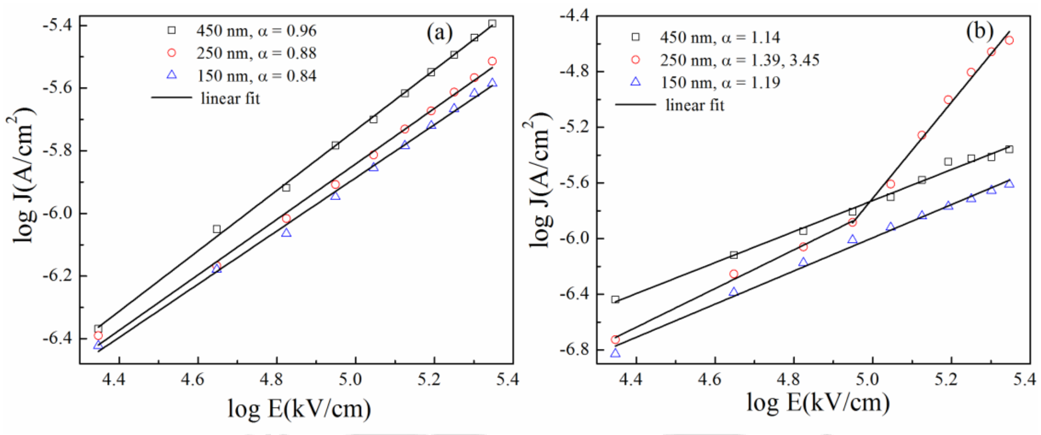

Fig. 3.32: *log J as a function of log E under the (a) negative electric field (b) positive electric field.*

The equivalent oxide thickness (EOT) of the Ba$_5$Nb$_4$O$_{15}$ thin films and the required thickness of the high - ε_r thin film when the EOT is taken as 1 nm can be calculated [58] using the formula

$$t_{eq} = \frac{t_{high-\varepsilon_r} \times 3.9}{\varepsilon_{high-\varepsilon_r}} \qquad (12)$$

Where, $t_{high-\varepsilon r}$ *is* the thickness, $\varepsilon_{high-\varepsilon r}$ is the dielectric constant of the high-ε_r material and t_{eq} is the equivalent oxide thickness. The obtained value is 10.5 nm for Ba$_5$Nb$_4$O$_{15}$ films with thickness 450 nm. The obtained excellent electric and dielectric properties of BNO films are promising for MIC and CMOS applications.

3.4 Conclusions

For the first time BNO ceramics were synthesized by a mechanical alloying method. The parent oxides were milled for 10 *h* show the formation of BNO and BaNb$_2$O$_6$ and the concentration of BNO weight percentage increases with milling time upto 40 *h*. However, BaNb$_2$O$_6$ phase could not be eliminated during the milling. BNO powders milled for 40 *h* showed a maximum density at 1250 ^{o}C and are explained on the basis of Herring's scaling law. The broadband dielectric properties of BNO ceramics show a stable response from 1 MHz to 0.2 GHz and from -140 ^{o}C to 350 ^{o}C. The dielectric response of these samples measured above 350 ^{o}C show, relaxation behaviour and is explained with HN equation, and the corresponding equivalent circuit show a parallel R_1C_1 in series with C_2. The obtained dielectric properties at microwave frequencies are ε_r = 34, $Q\times f_0$ = 32.5 THz, at 7 GHz are attributed to increase in density and uniform grain size. The dielectric response of BNO, makes this material suitable for type - I capacitor and DR applications.

The effect of $Ba_5Nb_4O_{15}$ (BNO) nanopowders on micron sized BNO polycrystalline powders had been studied systematically. Both at low and high temperature ranges, the broadband dielectric properties of BNO ceramics added with x wt% of nanosized particles shows a stable response with an increase in frequency upto 30 MHz. The ac conductivity spectrum of the samples obeyed Jonscher's universal power law ω^s with a frequency exponent $s > 1$. The extracted activation energies are found to be E_a = 0.0037, 0.0019 and 0.0010 *eV* for the BNO ceramics with the addition of BNO nanosized particles with x = 1, 2, and 3 wt%, respectively. The dielectric response of BNO ceramics with the variation in temperature and the relaxation behaviour is explained on the basis of Havriliak - Negami equation. The best microwave dielectric properties of ε_r and $Q\times f_0$ values of 39.2 and 59 THz, at 6.52 GHz are obtained for the x = 3 wt% sample, sintered at 1100 ^{o}C and is attributed to the maximum relative density, large and uniform microstructure. The obtained stable dielectric response of BNO ceramics with x wt% of nanosized particles is suitable for cryogenic electronic and dielectric resonator applications.

BNO thin films were prepared by RF magnetron sputtering at a different oxygen pressure ratio in OMP on to Pt-Si and amorphous SiO_2 substrates. The effects of annealing and thickness on the structural, dielectric and electrical properties were discussed in this chapter. The significant features of the BNO thin films from the current investigations are as follows:

- As deposited thin films were amorphous in nature and after annealing at 700 ^{o}C they were crystallined.
- The optical constants of the films studies as function of OMP ratio. With increasing the thickness of the film, dielectric constant advances whereas the loss tangent decreases.
- The best dielectric properties were obtained for film with 450 nm are ε_r = 41 and tanδ = 0.0005 at 1 MHz.
- The dielectric response of BNO capacitors has been explained by considering a dead layer connected in series with dielectric constant of the films. The extracted

values of dielectric constant and thickness for the dead layer are found to be 37.03 and 15.21 nm, respectively.

- The microwave dielectric properties were measured using split post dielectric resonator method at discrete frequencies (5, 10 and 15 GHz).
- The leakage current characteristics found to decrease with thickness and the leakage current density is about less than 10^{-6} A/cm^2 at an applied electric field of 50 KV/cm. The leakage current studies revealed ohmic behaviour during the negative cycle whereas space charge limited current and ohmic response during a positive cycle.
- Microwave dielectric properties of both bulk and thin films are almost comparable.

3.5 References

[1] P. Fu, Y. Xu, X. Wang, *Int. J. Appl. Ceram. Technol.* **12** (2015) 116.

[2] C. L. Huang, C. E. Ho, *Int. J. Appl. Ceram. Technol*. **7** (2010) E163.

[3] P. S. Anjana, M. T. Sebastain, M. N. Suma, P. Mohanan, *Int. J. Appl. Ceram. Technol*. **5** (2008) 325.

[4] L. Yi, X. Q. Liu, L. Li, X. M. Chen, *Int. J. Appl. Ceram. Technol*. **10** (2013) E177.

[5] L. Fang, Z. Wei, W. Liao, H. Zhou, H. Zhang, F. Xiang, *J. Am. Ceram. Soc*. **97** (2014) 498.

[6] R. Muhammad, Y. Iqbal, C. R. Rambo, H. Khan, *Int. J. Mater. Res. (*formerly Z. Metallkd.), **431** (2014) 105.

[7] F. Galasso, L. Katz, *Acta Cryst.* **14** (1961) 647.

[8] C. Vineis, P. K. Davies, T. Negas, *S. Bell, Mater.Res. Bull.* **31** (1996) 431.

[9] C. T. Lee, C. T. Chen, C. Y. Huang, *Jpn. J. Appl. Phys.* **47** (2008) 4634.

[10] Y. H. Jo, D. J. Shin, V. S. Saji, R. K. Gupta, H. S. Lee, Y. S. Cho, *J. Ceram. Soc. Jpn*. **115** (2007) 978.

[11] Y. J. Hsiao, Y. H. Chang, *J. Am. Ceram. Soc*. **90** (2007) 2287.

[12] H. Zhou, X. Chen, L. Fang, C. Hu, H. Wang, *J. Mater. Sci. - Mater.Electron.* **21** (2010) 939.

[13] R. K. Bhuyan, T. S. Kumar, D. Pamu, A. J. James, *Int. J. Appl. Ceram. Technol.* **10** (2013) E18.

[14] H. Yang, Y. Hu, A. Tang, S. Jin, G. Qiu, *J. Alloys Compd.* **363** (2004) 276.

[15] A.Yakubu1, Z. Abbas, M. Hashim, A. Fahad, *Journal of Materials Science and Chemical Engineering*, **2** (2014) 58.

[16] K. T. Paul, S. K. Satpathy, I. Manna, K. K. Chakraborty, G. B. Nando, *Nanoscale Res Lett*, **2** (2007) 397.

[17] L. B. Kong, J. Ma, W. Zhu, O. K. Tan, *J. Alloys Compd.* **322** (2001) 290.

[18] C. Suryanarayana, *Mechanical Alloying and Milling*, Marcel-Dekker, Inc., New York, (2004).

[19] D. Pamu**,** G. L. NarayanaRao, K. C. James Raju, *J. Am. Ceram. Soc.* **95** (2012)126.

[20] D. Pamu**,** G. Lakshminarayana Rao, K. C. James Raju, *Advances in Applied Ceramics*, **108** (2007) 202.

[21] T. Ahmad, A. K. Ganguli, *J. Mater Res*, **19** (2004) 2905.

[22] P. Jha, P. R. Arya, A. K. Ganguli, *Mater. Chem. Phys.* **82** (2003) 355.

[23] W.E. Courtney, *IEEE Trans. Microwave Theory Technol.* **18** (1970) 476.

[24] G. Balakrishnan, T.N. Sairam, P. Kuppusami, R. Thimurugesan, E. Mohandas, V. Ganesan, D. Sastikumar, *Appl. Surf. Sci.* **257** (2011) 8506.

[25] C. Y. Ma, F. Lapostolle, P. Briois, Q.Y. Zhang,*Appl. Surf.Sci.* **253** (2007) 8718.

[26] G.L. Liu, Z.R. Huang, J.H. Wu, X.J. Liu, *Surf. Coat.Technol.* **207** (2012) 204.

[27] R. A. Young, *The Rietveld Method, International Union of Crystallography*, Oxford University Press, London (1996).

[28] B. W. Hakki, P. D. Coleman, *IEEE Trans. Microwave Theory Technol.* **8** (1960) 402.

[29] H. Zhuang, Z. Yue, F. Zhao, L. Li, *J. Am. Ceram. Soc.* **91** (2008) 3275.

[30] T. Asanuma, T. Matsutani, C. Liu, T. Mihara, M. Kiuchi, *J. Appl. Phys.* **95** (2004) 6011.

[31] C. Herring, *J. Appl. Phys.* **21** (1950) 301.

[32] S. J. L. Kang, *Sintering*, Elsevier Butterworth-Heinemann, Oxford (2004).

[33] I. N. Jawahar, P. Mohanan, M. T. Sebastian, *Mater. Lett.* **57** (2003) 4043.

[34] H. Sreemoolanadhan, J. Isaac, S. Solomon, M. T. Sebastian, *Phys. Stat. Sol.* **143** (1994) K45.

[35] G. A. Samara, *J. Appl. Phys.* **68** (1990) 4214.

[36] G. A. Samara, *Phys. Rev.* **165** (1968) 959.

[37] G. A. Samara, *Phys. Rev. B* **13** (1976) 4529.

[38] E. Barsoukov, J.R. Macdonald, *Impedance Spectroscopy Theory, Experiment, and Applications*, John Wiley and Sons Inc., Second Ed., New Jersey 15 (2005).

[39] L. Liu, M. Flores, N. Newman, *PRL* **109** (2012) 257601.

[40] D. Pamu, K. Sudheendran, M. Ghanashyam Krishna, K. C. James Raju, Anil K. Bhatnagar, *Vacuum* **81** (2007) 686.

[41] C. G. P. Moraes, F. A. A. Jesus, Z. S. Macedo, *Advances in Condensed Matter Physics* **968349** (2014) 1.

[42] A. K. Jonscher (1983) Dielectric relaxation in solids (London: Chelsea Dielectrics Press).

[43] W. K. Lee, J. F. Liu, A. S. Nowick, *Rev. Lett.* **67** (1991) 1559.

[44] K. Funke, *Prog. Solid St. Chem.* **22**(1993) 111.

[45] S. A. El-Hakim, F. A. El-Wahab, A. S. Mohamed, M. F. Kotkata, *Phys. Stat. Solid A* **198** (2003) 128.

[46] N. E. Massa, *Phys. Rev. B.* **53** (1996) 8148.

[47] H. D. Fuchs, C. H. Grein, C. Thomsen, *Phys. Rev. B.* **43**(1991) 4835.

[48] T. S. Kumar, R. K. Bhuyan, D. Pamu, *Appl. Surf.Sci.* **264** (2013)184.

[49] J. C. Tauc, Optical properties of solids, North-Holland, Amsterdam, (1972) 66.

[50] H. W. Eng, P. W. Barnes, B. M. Auer, P. M. Woodward, *J. Solid state Chem.* **175** (2003) 94.

[51] F. E. Osterloh, *Chem. Mater.* **20** (2008) 35.

[52] D. Pamu, M. G. Krishna, K. C. J. Raju, A. K. Bhatnagar, *Solid State Commun.* **135** (2005) 7.

[53] J. C. Maxwell, Electricity and Magnetism, Vol 1, Oxford University Press, Oxford, (1929).

[54] K. C. Sekhar, S. H. Key, K. P. Hong, C. S. Han, J. M. Yook, D. S. Kim, Y. S. Cho, *Current applied physics* **12** (2012) 654.

[55] B. T. Lee, C. S. Hwang, *Appl. Phys. Lett.* **77** (2000) 124.

[56] J. Wu, J. Wang, *J. Appl. Phys.* **106** (2009) 066101.

[57] T. Li, G. Wang, K. Li, G. Du, Y. Chen, Z. Zhou, D. Rémiens, X. Dong, *Ceram. Int.* **40** (2014) 1195.

[58] R. M. Wallace, G. M. Wilk, *Mater. Res. Bull.* **27** (2002) 192.

Chapter 4

Studies on $BaWO_4$ bulk and thin films

4.1 Introduction

The microwave dielectric materials with low dielectric losses (low $tan\delta$), the moderate permittivity (depending on the application) and a stable temperature coefficient of resonant frequency (τ_f) are the most significant requirements for various wireless communication devices [1]. It is for this reason that dielectric materials have been so intensively investigated. The crystal structures based on the scheelite type structures AWO_4 (A = Pb, Ca, Ba, Sr) have attracted much interest because of their approved usage as scintillating medium in electro-optic and microwave ceramic applications [2 - 6]. $BaWO_4$ (BWO) ceramics are promising for the above applications due to its excellent dielectric properties in bulk form: dielectric constant (ε_r) ~ 8.0, Quality factor ($Q\times f_0$) ~ 57 500 GHz and temperature coefficient of resonance frequency (τ_f ~ -78 ppm/^{o}C). BWO ceramics reveal a tetragonal structure with $I4_1/a$ space group [7, 8]. There are few reports available on the microwave dielectric properties of BWO ceramics in bulk form [9, 10]. However, BWO ceramics prepared by solid state reaction method are brittle in nature (easily breaking). Further, we have prepared BWO ceramics with mechanical alloying method to induce the mechanical strength. Conversely, to the best of the author’s knowledge, there is no study on mechanically alloyed BWO ceramics, and we have characterized the samples by using different experimental techniques.

In the field of material science, the structure design, dimension control and morphology optimization have recently been viewed as the challenging issues. For achieving improved performance in their bulk counterparts, great efforts have been focused on the controlled synthesis of novel micro- and nanostructures with uniform size and shape [11 - 13]. The low permittivities and high-quality factor values of the scheelite ceramics BWO is regarded as promising material for microwave substrate applications [9]. In addition, there are only few studies have been reported on optical properties of BWO thin films [6, 14]. Hence, this motivated us to pursue this study.

Pontes et al. [15] studied structural and optical properties of BWO films by prepared by chemical route. Dinesh et al. [14, 16] demonstrated the growth of crystalline BWO films at room temperature and reported structural and microstructure of these films.

Cho et al. [17] obtained highly crystallized BWO films at room temperature by using electrochemical method. However, irreversible thermochromic behaviour was not observed in BWO films prepared by the above methods. The irreversible thermochromism can be used in protective layers and window color coatings. Moreover, most of the studies were focussed on the room temperature (RT) crystallization of BWO films. Further, it is known that the properties of the films dependent on the deposition technique. Also, the systematic study on optical properties and growth of BWO films using RF plasma has not been studied earlier. In the current study, we report the growth of BWO films at different substrate temperatures using RF reactive magnetron sputtering technique. The significance of this study is to demonstrate irreversible thermochromic response and optical properties of BWO films for the first time. In addition, there is no methodical reviews have been reported on the dielectric and electrical properties of BWO thin films. Therefore, we deposited nanocrystalline BWO thin films by RF Magnetron sputtering with versatile functional parameters which are very desirable for practical device applications. The Split-post dielectric resonator (SPDR) technique is used to measure the complex dielectric properties of BWO thin films at microwave frequencies and the details of the SPDR technique is given in chapter 2.

4.2 Experimental Details

4.2.1 Synthesis of $BaWO_4$ (BWO) ceramics by mechanical alloying method

The BWO ceramics were synthesized by the mechanical alloying (MA) process from individual high-purity powders of (99.99%) $BaCO_3$, WO_3 from (M/s Sigma Aldrich, St. Louis, MO) were used. The starting materials were mixed according to desired stoichiometry ratio, and the powders were ball milled for 50 hours (*h*) using a planetary ball mill (Fritsch, Germany) with the following parameters : (i) ball - to - powder ratio of 10:1; ball diameters of 5 and 10 mm; ball and vial material: tungsten carbide; milling speed of 400 rpm. The ball milling process was stopped periodically for every 10 *h* and collected some powder for further analysis. After drying and sieving, the samples were uniaxially pressed into pellets with dimensions of 10 mm in diameter and 4 - 5 mm in thickness under a pressure of 200 MPa. The pellets were sintered in the range of 700 - 850 ^{o}C for 5 *h* in air. The heating and cooling rates were 10 ^{o}C / min and 2 ^{o}C / min, respectively.

4.2.2 Deposition of BWO thin films by RF magnetron sputtering

The BWO powder milled for 50 *h* and sintered at 800 °C for 3 *h* exhibited the maximum density and best microwave dielectric properties. Hence, these optimized conditions were used to prepare the sputtering target of 62 mm in diameter with 3 mm in thickness. The BWO thin films were deposited by RF magnetron sputtering on amorphous SiO_2 substrates at different substrate (RT, 200, 400, 600 & 800 °C) temperatures under pure argon plasma and on <100> oriented Pt/Ti/SiO_2/Si (platinized silicon) substrates under different OMPs has been optimized, and equal thick films were deposited (film thickness is about 900 ± 20 nm). The deposition was carried out for 3 *h* at a fixed RF power of 40 *W*. The deposition chamber was pumped down to a base pressure of 1.0×10^{-6} *Torr* and the sputtering pressure of 5×10^{-3} *Torr* is maintained constantly throughout the deposition process. The substrate to target distance was maintained at 6 cm. The $BaWO_4$ target was pre - sputtered in argon ambient for 10 minutes to remove the impurities on the target surface.

4.3 Results and Discussions

4.3.1 Mechanically Alloyed BWO Ceramics

4.3.1.1 XRD and SEM analysis

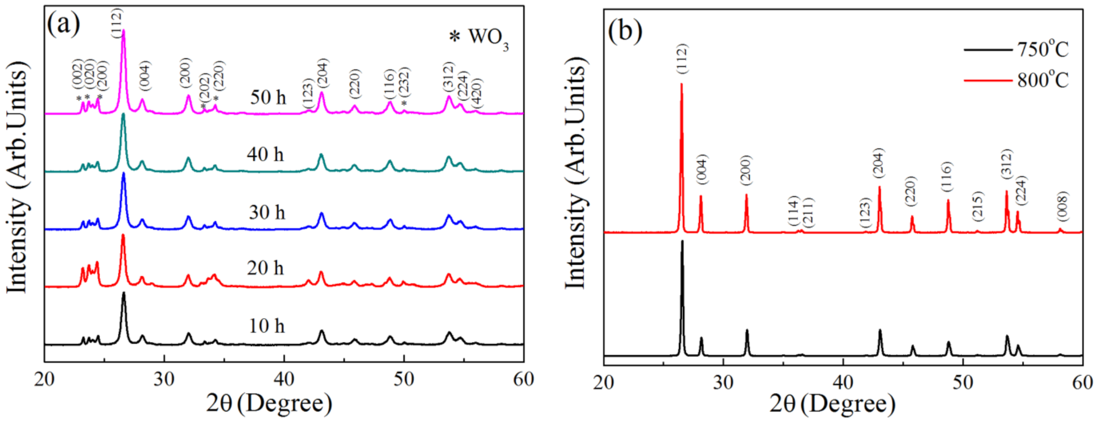

Fig. 4.1: *XRD patterns of (a) $BaCO_3$ and WO_3 powders milled for 10, 20, 30, 40, and 50 h, (b) $BaWO_4$ ceramics, sintered at different sintering temperatures for a constant duration of 5 h.*

To see the effect of milling on phase formation of $BaWO_4$ (BWO) ceramics, milled powders are collected for every 10 *h*. XRD patterns of the BWO powders milled for different milling hour (*h*) are shown in Fig. 4.1 (a). It was found that the pure BWO phase along with WO_3 as a minor secondary phase is obtained for the samples milled from 10 *h* to 50 *h*. With increasing milling time, the intensity of (112) reflection is found to be improved. Even after milling for 50 *h*; WO_3 phase could not be eliminated completely. Fig. 4.1 (b) shows the pure BWO single phase and did not show any secondary peaks for the sample, sintered at 750 °C and 800 °C.

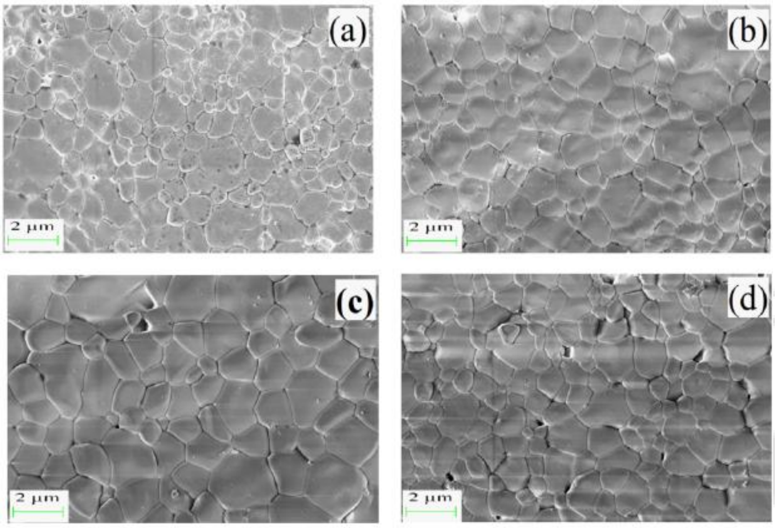

Fig. 4.2: *FESEM micrographs of $BaWO_4$ ceramics sintered at (a) 700 °C, (b) 750 °C, (c) 800 °C, and (d) 850 °C for 5 h.*

The obtained microstructures of the BWO ceramics, sintered at different temperatures are depicted in Fig. 4.2 (a - d). It is observed that the BWO ceramics sintered at 700 °C show a slightly porous microstructure, that can be attributed to the insufficient sintering temperature, whereas the sample sintered at 800 °C reveal a uniform microstructure with good densification and is ascribed to the deformed small initial particle sizes that enhanced the nucleation and densification of the BWO ceramics. However, the samples sintered 850 °C and above exhibited more porous microstructures. The pores are trapped between the large grains in the BWO ceramics at high sintering temperatures, which might be due to the small linear shrinkage at high temperature. The BWO ceramic sintered at 800 °C showed improved grain growth as compared to all other sintering temperatures. The average grain size was found to be 1.2 µm for the sample sintered at 800 °C.

4.3.1.2 Broadband dielectric properties as a function of temperature

Fig. 4.3 shows the frequency (1 MHz – 0.1 GHz) dependent dielectric properties of BWO ceramics, sintered at 800 °C measured in the temperature range of -140 to 180 °C.

It is observed that in this temperature range, both the dielectric constant (ε_r), and loss tangent ($tan\delta$) of BWO ceramics showed a stable behaviour up to 25 MHz. Further, with a rise in applied frequency up to 0.1 GHz, the dielectric constant (ε_r) of the samples decreases whereas the loss tangent ($tan\delta$) was enhanced, which is a typical characteristic of a linear dielectric. In addition, with an increase in measurement temperature, dielectric constant of the BWO ceramics is improved. In the low temperatures (-140 to 20 ^{o}C), the arrangement of dipoles along the direction of the field would be difficult due to the unavailability of thermal energy (i.e., the molecules are not in thermal motion) but slight increase in dielectric constant at low temperatures can be associated to variations in the polarization volume, which is explained using Clausius - Mossotti relation [18]. As the temperature rises, the molecules have more thermal energy and therefore the amplitude of thermal motion is greater. Hence, the effect of heating on orientational polarization is active and leading to an increase in dielectric constant. The obtained dielectric constant (ε_r) and loss tangent ($tan\delta$) values of BWO ceramics sintered at 800 ^{o}C, measured at different temperatures and at discrete frequencies were shown in **Table 4.1.**

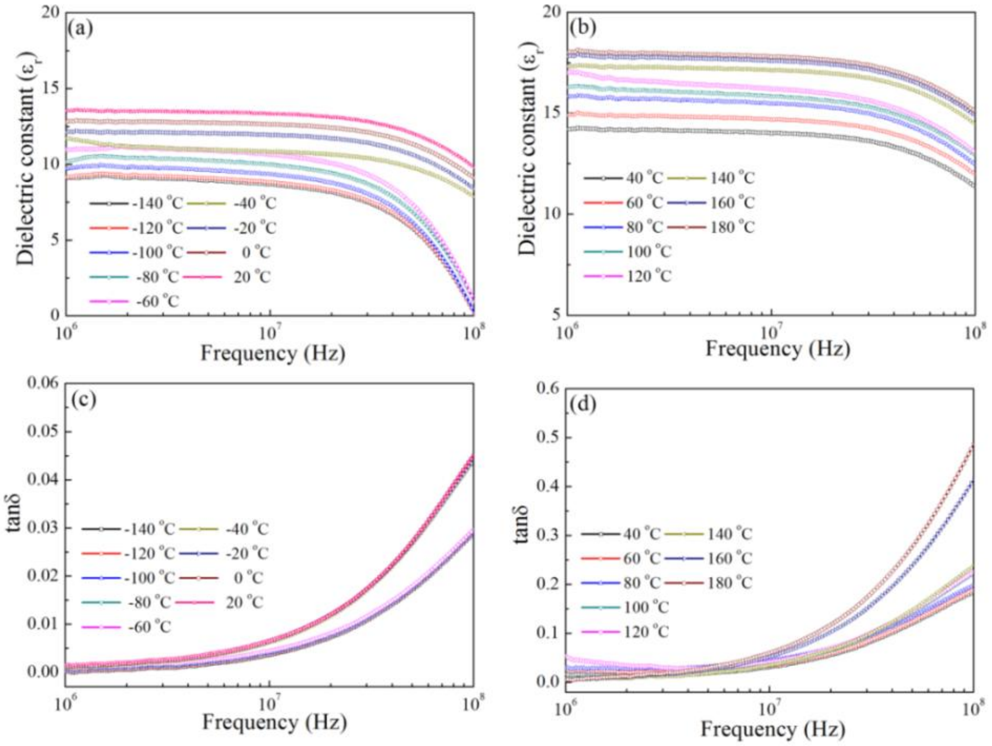

Fig. 4.3: *Variations in dielectric constant as a function of frequency measured in the temperature range of (a) (-140 ^{o}C to 20 ^{o}C) (b) (40 ^{o}C to 180 ^{o}C). Variations in loss tangent as a function of frequency measured in the temperature range of (c) (-140 ^{o}C to 20 ^{o}C) (d) (40 ^{o}C to 180 ^{o}C).*

Table 4.1: *Measured dielectric constant (ε_r) and loss tangent (tanδ) values of BWO ceramics, at different temperatures and at discrete frequencies.*

Sintering temperature	**Measured frequency**	**-140 °C**		**40 °C**		**180 °C**	
		ε_r	*tanδ*	ε_r	*tanδ*	ε_r	*tanδ*
800 °C	1 MHz	9.11	0.0002	14.20	0.0160	18.01	0.0050
	10 MHz	8.68	0.0030	14.01	0.0310	17.79	0.0600
	0.1 GHz	0.13	0.0280	11.36	0.1850	15.09	0.4870

4.3.1.3 Relative density and microwave dielectric properties

The variation in relative density of the samples milled for 50 *h* as a function of sintering temperature is shown in Fig. 4.4 (a). It is observed that as the sintering temperature increases from 700 °C to 800 °C, the relative density improved significantly and decreases thereafter. The obtained lower density at 700 °C may be due to the insufficient sintering temperature and decrease in density above 800 °C can be attributed to the increase of porous microstructure, which is confirmed from SEM image (Fig. 4.2 (d)). The samples sintered at 800 °C exhibited a maximum relative density of 97.51%. The enhancement in the relative density for the mechanically alloyed BWO ceramics, sintered at 800 °C is mainly ascribed to the following factors: (i) small initial particle size and (ii) uniform grain growth.

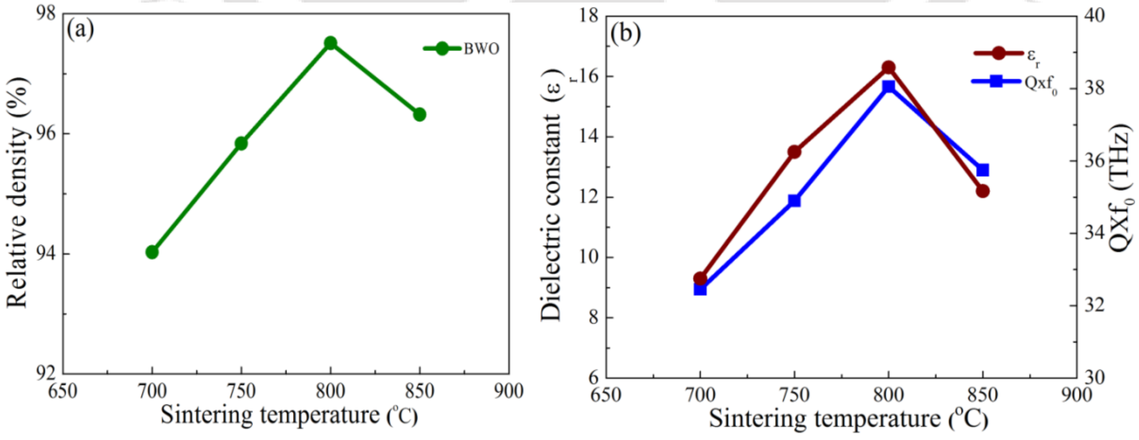

Fig. 4.4: *Variation in (a) relative density, (b) dielectric constant and $Q\times f_0$ values of BWO ceramics, sintered at different temperatures.*

Fig. 4.4 (b) shows the dielectric constant and $Q\times f_0$ values of BWO ceramics sintered at different sintering temperatures. The dielectric constant and *tanδ* were in the range of 9.3 - 16.3 and 0.0012 - 0.00135, respectively. The $Q\times f_0$ values enhanced with an increase in temperature up to 800 ^{o}C above that started decreasing and the values of $Q\times f_0$ are in the range 32.45 to 38.05 THz. The maximum $Q\times f_0$ value is found to be 38.05 THz at 11.6 GHz for the samples sintered at 800 ^{o}C for 5 *h*. Many microwave dielectric loss mechanisms are suggested including intrinsic and extrinsic. In polycrystalline materials the intrinsic losses are depends on the crystal structure and can described by the interaction between the phonon system and the ac electric field. Also, the dielectric losses depend on the crystal symmetry, ac field frequency and temperature. Extrinsic losses are connected with imperfections in the crystal lattice such as impurities, micro structural defects, grain boundaries, porosity, micro cracks, and vacancies etc. The extrinsic losses are caused by lattice defects and these losses can be reduced to the minimum by appropriate material preparation [19, 20]. The increase in $Q\times f_0$ value is primarily attributed to the increase in uniform grain size and higher densities. The decrease in $Q\times f_0$ values at higher temperatures (≥ 850 ^{o}C) can be attributed to the lower densities and the increase of porous microstructure. Since the grain boundary is a plane defect it decreases the $Q\times f_0$ value because the grain growth decreases the grain boundary area since the single crystal is expected to have highest $Q\times f_0$ value. In the present work, the mechanical alloying method played a significant role to enhance the microwave dielectric properties of BWO ceramics.

4.3.2 Irreversible Thermochromic Response of Nanocrystalline BaWO$_4$ (BWO) Films

4.3.2.1 Structural and morphological studies

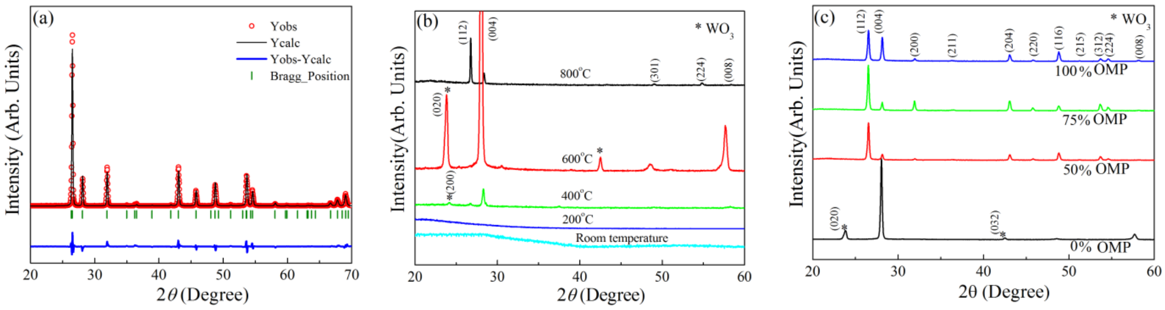

Fig. 4.5: *(a) The XRD pattern along with Rietveld refinement of BWO target, sintered at 800 °C for 3 h. (b) XRD patterns of BWO thin films deposited on amorphous SiO_2 substrates at different substrate temperatures. (c) XRD patterns of BWO thin films deposited at different oxygen mixing percentage (OMP) on amorphous SiO_2 substrates at 600 ^{o}C.*

The XRD pattern of BWO target along with the Rietveld refinement data of the sputtering target, sintered at 800 °C for 3 *h* is shown in Fig. 4.5 (a). $BaWO_4$ ceramics revealed the tetragonal structure with $I_{41/a}$ space group. The refinement is carried out by considering $I_{41/a}$ space group. The lattice parameters, atomic positions of the Ba, W, and O atoms, and occupancy are refined. The corresponding lattice constant values are found to be $a = b = 5.6102$ Å, $c = 12.7101$ Å, which are in agreement with earlier reports [JCPDF file # 850588]. The fitting parameters are: (i) $\chi^2 \approx 7.68$, (ii) R_{Brag} factor ≈ 5.091 and (iii) R_f factor ≈ 5.410.

BWO thin films deposited on amorphous SiO_2 substrates, at different substrate temperatures deposited in 0% OMP i.e., pure argon plasma are shown in Fig. 4.5 (b). It is observed that BWO films deposited both at an ambient temperature, and 200 °C depicted amorphous nature. As the deposition temperature increases, the films exhibit crystalline nature and the intensity of the peaks enhanced gradually. In general, oxide films grow in amorphous phase at ambient temperatures due to insufficient thermal energies and lattice mismatch between substrate and the film. At higher deposition temperatures, the thermal energy facilitates the atoms to find minimum energy sites, which assist the nucleation of microscopic crystals into large grains. BWO films deposited at 400 °C and 600 °C displayed WO_3 as a secondary phase. The major diffraction peaks observed for WO_3 phase are (2 0 0) and (0 2 0) at $2\theta = 24.19$ and 23.77 indicate that WO_3 exhibit an orthorhombic structure [JCPDF file # 710131] for the films deposited at 400 °C and 600 °C, respectively. In the presence of WO_3, the signatures of the (2 0 0) and (0 2 0) reflections disappear in the films deposited at 800 °C. BWO films deposited at 800 °C showed a pure tetragonal phase without any secondary phase. The formation of WO_3 is natural, because it needs lower thermal energy as compared to BWO. The average crystallite sizes of films are calculated by using the Scherrer's formula and are in the range of 33.6 - 51.75 nm, which confirmed the formation of nanocrystalline films. Further to quantify the presence of WO_3 and BWO phases, the weight ratios of orthorhombic (WO_3) and tetragonal (BWO) phases for the films deposited at 400 °C and 600 °C, are calculated using the following expression [21]

$$W_{WO} = \{1/[1+1.265(I_{BWO}/I_{WO})]\}\times 100 \qquad (1)$$

Where, W_{WO} denotes the weight fraction of the orthorhombic phase, I_{BWO} and I_{WO} are the intensity of tetragonal phase and orthorhombic phase, respectively. The weight fraction of the orthorhombic phase decreased from 20.81% to 8.34% with an increase in deposition temperature from 400 °C to 600 °C and subsides completely in the film deposited at 800 °C. XRD patterns of the BWO films deposited at 600 °C with different oxygen mixing percentage (OMP) were shown in Fig. 4.5 (c). The BWO films deposited under 0% OMP (i.e., pure argon plasma) displayed a mixture of WO_3 and $BaWO_4$ phases. With an increase in OMP from 50% to 100% OMP in the deposition chamber, the secondary phase vanished completely and the crystallinity of the BWO films enhanced with an increase in OMP.

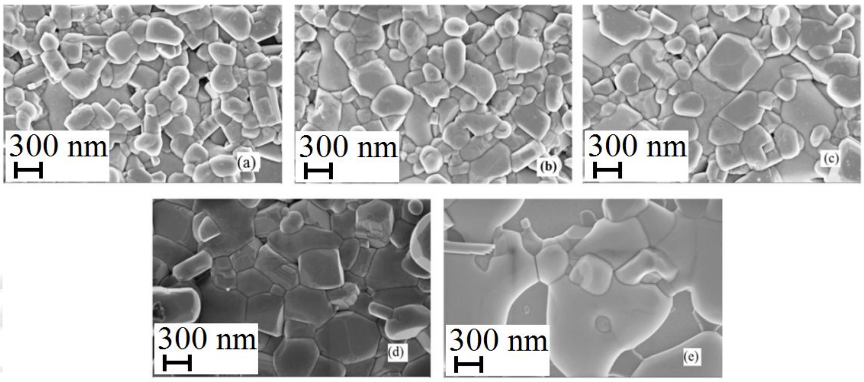

Fig. 4.6: *FESEM micrographs of BWO films deposited at different substrate temperatures (a) RT, (b) 200 °C, (c) 400 °C, (d) 600 °C and (e) 800 °C.*

FESEM images of the BWO films deposited at different substrate temperatures are depicted in Fig. 4.6. It is interesting to note that even the films deposited at ambient temperature show significant features. The average grain size of the films increases with a rise in substrate temperature and the film deposited at 800 °C exhibit abnormal grain growth. The average grain sizes of the films found to be 326, 361, 453, 536 and 784 nm for the films deposited at room temperature (RT), 200, 400, 600 and 800 °C, respectively. Further, it is significant to note that the average particle size of the films is higher as compared to the thickness of the films and this can be explained on the basis of Avrami type nucleation and growth. The thermal energy available on the surface of the substrate facilitates the particles to be nucleated continuously throughout the film with the termination caused by the impingement of neighbouring particles growing at a steady rate [14, 16].

4.3.2.2 Optical properties

The spectral transmittance spectra of nanostructured BWO thin films deposited at different substrate temperatures along with their photographs are shown in Fig. 4.7 (a). The transparency of BWO film, deposited at room temperature is about 90%. As the deposition temperature increases, the transparency of film decreases. Films deposited at 600 °C are in full deep - blue color and the transmittance of the film reduced to 20% and can be attributed to the release of oxygen vacancies during the deposition process [22, 23]. With a further increment in substrate temperature up to 800 °C, the transmittance of the film regains to 70%; this shows the evidence of thermochromic nature in BWO films. In addition, there are two regions, where a transparent oscillating region and a region of strong absorption. All the transmission spectra of BWO films above 420 nm exhibits peaks and valleys that are associated with the reflections from the incident light from the air - film, and film - substrate tends to interference effects. The strong absorption observed below 400 nm and the absorption edges of the films exhibited a red shift, which shows the effect of crystallinity in the deposited films. Temperature dependence of refractive index and packing density of the films are shown in Fig. 4.7 (b). It is observed that both the refractive index and packing density of the films follow the similar trend as a function of temperature that shows the dependence of refractive index on packing density of the films. Further, the refractive indices of the films are higher for the films deposited in the temperature range of 400 to 600 °C, this may be due to the appearance of mixed phases. Films deposited below 400 °C, show lower refractive indices, which are attributed to the smaller packing densities and low adatom mobilities of the films. The obtained refractive index values are in the range of 1.76 - 2.1 @ 600 nm and are comparable with the reported values [24, 25].

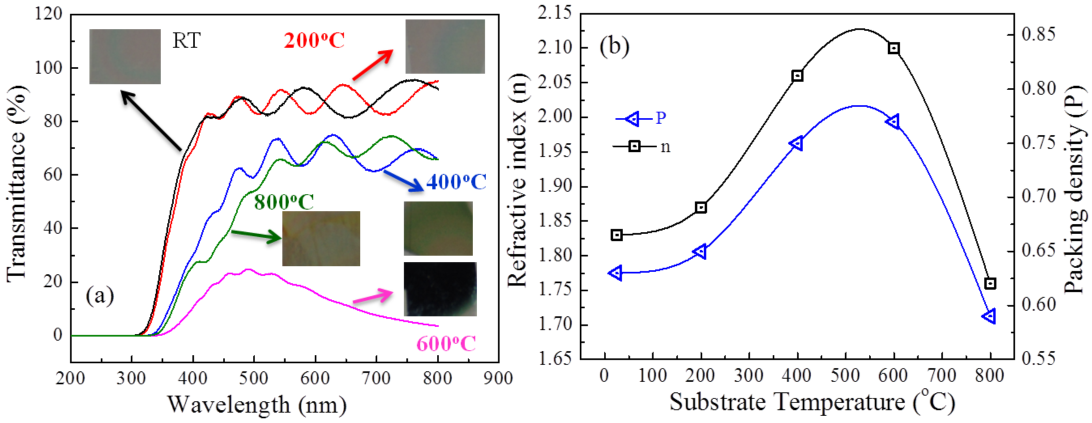

Fig. 4.7: *(a) Optical transmittance spectra and its corresponding photographs of the BWO thin films deposited at different substrate temperatures, (b) Refractive index and packing density as a function of substrate temperature.*

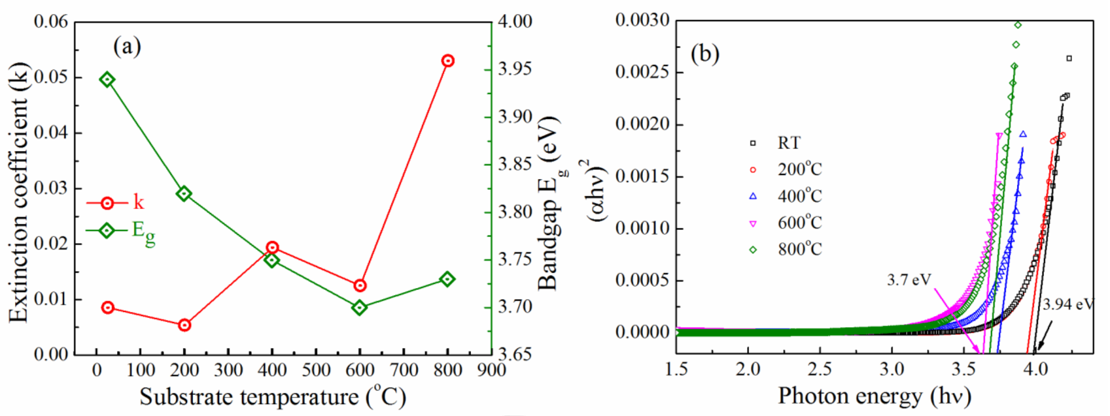

***Fig. 4.8:** (a) Extinction coefficient and optical bandgap as a function of substrate temperature (b) A plot of* $(\alpha h\upsilon)^2$ *versus* $h\upsilon$ *for the BWO thin films deposited at different substrate temperatures.*

The variation in extinction coefficient and optical bandgap as a function of deposition temperature is depicted in Fig. 4.8 (a). The extinction coefficient of the films increases progressively with a rise in deposition temperature. The enhancement in crystallinity, packing density and average grain size of the deposited films causes more scattering of incident light as a result the extinction coefficient increases. The optical absorption edge of the films deposited at different substrate temperatures are shown in Fig. 4.8 (b). The optical bandgap of the films decreases linearly with a rise in deposition temperature upto 600 °C and increases slightly thereafter. The decrease in optical bandgap and simultaneous increase in the extinction coefficient is attributed to the occurrence of thermochromism in BWO films. The slight increase in bandgap above 600 °C is attributed to the phase pure BWO, because WO_3 has the lower optical bandgap as compared with BWO [15, 26]. The obtained optical bandgaps of BWO films deposited under different substrate temperatures are in the range of 3.7 to 3.94 *eV*.

Further, to see the effect of OMP on the optical bandgap, BWO films are deposited under different OMP (25, 50, 75 & 100%) at 600 °C and their transmittance spectra’s and absorption edges are shown in Fig. 4.9 (a) and 4.9 (b), respectively. It is clearly seen that the films show higher transmittance and larger bandgap values. Also, with increase in OMP, the optical bandgap of films enhanced significantly from 3.6 to 4.5 *eV*.

The variations in the optical bandgap values can be attributed to the presence of oxygen vacancies. Further, to quantify the presence of oxygen vacancies, the change in optical density (ΔOD) is calculated and this is proportional to the amount of created colour centres. ΔOD is calculated using the following expression

$$\Delta OD = \log_{10}(T_b / T_c) \qquad (2)$$

Where, T_b and T_c are transmittances before and after coloration, respectively [27]. The change in ΔOD as a function of wavelength is shown in Fig. 4.10 (a). It is observed that ΔOD decreases with a rise in temperature, which shows the improvement in colour centres. Further, the variations of ΔOD as a function of substrate temperature measured at different wavelength are shown in Fig. 4.10 (b). It is observed that the change in ΔOD decreases both with increase in substrate temperature and the wavelength.

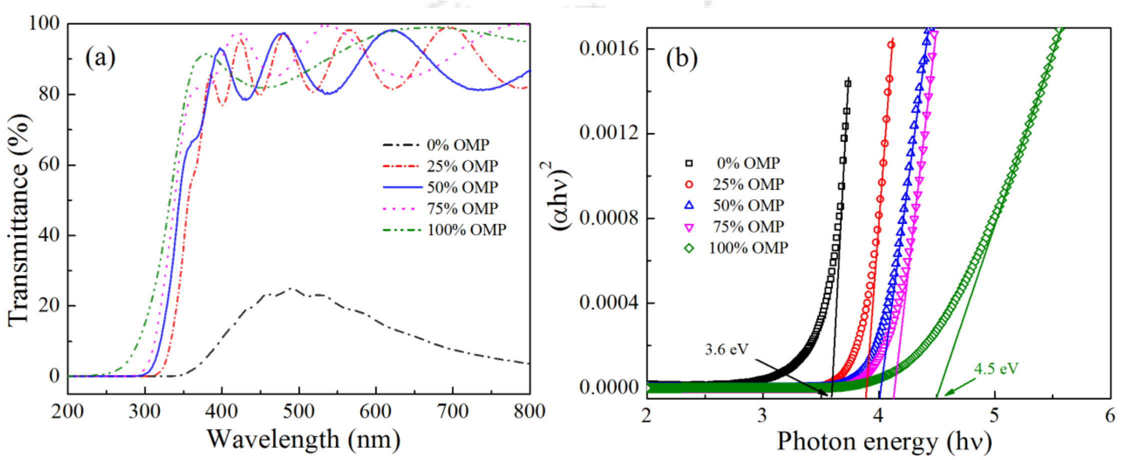

Fig. 4.9: *(a) Optical transmittance spectra and (b) A plot of* $(\alpha h\upsilon)^2$ *versus* hυ *of BWO thin films deposited at different OMP at 600* ^{o}*C substrate temperature.*

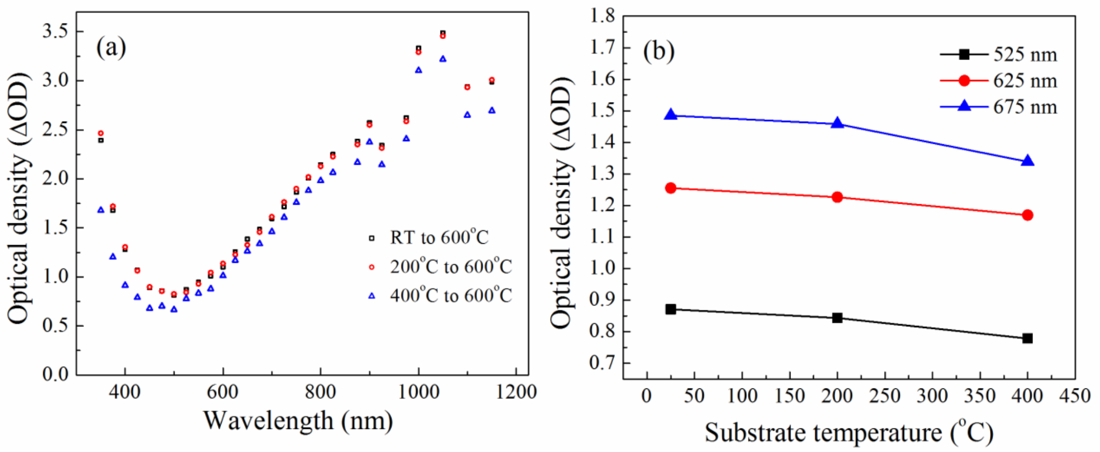

Fig. 4.10: *(a) The change in optical density as a function of wavelength and (b) Variation in optical density as a function of substrate temperature at different wavelengths.*

The reduction in transmittance with increasing deposition temperature can be described as follows: the higher deposition temperature intensifies the kinetic energy of the adatoms and surface mobility, which results in larger grain sizes and better crystallinity, and is evident from FESEM images (Fig. 4.6). The enhanced grain size scatters the light, which results lower transmittances. Further, to understand the variations in transmittance, we have measured the resistances of the deposited films and are in the range of 0.9 to 5.2 GΩ. We found that the resistance of the films decreases with an increase in deposition temperature and showed a lowest value at 600 °C, this shows the variations in the transmittances can be attributed to the oxygen vacancies, which complements the BWO films deposited at different OMP (See Fig. 4.9 (a) and 4.9 (b)). It is well known that the optical bandgap of oxide films depends on oxygen partial pressure / vacancies, and it is an indirect estimation of stoichiometry. As the oxygen mixing percentage increases in the deposition chamber, the films will grow in stoichiometric state as a result the optical bandgap of the film enhances, and the obtained optical bandgap values are slightly lower than the values for the BWO nanopowders prepared in sucrose - template method [28]. Also, these calculated bandgap values are comparable with BWO nanoparticles ($E_g \sim 4.1\ eV$) prepared by the modified combustion process [24].

From the above observations, it can be infer that the absorption edges of the films shifts towards lower energy side with an increase in deposition temperature, which is attributed to the improvement in crystallinity and coloring effect. At 600 °C, the shift in absorption edge towards lower energies may be due to the increase of energy for the charge transfer from oxygen to tungsten. As a result, the density of states at the top of the band decreases, whereas the density of states at the conduction band increases [29]. The similar response was observed for the WO_3 films and it is well known that the themochromic response in these films achieved by vacuum heating while bleaching is obtained after annealing in air [30]. For BWO films deposited at 600 °C, W^{6+} prefers lower oxidation states due to the release of oxygen as a result it deviates from the stoichiometric state [31]. The observed variations in the optical bandgap can be attributed to a small polaron transition between W^{6+} and W^{5+} or W^{5+} and W^{4+}. This inert valence can be described by the following expressions [32, 33]

$$h\nu + W^{5+}(A) + W^{6+}(B) \rightarrow W^{6+}(A) + W^{5+}(B) \quad …….. \qquad (3)$$

$$h\nu + W^{5+}(A) + W^{4+}(B) \rightarrow W^{5+}(B) + W^{4+}(A) \quad …….. \qquad (4)$$

Furthermore, the presences of created colour centres are quantified by calculating the change in ΔOD that estimates the presence of oxygen vacancies in the deposited films. Various mechanisms were proposed to explain the thermochromic response in various materials [34 - 36]. But, in the present study, the achieved irreversible thermochromic behaviour in BWO films is attributed mainly to the oxygen vacancies.

4.3.2.3 Raman analysis on BWO films

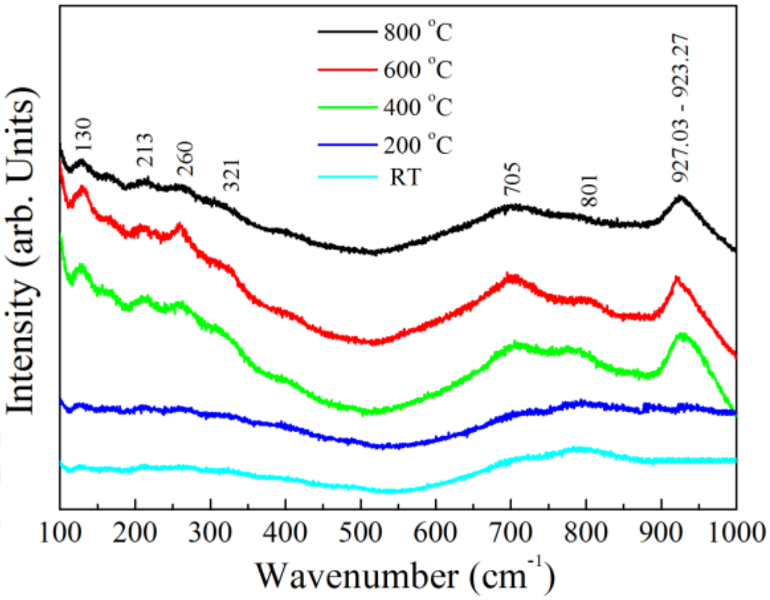

Fig. 4.11: *Raman spectra of BWO thin films deposited on amorphous SiO_2 substrates, at various substrate temperatures.*

Further to quantify the presence of oxygen vacancies in the BWO films, Raman spectra for the films deposited at different substrate temperatures are obtained and displayed in Fig. 4.11. The identified internal (927.03 - 923.27, 705, 213 cm^{-1}) and external (130 cm^{-1}) modes for the BWO films deposited at 400 °C, 600 °C and 800 °C are in consistent with the earlier reports [6, 14]. The obtained vibrational modes in Raman spectra of BWO films can be divided into two groups, internal and external. The internal vibrations correspond to the oscillations inside the $[WO_4]^{-2}$ molecular group with an immovable mass center. The external or lattice phonons correspond to the motion of the Ba^{2+} cation and the rigid molecular unit [37]. Raman spectra of the BWO films deposited at RT, and 200 °C revealed amorphous nature. Fig. 4.11 demonstrates all the vibrational modes corresponding to the BWO films deposited at ≥ 400 °C. Further, three modes connected to WO_3 are observed at 260 cm^{-1}, 321 cm^{-1} and 801 cm^{-1}. The modes appeared in the low-frequency region (260 cm^{-1}, 321 cm^{-1}) are due to the bending vibration of δ (W^{6+} - O), and the mode presented at the high – frequency (801 cm^{-1}) region can be assigned to the stretching vibration of ν (W^{6+} - O) [38 - 40]. The intensities of the vibrational modes related to WO_3 increased with a rise in deposition temperature from 400 °C - 600 °C and diminish at 800 °C, which indicates the formation of pure BWO phase. Furthermore, the full width at half maxima of the peak improves with an increase in deposition temperature. It is also interesting to note that as the deposited temperature increases from 400 °C to 800 °C, the prominent internal mode appeared at 927.03 cm^{-1} is shifted to 923.27 cm^{-1} that demonstrate the formation of pure BWO phase, and these effects complemented the results obtained by XRD. This internal mode shift from 927.03 cm^{-1} to 923.27 cm^{-1} arises due to the formation of more tungsten ion concentration as compared to oxygen, which represents larger oxygen vacancies [41].

Further, BWO exhibited pure phase for the films deposited at 800 °C, and it is significant to note that even pure BWO films also exhibited the irreversible thermochromic nature, and it changes its colour from transparent to pale yellow after a cycle from RT to 800 °C. For this purpose, a study of the temperature dependence of transmittance of this film's gains importance, which is the subject of matter for the future study.

4.3.3 Dielectric and Electrical Properties of $BaWO_4$ (BWO) Film Capacitors

4.3.3.1 Structural and morphological studies

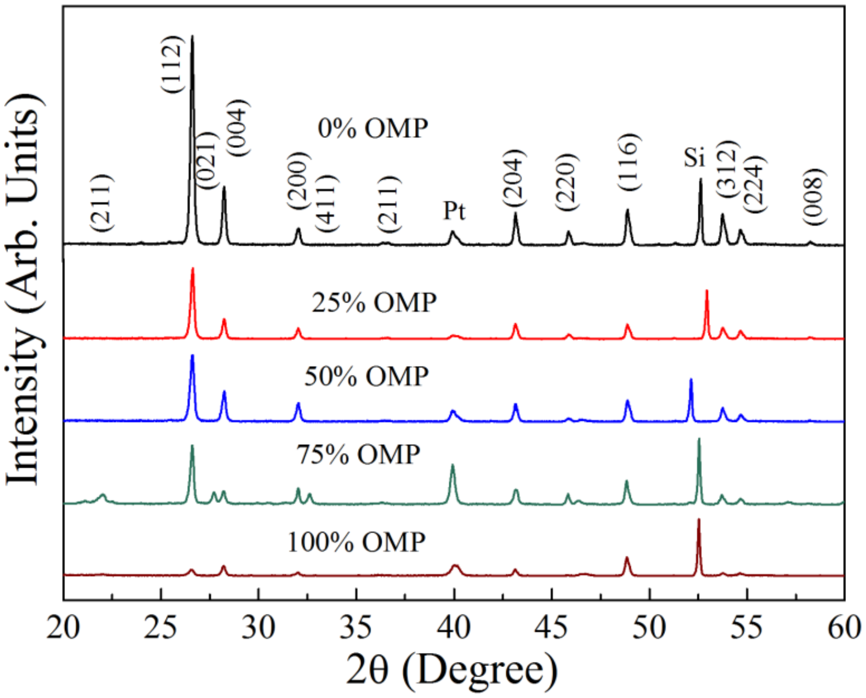

Fig. 4.12: *XRD patterns of $BaWO_4$ thin films deposited on platinized silicon substrates at different OMP, annealed at 700 °C for 3 h.*

Since, the as deposited BWO thin film on platinized substrates under various OMP depicts an amorphous nature. However, post annealing at 700 °C for 3 *h* in air, all the films are crystallined in tetragonal crystal structure and the XRD patterns of the BWO films deposited onto platinized silicon substrates are shown in Fig. 4.12.

The crystalline films are only produced when the atoms, ions, or molecules have an opportunity to organize themselves into regular arrangements, or lattices. It is interesting to note that oxide BWO films were obtained even in the pure oxygen atmosphere without any secondary phases. It is found that the intensity of peaks decreased and full width at half maxima (FWHM) increases with OMP. The average crystallite sizes of the films were extracted using the Scherer's formula and were found to be decreased by with the addition of OMP. The average crystallite sizes were in the range of 40 - 29 nm as OMP increases from 0 to 100% OMP in sputtering gas.

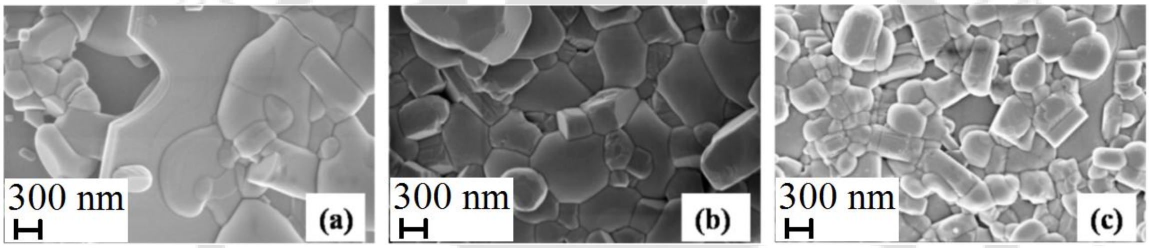

Fig. 4.13: *FESEM images of BWO thin films deposited on platinized silicon substrates deposited at (a) 0% (b) 50% and (c) 100% OMP, annealed at 700 °C for 3 h.*

FESEM images of the as-deposited films did not show any significant features, whereas the annealed films show an important difference in morphologies with OMP and are shown in Fig. 4.13. The surface morphology of the films reveals that all the films showed nanogranular grains distributed uniformly on the film surface with an average grain size of 300 - 800 nm. Non-uniform and larger grain sizes of BWO were observed for films deposited at 0% OMP (pure Ar atmosphere). Generally, films deposited under pure Ar, expected to have a rapid grain growth due to high deposition rates, because of higher momentum transfer obtained for heavier atoms (Ar atoms) as compared to lighter atoms like oxygen [42]. Furthermore, the surface resistivity of atoms is higher for 0% OMP deposition conditions. As the OMP increases to 50%, BWO film exhibits and well packed, denser and uniform grains. Further, with an increase in OMP, films showing a smaller grains and porosity are seen in the sample.

4.3.3.2 Raman studies on $BaWO_4$ thin films

The Raman spectra were recorded for all the annealed samples, with a Ar^+ laser with a excitation at 514.5 nm source at room temperature. The primitive cell of the $BaWO_4$ crystal includes two formula units. The molecular ionic group of $[WO_4]^{-2}$ with strong covalent bonds W - O is the distinctive feature of the scheelite phase. Due to weak coupling between the ionic group and the Ba^{2+} cation, the vibrational modes in Raman spectra of $BaWO_4$ can be divided into two groups, internal and external. The internal vibrations correspond to the oscillations inside the $[WO_4]^{-2}$ molecular group with an immovable mass center. The external or lattice phonons correspond to the motion of the Ba^{2+} cation and the rigid molecular unit [37].

The group theory calculation presents 26 different vibrations, which are represented by equation [37, 43].

$$\Gamma = 3A_g+5A_u+5B_g+3B_u+5E_g+5E_u \tag{5}$$

Where, Raman active vibrational modes are A_g, B_g and E_g in which A_g, B_g modes are non-degenerate, E_g modes are doubly degenerate.

Fig. 4.14 (a) shows the Raman spectrum of $BaWO_4$ films deposited at different OMP. All the observed modes are in concert with Raman vibrations of scheelite tetragonal and are in agreement with the earlier reports [6, 14]. The internal modes $\nu_1(A_g)$, $\nu_2(E_g)$, $\nu_3(E_g)$ and $\nu_4(B_g)$ were observed at 927, 808, 716, 328, 274, 224 cm^{-1}. The free rotation mode $\nu_{f.r}$ = 185 cm^{-1} and external mode ν_{ext} = 136 cm^{-1}. The local symmetry in $BaWO_4$ thin films are different from the earlier reports, which may vary with preparation technique and the Raman spectrum is also sensitive to the oxygen non-stoichiometry [44].

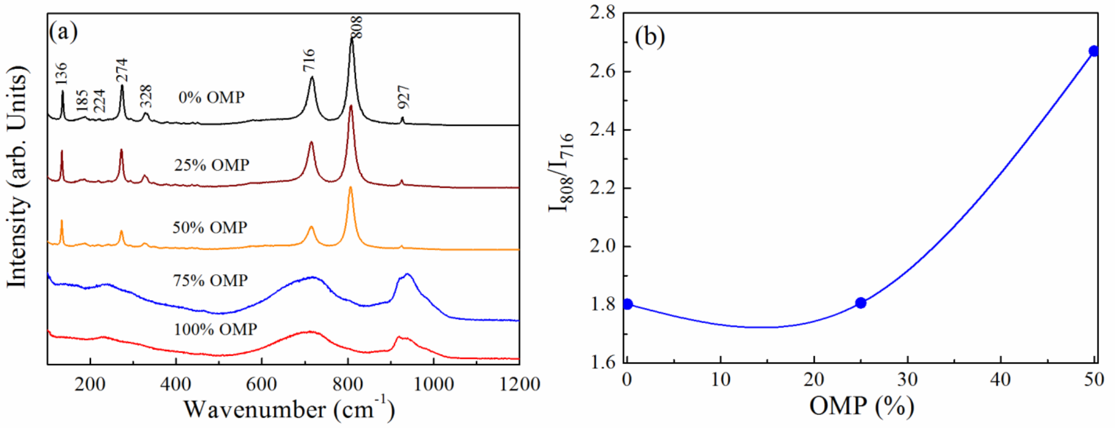

Fig. 4.14: *(a) Raman spectra of $BaWO_4$ thin films deposited on Pt-Si substrates at different OMP. The numbers above the peaks is the raman shifts in cm^{-1}. (b) Dependence of Raman band intensity ratio I_{808}/I_{716} as a function of OMP.*

BWO films deposited upto 50% OMP exhibited all Raman vibrational modes. Further, with an increase in OMP, the films displayed lesser vibrational modes. In addition, the intensity of 808 cm^{-1} mode decreases slightly upto 50% OMP and disappears completely above this, and it may happen due to the rigidity of $[WO_4]^{-2}$ in $BaWO_4$ films affected by OMP. Fig. 4.14 (b) depicts the dependence of Raman band intensity ratio I_{808}/I_{716} as a function of OMP and it shows that the intensity ratio I_{808}/I_{716} depends upon the oxygen partial pressure, and it was non-linear. This trend suggests that this ratio is sensitive to changes in the most frequent type of defects occurring in the $BaWO_4$ films with an increase in OMP.

4.3.3.3 Dielectric properties

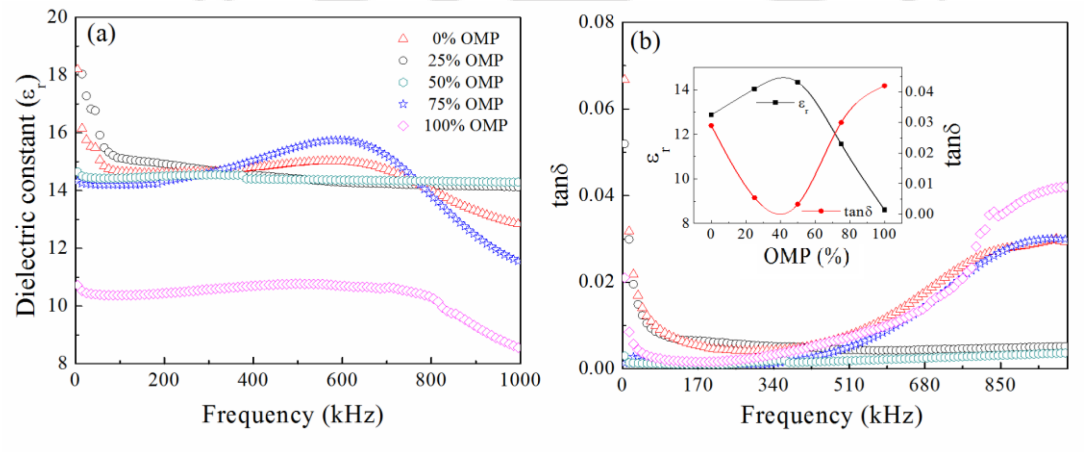

Fig. 4.15: *Variation in (a) dielectric constant, (b) loss tangent of $BaWO_4$ thin films deposited at different OMP as a function of frequency. Inset (b) Dielectric constant and loss tangent as a function of OMP.*

The frequency dependence of dielectric constant (ε_r) and loss tangent (*tanδ*) of BWO films deposited under different OMPs are shown in Fig. 4.15 (a, b), respectively. The ε_r showed a frequency dispersion with frequency in the range 5 to 95 kHz and above that it decreases linearly, which is a characteristic behaviour of linear dielectric. The dispersion in ε_r with frequency can be explained on the basis of Maxwell polarization theory and Koop's two layer model [45]. The obtained ε_r and *tanδ* values are in the range of 10.5 - 15 and 0.01 - 0.001, respectively for the films deposited at different OMPs. It is well known that strain in the films plays a vital role in determining its dielectric properties because the strain in the BWO films arises due to the lattice miss match with the bottom electrode (Pt) and may be due to the deposition parameters such as OMP and substrate temperature etc. We also observed that dielectric relaxation in the vicinity of

645 kHz for film with deposited at 75% OMP, and is may be due to the production of space charges and oxygen vacancies in the grain boundaries or may be caused due to delay in molecular polarization with respect to a changing electric field in a dielectric medium.

The variations in ε_r and *tanδ* as a function of OMP is shown in inset of Fig. 4.15 (b) and it found that ε_r and *tanδ* progressively improved upto 50% OMP decreases thereafter. The improvements in the dielectric properties are attributed to the uniform grain growth (See Fig. 4.13 (b)) and reduction in oxygen vacancies. When films deposited under 0% OMP, there may be some oxygen vacancies, which can be reduced with increase in oxygen concentration. Further rise in OMP beyond 50%, surface poisoning of target may cause lower deposition rates and smaller grain size that may significantly decrease the dielectric response of the BWO films.

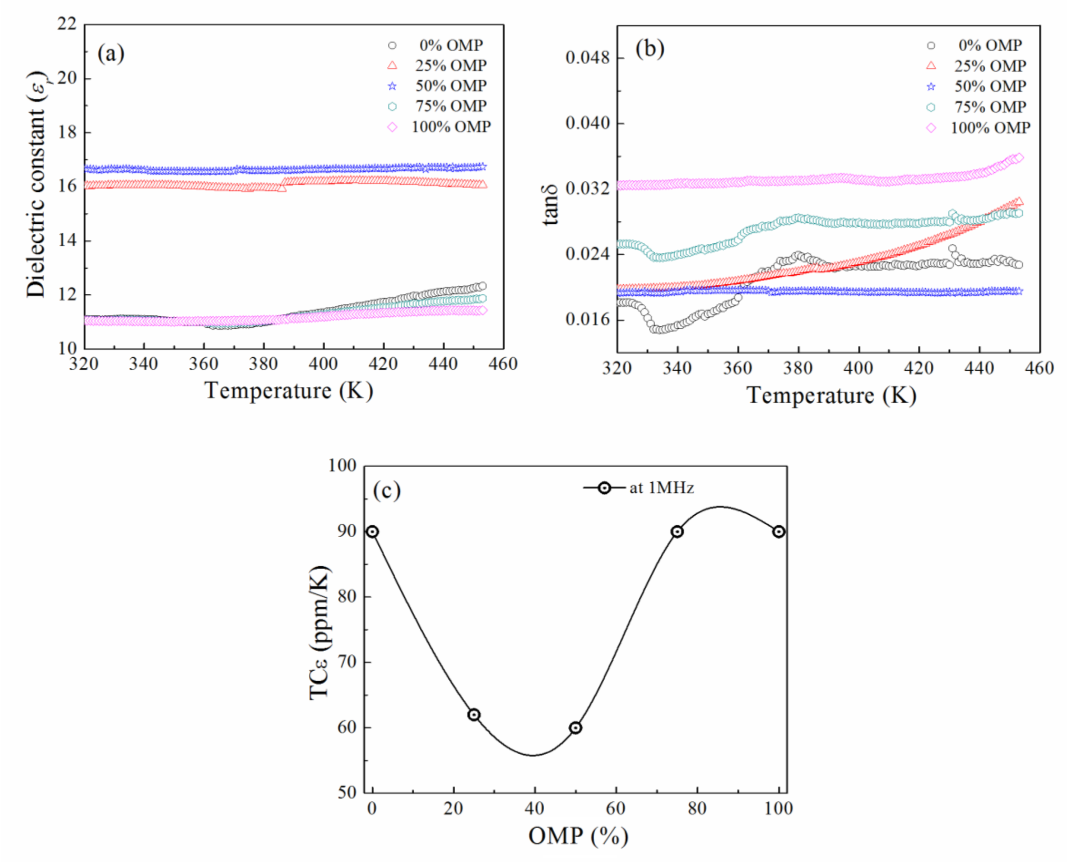

Fig. 4.16: *Variation in (a) dielectric constant (b) loss tangent of BWO thin films deposited at different OMP as a function of temperature and (c) Plot of TCε versus different OMP measured at 1MHz.*

The temperature-dependent dielectric constants and *tanδ* of BWO films fabricated with different OMPs are shown in Fig. 4.16 (a) and 4.16 (b), respectively. Both the dielectric constant and *tanδ* increases with temperature. The improvement in dielectric constant with temperature is due to an increase of total polarization arising from dipoles and trapped charge carriers [46]. However, the thermal energy alleviates dipoles to align along the field direction that contributes to the dielectric constant of the films. The best dielectric properties of ε_r = 16.6 and *tanδ* = 0.019 @ 1 MHz observed for film deposited at 50% OMP. On the other hand, with an increase in temperature the vibrations of atoms, molecules or maybe introduction of interstitial oxygen ions can occur which enhances the dielectric loss.

The microwave dielectric properties of as - deposited and annealed BWO thin films were measured at 5, 10 and 15 GHz using a split post dielectric resonator (SPDR) method are tabulated in **Table 4.2** and **Table 4.3**, respectively. In both the cases, it is found that the dielectric properties show profound frequency dispersion. Furthermore, the annealed films (deposited in pure oxygen plasma) showed better enhancement in the dielectric properties as compared to as-deposited films, which are assigned to the improvement in the grain sizes and crystallinity.

Table 4.2: *Microwave dielectric properties of as-deposited BWO thin films on quartz substrates measured by using split post dielectric resonator method.*

As-Deposition						
	At 5 GHz		At 10 GHz		At 15 GHz	
OMP (%)	ε_r	*tanδ*	ε_r	*tanδ*	ε_r	*tanδ*
0	12.42	0.056	10.16	0.067	8.54	0.073
50	13.41	0.047	11.76	0.048	8.95	0.065
100	14.51	0.035	12.36	0.040	9.76	0.057

Table 4.3: *Microwave dielectric properties of annealed BWO thin films on quartz substrates measured by using split post dielectric resonator method.*

After Annealing						
	At 5 GHz		At 10 GHz		At 15 GHz	
OMP (%)	ε_r	*tanδ*	ε_r	*tanδ*	ε_r	*tanδ*
0	16.35	0.015	14.91	0.027	11.94	0.030
50	17.52	0.012	15.58	0.024	12.67	0.026
100	18.16	0.010	16.53	0.020	13.48	0.023

The temperature stability of the BWO films is evaluated by calculating the temperature coefficient of dielectric constant ($TC\varepsilon$). $TC\varepsilon$ is obtained by using the following expression

$$TC\varepsilon = \frac{\Delta\varepsilon_r}{\varepsilon_0 \Delta T}(ppm/^{o}C) \tag{6}$$

Where, $\Delta\varepsilon_r$ is the change in ε_r with respect to the value ε_0 (T = 320 K) and ΔT is the change in temperature relative to 320 K. The variation in $TC\varepsilon$ as a function of OMP is shown in Fig. 4.16 (c). It is observed that all BWO films revealed a positive $TC\varepsilon$ values. It is evident that as the OMP rises from 0 to 50% OMP, the $TC\varepsilon$ of BWO films decreases linearly and increases beyond. BWO film deposited at 50% OMP exhibits better temperature stability (60 ppm/K) [47].

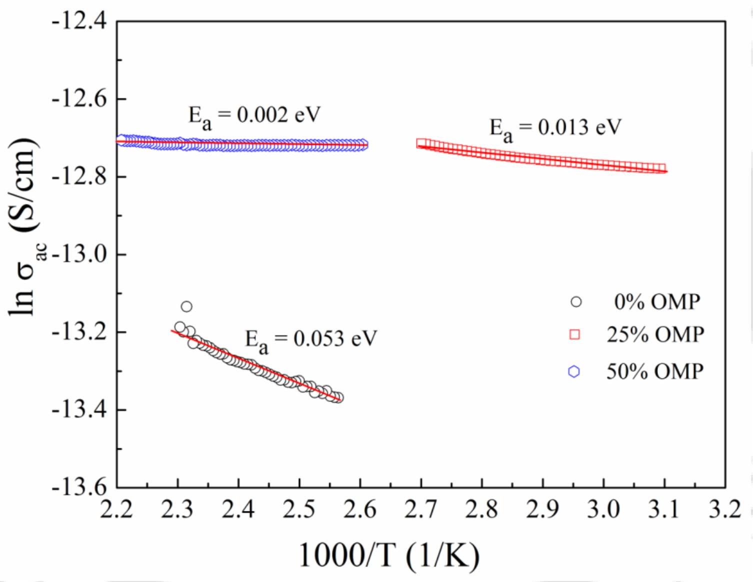

Fig. 4.17: *Variation of σ (ac) versus 1000/T.*

Fig. 4.17 shows the variation of AC conductivity (σ_{ac}) versus *1000/T* of BWO films deposited at different OMP, measured at 1 MHz follows an Arrhenius relation and is given by

$$\sigma_{ac} = \sigma_0 exp^{(-E_a/k_B T)} \tag{7}$$

Where, σ_0 is pre - exponential factor, E_a is the activation energy, K_B is the Boltzmann constant and T is the absolute temperature. From above equation (7), the activation energy has been calculated for all the BWO films. It is significant to note that the activation energy tends to decrease with the increase in OMP and gradually reaches a very low value. The extracted energies are found to be E_a = 0.053, 0.013 and 0.002 *eV* for the films deposited at 0%, 25% and 50% OMP, respectively.

4.3.3.4 Electrical properties of $BaWO_4$ film capacitors

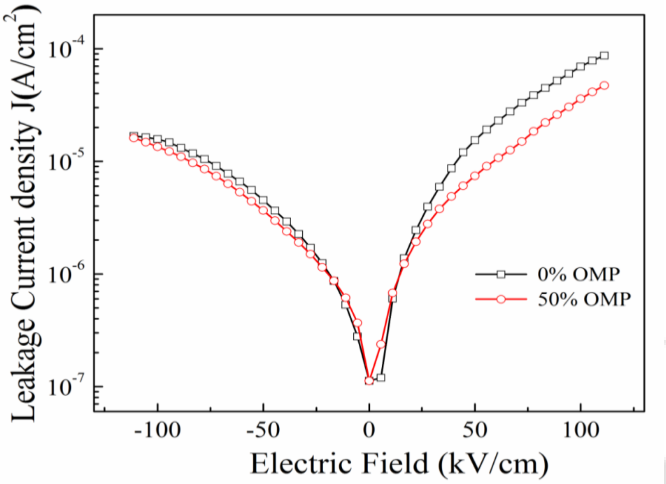

Fig. 4.18: *Room temperature leakage current densities of $BaWO_4$ films measured at different applied electric fields.*

Fig. 4.18 shows the leakage current density as a function of applied voltage for the BWO films deposited at different OMP. The leakage currents were measured with a voltage step of 1 Volt and step duration of 10 sec. The average leakage current density is less than 10^{-5} A/cm^2 at an applied electric field of 50 kV/cm. The leakage current density increases with applying electric field and decreases with OMP, and this may be due to the structured grain boundaries and crystal defects. The J - E characteristics of the BWO films showed a combined response of grain, grain boundaries and film - electrode interfaces. The asymmetric J - E curves may be associated with the different interfacial layer indentation between the bottom electrodes - film and film - top electrode interfaces.

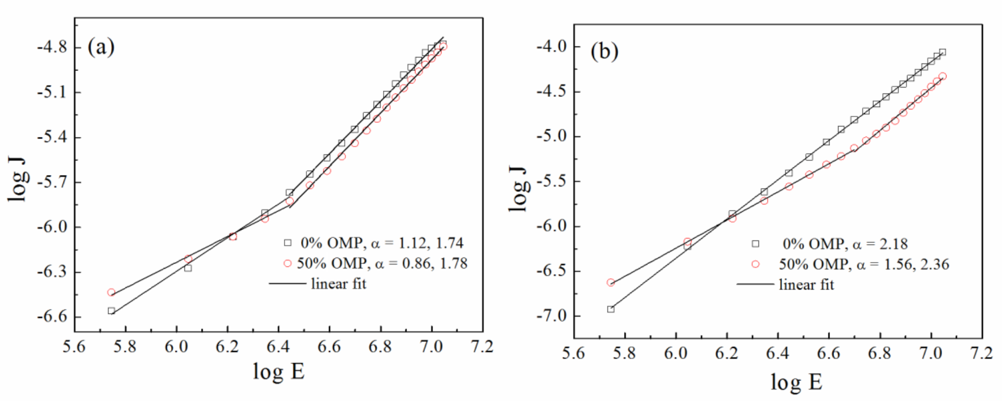

Fig. 4.19: *log J as a function of log E under (a) negative electric field (b) positive electric field.*

Fig. 4.19 shows the logarithmic dependence of current density as a function of logarithmic electric field for BWO thin films. Here, the conduction behaviour of BWO films with different OMP is described on the basis of Ohmic and space charge-limited current (SCLC) model [48, 49]. In the negative electric field region; the BWO films exhibit both the Ohmic conduction ($J \sim E^{\alpha} : \alpha \sim 1$) behaviour and SCLC ($J \sim E^{\alpha} : \alpha \gg 1$) nature. The obtained α values are found to be 1.12, 1.74 and 0.86, 1.78 for 0, 50% OMP, respectively. On the other hand, in the positive electric field region, BWO films exhibit SCLC ($J \sim E^{\alpha} : \alpha \gg 1$) behaviour. The extracted α values are 2.18 and 1.56, 2.36 for 0, 50% OMP, correspondingly.

4.4 Conclusions

For the first time, BWO ceramics were synthesized by mechanical alloying method. Parent oxides milled for 50 *h* showed the formation of BWO and WO_3 phases. However, WO_3 phase could not be eliminated during the milling process. The mechanical alloying method reduced the sintering temperature of BWO ceramics along with the significant improvement in the density and microstructure. Effects of sintering temperature on the microwave dielectric properties of the BWO ceramics were investigated. The broadband dielectric properties of BWO ceramics show a stable response from 1 MHz to 25 MHz in the temperature range of -140 °C to 180 °C. The obtained dielectric properties at microwave frequencies are $\varepsilon_r = 16.3$, $Q \times f_0 = 38.05$ THz, at 11.6 GHz are attributed to the maximum density and uniform grain size. The obtained properties of BWO ceramics are suitable for various microwave communication applications.

Irreversible thermochromic response in RF sputtered nanocrystalline BWO films observed for the first time. The impact of deposition temperature on structural, microstructural and optical properties of BWO films were studied systematically.

- The optical bandgap of the BWO films deposited at different temperatures in 0% OMP (i.e., pure argon plasma), are in the range of 3.7 to 3.94 *eV* whereas the films deposited at 600 °C under distinct OMP are in the range of 3.6 - 4.5 *eV*.
- The observed thermochromic behavior in BWO films was attributed to the presence of oxygen vacancies due to electrons trapped at oxygen vacancies causing an inter valence charge transfer of W^{5+} to W^{6+} in coloured BWO and is confirmed through the change in ΔOD.
- The Raman spectra of BWO films deposited at 800 °C exhibit pure BWO vibrational modes and this study compliments the obtained XRD results.

- The obtained response of BWO films was suitable for decorative and smart window applications.

BWO thin films deposited on the platinized silicon substrates also.

- As deposited thin films were amorphous in nature and after annealing at 700 °C films were crystallined.
- Surface morphology and Raman vibrational modes showed a significant dependence on OMP.
- The measured dielectric properties showed a progressive improvement with OMP up to 50% and decreases thereafter. The best dielectric properties of ε_r =15 and $tan\delta$ = 0.019 @ 1 MHz observed for film deposited at 50% OMP.
- The microwave dielectric properties were measured with split post dielectric resonator method at discrete frequencies (5, 10 and 15 GHz).
- The average leakage current density is less than 10^{-5} A/cm^2 at an applied electric field of 50 kV/cm.
- The J-E characteristics of the BWO films show a combined response of grain, grain boundaries and film-electrode interfaces.
- The leakage current studies revealed Ohmic and space charge limited current behaviour during the negative cycle whereas space charge limited current during a positive cycle.

4.5 References

[1] Z. Zhang, H. Su, X. Tang, H. Zhang, T. Zhou, Y. Jing, *Ceram. Int.* **40** (2014) 1613.

[2] M. Nikl, P. Bohacek, P. Fabeni, M. Kobayashi, *J. Appl. Phys.* **91** (2002) 5041.

[3] M. Nikl, P. Bohacek, V. Babin, S. Zazubovich, M. Bacci, *J. Lum.* **87** (2000) 1136.

[4] M. Kobayashi, H. Yahagi, *Nucl. Instrum. Methods Phys. Res. A.* **333** (1993) 429.

[5] H. Feng, Y. Yang, X. Wang, *Ceram. Int.* **40** (2014) 10115.

[6] F. M. Pontes, E. R. Leite, *J. Eur. Ceram. Soc.* **23** (2003) 3001.

[7] S. H. Yoon, D. W. Kim, S. Y. Cho, K. S. Hong, *J. Eur.Ceram. Soc.* **26** (2006) 2051.

[8] Y. Zhang, N. A. W. Holzwarth, R. T. Williams, *Phys. Rev. B* **57** (1998) 12738.

[9] M. M. Krzmanc, M. Logar, *J. Am. Ceram. Soc.* **94** (2011) 2464.

[10] J. L. Solano, R. S. Kumar, G. Aquilanti, *Phys. Stat. Sol. B* **244** (2007) 325.

[11] A. L. Tiano, C. Koenigsmann, *Chemical Communications* **46** (2010) 8093.

[12] T. Kinoshita, M. Senna, Y. Doshida, H. Kishi, *Ceram. Int.* **38** (2012) 1897.

[13] A. Paulraj, P. Natarajan, J. Duraisamy, *J. Am. Ceram. Soc.* **94** (2011) 1627.

[14] R. Dinesh, T. Fujiwara, T. Watanabe, *J. Mater. Sci.* **41** (2005)1541.

[15] F. M. Pontes, M. A. Maurera, R. Magnani, *J. Eur. Ceram. Soc.* **23** (2003) 3001.

[16] R. Dinesh, T. Fujiwara, M. Yoshimura, *Solid State Sciences* **8** (2006)1074.

[17] W. S. Cho, M. Yoshimura, *J. Am. Ceram. Soc.* **80** (1997) 2199.

[18] G. A. Samara, *J. Appl. Phys.* **68** (1990) 4214.

[19] L. Liu, M. Flores, N. Newman, *PRL* **109** (2012) 257601.

[20] D. Pamu, K. Sudheendran, K. C. J. Raju, Anil K. Bhatnagar, *Vacuum* **81** (2007) 686.

[21] T. Asanuma, T. Matsutani, *J. Appl. Phys.* **95** (2004) 6011.

[22] F. Wang, C. Di Valentin, G. Pacchioni, *Phys. Rev. B* **84** (2011) 073103.

[23] M. B. Johansson, G. A. Niklasson, L. Osterlund, *J. Mater. Res.* **27** (2012) 3130.

[24] S. Vidya, J. K. Thomas, *Advances in Condensed Matter Physics* 409620 (2013).

[25] L. S. Cavalcante, J. C. Sczancoski, E. Longo, *J Alloy Compd.* **474** (2009) 195.

[26] M. C. Rao, O. M. Hussain, *Res. J. Chem. Sci.* **1** (2011) 76.

[27] M. A. Quevedo-Lopez, R. F. Reidya, R. A. Orozco-Terana, *Journal of Physics and Chemistry of Solids* **61** (2000) 727.

[28] S. M. M. Zawawi, R. Yahya, H. N. M. Ekramul Mahmud, M. N. Daud, *Chemistry Central Journal* **7** (2013) 80.

[29] J. J. Kleperis, P. D. Cikmach, A. R. Lusis, *Phys. Stat. Sol. (a)* **83** (1984) 291.

[30] S. N. Alamri, *Smart Mater. Struct.* **18** (2009) 025010.

[31] A. Siokou, G. Leftheriotis, P. Yianoulis, *Surface Science* **482** (2001) 294.

[32] S. H Lee, M. J. Seong, E. C. Tracy, S. K. Deb, *Solid State Ionics* **156** (2003) 447.

[33] J. G. Zhang, D. K. Benson, A. W. Czanderna, *J. Elecrochem. Soc.* **144** (1997) 2022.

[34] C. G. Granqvist, “Handbook of inorganic electrochromic materials, Amsterdam, Elsevier,” 1995.

[35] H. N. Cui, V. Teixeira, J. Y. Gao, E. Fortunato, *Thin Solid Films* **516** (2008) 1484.

[36] M. Nazemiyan, and Y. S. Jalili, *AIP Advances* **3** (2013) 112103.

[37] T.T. Basiev, A.A. Sobol, Yu.K. Voronko, P.G. Zverev, *Opt. Mater.* **15** (2000) 205.

[38] C. V. Ramana, S. Utsunomiya, U. Becker, *J. phys. Chem. B* **110** (2006) 10430.

[39] A. Rougier, F. Portemer, M. E. Marssi, *Applied Surface Science* **153** (1999) 1.

[40] N. E. Stankova, R. W. Eason, *Applied Surface Science* **247** (2005) 401.

[41] J. E. Flores-Mena, J. A. Balderas-Lopez, *Revista Mexicana de Fisica* **58** (2012) 504.

[42] D. R. James, Optical Thin Films, SPIE, Washington (1987).

[43] S. Desgreniizrs, S. Jandl, C. Carlon, *J. phys. Chem. Solids* **45** (1984) 1105.

[44] J. R. Ferraro, K. Nakamoto, C. W. Brown, Introductory raman spectroscopy second edition, Elsevier, (2003).

[45] J. C. Maxwell, Electricity and Magnetism, Vol 1, Oxford University Press, Oxford, 1929.

[46] T. Tunc, I. Uslu, S. Altindal, *International Journal of Polymeric Materials* **59** (2010) 739.

[47] T. Santhosh Kumar, P. Gogoi, S. Thota, D. Pamu, *AIP Advances* **4** (2014) 067142.

[48] J. Wu, J. Wang, *J. Appl. Phys.* **106** (2009) 066101.

[49] T. Li, G. Wang, K. Li, G. Du, Y. Chen, X. Dong, *Ceram. Int.* **40** (2014) 1195.

Chapter 5

Studies on $Ba_5Nb_4O_{15}$ – $BaWO_4$ bulk and thin films

5.1 Introduction

In global communication, in a broad range of applications such as local area network (LAN) and mobile phones, the microwave dielectric materials are playing a significant role. Consequently, to assemble the desired specifications of the current and future systems, new designs and devoted dielectric materials are required for the microwave components. As a result, a large number of dielectric materials have been developed to be used as dielectric resonators, capacitors, substrates and for electronic packages. The importance of good quality dielectric resonators in the microwave technology is increasing and there are few essential requirements, which are required for microwave applications, i.e., high dielectric constant (ε_r), a high quality factor ($Q\times f_0$) and a near-zero temperature coefficient of resonant frequency (τ_f) [1 - 5]. A large number of microwave dielectric materials have been studied for these applications and among them $Ba_5Nb_4O_{15}$ - $BaWO_4$ composite ceramics have been studied broadly due to their promising microwave dielectric properties at lower sintering temperatures: ε_r = 16.9 - 21, $Q\times f_0$ = 49.5 - 56.7 THz and τ_f = 8.9 to -4.3 ppm / °C [6, 7]. The Low temperature co-fired ceramics (LTCC) technology can be customized to provide controlled sintering during the firing operation allowing the precise placement of embedded components such as resistors, capacitors, transmission lines, etc [8]. LTCC materials are based either on crystallizable glass or a mixture of glass and ceramics, e.g. alumina, silica. The LTCC technology is widely used for miniaturization of microwave devices to reduce the size of wireless communication systems and this technology is well-known for both high volume, low cost application (wireless communication, car industry) and low volume high performance applications (military, space) [9 - 12]. The recent development in LTCC technology is demanding for high frequency wireless communication systems, which is an advanced approach to fabricate the ceramic structures with high speed and high frequency processing devices in the electronic industry [13]. In the present work, we developed $Ba_5Nb_4O_{15}$ - $BaWO_4$ composite ceramic with the addition of their own nanoparticles of $Ba_5Nb_4O_{15}$ and $BaWO_4$ and studied the effect of sintering temperature on their physical properties such as structural, microstructural, electrical and microwave dielectric properties of the prepared composite ceramics. However, to the best of the author's knowledge there is no study available on the preparation of nanoparticles of BNO and BWO ceramics and their addition as a sintering aid to BNO - BWO composite ceramics hence, this study. Different types of additives were added to reduce the sintering temperature of BNO -BWO ceramics to make this material suitable for low temperature co-fired ceramics (LTCC) applications. However, the microwave dielectric loss was enhanced by these additives [7, 14]. In general, to reduce the sintering temperature, the following methods were adopted in the literature: (i) smaller initial particle sizes, (ii) chemical processing methods and (iii) low melting glassy additives [15 - 17]. Further, the addition of sintering aids significantly affected the dielectric response of the ceramics, especially the loss tangent. In the current study, the BNO - BWO composite ceramics matrix added with their own nanoparticles as a sintering aid to reduce the sintering temperature and improvement in the densification. Also, due to the similar chemical nature of these nanoparticles the microwave dielectric properties would not deteriorated.

Further, we would like to know how this material behaves in thin film form. In general, to deposit the composite films pulsed laser deposition is being used, which is a costly technique. Hence, in the present study, we have used RF magnetron sputtering to deposit nanocomposite BNO - BWO films. Sputtering has attracted a considerable attention due to its simplicity, large throughput, and deposition over a wide range of pressures and transfer of stoichiometry of the target to the films.

In addition, oxide nanocomposite thin films acquired more attention due to their complementary behavior possess unique physical, chemical, optical, mechanical, magnetic, dielectric and electrical properties unavailable from that of the component materials and have attracted much attention for a wide range of device applications [18]. Besides, the response of oxide nanocomposite films depends not only upon the individual counter parts being used but also on the morphology and the interfacial characteristics. Hence, it is important to understand the functionality of nanocomposite thin films, which are profoundly dependent on the deposition technique and the processing parameters. In order to comprehend the performance of the nanocomposite BNO - BWO films, we have individually studied and optimized the deposition parameters of BNO and BWO films. Then we have prepared a composite sputtering target of BNO – BWO ceramics.

Nanocomposite BNO - BWO films are deposited on to amorphous SiO_2 and Pt/Ti/SiO_2/Si substrates using RF magnetron sputtering. The effect of oxygen mixing percentage (OMP) on structural, microstructural, optical, electrical and dielectric properties of these films both at low and microwave frequencies studied systematically. The dielectric properties of BNO - BWO thin films at microwave frequencies were studied using SPDR technique.

5.2 Experimental Details

5.2.1 Sol-gel synthesis of BNO and BWO nanopowders

The BNO and BWO nanopowders were prepared by using the high - pure chemicals barium nitrate (99.95%) $Ba(NO_3)_2$, niobium penta chloride (99.90%) $NbCl_5$, ethylene glycol (99%) $C_2H_6O_2$, and ethanol (90%) C_2H_5OH, tungstic acid (99%) H_2WO_4, barium carbonate (99.99%), $BaCO_3$ (M/s Alfa Aesar, Massachusetts, USA), and citric acid anhydrous (99.5%) $C_6H_8O_7$ (M/s Fisher Scientific, Mumbai, India).

Initially, the chemicals with desired stoichiometry ratio of $Ba(NO_3)_2$ and $Nb(OC_2H_5)_5$ were dissolved in distilled water. Niobium ethoxide $Nb(OC_2H_5)_5$ was prepared from niobium penta chloride, and ethanol [19]. The aqueous solutions of $Ba(NO_3)_2$ and $Nb(OC_2H_5)_5$ added to citric acid (chelating agent) in molar ratio of 1:2, ethylene glycol was used as a stabilizing or capping agent. Further, this solution was dried in an oven at 120 ^oC and calcined at 700 ^oC for 2 *h*.

The tungstic acid (H_2WO_4) dissolved in an aqueous solution of citric acid to form the tungsten citrate solution [20]. The barium carbonate solution was slowly added to homogenized tungsten citrate solution. Further, the obtained solution was stirred at 80 - 90 ^oC for 3 *h* to produce a homogeneous solution. To maintain the acidic nature of solution, ammonium hydroxide (adjust pH level 5 - 6) was used. The molar ratio between tungstic acid, citric acid was 1:2, and ethylene glycol was used as a stabilizing or capping agent. Furthermore, the prepared solution was dried in oven at 120 ^oC and calcined at 700 ^oC for 2 *h* to get BWO powders.

5.2.2 Preparation of BNO – BWO composites by solid-state reaction method

The BNO and BWO polycrystalline powders were prepared using the conventional solid-state reaction method. The starting materials with the high-purity powders of (99.99%) $BaCO_3$, WO_3 from (M/s Sigma Aldrich, St. Louis, MO), Nb_2O_5 (M/s Nuclear Fuel complex, Hyderabad, India) were used and stoichiometric mixtures of $BaCO_3$,

Nb_2O_5, and $BaCO_3$, WO_3 were ball milled for the duration of 5 and 7 *h*, respectively. The powders were mixed using tungsten carbide jar and balls in a planetary ball mill (M/s Fritsch Pulverisette 6, Germany) with distilled water as a mixing medium. The wet mixtures of the powders were dried and calcined at 1000 °C, 800 °C for constant durations of 5 and 6 *h*, correspondingly. The calcined BNO and BWO powders again mixed with BNO and BWO nanosized particles (prepared by sol-gel process) with different (1, 2 and 3 wt%) weight percentages for duration of 5 *h* in a planetary ball mill. Afterwards, powders were pressed into pellets with dimensions of 10 mm in diameter with 4 - 5 mm in thickness, and the samples were sintered in the temperature range of 800 - 950 °C for 3 *h* in air. The maintained heating and cooling rates were 8 °C / min and 1 °C / min, respectively.

5.2.3 Deposition of BNO - BWO thin films by RF magnetron sputtering

The (1-x) $Ba_5Nb_4O_{15}$ - x $BaWO_4$ ($x = 0.46$) composite prepared by $Ba_5Nb_4O_{15}$ and $BaWO_4$ composite powders with weight ratio, calcined at 1000 °C and 800 °C for 5 *h*, respectively by using conventional solid - state reaction method and this particular composition is chosen due to its best microwave dielectric properties. Subsequently, the calcined powders were milled for 10 *h* at higher speeds to reduce the initial particle sizes. Afterwards composite BNO - BWO powders were pressed into a cylindrical target of 62 mm in diameter with 3 mm in thickness. The BNO - BWO composite target was sintered at 1200 °C for 6 *h*. The composite BNO - BWO thin films were deposited by RF magnetron sputtering on to <100> oriented Pt/Ti/SiO_2/Si (Platinized silicon / Pt - si substrates) and amorphous SiO_2 substrates at ambient temperatures. The deposition chamber was pumped down to a base pressure of 5.0×10^{-6} *Torr*. The substrate to target distance was maintained at 5 cm and the films were deposited at a fixed RF power of 40 *W*. A mixture of high pure argon (99.999%) and oxygen (99.999%) were introduced into deposition chamber using mass - flow controllers. The sputtering pressure of 5×10^{-3} *mTorr* is maintained constantly throughout the deposition process by varying the argon / oxygen ratio in a standard cubic centimeter per minute (SCCM) in the sputtering gas. The BNO - BWO composite target was pre - sputtered in argon ambience for 5 min to remove the impurities on the target surface.

The $Ba_5Nb_4O_{15}$ - $BaWO_4$ composite thin films were deposited by RF reactive magnetron sputtering under the influence of different oxygen mixing percentages (OMPs) to study the electrical and dielectric properties of Ag / BNO – BWO / Pt/Ti/SiO_2/Si

(MIM) capacitor structures. The rate of deposition under different OMPs have been optimized to achieve the constant thickness of the film. The thickness of the films deposited on quartz and Pt coated substrate was estimated using the surface profilometer (M/s Veeco Dektak, 150). The values of thickness and deposition rate of the as-deposited BNO - BWO films as a function of OMP are given in **Table 5.1.**

Table 5.1: *The deposition rates of as- deposited BNO - BWO films on quartz and platinized silicon substrates under different OMPs.*

BNO-BWO Films as-deposited at different OMPs (%)	Deposition (nm/minute)	Thickness (nm)
0	3.5	630 ± 8 nm
25	3.2	630 ± 8 nm
50	2.9	630 ± 8 nm
75	2.5	630 ± 8 nm
100	2.3	630 ± 8 nm

It is observed that with an increase in OMP, the rate of deposition of the films decreases and is attributed to the oxidation of the target. However, to achieve the same order of thickness the deposition duration has been enhanced accordingly.

5.3 Results and Discussions

5.3.1 Effect of BNO and BWO nanoparticles on BNO - BWO composite ceramics

5.3.1.1 Phase analysis of BNO - BWO composite ceramics

Fig. 5.1 display the XRD patterns of the BNO - BWO composite ceramics added with *x* wt% of their nanoparticles (*x* = 0 - 3 wt%), sintered at 900 ^{o}C for 3 *h*. The XRD patterns of $Ba_5Nb_4O_{15}$ - $BaWO_4$ composite ceramics exhibits a reasonably polycrystalline structure with hexagonal perovskite crystalline phase of $Ba_5Nb_4O_{15}$ [JCPDF file # 17-0794] and tetragonal scheelite structure of $BaWO_4$ [JCPDF file # 85-0588].

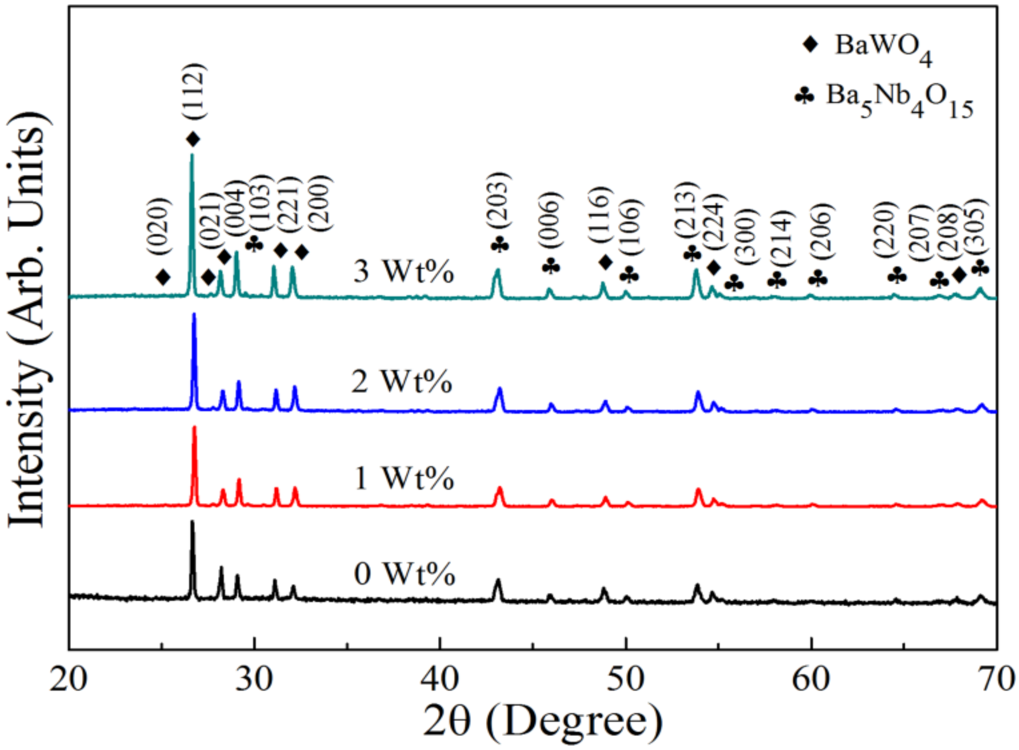

Fig. 5.1: *XRD pattern of the BNO - BWO composite ceramics added with x wt% of their nanoparticles (x = 0 - 3 wt%), sintered at 900 °C for 3 h.*

All the samples displayed the coexistence of both BNO - BWO ceramics. The observed (103) and (112) reflections in the neighbourhood of 29.0° and 26.6° corresponds to prominent peaks of both $Ba_5Nb_4O_{15}$ (♣) and $BaWO_4$ (♦), respectively. It is interesting to note that the pure phases were preserved in the sintered ceramics and no secondary phases were detected. The intensities of (103) and (112) orientations of BNO and BWO in the BNO - BWO composite ceramics increases with the addition of *x* wt% of their nanoparticles (*x* = 0 - 3 wt%). Considering the prominent reflections of BNO and BWO, the average crystallite sizes were calculated by using Scherrer's expression, and the crystallite sizes were found to be in the range of 50 - 55 nm and 52 - 58 nm, respectively for the BNO - BWO composite ceramics, added with their nanoparticles (*x* = 0 - 3 wt%).

5.3.1.2 Thermal analysis

Fig. 5.2 (a, b) shows the DSC/TGA analysis for the as-synthesized dry BNO and BWO precursors prepared by sol-gel process. To study the thermal properties of these powders, the samples were heated all the way from room temperature to 950 °C in argon atmosphere at a heating rate of 10 °C/min.

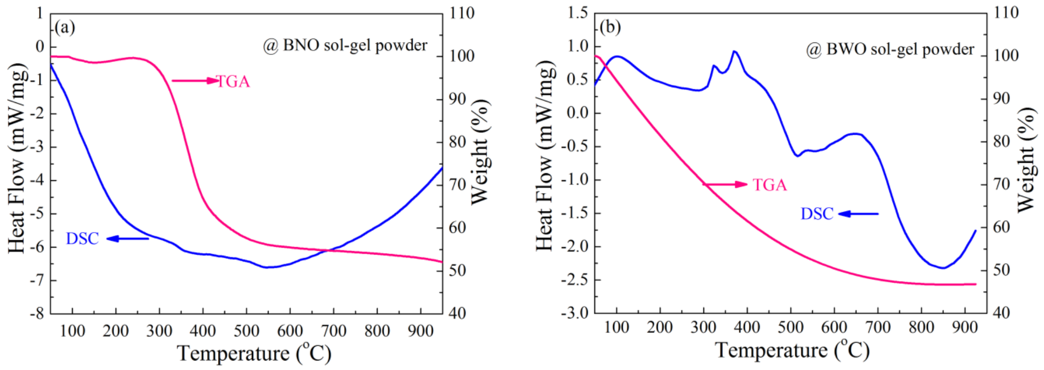

Fig. 5.2: *DSC and TGA plot of the as-synthesized dry BNO and BWO powders derived from BNO and BWO precursor solutions.*

The DSC curve (Fig. 5.2 (a)) of BNO dry precursor displayed small exothermic broad peaks around 310 °C and 460 °C. The thermogravimetric curve with increasing the temperature showed the significant changes in weight loss around 600 °C and in between 600 and 950 °C and exhibited nearly a flat characteristic response. This can be attributed to the formation of BNO phase and this in well agreement with powders prepared by solid state route. In the case of BWO, the highest weight loss (44%) was observed between 300 and 600 °C and afterwards it shows a stable weight loss until 950 °C. DSC curve of BWO powders display exothermic peaks at 100, 322, 370, and 647 °C and endothermic peaks at 515 and 847 °C and are shown in Fig. 5.2 (b). The observed exothermic and endothermic peaks may be attributed to the evaporation of excessive citric acid and the organic groups in citric acid. Further, the thermogravimetric curve for dry BWO precursor shows a weight loss of about 50% occurred at 700 °C and this may be due to the carbonate removal and formation of perovskite BWO structure.

5.3.1.3 Particle size analysis of BNO and BWO powders

The well defined nanosized polycrystalline BNO and BWO particles have been prepared by using sol - gel process and calcined at 700 °C for 3 *h* were characterized by TEM. Fig. 5.3 (a, b) displays the TEM images of BNO and BWO nanoparticles. It is observed that BNO particles reveal cylindrical grains where as BWO particles are in hexagonal shaped with an average particle size of 140 and 215 nm, respectively. During the preparation of BNO and BWO nanoparticles, the ethylene glycol was used as a binder, which minimizes the agglomeration [21]. This limits the diameter of different shaped particles with good dispersion. Fig. 5.3 (c, d) shows the presence of individual diffraction spots in selected area diffraction (SAD) pattern again confirms the formation of polycrystalline phases of the hexagonal BNO and tetragonal BWO ceramics, correspondingly.

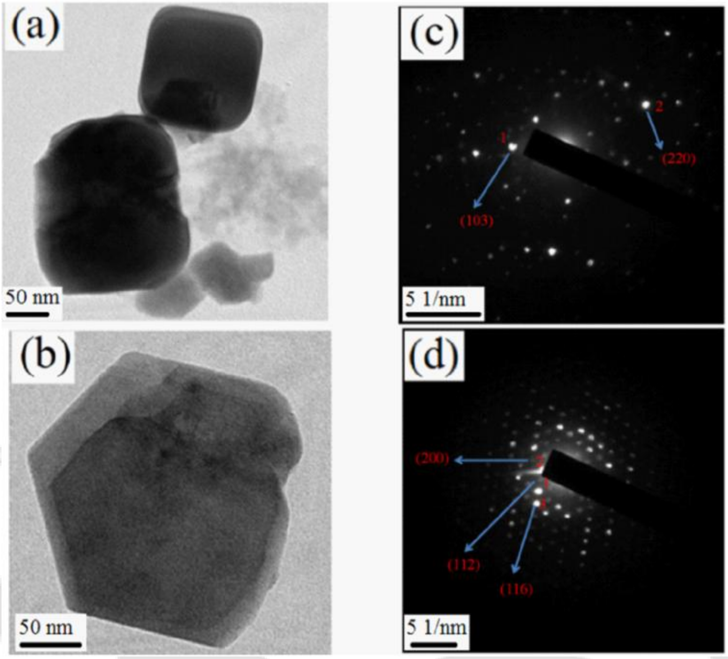

Fig. 5.3: *TEM image of the BNO and BWO calcined powders (a, b) prepared by sol - gel process, and (c, d) are the selected area diffraction (SAD) patterns of BNO and BWO, respectively.*

5.3.1.4 Microstructure and densification of BNO - BWO composite ceramics

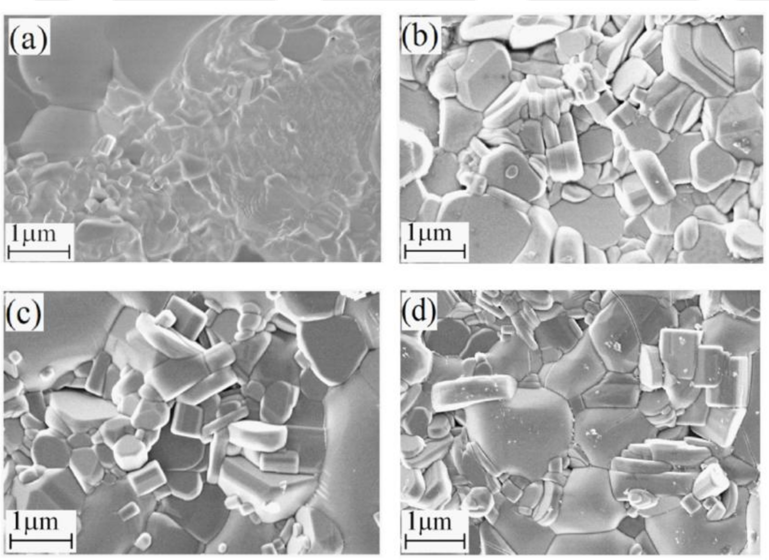

Fig. 5.4: *SEM images of various compositions of BNO - BWO composite ceramics (a) x = 0, (b) x = 1, (c) x = 2, and (d) x = 3 wt%.*

Fig. 5.4 (a - d) shows the surface morphologies of the BNO - BWO composite ceramics, added with different *x* wt% of their own nanoparticles, sintered at 900 °C for 3 *h*. The microstructures of the pure BNO - BWO ceramics and samples prepared with $x >$ 3 wt% of nanoparticles were non uniform. Further, BNO - BWO composite ceramics consist of cylindrical and hexagonal shaped grains, which belong to the BNO and BWO ceramics, respectively. Furthermore, in the bulk dense composite ceramics, the average grain size diameters of $Ba_5Nb_4O_{15}$ are 0.35, 0.43, and 0.60 μm and the grain sizes of $BaWO_4$ are 1, 1.2, and 1.4 μm for the samples added with $x = 1$, 2 and 3 wt%, respectively. However, the grain size was quite elongated with further addition of $x = 2$, 3 wt% of their own nanosized particles. In this case, BNO and BWO nanosized particles may distributed at grain boundary and facilitates the grain growth. From the SEM analysis, one can conclude the formation of both BNO and BWO grain shapes are coexisted and complemented the TEM results.

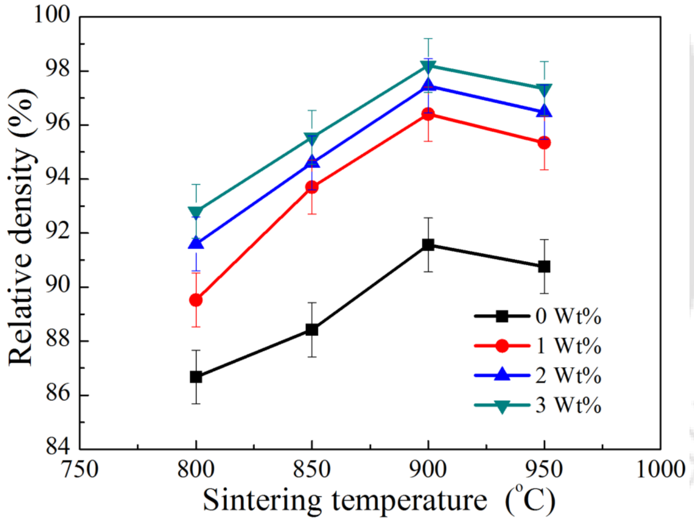

Fig. 5.5: *Variations in relative density as a function of sintering temperature for various compositions of BNO - BWO composite ceramics added with x wt% of their nanoparticles (x = 0 - 3 wt%).*

Fig. 5.5 shows the bulk relative densities of the BNO - BWO composite ceramics, with the addition of different *x* wt% of their own nanoparticles ($x = 0$ - 3 wt%), sintered between 800 °C - 950 °C for 3 *h*. It can be seen that for the BNO - BWO composition added with $x = 3$ wt% exhibited a maximum relative density of 98.2 % of the theoretical density. Further, enhancement of sintering temperature produces deformation of the sintered BNO - BWO composite ceramics added with *x* wt% of their own nanoparticles.

In addition, the BNO - BWO composite ceramic with x = 0 wt% sample i.e., parent BNO - BWO exhibited lower relative density of 91.56 % of the theoretical density and can be attributed to the insufficient sintering temperature. However, the addition of nanosized particles (x = 0 - 3 wt%) accelerates the sintering process, because the sintering velocity is inversely proportional to the particle size. When a different particle sizes, and shapes of BNO and BWO nanoparticles added to the micron sized BNO - BWO composite matrix, surface energy of the particles plays a vital role on the densification. The smaller particle size has a large surface-to-volume ratio due to its small radius of curvature in comparison with a similar volume of bulk solid, as a result the density of the compact increases. In addition, the lower melting temperature of both BNO and BWO nanoparticles would act as a liquid phase sintering aid. When particles of different sizes are dispersed in a ceramic matrix, material transport occurs from tiny to large grains because of the difference in solubility between the grains. Therefore, smaller grains dissolve and large grains grow further, and the average grain size increases. This phenomenon is called as 'Ostwald ripening' [22, 23].

5.3.1.5 Broadband dielectric properties at cryogenic temperatures

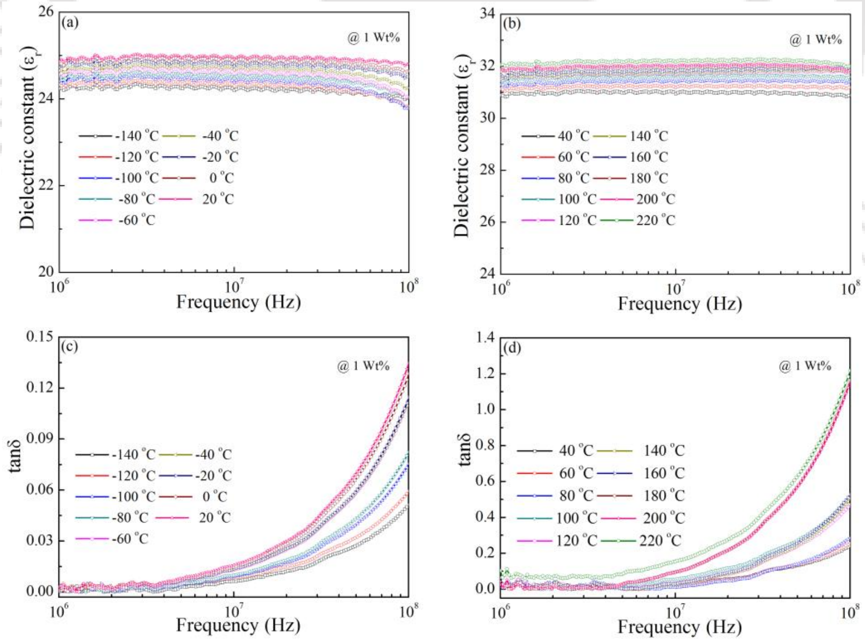

Fig. 5.6: *Variations in dielectric constant as a function of frequency measured in the temperature range of (a) (-140 ^oC to 20 ^oC) (b) (40 ^oC to 220 ^oC). Variations in loss tangent as a function of frequency measured in the temperature range of (c) (-140 ^oC to 20 ^oC) (d) (40 ^oC to 220 ^oC) for compositions of BNO - BWO composite ceramics added with x = 1 wt% of their own nanosized particles, sintered at 900 ^oC for 3 h.*

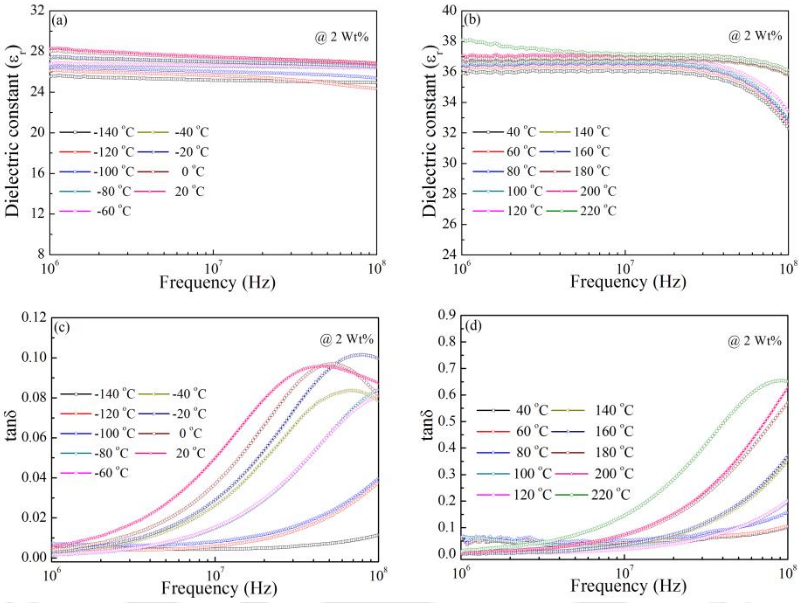

Fig. 5.7: *Variations in dielectric constant as a function of frequency measured in the temperature range of (a) (-140 °C to 20 °C) (b) (40 °C to 220 °C). Variations in loss tangent as a function of frequency measured in the temperature range of (c) (-140 °C to 20 °C) (d) (40 °C to 220 °C) for compositions of BNO - BWO composite ceramics added with x = 2 wt% of their own nanosized particles, sintered at 900 °C for 3 h.*

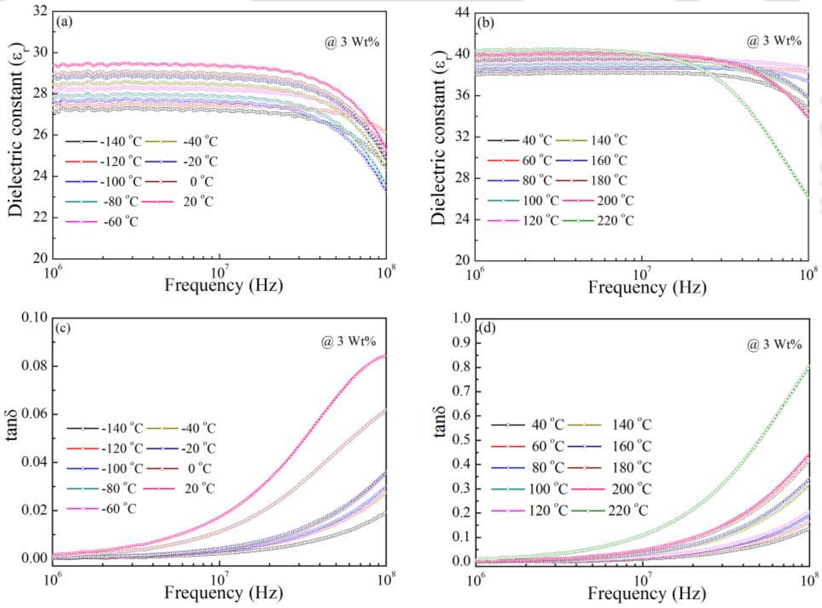

Fig. 5.8: *Variations in dielectric constant as a function of frequency measured in the temperature range of (a) (-140 °C to 20 °C) (b) (40 °C to 220 °C). Variations in loss tangent as a function of frequency measured in the temperature range of (c) (-140 °C to 20 °C) (d) (40 °C to 220 °C) for compositions of BNO - BWO composite ceramics added with x = 3 wt% of their own nanosized particles, sintered at 900 °C for 3 h.*

Fig. 5.6, 5.7, and Fig. 5.8 shows the frequency dependence of dielectric constant (ε_r) and loss tangent ($tan\delta$) for the BNO - BWO composite ceramics added with different x wt% of their nanoparticles, measured in the temperature range of -140 °C to 220 °C. It can be seen that both ε_r and $tan\delta$ of samples showed nearly a stable response with frequency upto 10 MHz, in the temperature range (-140 °C to 220 °C) for all the samples added with x = 1 - 3 wt%. Further, as the frequency increases, the dielectric constant of the samples decreases whereas the loss tangent was enhanced, which is a characteristic of a linear dielectric. In addition, with a rise in measurement temperature, dielectric constant of the BNO - BWO composite ceramics is improved. In the low temperature region, molecules possess energy less than the height of energy barrier and it cannot cross the energy barrier. Therefore, it cannot change its orientation. Hence, dipoles can no longer contribute to overall polarization, which causes a drop in the dielectric constant. As the temperature increases, the molecules have more thermal energy and therefore the amplitude of thermal motion is greater. Hence, the effect of heating on orientational polarization is active and leading to an increase in dielectric constant.

Further, it is observed that in the high frequency region, the $tan\delta$ increases with a rise in temperature from -140 °C to 220 °C. This might be possible because, the rapid rise in the $tan\delta$ values has been assigned to the conduction losses, which is due to the increased conduction at higher frequency and temperatures. The obtained dielectric constant (ε_r) and loss tangent ($tan\delta$) values of BNO - BWO composite ceramics with x wt% of their own nanoparticles (x = 1 - 3), measured at different temperatures and at discrete frequencies were shown in **Table 5.2.**

***Table 5.2**: Measured dielectric constant (ε_r) and loss tangent ($tan\delta$) values of BNO - BWO composite ceramics with x = 3 wt% of its own nanosized particles at different temperatures and at discrete frequencies, sintered at 900 °C for 3 h.*

BNO and BWO Nano addition in weight (%)	**Measured frequency**	**-140 °C**		**40 °C**		**220 °C**	
		ε_r	$tan\delta$	ε_r	$tan\delta$	ε_r	$tan\delta$
1 Wt%	1 MHz	24.24	0.0033	30.89	0.0046	32.05	0.0102
	20 MHz	24.18	0.0124	30.97	0.0137	32.20	0.0279
	0.1 GHz	24.03	0.0514	30.87	0.0642	32.00	0.1217
2 Wt%	1 MHz	25.54	0.0102	35.91	0.0108	38.10	0.0112
	20 MHz	25.11	0.0297	35.93	0.0596	37.07	0.2865
	0.1 GHz	24.95	0.0314	32.28	0.1015	36.12	0.6515
3 Wt%	1 MHz	27.20	0.0007	38.05	0.0033	40.31	0.0076
	20 MHz	27.05	0.0420	38.10	0.0258	38.86	0.2193
	0.1 GHz	24.41	0.1637	34.77	0.1778	26.12	0.8057

5.3.1.6 Conductivity studies

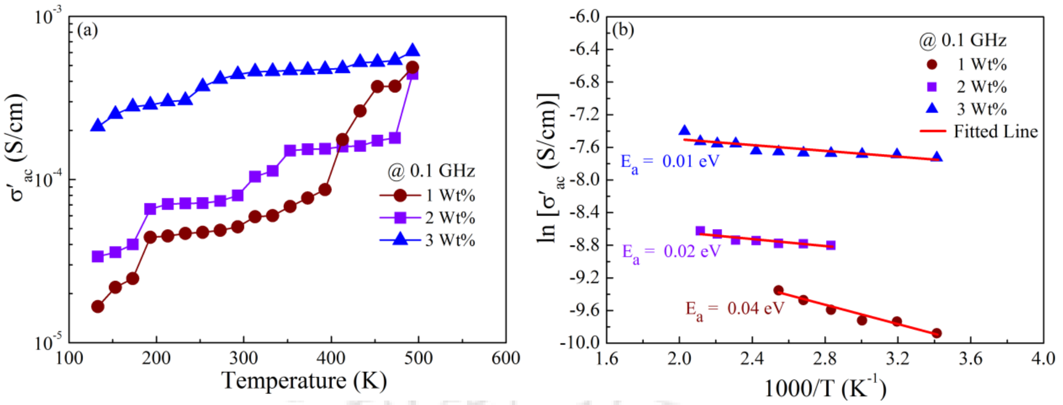

Fig. 5.9: *(a) variation of ac conductivity (σ'_{ac}) versus temperature, (b) variation of ln σ'_{ac} versus 1000/T for BNO - BWO composite ceramics added with x wt% of their nanoparticles (x = 1 - 3 wt%), sintered at 900 °C for 3 h, and measured at 0.1 GHz.*

The temperature dependent AC conductivity (σ_{ac}) measurements have been carried out on BNO - BWO composite ceramics added with different *x* wt% of their nanoparticles, measured at a constant frequency of 0.1 GHz is shown in Fig. 5.9 (a). As the temperature raises, the conductivity increases, it may be due to the maximum number of ions gained kinetic energy in the BNO - BWO composite ceramics and are influenced by thermally activated hopping of charge carriers between trapped sites. Fig. 5.9 (b) Shows the plot of ln (σ_{ac}) versus *1000/T* for BNO - BWO composite ceramics with different *x* wt%. The activation energy (E_a) required for the mobile charge carriers to jump over to their neighboring sites was obtained by fitting the conductivity data with the Arrhenius relation and the expression is given below

$$\sigma_{ac} = \sigma_0 exp^{(-E_a/k_BT)} \tag{1}$$

Where, σ_o is pre-exponential factor, E_a is the activation energy, K_B is the Boltzmann constant and *T* is the absolute temperature. The extracted activation energies are found to be E_a = 0.04, 0.02 and 0.01 *eV* for the BNO - BWO composite ceramics with various *x* wt% of their own nanoparticles. Further, it was observed that the decrease in activation energy values indicates high mobility of ions in the BNO - BWO composite ceramics.

5.3.1.7 Impedance spectroscopy

Fig. 5.10 shows the plot of the complex dielectric constant (ε'' versus ε') in the frequency range of 1 MHz - 0.1 GHz for the BNO - BWO composite ceramics added with *x* = 3 wt% of their own nanoparticles.

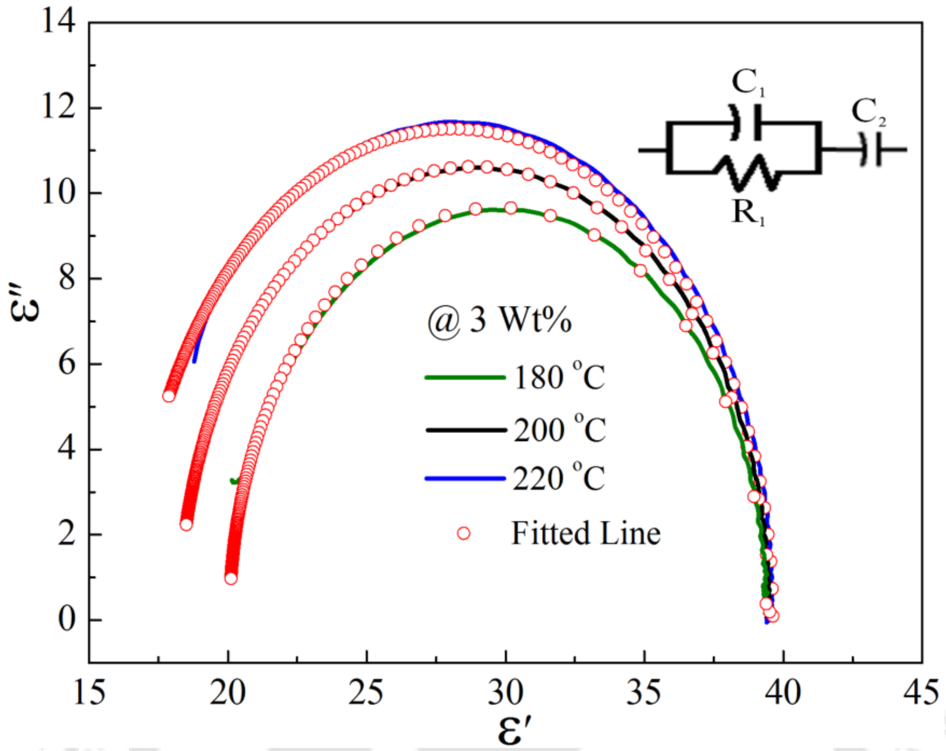

Fig. 5.10: *Cole-Cole plots, measured at range of different temperatures (180 °C - 220 °C), for BNO - BWO compostie ceramics added with x = 3 wt% composition of its own nanosized particles, sintered at 900 °C for 3 h, (inset) shows an equivalent circuit which describes the electrical response of polycrystalline BNO - BWO composite ceramics added with x = 3 wt% of its own nanosized particles.*

All the samples reveal a Cole - Cole plot, which are in the form of semicircle arc measured in the temperature range of 180 °C to 220 °C. To understand the relaxation behaviour of the complex permittivity ε^* in the frequency domain, the Havriliak - Negami (HN) equation is used and is given below

$$\varepsilon^*_{HN} = \varepsilon_\infty + \frac{\varepsilon_\circ - \varepsilon_\infty}{[1+(j\omega\tau_\circ)^\alpha]^\beta} \qquad (2)$$

Where, ε_∞ is the high - frequency dielectric constant, ε_o is the low - frequency permittivity, τ_o is the characteristic relaxation time, for the fractional shape parameters α and β, which describe the symmetric and asymmetric broadening of the complex dielectric function $0 < \alpha, \alpha\beta \leq 1$ holds. The experimental data of semicircle arc fitted by using equation (2), depends on the electrical properties of the material. **Table 5.3** shows the obtained HN function parameters, which gives the relaxation at a given temperature.

Table 5.3: *Obtained HN parameters (From WinFIT$_{3.4}$ software) from the fitting data to the equation for BNO - BWO composite ceramics with x = 3 wt% of its own nanosized particles, sintered at 900 °C for 3 h.*

Fit parameters of test sample	180 °C	200 °C	220 °C
$\Delta\varepsilon$	22.35 ± 0.02	22.26 ± 0.02	20.80 ± 0.01
$\tau_o\,[s] \times (10^{-10})$	07.29 ± 0.01	06.93 ± 0.01	05.71 ± 0.02
α	1.00 ± 00	1.00 ± 00	1.00 ± 00
β	1.00 ± 00	1.00 ± 00	1.00 ± 00

One attractive feature of dielectric spectroscopy lies in its applicability to the studies aimed towards the development of direct correlation between the response of a real, and an idealized model circuit composed of discrete electrical components. The simplest R-C parallel circuit, is often a suitable model of polarization by charge migration over a given frequency range. A single resistance that encompasses the dissipative contributions of all migrating charges, extrinsic (e.g., ionic impurities) and intrinsic (e.g., proton transfer along ionic bonds) alike, is all that is needed to describe the overall loss because the dissipative contributions due to electrode polarization and dipole relaxations occur at lower and higher frequencies, respectively. The lone capacitance, on the other hand, embodies the overall ability of the dielectric to store the electric field by all polarization mechanisms in dielectric materials [24]. Further, fitting the complex dielectric data to the electrical circuit in which the physical process taking place and the properties of linear systems are unchanged in passing from ionic to electronic materials. Inset of Fig. 5.10 shows an equivalent circuit of parallel R_1C_1 combination in series with capacitance C_2 filled with material dielectric constant. In this circuit model, R_1 denotes the dielectric loss (dissipates energy) of the polycrystalline composite material and is represented in equivalent circuit by a resistance and C_1 is the main element of the capacitor, which stores the energy. In general, circuits involving geometrical capacitance $C_g = C_\infty = C_1$ and a bulk high frequency limiting resistance $R_b = R_\infty = R_1$ in parallel with it. In the present study, the oxide ions are sequentially blocked at grain interiors, which is demonstrated by parallel R_1C_1 combination and additional series capacitance C_2 (stray capacitance in the high frequency region) would occur from the stray fields in air outside of the composite dielectric material. The other possibility is that the grain boundary regions where good intergranular contact is established for the occurrence of C_2 [25]. From the best fitting of Cole - Cole plots, the obtained parameters are listed in **Table 5.4**. It is found that with an increase in measurement temperature from 180 °C to 220 °C, the resistance values have been decreased and capacitance values are enhanced for BNO - BWO composite ceramics with x = 3 wt%, sintered at 900 ^{o}C for 3 *h*.

Table 5.4: *Obtained equivalent circuit parameters (From WinFIT$_{3.4}$ software) from Cole-Cole plots measured for BNO - BWO composite ceramics with x = 3 wt% of its own nanosized particles, sintered at 900 ^{o}C for 3 h.*

Fit parameters of test sample	**180 ^{o}C**	**200 ^{o}C**	**220 ^{o}C**
R_1	64.01 ± 0.34	31.89 ± 0.10	30.37 ± 0.09
$C_1 \times (10^{-12})$	03.47 ± 0.04	03.47 ± 0.04	05.16 ± 0.06
$C_2 \times (10^{-12})$	18.30 ± 0.02	18.38 ± 0.01	18.43 ± 0.01

5.3.1.8 Microwave dielectric properties

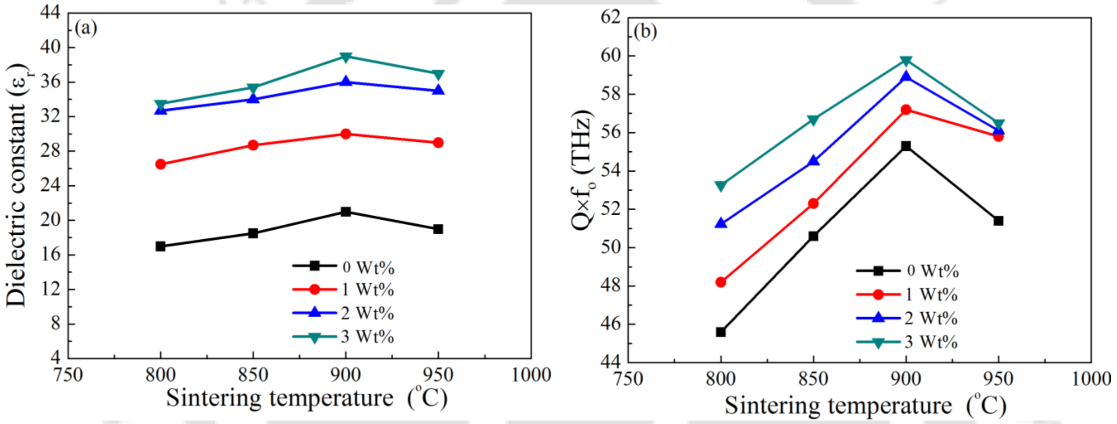

Fig. 5.11: *Variations in (a) dielectric constant, (b) $Q\times f_0$ values as a function of sintering temperature for various compositions of BNO - BWO composite ceramics added with x wt% of their nanoparticles (x = 0 - 3 wt%).*

Fig. 5.11 (a, b) shows the dielectric constant (ε_r) and $Q\times f_0$ of BNO - BWO composite ceramics added with x wt% of their nanoparticles, sintered between 800 ^{o}C - 950 ^{o}C for a constant duration of 3 *h*. Both the ε_r and $Q\times f_0$ values enhanced for the BNO - BWO composite ceramics added with x wt%, and sintered between 800 - 900 ^{o}C range and thereafter they decreases. Both ε_r and $Q\times f_0$ followed the similar trend, which is shown in Fig. 5.5. The best microwave dielectric properties were obtained for BNO - BWO composite ceramics with x = 3 wt%, sintered at 900 ^{o}C shows a maximum ε_r of 39 and $Q\times f_0$ of 59.8 THz at 9.44 GHz. The increase in ε_r and $Q\times f_0$ values could be attributed to maximum relative density and grain growth of BNO - BWO composite ceramics and these ceramics become uniform with increasing x wt% of their nanoparticles. The obtained ε_r and $Q\times f_0$ values of the BNO - BWO composite ceramics with *x* wt% of their own nanosized particles (*x* = 1 - 3) is much higher than that of the previous reported values in the literature [6, 7]. The addition of these nanoparticles not only reduced the sintering temperature but also minimized the dielectric loss. Hence, the addition of BNO and BWO nanosized particles in the bulk BNO - BWO composite matrix, displayed a good densification, enhancement in grain growth, and microwave dielectric properties. Further, the prepared BNO - BWO composites ceramics are most promising for LTCC applications.

The temperature coefficient of resonant frequency (τ_f) is known to be related to the composition. The sintering temperature of the BNO - BWO composite ceramics added with *x* = 3 wt% of their nanoparticles had little effect on τ_f value in the range of 800 ^{o}C - 950 ^{o}C and τ_f ranged from + 0.8 to + 1.3 ppm/^{o}C. The BNO - BWO composite ceramics added with *x* = 3 wt% sample, sintered at 900 ^{o}C exhibits best τ_f = + 0.8 ppm/^{o}C.

5.3.1.9 Raman spectra analysis

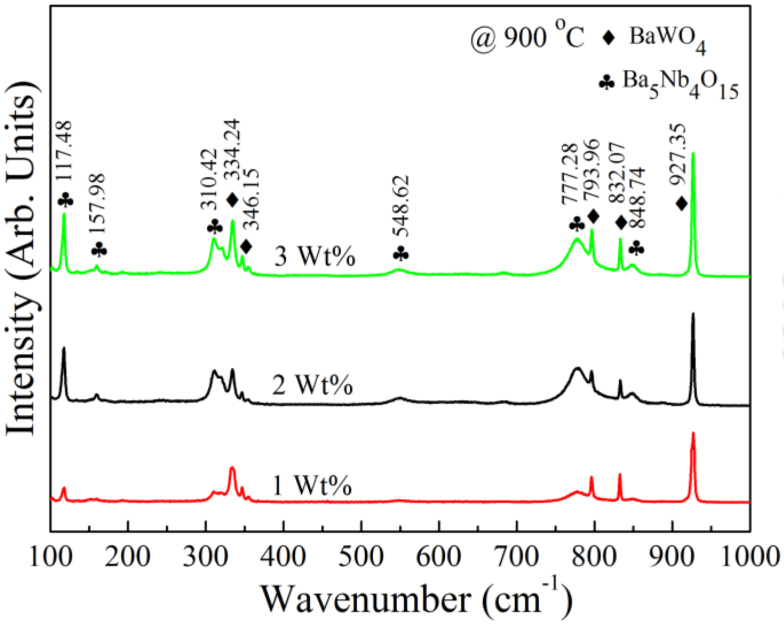

Fig. 5.12: *Raman spectra of BNO - BWO composite ceramics added with x wt% of their nanoparticles (x = 1 - 3 wt%), sintered at 900 ^{o}C for 3 h. The numbers above the peaks is the Raman shift in cm^{-1}.*

Further to comprehend the coexistence of BNO - BWO ceramics, Raman spectra of these samples were obtained. Fig. 5.12 shows the Raman spectra of BNO - BWO composite ceramics with *x* wt% of their own nanosized particles (*x* = 1 - 3). The samples were excited by the 488 nm line of an Ar - ion laser processed at room temperature. The BNO - BWO composite matrix with addition of their own nanosized particles shows both the BNO and BWO vibrational modes. The Raman vibrational modes for BNO are 117.48, 157.98, 310.42, 548.62, 777.28, 848.74 cm^{-1} and BWO vibrational modes 334.24, 346.15, 793.96, 832.07, 927.35 cm^{-1} and the appearance of these modes are complement with the earlier reports [20, 26, 27]. The vibrational modes 117.48 and 927.35 cm^{-1} is ascribed to strong vibrational modes of BNO and BWO phase, respectively. In addition, the intensities of these modes increases with x wt% of their own nanosized particles (x = 1 - 3) and these results are in agreement with the obtained XRD patterns and microstructures.

5.3.2 Dielectric and Optical Characterization of RF Sputtered BNO - BWO Composite Films

5.3.2.1 Structural properties

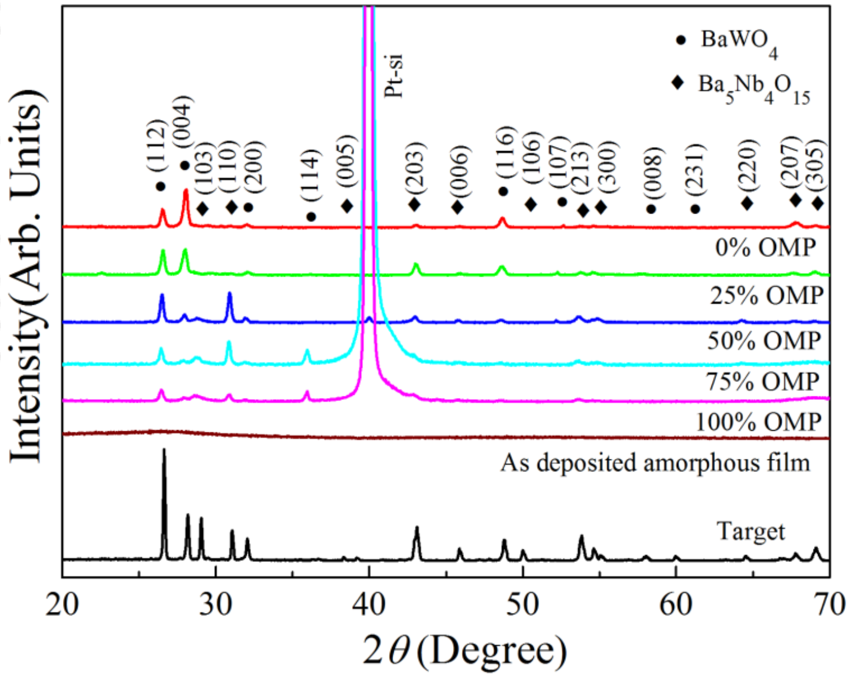

Fig. 5.13: *XRD patterns of the BNO - BWO composite sputtering target, BNO - BWO as deposited amorphous film and annealed films deposited at different OMPs.*

Fig. 5.13 shows the XRD pattern of the composite BNO – BWO sputtering target, sintered at 1200 °C for 3 *h*. It is observed that all the prominent peaks related to both BNO (♦) and BWO (•) are co existing and there is no signature of any secondary phases. The coexistence of BNO hexagonal perovskite structure with BWO scheelite structure is due to the differences in crystal structure and in the coordination numbers of the Nb and W in their crystal structures, which prevent the formation of solid solution between BNO and BWO. The coordination number for Nb^{5+} in hexagonal perovskite structure is 6 whereas w^{6+} in scheelite structure is 4 [6, 7].

By considering the individual BNO and BWO deposition parameters, the following processing parameters (substrate to target distance, working pressure and RF power) are optimized for BNO – BWO composite thin films. The as – deposited BNO – BWO composite films were X – ray amorphous. It is expected that oxide films spontaneously grow in an amorphous state due to less activation energy during the deposition and also due to the lattice mismatch between the substrate and film. It is well known that the crystalline films show better performance as compared to the amorphous films. In order to induce the crystallinity in the as – deposited BNO – BWO films, these films are annealed at 700 °C for 2 *h* in air.

Fig. 5.13 depicts the XRD patterns of the BNO - BWO composite sputtering target and BNO - BWO as deposited amorphous film and annealed films deposited at different OMPs. The XRD patterns of nanocomposite $Ba_5Nb_4O_{15}$ - $BaWO_4$ films exhibits a reasonably polycrystalline structure with tetragonal scheelite structure of $BaWO_4$ [JCPDF file # 85-0588] and hexagonal perovskite crystalline phase of $Ba_5Nb_4O_{15}$ [JCPDF file # 17-0794]. The (112) and (110) orientation corresponds to prominent peaks in the diffraction pattern for both $BaWO_4$ (•) and $Ba_5Nb_4O_{15}$ (♦) components, respectively. The XRD pattern indicates that $BaWO_4$ and $Ba_5Nb_4O_{15}$ coexisted in the $Ba_5Nb_4O_{15}$ - $BaWO_4$ composite thin film for all the variations in 0 - 100% OMPs. It is noticed that the diffraction peaks corresponding to $Ba_5Nb_4O_{15}$ [(005), (106)] and $BaWO_4$ [(008), (231)] were present in the $Ba_5Nb_4O_{15}$ - $BaWO_4$ composite target, but they disappear in the thin film form. On the other hand, the identified (114), (107) reflections in the thin film form were not existing in the bulk $Ba_5Nb_4O_{15}$ - $BaWO_4$ composite ceramics. These variations can be attributed to the differences in the free energies available during the deposition and sintering processes, respectively.

In addition, it is interesting to note that no secondary phases were detected as in the case of bulk $Ba_5Nb_4O_{15}$ - $BaWO_4$ composite sputtering target. Further, it is important to note that BNO – BWO composite films are deposited even in the pure oxygen environment, which shows that the target is not completely poisoned even in the pure oxygen plasma (100% OMP).

Further, it is observed that the prominent peak intensities of BNO (110) and BWO (112) enhanced with an increase in OMP, which shows that the crystallinity of the BNO – BWO composite films improved with OMP. The average crystallite sizes of these films are calculated using Scherrer’s expression, by taking the prominent reflections of BNO and BWO are in the range of 14 - 35 nm and 28 - 34 nm, respectively. The average crystallite size of the films enhanced with a rise in OMP and is explained as follows: as the OMP concentration increases in the chamber, the sputtered atoms react with oxygen molecules that cause the heat generation and energy redistribution on the surface of the substrate. This process simultaneously promotes the migration of the adatoms. It is significant to note that the nanocomposite BNO – BWO films are grown in the stoichiometric state using the RF reactive magnetron sputtering, which shows that by the optimization of processing parameters it’s possible to deposit multi component films using this technique.

5.3.2.2 Microstructure of BNO – BWO nanocomposite films

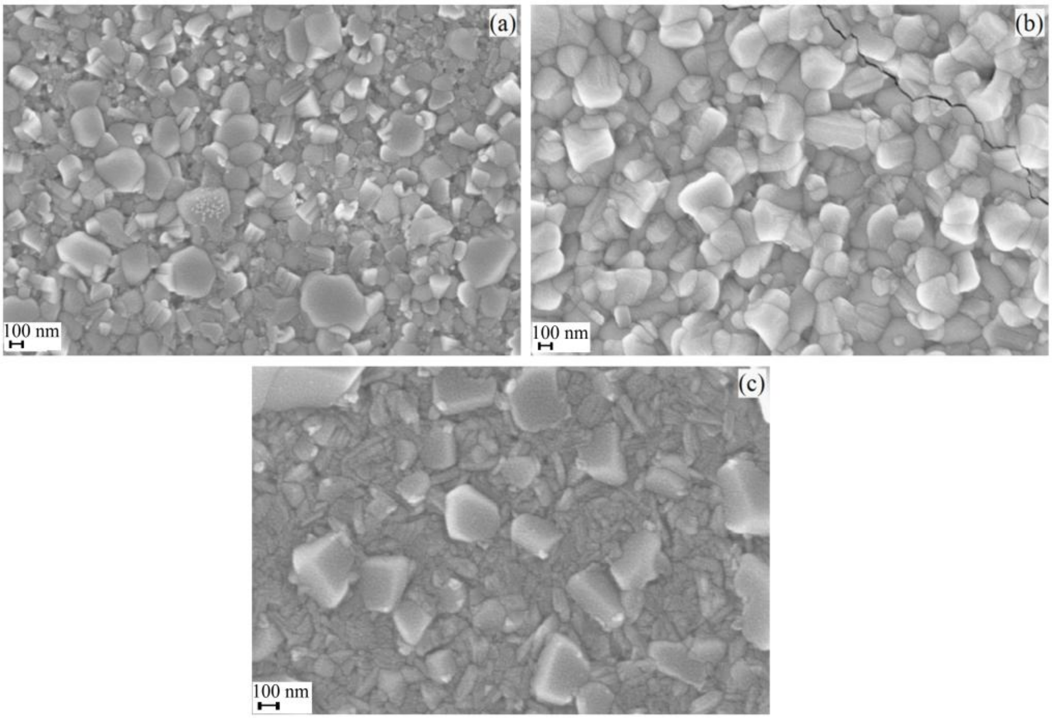

Fig. 5.14: *SEM images of the BNO - BWO nanocomposite films annealed at 700 °C for 2 h at different OMPs (a) 0%, (b) 50%, (c) 100%.*

The as - deposited films did not show any feature in the obtained images. The microstructures of the composite films, annealed at 700 ^{o}C are shown in Fig. 5.14 (a - c) where a, b and c correspond to the films deposited under 0, 50 and 100% OMPs, respectively. It is observed that as the OMP raises, the particle sizes of the films increases significantly. Further, it is interesting to note that the coexistence of both the BNO and BWO phases. From the SEM images, it is noticed that there exist two types of grain in all the films: one is with large grains in hexagonal shape, and the other is with small rod like shape. BNO exhibited a small rod shaped grains for the films deposited within the range of 0% OMP and 50% OMP. However, films deposited at 100% OMP display this shape clearly (Fig. 5.14 (c)). Films deposited under pure argon plasma (0% OMP), show the smaller particles of both BNO and BWO and difficult to differentiate their phases noticeably. Further increase in OMP up to 50%, we could evidently distinguish the BNO and BWO phases clearly. In addition, films deposited in pure oxygen plasma displayed the coexistence of both the phases distinctly. The enhancement in average grain sizes of the films is attributed to the increase in crystallinity, which is confirmed from the XRD patterns. In order to confirm the chemical composition of these phases, EDS analysis is performed on these grains and EDS spectrum of the BNO – BWO composite film deposited in pure oxygen plasma is shown in Fig. 5.15.

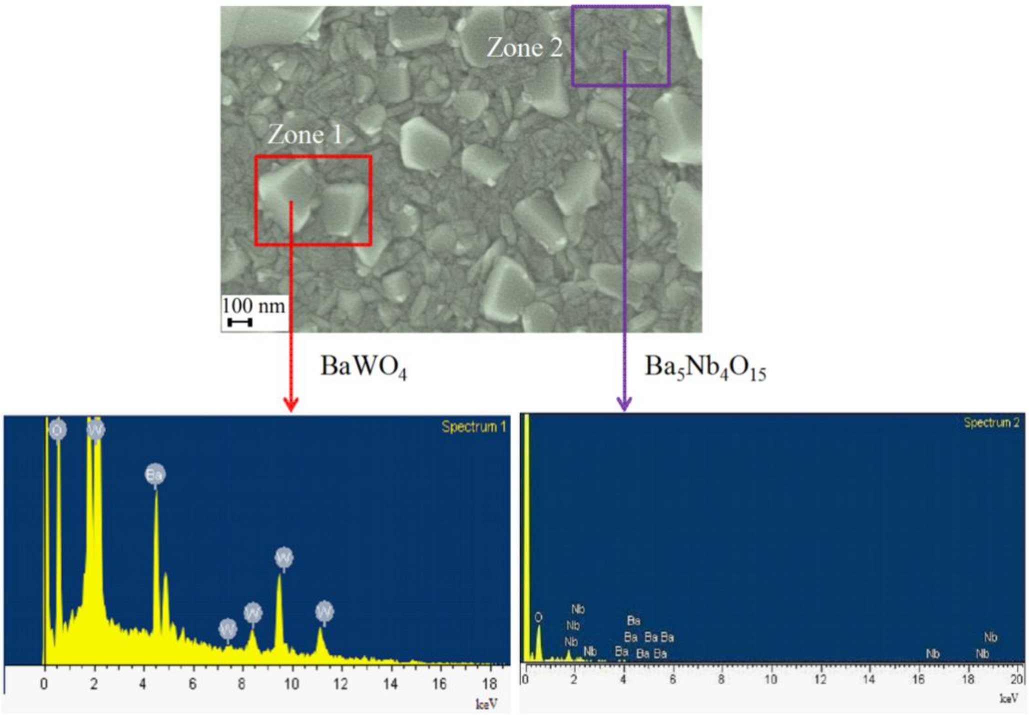

Fig. 5.15: *EDS spectrum of BNO - BWO nanocomposite (bottom) films deposited in 100% OMP and SEM image of their emission area (top).*

Table 5.5: *Elemental analysis for the BNO - BWO nanocomposite film deposited at 100% OMP.*

	Element	Weight (%)	Atomic (%)	Required	Obtained
$BaWO_4$ Nanocomposite	O (K)	16.62	66.67	4	4.0002
	Ba (L)	35.66	16.67	1	1.0002
	W (M)	47.72	16.66	1	0.9996
$Ba_5Nb_4O_{15}$ Nanocomposite	O (K)	18.47	62.48	15	14.9952
	Nb (L)	28.64	16.68	4	4.0032
	Ba (L)	52.89	20.84	5	5.0016

Table 5.5 shows the elemental analysis for the BNO - BWO nanocomposite film at 100% OMP. It is found that the rod - shaped grain exhibited the chemical composition of $Ba_5Nb_4O_{15}$ while the hexagonal grains show a chemical composition of $BaWO_4$. The variations in the grain sizes are attributed to the differences in their sintering temperatures. BNO (1250 ^oC) requires higher sintering temperature as compared to BWO (800 ^oC). The obtained microstructures of the BNO - BWO composite films complement our previous reports on BNO and BWO individually. BNO films display rod-shaped grains whereas the BWO films show hexagonal shaped grains, and both the films were deposited by RF reactive magnetron sputtering. Zhuang et al [7] observed the similar microstructures for the bulk composite BNO – BWO ceramics.

5.3.2.3 Optical properties of BNO – BWO nanocomposite films

In order to understand the optical response of these composite films, optical constants are calculated from the transmittance spectra using the envelope method [28]. Optical transmittance spectra of nanocomposite BNO - BWO thin films deposited on to amorphous SiO_2 substrates measured in the wavelength range of 200 – 800 nm are shown in Fig. 5.16 (a). All the as deposited films are found to be transparent (> 90%) in the visible range and the multiple reflections between air - film and film - substrates due to the Fabry - Pérot interference behavior. The obtained high transparency of the nanocomposite films makes these films suitable for smart window applications. These oscillations arise due to the uniform thickness in the composite BNO – BWO deposited films and plane surface. The transmittance found to be decreased to zero around 310 nm due to the fundamental absorption of the films. The absorption edges show a blue shift with increasing the OMP for as - deposited films. The optical constants were calculated by using envelope method [28].

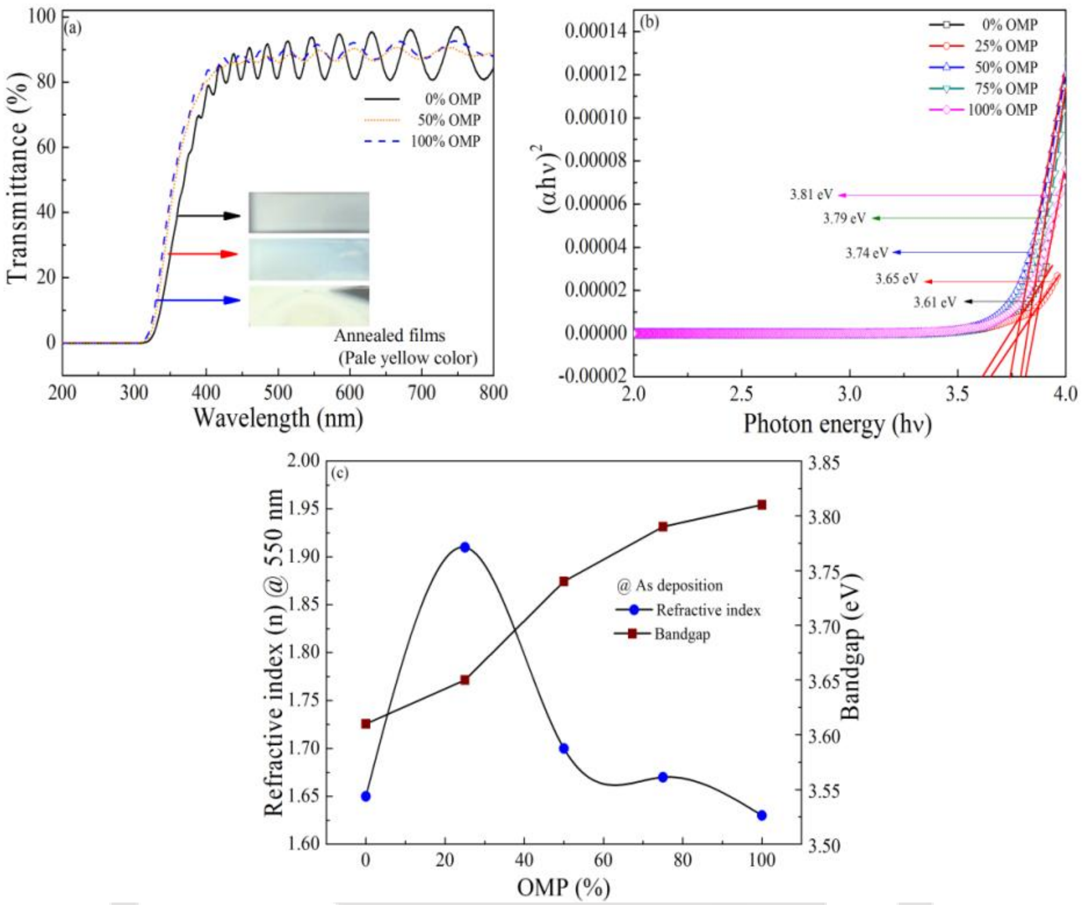

Fig. 5.16: *(a) Optical transmittance spectra of the BNO-BWO thin films deposited at different OMPs (b) Refractive index and bandgap as a function of different OMPs (c) A plot of* $(\alpha h\upsilon)^2$ *versus* $h\upsilon$ *for the BNO - BWO thin films deposited at different OMPs.*

The thicknesses of the films were found to be in the range of 280 - 300 nm for the annealed films. The variation in refractive index and optical bandgap as a function of OMP is shown in Fig. 5.16 (c). It is observed that refractive index (*n*) of the as - deposited films found to be improved with an increase in OMP up to 25%, above that they started decreasing and the values are in the range of 1.63 to 1.91. The obtained low refractive index values are attributed to the amorphous nature of the films, which are in the disorder state with low adatom mobility because the films are grown at ambient temperatures.

It is interesting to note that the annealed films did not show any transmittance behavior and all the films turned into pale yellow color and the photographs of these films are shown in Fig. 5.16 (a). In order to confirm the nature of chromic response, we have annealed the films at different temperatures and the transmittance (color) of the films is not regained, which shows the irreversible thermochromic behavior. Further, composite films are excited with UV lamp and there is no change in the transmittance (color); this confirms that these films will not exhibit photochromism, and these films may exhibit electrochromism. The obtained chromic response of BNO – BWO composite films find applications in information display devices. However, understanding the chromic behavior in BNO – BWO films is a subject for the future study. The optical bandgap of the films increases with an increase in OMP and might be associated with the reduction in oxygen vacancies and small particle sizes. The Tauc equation [29] was used to estimate the optical band gap of films, which was given by

$$(\alpha h\upsilon) = c(h\upsilon - E_g)^{\gamma} \tag{3}$$

Where, α is the optical absorption coefficient, $h\upsilon$ is the incident photon energy, c is energy independent constant, E_g is the optical band gap and γ is a constant which characterize the nature of band transition. γ = 0.5, 1.5 represents to direct allowed and direct forbidden transition and γ = 2, 3 correspond to indirect allowed and indirect forbidden transitions, respectively. The optical bandgap values are in the range of 3.61 to 3.81 *eV*. To see the differences in the absorption edges of the films, $(\alpha h\upsilon)^2$ versus $h\upsilon$ for the BNO - BWO nanocomposite films deposited at different OMPs are depicted in Fig. 5.16 (b), it is clearly shows the blue shift in the absorption edges with an increase in OMP.

5.3.2.4 Dielectric studies

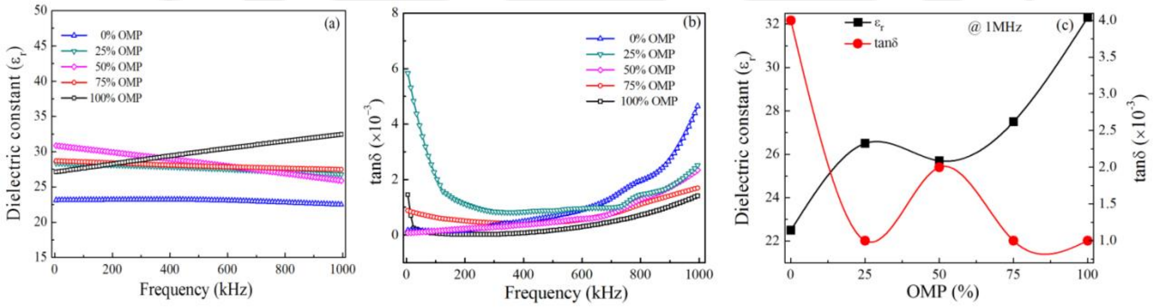

Fig. 5.17: *Variation in (a) dielectric constant, (b) loss tangent of BNO - BWO thin films deposited at different OMPs and measured as a function of frequency, (c) Dielectric constant vs. loss tangent as a function of OMP measured at 1 MHz.*

The frequency dependent dielectric response of BNO – BWO nanocomposite films as a function of frequency is depicted in Fig. 5.17 (a) and 5.17 (b). It is observed that the dielectric constant of the films remained constant throughout the measured frequency range, and shows that the deposited films are not much dependence on frequency. On the other hand the dielectric constant of the films enhanced with an increase in OMP. But the loss tangent of the films decreases linearly up to 150 kHz above that progressively increases with a rise in frequency, and is a typical behavior of a linear dielectric. This can be explained as with interfacial polarization predicted by the Maxwell - Wagner model [30] in agreement with Koop's phenomenological theory [31]. According to these models, the dielectric materials can be imagined as a heterogeneous structure consisting of well conducting grains separated by thin layers of poorly conducting grain boundaries. These grain boundaries could be formed during the annealing process either by superficial reduction or oxidation of crystallites in the pores materials as a result of their direct contact with the firing atmosphere. Further, the loss tangent of the films decreases with an increase in OMP.

Further to see the influence of OMP on dielectric response of BNO - BWO nanocomposite films, dielectric constant and loss tangent is plotted as a function of OMP and displayed in Fig. 5.17 (c). It is found that the dielectric constant of the films enhanced with an increase in OMP whereas the loss tangent decreases except in the case of 50% OMP and these variations are attributed to the increase in crystallinity and average grain size. The variation in dielectric constant and *tanδ* of the BNO - BWO nanocomposite films, measured at 1 MHz as a function of temperature is shown in Fig. 5.18 (a) and 5.18 (b), respectively.

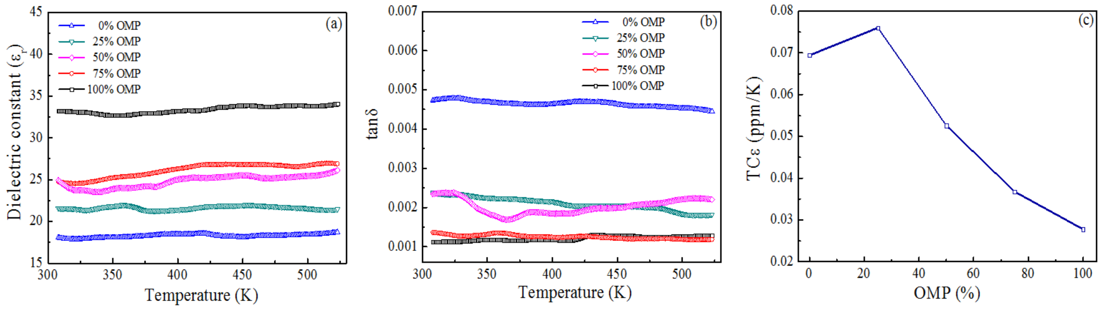

Fig. 5.18: *Variation in (a) dielectric constant, (b) loss tangent of BNO - BWO thin films deposited at different OMPs and measured as a function of temperature. (c) plot of TCε versus different OMPs.*

It is observed that there is not much variation in both the dielectric constant and *tanδ* with increase in temperature; this shows the stability of the films over the measured temperature range. Further as the OMP increases, the dielectric constant of the films enhanced whereas the *tanδ* reduced significantly. Films deposited in pure argon atmosphere exhibited low dielectric constant (18.7) and high loss tangent (0.0047) whereas the films deposited in pure oxygen plasma showed high dielectric constant (34) and low loss tangent (0.0011). However, there is no report available on the dielectric properties of these films. In the case of bulk the reported dielectric properties are found to be in the range of ε_r = 16.9 - 21, $Q\times f_0$ = 49.5 - 56.7 THz and τ_f = 8.9 to -4.3 ppm / °C [7].

The microwave dielectric properties of as - deposited and annealed BNO – BWO thin films were measured at 5, 10 and 15 GHz using a split post dielectric resonator (SPDR) method are tabulated in **Table 5.6** and **Table 5.7**, respectively. In both the cases, it is found that the dielectric properties show a profound frequency dispersion that is expected in the case of a linear dielectric. Furthermore, as the OMP increases, the dielectric properties of the films enhanced and films deposited in pure oxygen plasma exhibited the best microwave dielectric properties. The annealed films show better properties as compared to the as deposited films, and are attributed to the increase in crystallinity and enhanced uniform grain sizes.

Table 5.6: *Microwave dielectric properties of as-deposited BNO - BWO thin films deposited on quartz substrates, measured by using split post dielectric resonator method.*

As-Deposition						
	At 5 GHz		At 10 GHz		At 15 GHz	
OMP (%)	ε_r	*tanδ*	ε_r	*tanδ*	ε_r	*tanδ*
0	31.71	0.0045	18.94	0.0052	14.87	0.0064
50	34.43	0.0025	19.55	0.0029	15.37	0.0058
100	34.91	0.0015	19.62	0.0023	15.63	0.0032

Table 5.7: *Microwave dielectric properties of annealed BNO - BWO thin films deposited on quartz substrates, measured by using split post dielectric resonator method.*

After Annealing						
	At 5 GHz		At 10 GHz		At 15 GHz	
OMP (%)	ε_r	*tanδ*	ε_r	*tanδ*	ε_r	*tanδ*
0	38.63	0.0027	29.89	0.0035	22.47	0.0038
50	43.25	0.0018	31.26	0.0020	27.48	0.0025
100	49.81	0.0010	33.43	0.0016	28.42	0.0019

The obtained microwave dielectric properties can be correlated with XRD data using the Lotgering orientation factor (*F*) as distinct from the XRD patterns (Fig. 5.19) of annealed BNO – BWO films, deposited on quartz substrates under various OMPs. Fig. 5.19 (b) shows the orientation factor (*F*) of BWO (112) and BNO (110) reflections as a function of OMP and the preferred orientation growth mechanism can be demonstrated on the basis of Lotgering analysis [32] with respect to a reference plane (*abc*) defined as

$$F = \frac{(P - P_0)}{(1 - P_0)} \tag{4}$$

$$P = \sum I_{(abc)} / \sum I_{(hkl)} \tag{5}$$

Where, *abc* indicates the Miller indices and *P* is specially appointed to stand for the ratio of the sum of intensities of the evaluated reflections (*abc*) to the sum of all reflections of the textured thin film. The value P_0 stands for the equivalent ratio for the ceramic powder of the BNO – BWO composite target with random orientation. Generally, the value of the orientation factor for preferred orientation factor should lie within the range of 0 to 1. Thus, $F = 0$ designates a film with randomly oriented grains, while $F = 1$ represents a perfect epitaxial growth.

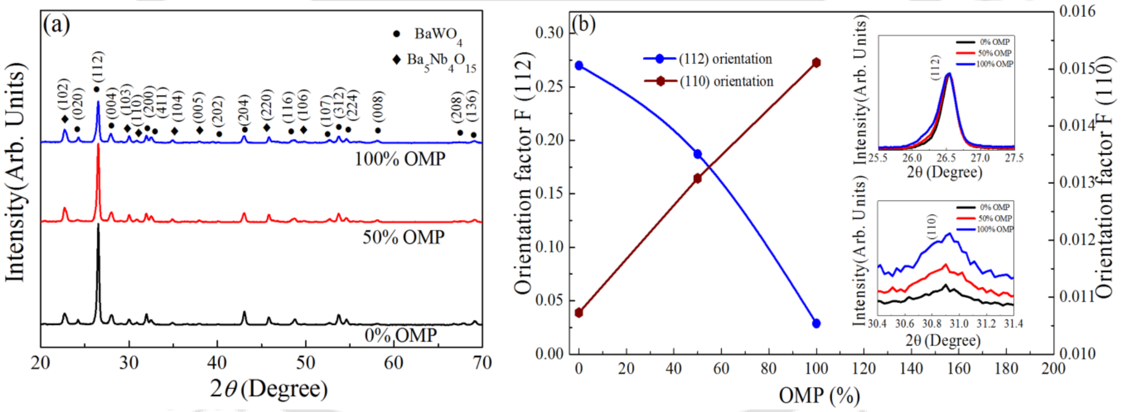

Fig. 5.19: *(a) XRD patterns of the BNO - BWO nanocomposite films and annealed on quartz substrates at 700 °C for 2 h at different OMPs. (b) Dependence of Lotgering orientation factor (F) of as a function of OMP (inset) shows the variation of XRD peak intensity of BWO (112) and BNO (110) reflections as a function of OMP.*

In the present case, all the diffraction peaks lie in the range $2\theta = 20° - 70°$ has been used to calculate *P* and P_0. The P_0 values obtained from the BNO – BWO sputtering targets are found to be 0.2633 and 0.0073 for the BWO (112) and BNO (110) planes, respectively. The calculated orientation factors for the BWO (112) and BNO (110) reflections are plotted against a function of OMP and are shown in Fig. 5.19 (b). Further, the orientation factor (inset of Fig. 5.19 (b)) and intensities of peaks for a BWO (112) and

BNO (110) plane decreased and increase continuously with OMP. Furthermore, the orientation factor values are positive and found to be 0.269 – 0.028 and 0.010 – 0.015 for BWO (112) and BNO (110) reflections, correspondingly, and we observed that with an increase in OMP, the film grows in BNO (110) preferred orientation. The possibility of variation in orientation factor values of BWO (112) and BNO (110) reflections may be caused due to the geometry of atoms/particles and the kind of reaction, that is taking place in the sputtering chamber. Thereafter, we confirm that the increase in intensity, orientation factor of BNO (110) reflections with the increase in OMP, is causing the enhancement in microwave dielectric properties. To compare the microwave dielectric properties of BNO – BWO films with bulk properties, the microwave dielectric properties of BNO – BWO ceramics were measured using the Hakki - Colemann method. The observed dielectric properties were found to be $\varepsilon_r = 18$, $Q\times f_0 = 55.6$ THz.

The observed dielectric constant is larger as compared to the bulk value whereas the loss tangent is enhanced. The variations in dielectric constant are attributed to the increase in density and crystallinity of the films. Whereas the changes in the loss tangent is due to the partial crystallinity, small particle size and strain in the deposited films. Further, it is known that the strain in the films arises due to the lattice mismatch between the substrate and film and insufficient thermal energy during the deposition. Large grain size and strain in bulk ceramics would minimizes the loss tangent due to high sintering temperatures.

The temperature stability of the dielectric constant of the BNO – BWO nanocomposite films are evaluated by calculating the temperature coefficient of dielectric constant ($TC\varepsilon$). $TC\varepsilon$ is obtained by using the following expression

$$TC\varepsilon = \frac{\Delta\varepsilon_r}{\varepsilon_0 \Delta T}(ppm/^o C) \tag{6}$$

Where, $\Delta\varepsilon_r$ is the change in ε_r with respect to the value ε_0 (T = 310 K) and ΔT is the change in temperature relative to 310 K. The variation in $TC\varepsilon$ as a function of OMP is shown in Fig.5.18 (c), and it observed that all BNO – BWO films revealed positive $TC\varepsilon$ values across. It demonstrates that as the OMP of the film increases, the $TC\varepsilon$ of BNO – BWO films decreased linearly and the film with 100% OMP film exhibits a better stability 0.027 ppm/K.

5.3.2.5 AC conductivity studies

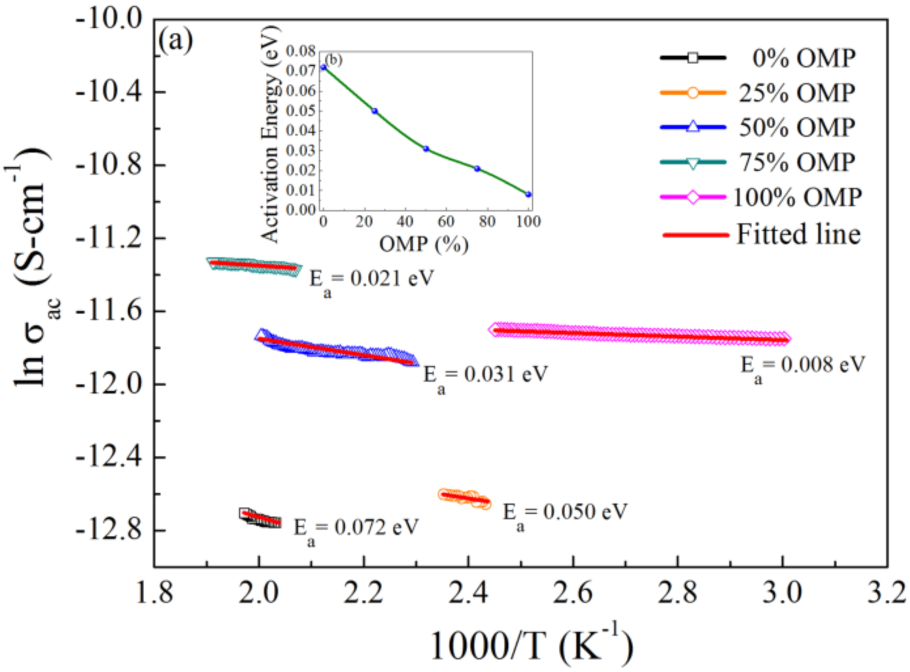

Fig. 5.20: *(a) Temperature dependence of ac conductivity of BNO - BWO nanocomposite films in the temperature range from 310 K to 520 K, (inset) (b) plot of Activation energy versus OMP.*

Fig. 5.20 (a) shows the temperature dependence of ac conductivity of BNO - BWO nanocomposite films in the temperature range from 310 K to 520 K. The Arrhenius plot has been obtained by plotting the logarithm of ac conductivity $\sigma_{ac,}$ versus the inverse temperature *1000/T*, measured at 1MHz. The activation energy of the films was found out using the below equation

$$\sigma_{ac} = \sigma_0 exp^{(-E_a/k_BT)} \qquad (7)$$

Where, σ_o is pre - exponential factor, E_a is the activation energy, k_B is the Boltzmann constant and T is the absolute temperature. The estimated values of activation energies of the composite films are found to be E_a = 0.072, 0.050, 0.031, 0.021 and 0.008 *eV* for the films deposited at 0, 25, 50, 75 and 100% OMPs, respectively. The inset of Fig. 5.20 (a) shows linear decrement of E_a value with respect to OMP. The activation energy can be divided into two parts: a contribution arising from the thermal activation of charge carriers into the conduction band and one more contribution from the energy that is required to form the defects and is instantly linked to the change in the number of charge carriers in the conduction band [33]. The temperature dependence of ac conductivity designates that the electrical conduction in the deposited films is a thermally activated process. When sufficient thermal energy is available to mobile ions, they start to jump over their sites and subsequently to neighboring sites, giving a contribution to the ac conductivity.

5.3.2.6 Raman analysis on $Ba_5Nb_4O_{15}$ - $BaWO_4$ composite thin films

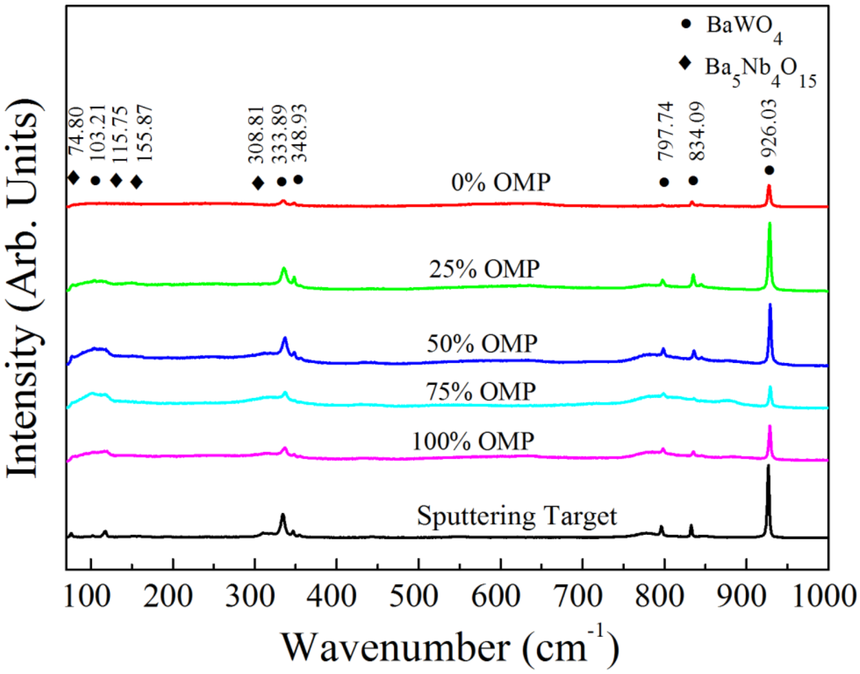

Fig. 5.21: *Raman spectra of BNO-BWO thin films deposited on Pt-Si substrates, deposited at different OMPs. The numbers above the peaks is the Raman shift in* cm^{-1}.

Fig. 5.21 shows the Raman spectra in the range from 70 to 100 cm^{-1} of annealed BNO - BWO nanocomposite thin films excited by the 514.5 nm line of an Ar - ion laser processed at room temperature. The Raman active phonon modes can be employed to estimate the structural order at short - range in the materials. In the case of BWO, the vibration modes in the Raman spectra of tungstates can be classified into internal and external groups. The internal vibrations are related to the $[WO_4]^{2-}$ and external vibrations are associated to the motion of the Ba^{2+} cation and rigid molecular units. The internal vibrations 926.03, 834.09, 797.74, 348.93, 333.89 cm^{-1} and the external vibration modes were localized at 103.21 cm^{-1}. The Raman spectra of $Ba_5Nb_4O_{15}$ shows that the symmetric stretching of weak vibration modes at 844.50, 312.51 cm^{-1}. The $Ba_5Nb_4O_{15}$ also had extra lines at 155.81, 115.75, 74.80 cm^{-1} with an increase in OMP and the obtained response is similar to the earlier reports [26]. It is significant to note that the BNO – BWO composite films displayed all the Raman actives correspond to the individual BNO and BWO, which demonstrate that the coexistence of composite phase and this result is in agreement with the obtained XRD patterns and microstructures.

5.4 Conclusions

The $Ba_5Nb_4O_{15}$ (BNO) and $BaWO_4$ (BWO) nanosized particles powders were prepared by sol – gel process. The particle size and shape analysis of these powders characterized by TEM and these nanoparticles are in cylindrical and hexagonal shapes, respectively. The influence of BNO and BWO nanosized particles on BNO - BWO composite matrix have been studied systematically with regard to phase development, and fine grained microstructure by using XRD and SEM techniques, respectively. The broadband dielectric studies reveal that both the dielectric constant (ε_r) and loss tangent ($tan\delta$) of samples showed nearly a stable response with frequency upto 10 MHz, in the temperature range (-140 ^{o}C to 220 ^{o}C) for the samples added with different x wt%. HN equation was used to fit the experimental complex dielectric data at a given temperature and this HN function explains the electronic equivalent circuit, and is found to exhibit a parallel R_1C_1 combination in series with C_2. The samples added with x = 3 wt%, fired at 900 ^{o}C displayed the best microwave dielectric properties with maximum relative density of 98.2% and denser in microstructure, shows a maximum ε_r and $Q\times f_0$ values of 39 and 59.8 THz at 9.44 GHz, respectively. The fabricated fully densed BNO - BWO composite ceramic at lower sintering temperature, with best microwave dielectric properties are suitable for LTCC based applications.

Nanocrystalline BNO – BWO composite films were deposited by using RF magnetron sputtering under different OMPs. The effect of OMP and annealing temperature on structural, microstructural, optical, electrical and dielectric properties of BNO – BWO nanocomposite films studied systematically.

- The XRD patterns of the films reveal the coexistence of both BNO – BWO films, and the SEM images of these films show the coexistence of rod - shaped BNO particles and hexagonal BWO particles.
- The as deposited films exhibit transmittance above 90% whereas the annealed films display a change in color, this may be due to the electrochromic response of these films.

- The dielectric response of these films indicates a frequency and temperature independent behavior and indicated a profound dependence on OMP.
- AC conductivity studies reveal that the conduction in these films arises due to thermal activation.
- Raman spectroscopy of the films showed the signature of both the phases.
- The obtained dielectric and optical response of these films are suitable for microelectronic devices, smart window and display applications.

5.5 References

[1] H. Zhuang, Z. Yue, S. Meng, F. Zhao, L. Li, *J. Am. Ceram. Soc.* **91** (2008) 3738.

[2] K. Sudheendran, K. C. James Raju, M. V. Jacob, *J. Am. Ceram. Soc.* **92** (2009) 1268.

[3] P. S. Anjana, M. T. Sebastian, *Int. J. Appl. Ceram. Technol.* **5** (2008) 84.

[4] D. Pamu, G. L. Narayana Rao, K. C. James Raju, M. V. Jacob, *Science and Technology of Advanced Materials* **8** (2007) 469.

[5] S. Kamba, J. Petzelt, I. N. Jawahar, M. T. Sebastian, *J. Appl. Phys.* **89** (2001) 3900.

[6] H. Zhuang, Z. Yue, F. Zhao, J. Pei, L. Li, *J. Alloys Compd.* **472** (2009) 411.

[7] H. Zhuang, Z. Yue, F. Zhao, L. Li, *J. Am. Ceram. Soc.* **91** (2008) 3275.

[8] B. Geller, B. Thaler, A. Fathy, V. Pendrick, Technologies for Wireless Applications, Digest, IEEE MTT-S Symp. (1999) 189.

[9] L. Golonka, P. Bembnowicz, D. Jurkow, *Optica Applicata* **41** (2011) 383.

[10] T. Joseph, M. T. Sebastian, H. Jantunen, M. V. Jacob, H. Sreemoolanadhan, *Int. J. Appl. Ceram. Technol.* **8** (2011) 854.

[11] C. H. Shen, C. L. Huang, *Int. J. Appl. Ceram. Technol.* **7** (2010) 207.

[12] L. J. Golonka, *Bulletin of the Polish Academy of Sciences Technical Sciences* **54** (2006) 221.

[13] J. Mazierska, M. V. Jacob, A. Harring, J. K. Peter Barnwell, *Journal of the European Ceramic Society* **23** (2003) 2611.

[14] J. R. Long, S. Hua, T. X. Li, J. Y. Lan, *Chinese Physics B* **23** (2014) 47801.

[15] T. Joseph, M. T. Sebastian, H. Sreemoolanadhan, V. K. S. Nageswari, *Int. J. Appl. Ceram. Technol.* **7** (2010) E98.

[16] C. L. Huangw, J. J. Wang, C. Y. Huang, *J. Am. Ceram. Soc.* **90** (2007) 1487.

[17] C. L. Huang, M. H. Weng, C. T. Lion, C. C. Wu, *Materials Research Bulletin* **35** (2000) 2445.

[18] B. Zhu, C. Xia, X. Luo, G. Niklasson, *Thin Solid Films* **385** (2001) 209.

[19] Y. J. Hsiao, Y. H. Chang, *J. Am. Ceram. Soc.* **90** (2007) 2287.

[20] F. M. Pontes, M. A. Maurera, E. R. Leitea, R. Magnani, J. A. Varel, *Journal of the European Ceramic Society* **23** (2003) 3001.

[21] A Pandey, R Manivannan, *Recent Patents on Nanomedicine* 5 (2015) 33.

[22] Suk - Joong L. kang, Sintering: Densification, Grain Growth and Microstructure, Elsevier Butterworth - Heinemann, Linacre House, Jordan Hill, Oxford OX2 8DP, Burlington, Massachusetts 01803 (2005).

[23] M. J. Kirchhof, H. Forster, H. J. Schmid, W. Peukert, *Journal of Aerosol Science* **45** (2012) 26.

[24] F. Kremer, and A. Schönhals, Broadband Dielectric Spectroscopy, Springer – Verlag Berlin Heidelberg New York 2003.

[25] E. Barsoukov, and J. R. Macdonald, Impedance Spectroscopy Theory, Experiment, and Applications, John Wiley and Sons Inc., 2nd Ed., River street, Hoboken, New Jersey (2005).

[26] N. E. Massa, *Phys. Rev. B* **53** (1996) 8148.

[27] R. Dinesh, T. Fujiwara, T. Watanabe, *J. Mater. Sci.* **41** (2005) 1541.

[28] R. Swanepoel, *J. Phys. E: Sci. Instrum.* **16** (1983) 1214.

[29] J. C. Tauc, Optical Properties of Solids, (North-Holland, Amsterdam, 1972).

[30] J. Maxwell, Electricity and Magnetism, (Oxford University Press, London, 1873).

[31] C. G. Koops, *Phys. Rev.* **83** (1951) 121.

[32] F. K Lotgering, *J. Inorg. Nucl. Chem.* **9** (1959) 113.

[33] C. H. Kwon, H. K. Hong, B. H. Leeb, *Sens. Actuators B* **24** (1995) 610.

Chapter 6

Summary and future scope

In this chapter we conclude this dissertation by summarizing our contributions on the structural, microstructural and microwave dielectric properties of BNO, BWO and BNO - BWO composite based on both bulk and thin films samples. The most significant highlights of the current investigations and possibilities of supplementary extension of the work in future directions are also summarized.

6.1 Summary of the works

In summary, dielectric resonators (DRs) of $Ba_5Nb_4O_{15}$ and $BaWO_4$ ceramics have been prepared using mechanical alloying method and semi - alkoxide precursor (sol - gel) method. The $Ba_5Nb_4O_{15}$ - $BaWO_4$ composite have been prepared in the bulk form using the conventional solid - state reaction method. The overall efforts in this study are to enhance the microwave dielectric properties of the bulk samples by improving the microstructure and relative density of this material prepared with the addition of their own nanoparticles prepared by sol - gel process. Successful efforts were made to reduce the sintering temperature without affecting the microwave dielectric properties of the $Ba_5Nb_4O_{15}$ and $Ba_5Nb_4O_{15}$ - $BaWO_4$ ceramics by supplementing with their own nanoparticles. Furthermore, it is proposed to compare the microwave properties of $Ba_5Nb_4O_{15}$ (BNO), $BaWO_4$ (BWO) and $Ba_5Nb_4O_{15}$ - $BaWO_4$ (BNO - BWO) in bulk and thin film forms. In addition, we have also investigated their optical and electrical properties, which could not only be useful in various applications but also helps in arriving at a comprehensive picture of the physics of these materials, and the results were compared with the existing literature. The investigations performed in my present thesis work are divided into six chapters.

First chapter provides the brief introduction to dielectric materials, dielectric resonators (DRs) and related areas. A historical background and the development of DRs from the physics and device point of view are presented with their technological importance at current trends. The basic requirements of a material to be used as DR, a brief overview on DR materials are described. The basic applications of dielectric thin films with their importance in various areas of interest in the present technological world.

Subsequently, the importance of $Ba_5Nb_4O_{15}$ (BNO), $BaWO_4$ (BWO) and $Ba_5Nb_4O_{15}$ - $BaWO_4$ (BNO - BWO) as a DR and a brief overview on its crystal structure and microwave dielectric properties are presented. In second chapter, various preparation and structural, microstructural and microwave characterization techniques, being used for both bulk and thin films of BNO, BWO and BNO - BWO composite ceramics are presented.

The third chapter describes the preparation of pure phase BNO ceramic in two different methods: while the former one is a mechanical alloying method, the later one is a conventional solid-state reaction method. The BNO samples prepared by using mechanical alloying method by optimizing the process conditions such as milling time, ball to powder ratio, milling speed, sintering temperature and sintering duration. The obtained best dielectric properties at microwave frequencies are ε_r = 34, $Q{\times}f_0$ = 32.5 THz (7 GHz) are attributed to increase in density and uniform grain size for the BNO samples milled for 40 *h*, sintered at 1250 ^{o}C. Furthermore, we have studied the effect of BNO nanoparticles (prepared by sol - gel process) on the microstructure, high frequency dielectric and microwave dielectric properties of bulk $Ba_5Nb_4O_{15}$ ceramics (prepared by conventional solid-state reaction method) are discussed. The BNO thin films prepared by RF magnetron sputtering are described by optimization of all processing conditions. The sputtering targets of BNO ceramics prepared by optimized processing conditions of the mechanical alloying method. The BNO thin films were deposited on to various substrates (amorphous SiO_2 and on platinized silicon ($Pt/TiO_2/SiO_2/Si$)) under different oxygen mixing percentage (OMP) in the sputtering gas. The effect of OMP and post annealing temperature on the structural, microstructural, optical and dielectric properties were presented. To the best of the authors' knowledge, there is no report available on the BNO thin films; this motivated us to pursue these studies. Upon annealing, refractive indices of the films enhanced whereas the bandgap is decreased. The obtained refractive index values are in the range of 1.82-2.05, and 1.89-2.16 @ 550 nm for the as-deposited and annealed BNO films, respectively. The estimated optical bandgap values for the as deposited and annealed films are in the range of 4.13 - 4.36 *eV* and 4.07- 4.24 *eV*, respectively. The best dielectric properties were obtained for the BNO film with thickness of 450 nm are ε_r = 41 and $tan\delta$ = 0.0005 at 1 MHz. Split-post dielectric resonator method was used to measure dielectric properties at discrete microwave frequencies (5, 10 and 15 GHz) and are in the range of ε_r = 29.65 - 43.56 and $tan\delta$ = 0.0074 - 0.0020, for BNO annealed films. The detailed observations, discussion and possible explanations are presented in this chapter.

In fourth chapter, we have prepared $BaWO_4$ (BWO) samples by using mechanical alloying method. The crystal structure, microstructure, and microwave dielectric properties of BWO ceramics are discussed. The obtained best dielectric properties at microwave frequencies are $\varepsilon_r = 16.3$, $Q\times f_0 = 38$ THz (11.6 GHz) are attributed to increase in density and uniform grain size for the BNO and BWO samples milled for 50 *h*, sintered at 800 ^{o}C, respectively. The BWO thin films were deposited by RF magnetron sputtering on amorphous SiO_2, and on platinized silicon ($Pt/TiO_2/SiO_2/Si$) substrates under the influence of different oxygen mixing percentage (OMP) in the sputtering gas by optimizing all processing conditions. The sputtering target of BWO was prepared by optimized processing conditions in the mechanical alloying method. The effect of OMP and post annealing temperature on the structural, microstructural, optical and dielectric properties were presented. To the best of the authors' knowledge, there is no report available on the BWO thin films. BWO films have been deposited at different substrate temperatures (RT, 200, 400, 600 and 800 ^{o}C) using RF magnetron sputtering in pure argon plasma. BWO films deposited at 800 ^{o}C exhibit crystalline nature. First time we are reporting the irreversible thermochromic behaviour of $BaWO_4$ (BWO) films. The optical bandgap of BWO films increases significantly with an increase in Oxygen mixing percentage (OMP) during the deposition. The optical bandgap of the BWO films deposited at different temperatures in pure argon plasma, are in the range of 3.7 to 3.94 *eV* whereas the films deposited at 600 ^{o}C under different OMP plasma are in the range of 3.6 - 4.5 *eV*. Metal-Insulator-Metal (MIM) capacitors were fabricated under different OMPs for the films deposited on platinized silicon substrates. The measured dielectric properties show a progressive improvement with OMP and a maximum asset value of $\varepsilon_r = 15$ and $tan\delta$ = 0.019 at 1 MHz are obtained for the BWO film deposited at 50% OMP. The detailed observations, discussion and possible explanations are presented in this chapter. The microwave dielectric properties measured at different frequencies (5, 10 and 15 GHz) and are in the range of ε_r = 11.94 - 18.16 and $tan\delta$ = 0.010 - 0.030, for BWO annealed films.

In fifth chapter, we describe the prepared BNO - BWO composite in the bulk form using the conventional solid - state reaction method. The best microwave dielectric properties of $\varepsilon_r \sim 39$, $Q\times f_0 \sim 59.8$ THz (9.44 GHz) were obtained for the BNO - BWO composite ceramics, sintered at 900 ^{o}C. Also studied the effect of BNO and BWO nanosized particles (prepared by sol - gel process) addition on the microstructure, high frequency dielectric and microwave dielectric properties of the $Ba_5Nb_4O_{15}$ - $BaWO_4$

composite ceramics are discussed. The BNO - BWO composite thin films were prepared by using RF magnetron sputtering. The dielectric constant of the BNO - BWO films enhanced with increase in OMP, whereas the $tan\delta$ reduced significantly. The BNO - BWO films deposited in pure argon atmosphere exhibited low dielectric constant (18.7) and high loss tangent (0.0047) whereas the films deposited in pure oxygen plasma showed high dielectric constant (34) and low loss tangent (0.0011). The obtained microwave dielectric properties are in the range of ε_r = 22.47 - 49.81 and $tan\delta$ = 0.0038 - 0.0010, for BNO - BWO annealed films. The detailed observations, discussion and possible explanations are presented in this chapter.

In the present study, DRs of BNO, BWO and BNO - BWO composite have been prepared by mechanical alloying and solid state reaction method. The BNO, BWO and BNO - BWO thin films were prepared with RF reactive magnetron sputtering respectively. In bulk form BNO, BWO and BNO - BWO has dielectric constant of 34, 16.3 and 39, and $Q\times f_o$ of 32.5 THz, 38.05 THz, and 59.8 THz observed for the sample sintered at 1250 ^{o}C, 800 ^{o}C, and 900 ^{o}C respectively, where as in BNO, BWO and BNO - BWO composite thin film form dielectric constant of 35.45, 16.53 and 38.63, and $tan\delta$ = 0.0070, 0.020 and 0.0027 were observed at 10 GHz, and 5 GHz, respectively. The dielectric constant of each film is close to the bulk value whereas the dielectric losses of the films are observed to be higher than the bulk value.

From the present study, the obtained excellent microwave dielectric properties of the BNO, BWO and BNO - BWO based ceramics makes these materials suitable for type -I capacitor, dielectric resonators for various microwave communication applications. The fabricated fully densed BNO - BWO composite ceramic at low sintering temperature (900 ^{o}C), with best microwave dielectric properties are suitable for LTCC based applications. Furthermore, the optimized best optical and dielectric properties of pure BNO, BWO and BNO - BWO composite thin films are suitable for optoelectronic, antireflection, integrated electronic and CMOS applications. Further, the observed irreversible thermochromic behavior of BWO films was suitable for decorative and smart window applications.

6.2 Scope for the future work

To reduce the sintering temperature of the BNO and BNO - BWO composite based ceramics, by improving densification, microstructural and microwave dielectric properties. We have studied the ceramic matrix system with the addition of their own nanoparticles of BNO and BWO as sintering aids. We have paying attention on to reduce microwave dielectric losses that are extrinsic in nature by process optimization. It's essential to understand the loss mechanisms of BNO - BWO composite and its individual components. So, it's important to study the nature of loss mechanisms especially intrinsic losses. However, we have not studied the intrinsic loss mechanisms and can be studied with far IR reflectivity spectroscopy.

For the thin films cases, since the crystallinity and microstructure are playing a significant role on optical, electrical and microwave dielectric properties, a systematic study of the films by varying the substrate temperature during deposition and different film thickness will be beneficial. A comprehensive compositional analysis of BNO, BWO and BNO - BWO thin films deposited at different substrate temperatures and pressure are considered necessary to explain the loss mechanisms of the films. Films deposited with same oxygen mixing percentages (OMPs) but having different microstructures can be obtained by annealing or heating during deposition. A detailed compositional analysis with independent control over the microstructure will help in interpreting the observed variations in optical and dielectric properties with changes in OMP during deposition.

The dielectric properties of these films are measured only at a few spot frequencies in the microwave range. It will be interesting to do a broad - band measurement of dielectric constant (ε_r) and loss tangent ($tan\delta$) of these films spanning over a few bands to ascertain the loss mechanisms in these films at such frequencies.

List of publications

1) **C. Anil Kumar**, D. Pamu, Dielectric, Optical and Electric Studies on Nanocrystalline $Ba_5Nb_4O_{15}$ Thin Films Deposited by RF Magnetron Sputtering, *Appl. Surf. Sci.* **340** (2015) 56.
2) **C. Anil Kumar**, T. Santhosh Kumar, and D. Pamu, Irreversible Thermochromic Response of RF Sputtered Nanocrystalline $BaWO_4$ Films for Smart Window Applications, *AIP Advances* **5** (2015) 107232.
3) **C. Anil Kumar**, D. Pamu, Dielectric And Electrical Properties of $BaWO_4$ Film Capacitors Deposited by RF Magnetron Sputtering, *Ceram. Int.* **41** (2015) S296.
4) **Chikkala Anil Kumar**, Dobbidi Pamu, Sylvester Josephine, Impedance Spectroscopy, Broadband, and Microwave Dielectric Properties of Mechanically Alloyed $Ba_5Nb_4O_{15}$ Ceramics, *Int. J. Appl. Ceram.Technol.*, **13** (2016) 554.
5) **C. Anil Kumar**, D. Pamu, Dielectric and Optical Characterization of RF Sputtered $Ba_5Nb_4O_{15}$–$BaWO_4$ Composite Films for Electronic and Smart Window Applications, *J. Electron. Mater.* **45** (2016) 3101.
6) **C. Anil Kumar**, D. Pamu, Broadband and Microwave Dielectric Studies on $Ba_5Nb_4O_{15}$ Ceramics Supplemented with its Nanoparticles for Cryogenic Electronic Applications, *J. Electron. Mater.* DOI: 10.1007/s11664-016-5004-5.
7) **Anil Kumar. C**, Pamu D, Microwave Dielectric Properties of Low Temperature Fired $Ba_5Nb_4O_{15}$–$BaWO_4$ Ceramics Supplemented with their Own Nanoparticles for LTCC Applications, *Int. J. Appl. Ceram.Technol.*, DOI: 10.1111/ijac.12639.

Conferences and workshops

1) **Anil Kumar. C**, Pamu D, Deposition and Characterization of RF Sputtered Nanocrystalline $Ba_5Nb_4O_{15}$ Thin Films for Wide Bandgap Applications, presented in **"*International Conference on Advanced Nanomaterials and Nanotechnology*"** (ICANN- **2013), IIT Guwahati, India.**

2) **Anil Kumar. C**, Pamu D, Dielectric and Electrical Properties of Nanocrystalline $Ba_5Nb_4O_{15}$ Thin Films Deposited by RF Magnetron Sputtering for Microwave Integrated Capacitor Applications, presented in **"*International Conference on Nano Science & Engineering Applications*" (ICONSEA-2014), Hyderabad, India.**

3) **Anil Kumar. C**, Pamu D, Effect of V_2O_5 on $BaWO_4$ thin films deposited by RF sputtering for microwave decorative and dielectric capacitor applications, presented in ***"Interantional conference on Technologically Advanced Materials and Asian Metting on Ferroelectricity" (ICTAM-AMF 10) November 7-11, 2016, New Delhi, India.***

4) **Anil Kumar Chikkala**, Susmita Rabha, Pamu Dobbidi, Structural and Dielectric Properties of (1-x)$MgTiO_3$-x $Ba_5Nb_4O_{15}$ Composite, presented in ***"The 10th Asian Meeting on Electroceramics"*** (***AMEC-2016) Dec. 04-07, 2016, Taipei, Taiwan.***

5) Participated in National Workshop on "Advanced Probing Techniques in TEM," ***Organized by Indian Institute of Technology Guwahati & Electron Microscopy Society of India Venue: Conference Center, IIT Guwahati Date: February 15-16, 2016, India.***

6) Participated in National Workshop on "NEMS/MEMS and Theranostic Devices," ***21st-22nd March 2016, at Centre for Excellence in Nanoelectronics & Theranostic Devices under the aegis of Centre for Nanotechnology at the Indian Institute of Technology Guwahati, India.***